Imperial College London

Department of Materials

Mesoscale modelling of steel processing

Tansel Tanner Arif

STATEMENT OF COPYRIGHT

DECLARATION OF ORIGINALITY

I, Tansel T. Arif, hereby declare that the contents of this thesis are my own. Neither this thesis nor the work contained within have been submitted elsewhere for any other qualification. All work of others have been acknowledged and referenced in the form of a list of sources.

Abstract

Numerical methods are utilised to reproduce the evolution of a system observed in natural phenomena. Within the area of materials science there is an increase of interest in modelling techniques that can accurately predict the microstructure of a material subject to various processing conditions. Recently, there is a requirement of techniques that have the ability to be applied to systems involving microstructural change in the presence of fluid flow. This presents a challenge since the forces governing these processes involve those predominately influenced by thermodynamics as well as those influenced by hydrodynamics.

The phase-field method, a popular technique used in this area, has been shown to have the ability to cope with phase transformation dynamics such as solidification and solid-state phase transformations. However, its predictive capabilities mainly apply to a flow free environment where flow effects are minimal compared to other effects. Other techniques such as smoothed particle hydrodynamics exist that are more than capable of describing the mechanisms of flow demonstrating superiority in many complex flow problems. The thermodynamic quantities related to the evolution of a system to which this method is applied must then be consistent in order to be translated between models.

This thesis develops the tools necessary to deal with phase growth and microstructural change within the presence of flow. This is done by developing phase-field models that can efficiently deal with displacive transformations in steels as well as diffusive, and SPH models with the ability to be coupled with thermodynamics. The phase-field models are developed to be applied to structure growth observed at relatively low temperatures within steels, namely martensite and bainite growth. The SPH method is analysed in order to assess and provide solutions for consistency when considered for coupling with models mainly dependent on thermodynamics.

Acknowledgements

'Nobody made a greater mistake than he who did nothing because he could only do a little.'

Edmund Burke

Contents

List of Figures

Symbols

k_c - curvature of the interface

$\tilde{\sigma}_s(\theta)$ - function of the surface tension

λ - half interface length

c_h - heat capacity

$M(\theta)$ - interfacial mobility

L - latent heat of fusion

T_M - melting temperature

$\mathbf{v}_n$ - normal velocity of the interface

T - temperature

D_T - thermal diffusivity

M_c - phase-field mobility for the concentration

M_T - phase-field mobility for the temperature

η - phase-field order parameter

M_ϕ - phase-field mobility for the phase-field variable

ϕ - phase-field variable

$\mathbf{r}$ - position vector

V - volume

g_0 - homogeneous free energy density

g - total free energy density

$g_{\alpha'}$ - homogeneous free energy density of martensite

$g_{\gamma'}$ - homogeneous free energy density of austenite

ϵ - gradient energy coefficient

G - total Gibbs free energy

G_m - total molar Gibbs free energy

c - composition

ω - kinetic coefficient

t - time

σ - interfacial energy

Ω - system volume

Ω_L - the set of points corresponding to the liquid phase

Ω_S - the set of points corresponding to the solid phase

Γ - the set of points corresponding to the interface

s - entropy density

e - internal energy density

S - total entropy

E - total internal energy

f - Helmholts free energy density

F - Helmholts free energy

f^s - free energy density of the solid phase

f^L - free energy density of the liquid phase

μ^s - chemical potential in the solid phase

μ^L - chemical potential in the liquid phase

C_p - specific heat capacity at constant pressure

c_s - solid composition

c_L - liquid composition

D_c - solute diffusivity

ϵ - secondary order parameter, gradient energy coefficient

ϵ_c - gradient energy coefficient for composition

ϵ_e - gradient energy coefficient for internal energy

ϵ_ϕ - gradient energy coefficient for the phase-field variable

n - number of moles

n_i - number of moles of component i

X_i^s - mole fraction of component i in sublattice s

Y_i^s - site fraction of component i in sublattice s

G_i - Gibbs free energy of component i

$°G_i$ - Gibbs free energy of component i

G - total molar Gibbs free energy

$^E G$ - excess molar Gibbs free energy

G^{mo} - contribution to the total molar Gibbs free energy due to magnetic ordering

$W(\mathbf{r})$ - weight function or kernel at position $\mathbf{r}$

$\delta(\mathbf{r})$ - Dirac delta function

h - smoothing length

$B(h)$ - support domain of a kernel

ρ - density

$\mathbf{v}$ - velocity

P - pressure

η_V - shear viscosity

ζ - bulk viscosity

K - thermal conductivity

$\mathbf{P}$ - stress tensor

σ - viscous stress tensor

ϕ - viscous heating field

d - dimension

$D(T)$ - atom diffusivity

K_b - kinetic barrier

$\tilde{\sigma}$ - external stress

σ_N - normal component of applied stress

τ - tangential component of applied stress

δ - dilatation

s - shear

μ - shear modulus

σ_p - poisson's ratio

Δ - uniform dilatation

a - dimension of oblate ellipsoid

c_a - dimension of oblate ellipsoid

s_x - shear in the x-direction

s_y - shear in the y-direction

U - energy due to an applied stress

m_i - mass of particle i

ρ_i - mass density of particle i

$\mathbf{r}_i$ - position of particle i

D_L - a constant in the Leonard-Jones potential related to the maximum velocity

r_0 - a specified reference distance

ρ_0 - an initial reference density

U_i - internal energy of particle i

$\bar{k}$ - scaled Boltzmann constant

k_B - Boltzmann constant

$\bar{a}$ - vdW parameter

$\bar{b}$ - vdW parameter

β_Π - antipenetration parameter

α_Π - artificial viscosity parameter

b - equation of state constant

χ - equation of state constant

Chapter 1

Introduction

1.1   Steel processing

Steels are iron-based multicomponent alloys and are utilised in many industries such as automotive, machining, construction and transport. The steel industry involves many complex processes from extraction of iron to manufacturing of components. The steel process may be summarised in steps as: ironmaking, steelmaking, casting, thermomechanical treatment and plastic deformation. Ironmaking is the process of extracting iron from iron ore. In blast furnace ironmaking, iron ore reacts with coke and limestone and eventually forms immiscible liquid iron and liquid slag. Complex fluid flow (e.g. CO and CO_2 gases flow through a packed bed formed by iron ore, coke and limestone) and chemical reactions (e.g. $Fe_2O_3 + CO = 2FeO + CO_2$, $Fe_3O_4 + CO = 3FeO + CO_2$ and $FeO + CO = Fe + CO_2$) are the major issues to be considered in ironmaking in order to improve the productivity and energy efficiency. The resulting liquid iron from ironmaking is called hot metal and contains a much higher than required carbon content. The hot metal is then refined in oxygen converters in order to adjust its carbon content, together with the chemical compositions of other elements to their desirable levels. Oxygen gas is pumped into the converter with supersonic speed which generates vigorous flow in the converter. The reactions between elements in liquid metal and oxygen (e.g. $C + O_2 = CO_2$, $S_i + 2O = S_iO_2$) are required to be managed precisely to produce steels with

the desired compositions. The reacting zone is usually an emulsion consisting of gas bubbles (e.g. CO_2 and O_2), liquid droplets (e.g. Fe and slag) and small oxide particles (e.g. S_iO_2 and Al_2O_3). Complex fluid and chemical reactions are again the most important processes to be controlled in steelmaking. During this step, the liquid steel is often treated by mechanical/electromagnetic/bubbling stirrings and/or adding elements to adjust its composition or to remove impurities depending on the requirement of the final product. In continuous casting, flow of liquid steel in the tundish, ladle and casting mould affect the cleanliness, porosity, solute segregation and quality of the slab/billet/ingot. The continuous casting process is shown in Figure 1.1. The flow behaviour in the casting mould is also affected by the moving solid-liquid interface during solidification. Flow behaviour and phase transition are the two most important processes to be controlled in casting. In thermomechanical processing, heat and mechanical deformation (rolling) are implemented to alter the microstructure and mechanical properties of steels. The solid-solid phase transition and strain-stress distribution are important factors to be considered in this processing step. Displacive phase transformations are affected by the strain-stress field. After the thermomechanical processing, the steel products are frequently coated with metallic elements (e.g. Zn galvanization) and polymers to improve the surface properties such as corrosion and wear resistance. Free surface flow and thin film complex flow are the phenomenon that need to be considered in this step. Plastic deformation in the manufacturing of the steel product to the engineering component is also an important scientific topic. This is sometimes not classified as steel processing but manufacturing.

Flow affects chemical distribution and heat transfer. In turn, these influence phase transition and subsequently microstructure formation in steels. The mechanical properties of steels are determined by the corresponding microstructure. The processing-structure-property relationship indicates the importance of processing conditions when it comes to the final quality of steels. It is apparent that the mechanisms involved in steel processing are governed by complex fluid flow and phase transformations, either distinctly or in parallel. In order sufficiently to model and simulate these processes, models must be developed which can deal with mechanisms such as the effects of stirring on transport properties, the effect of adding alloying elements on phase
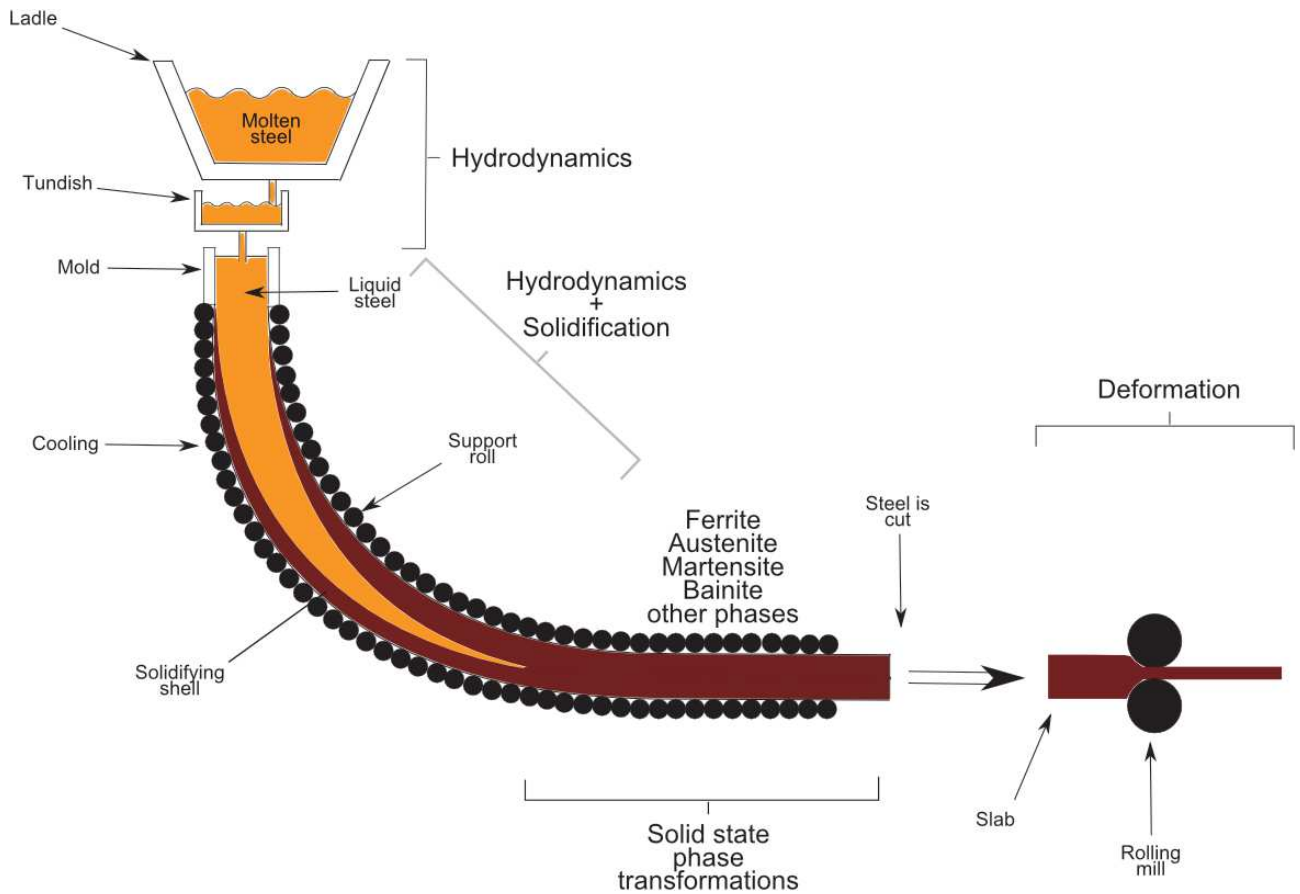
Figure 1.1: A diagram describing the continuous casting process and the important processes involved. As seen in the diagram, hydrodynamic/fluid flow effects are important in the initial stages of the continuous casting process. As the steel solidifies, phase transformations begin to occur. Phases such as martensite and bainite are able to form after the steel solidifies and can form during the deformation stage as well.

transformations, phase transformations during heat treatment and solidification. It turns out this is not a simple task.

1.2 Multiscale models for steel processing

1.2.1 Multiscale fluid flow models

When it comes to using numerical methods to describe or predict the evolution of a fluid system, there is a notion of scale, say, microscale, mesoscale and macroscale. The smallest of these, the microscale (e.g. *ab* initio, density functional theory and molecular dynamics), is mostly concerned with thermodynamics and intermolecular forces and enables the calculation of the most fundamental mechanisms which the larger scales can not. One such method is molecular dynamics (MD). MD focuses on the properties and evolution of individual atoms or molecules. While useful for determining properties for use in larger scale modelling [GLAR15], MD is not suitable for describing the evolution on a larger scale such as microstructure evolution and hydrodynamic effects. The length scale for MD simulations is usually less than 10 nm. Macroscale modelling is the largest of the three scales and can be described by the popular computational fluid dynamics (CFD) method. Concerned mostly with hydrodynamics, traditional CFD models have a hard time dealing with free surface flows and due to its application on a large scale, sometimes fail to capture small scale effects [Bes14]. It is particularly difficult to use this method to deal with systems containing phase transitions where the volume of each phase and the total area of the interface are not conserved. The method is suitable for systems with characteristic length larger than 1 mm. Mesoscale computation bridges the gap between microscale and macroscale calculations, and is particularly suitable for the simulation of a system where both flow dynamics and phase transitions are equally important. Of the mesoscale hydrodynamic models, the three prominent methods are dissipative particle dynamics (DPD), Lattice Boltzmann equation (LBE) and Smoothed particle hydrodynamics (SPH). DPD is a particle based off-lattice method and has been known to be unable to deal with fluid with high Reynolds numbers and complex boundary conditions. This means its application to the pro-

duction of steel is limited due to the complex boundaries formed by phase transitions. While LB is a method reliant on a mesh and is superior to conventional methods when considering systems with irregular interfaces, it is restricted by the requirement of a uniform temperature field which is clearly not true for steel processing as well as being unsuitable for thermodynamic consistency [YL03, HBTQ04]. Continuous casting is one example of applying a temperature gradient during cooling. An extreme example is that of the growth of a single crystal for use in turbines. A large temperature gradient is encouraged in order to result in a single orientation-single crystal growth. The flows involved in steel processing are often turbulent and have high Reynolds numbers, i.e. with large inertial forces compared to viscous forces, as high as over 20,000 making it difficult to provide a numerical method description [ZTVO05]. DPD is unable to deal with such high Reynolds numbers with its accuracy restricted to flows with a Reynolds number of around 100 and below [KP04, MDPPTK13, PPTMDK13]. SPH however, does not share these difficulties. In fact, SPH is renowned for its ability to deal with complex interfaces and boundaries and has no trouble describing free surface flows.

1.2.2 Multiscale phase transition models

The treatment of computational microstructure evolution also comes in multiple scales. There are significant efforts on using *ab* initio, density functional theory and molecular dynamics to calculate nucleation and early stage crystal growth. Microscopic methods are also applied to calculate the interface property and its kinetics. In engineering, macroscopic computation of the phase transition includes the application of computational phase diagrams to predict the fraction of individual phases and precipitates. In mesoscopic simulations, the phase-field (PF) method has proven to be very popular and capable [MBW08]. The PF method has been applied successfully to microstructure evolving via diffusion [NC11, MMSV06], including solidification and high temperature solid-solid phase transitions [CYY01, TA98]. Another type of phase transformation has a displacive nature, forming via a coordinated movement of atoms. Displacive transformations, specifically martensite and bainite, have become increasingly popular and sought after for applying the PF method [MZE13]. The general approach is usually from

microscopic theory and satisfactory results have been obtained by the addition of multiple order parameters and governing equations for these order parameters and the strain [MZE13]. These put great strain on computational resources especially when applied to large systems and jointly with other models for competing structures. Bainite has hardly been studied using the PF method and requires much more attention. Therefore, further study on the PF modelling of these transformations which are not as computationally demanding are required.

Other mesoscopic phase transition models include the classical sharp-interface model (Stephan model). The typical description of the Stefan problem involves a diffusion equation governing heat transport for each phase separately with additional equilibrium equations over the interface acting as boundary conditions. There are very few cases with an analytical solution. Direct computation of these equations is very tedious and time consuming.

Suppose Ω is the set of points corresponding to the entire simulation domain and $\Omega_S(t)$, $\Omega_L(t)$ and $\Gamma(t)$ are subsets corresponding to the solid, liquid and interface regions at time t respectively. Then the Stefan problem takes the form of the heat diffusion equation, the equation for the normal velocity of the interface and the Gibbs-Thomson condition:

$$\begin{cases} T_{,t}(\tilde{\mathbf{r}}) = D_T \Delta^2 T & \tilde{\mathbf{r}} \in \Omega \backslash \Gamma(t) \\ c_h D_T T_{,n}|_S^L = -L v_n & \tilde{\mathbf{r}} \in \Gamma(t) \\ T = T_M - \tilde{\sigma}_s(\theta) T_M \kappa_c / L - v_n / M(\theta) & \tilde{\mathbf{r}} \in \Gamma(t) \end{cases} , \qquad (1.1)$$

where $T_{,t} \equiv \frac{\partial T}{\partial t}$ and D_T, L, c_h, v_n, T_M and κ_c is the thermal diffusivity, the latent heat of fusion, the heat capacity, the normal velocity of the interface, the melting temperature and the curvature of the interface respectively. $M(\theta)$ is the interfacial mobility while $\tilde{\sigma}_s(\theta)$ is a function of the surface tension. $T_{,n}$ is the rate of change of temperature in the normal direction to the interface and the notation $|_S^L$ denotes the solid-liquid interface. In addition to heat diffusion, for a general non-pure material one may include equations governing solute diffusion to the equations for the Stefan problem which have been omitted for simplicity.

To begin the evolution of such a system, one must place an initial seed with a temperature below the melting temperature presenting a metastable state. This will create an inhomogeneity in the liquid and heat can begin to diffuse from the solid seed to the liquid. The morphology of the seed with time depends on the preference to increase or decrease the surface area. The interface between two domains naturally serves to increase the free energy thus reducing surface area is preferable. However, the diffusion of heat from the solid is aided by a larger surface area prompting a requirement to increase the interfacial area. This usually results in anisotropic growth in the shape of a dendrite.

1.3 Numerical simulation methods

Simulation methods give us a means to the discretization of natural phenomena. It enables the numerical solving of the mathematical equations representing the problem at hand, which may not even be possible analytically without an extensive number of assumptions. In cases where hands-on experiments are not feasible, or the costs for experimental investigation are too high, numerical simulation is a worthy substitute. It is also often the case where simulations are used to verify theoretical considerations as well as discover new phenomena or to observe how a particular development occurs where in reality this would not be detectable due to technical problems.

Before any numerical simulation can take place, one must first obtain or develop a mathematical model (governing equations) representing the physical phenomena. It is then necessary to determine how these equations are to be solved, which method is best suited to deal with this type of problem, the nature of the boundary conditions and the implementation of all these in code. The type of domain discretization becomes important when selecting a numerical method. Some numerical methods employ fixed grids suitable for solid-state phase transformations whereas others do not use a mesh at all enabling the tracking of individual volume elements in fluid motion especially useful when free surfaces and irregular interface geometries are involved. The nature of the governing equations may also be different depending on the

choice of domain discretization. For instance, for a fixed grid, the Eulerian form of the equations of motion must be used for fluid dynamics. This involves a convective term which is not present in the Lagrangian description used for the case where the interpolation points/grid nodes move along with the fluid elements. While initially it may seem that using a Lagrangian approach to modelling fluid flow is an obvious choice, if using a Lagrangian mesh, the mesh may become too distorted if the corresponding fluid is subjected to large distortions [LL03, Ben92]. In other words, the selection of an appropriate method for the simulation of a particular phenomenon is vital.

1.4   Research aim

The aim of this research was to develop the tools to bridge the gaps in modelling and simulation of steel processing. Two of the biggest gaps in steel processing simulation is the modelling of solidification in the presence of flow and transformations not involving diffusion such as martensite and bainite (Figure 1.1). During solidification, solidifying structures may break off, rotate and collide with one another while solidifying. In order to simulate the complex fluid in steel processing, the methods used must be able to deal with rapid fluid flow in the presence of large distortions and cases where there is a free surface i.e. the surface of the molten steel where it is in contact with air. In addition to this, the possibility of incorporating thermodynamics should also be a reality. In order to do this, smoothed particle hydrodynamics (SPH) and the phase-field (PF) method are to be utilised. The SPH method though has a Lagrangian nature (i.e. the coordinate system follows the flow) is not reliant on a mesh. Instead it represents fluid volume elements with particles and uses these as the interpolation points. The method is efficient in dealing with shock waves, free boundaries and irregular interface geometries. The PF method is selected to address the problem in microstructure computation in diffusionless/displacive transformation. The PF method relies on a fixed grid, is derived from statistical thermodynamics and is very popular in the area of materials science and solid-state phase transformations. It has been very successful in the computation of microstructure evolution in diffusive phase transitions. The problem that arises here is how to integrate a

mesh-free method such as SPH and a grid dependent method such as PF. In fact, Eulerian and Lagrangian methods [Ben92, HAC74] and Eulerian and meshfree methods [WWGB09] have already been jointly used to tackle physical problems. In summary, both these methods have no problems with complex geometries, have no requirement to explicitly track interfaces and can be combined to represent the evolution of a physical system. In particular, the following questions are to be addressed fundamentally in this thesis:

- A phase-field model for martensite transformation

  There is a need for advancement in the modelling of martensitic phase transformations. Models currently in circulation utilise the evolution of strain energy fields as well as other fundamental quantities in order to determine plate growth. The reality is that the processes involved in steels are much more abundant than the growth of martensite. This means multiple effects and models need to be applied in tandem. It is required that less computationally demanding models are researched for cases which do not require such complexity.

- A phase-field model for bainitic transformation

  Bainitic transformation is more complicated than martensite transformation because it is driven not only by displacive transformation but also the carbon diffusion and crystal orientation selections. A phenomenological approach to the modeling of displacive transformations is utilised. This enables the orientation dependent growth of bainite platelets as well as the treatment of autocatalysis. Since the chemical free energy is incorporated into the model along with diffusion, the experimentally observed trapping of carbon in films of austenite is reproduced.

- Application of smoothed particle hydrodynamics in non-ideal fluids

  The SPH method has been applied before however its effects on entropy is seen to be inconsistent when it is applied to the same system with different parameters such as smoothing length. This inconsistency is shown here and possible steps are shown to limit this inconsistency so that the difference in the total entropy change when attempting to increase accuracy is minimised. This is important when coupling the SPH with an

entropy dependent PF model.

With the availability of a suitable hydrodynamic model to deal with mesoscopic complex fluids and a suitable mesoscopic method to deal with microstructure evolution due to displacive transformation, mesoscopic simulation of the overall steel processing is possible. PF for diffusive phase transformations has been addressed well in literature. Integration of SPH and PF for diffusive transformation, PF for displacive transformation along with thermodynamic and physical databases will enable the functionality. The integration is a coding problem and will not be discussed in detail in this thesis.

Chapter 2

Assessment of the literature

In this chapter, the theoretical fundamentals of the PF method, thermodynamics, the SPH method and hydrodynamics are introduced.

2.1 The phase-field method

2.1.1 Introduction

The PF method is a diffuse interface method in that infinitesimally thin interfaces are replaced with thin regions over which the variables in the method vary continuously. A distinct feature of the method is the introduction of a PF variable or an order parameter which varies over the non-zero thickness interfacial region. The PF variable is then used implicitly to track the location of the interface. In other words, the state of the system is determined by the PF variable. This immediately presents an advantage over sharp interface methods that require explicit tracking of the interface. However, the interface being of non-zero thickness means that in order to capture certain physical characteristics of some phase transformations, higher resolution simulations must be carried out due to the large gradients present across the interface (Figure 2.1). The evolution equations for the phase-field variables are derived to comply with the second law of thermodynamics (Section 2.2) which defines equilibrium and the direction

of phase transformation. The free energy representation of the system, from which the evolution equations are derived, can be suitably adjusted in order to deal with different physical phenomena. This is discussed in more detail in Section 2.1.2.
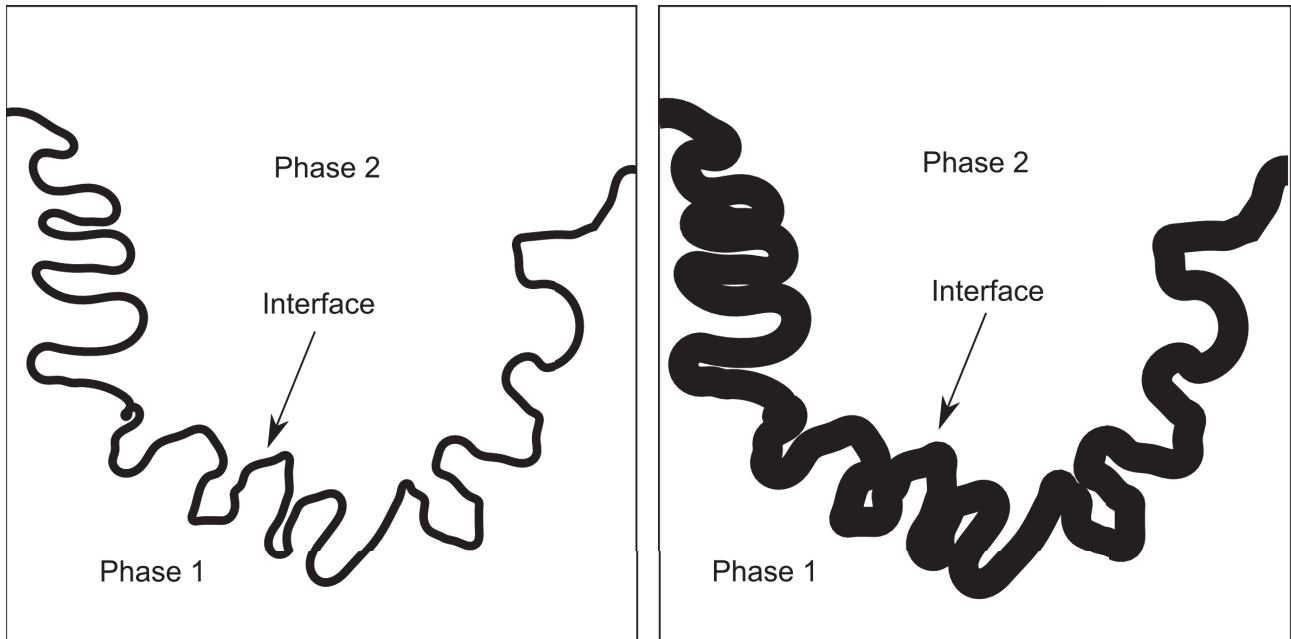
Figure 2.1: A theoretical simulation of an interface between two phases. It can be seen that the details of the interface can be lost if an interface thickness which is too large is chosen in the PF method.

Take the solidification of a pure material from its liquid state. This problem is typically represented by two mathematical equations, one in the solid and one in the liquid, and another equation at the boundary between the two to represent boundary conditions. This representation is called a sharp-interface model (Section 1.3) due to the interface between domains having zero thickness. Analytically, there are solutions for only a few special cases. Due to its industrial significance, models are required with the ability to simulate such problems accurately.

Sharp-interface models are incredibly tedious to solve computationally due to the requirement to explicitly track the interface. Diffuse interface methods such as the PF method do not suffer from this problem. Instead, the PF method introduces a field variable called the PF variable ϕ or order parameter η that is used implicitly to track the interface. The interface is no longer infinitesimally wide but is assumed to have a finite thickness 2λ. The value of ϕ or η is used

to determine the location of the interface and the evolution of these variables is governed by equations derived from thermodynamics.

Thus, in cases with little to no hydrodynamic effects, the thermodynamic description of the PF method is naturally sufficient to describe and predict microstructure evolution. In contrast, the PF method has also been used to solve the Navier-Stokes equations for multiphase systems involving flows [BCB03, BDS+99, TA98, TA00]. In the following chapters, the PF method is shown to have the ability to be applied to a wide range of cases in liquid-solid and solid-state phase transformations.

2.1.2   Mathematical description of the phase-field method

Where a precipitate grows within a matrix, consider the three instances: precipitate, matrix and the interface between the two. Taking the interface to be a surface with infinitesimal width coincides with a *sharp interface* description. The PF method deals with the formulation of such a system by assigning each location in the domain a field variable ϕ. The value of ϕ at a location determines the phase that is present at that location, whether it be precipitate, matrix or interface. The precipitate and matrix are often represented by $\phi = 1$ and $\phi = 0$ respectively. The PF variable changes continuously from its matrix value to its precipitate value, i.e. $0 < \phi < 1$ within the interface (Figure 2.2). This region is interpreted as the interface and the length over which this continuous change occurs is the width of the interface. Here, it can be seen that the interface has a non-zero width. If more than two phases, say N phases, exist, then each phase typically has a corresponding PF variable. The presence of phase $i < N$ at location $\mathbf{r}$ is then determined by $1 \geq \phi_i(\mathbf{r}) \geq 0$. If $\phi_i(\mathbf{r}) = 1$, phase i exists, if $\phi_i(\mathbf{r}) = 0$ it does not exist at this location. At any interface involving phase i we have $1 > \phi_i > 0$. This way we have that for any $\mathbf{r}$,

$$\sum_{i=0}^{N} \phi_i(\mathbf{r}) = 1.$$
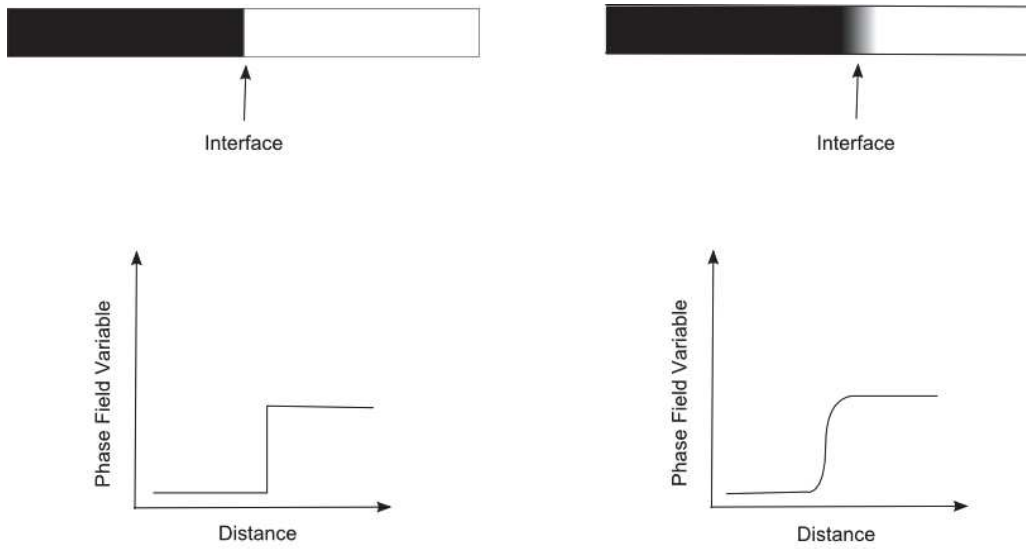
Figure 2.2: A visual comparison of a sharp interface (left) and a diffuse interface (right) (adapted from [MBW08]).

The evolution of the PF variable and subsequently the microstructure, is governed by a set of evolution equations for ϕ. These governing equations are derived from thermodynamic considerations of the state functions of the system. For instance, the Gibbs free energy of the system as a state function can be expressed in terms of ϕ as,

$$G = \int_V \left[g_0(\phi, T) + \frac{1}{2}\epsilon(\nabla\phi)^2 \right] dV, \tag{2.1}$$

where V and T is the volume of the domain and the temperature, respectively. g_0 is the sum of the homogeneous free energies of the two phases while also involving a free energy barrier and ϵ is termed the gradient energy coefficient. Other circumstances may prompt the use of other state functions such as entropy, internal energy or Helmholtz free energy. The gradient of the PF variable in the second term on the right-hand side of Equation (2.1) is non-zero only over the interface and it can be guessed that this term is responsible for describing the interface region. The derivation of the general form of Equation (2.1) is given in Appendix (A).

One of the key assumptions in deriving the evolution equation for ϕ from Equation (2.1) is that the rate of evolution is proportional to the force driving the microstructural change

[Ons31, Mil60],

$$\frac{\partial \phi}{\partial t} = -M_\phi \frac{\delta G}{\delta \phi}, \tag{2.2}$$

where $M_\phi > 0$ is termed the mobility and $\frac{\delta G}{\delta \phi}$ plays the role of the force.

The PF variable ϕ can be chosen to represent a conserved variable such as composition or a non-conserved quantity such as the amount of precipitate formed. A popular form for $g_0(\phi, c, T)$ is given as [WBM92],

$$g_0(\phi, c^\alpha, c^\beta, T) = h(\phi)g_0^\alpha(c^\alpha, T) + (1 - h(\phi))g_0^\beta(c^\beta, T) + \frac{1}{4\omega}\phi^2(1 - \phi)^2, \tag{2.3}$$

where $h(\phi) = \phi^3(6\phi^2 - 15\phi + 10)$ [WB95] and $g_0^\alpha(c^\alpha, T)$ and $g_0^\beta(c^\beta, T)$ are the homogeneous free energy densities of the phases α and β and are known in advance. The composition in the α and β phases are denoted by c^α and c^β respectively. The last term gives a double well nature to Equation (2.3) with ω responsible for the height of the energy barrier. Figure 2.3 shows a plot of g_0 and h. The values for g_0^α and g_0^γ are obtained from Section 2.2 at $c = 0.0111$ atomic fraction carbon and $T = 720°C$ as $-41785MJ/m^3$ and $-41795MJ/m^3$ respectively. We set $\omega = 0.75 \times 10^{-9}m^3/J$ (using Equation (2.11) with $\lambda = 14.3nm$ and $\sigma = 0.72J/m^2$).
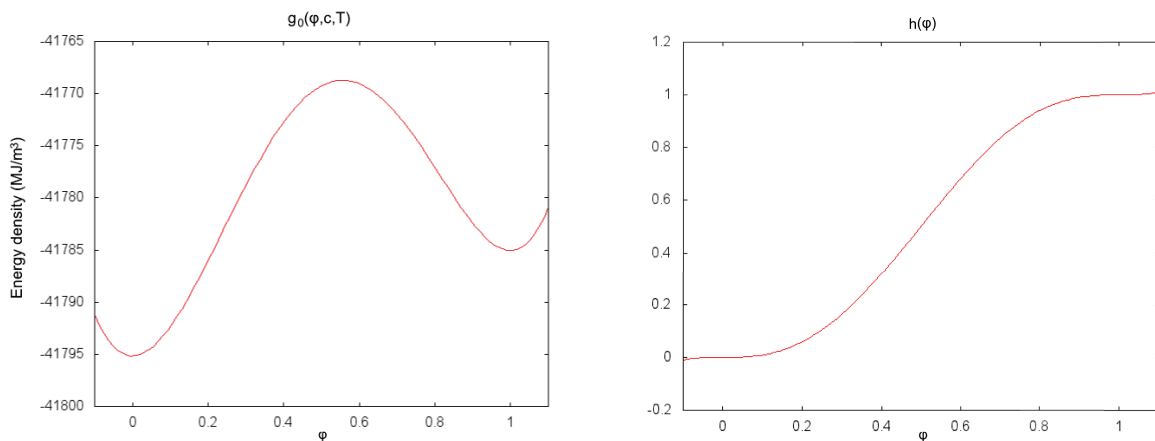
Figure 2.3: A plot of Equation (2.3) on the left with $g_0^\alpha = -41785MPa$, $g_0^\gamma = -41795MPa$ and $\omega = 0.75 \times 10^{-9}$. A plot of the function $h(\phi)$ on the right.

Let G be the Gibbs free energy of the system. Then the evolution of an irreversible process conforms with,

$$\frac{dG}{dt} \leq 0, \tag{2.4}$$

Since G is a functional of multiple variables evolving through time, it can be expanded to give,

$$\frac{dG}{dt} = \left(\frac{\delta G}{\delta \phi}\right)_{c,T} \frac{\partial \phi}{\partial t} + \left(\frac{\delta G}{\delta c}\right)_{\phi,T} \frac{\partial c}{\partial t} + \left(\frac{\delta G}{\delta T}\right)_{\phi,c} \frac{\partial T}{\partial t} \leq 0, \tag{2.5}$$

where the subscript $\left(\frac{\delta G}{\delta \phi}\right)_{c,T}$ means the functional derivative of G with respect to ϕ is taken with constant c and T.

We consider the terms in Equation (2.5) separately,

$$\left(\frac{\delta G}{\delta \phi}\right)_{c,T} \frac{\partial \phi}{\partial t} \leq 0, \quad \left(\frac{\delta G}{\delta c}\right)_{\phi,T} \frac{\partial c}{\partial t} \leq 0, \quad \left(\frac{\delta G}{\delta T}\right)_{\phi,c} \frac{\partial T}{\partial t} \leq 0 \implies \frac{\delta G}{\delta t} \leq 0. \tag{2.6}$$

(Note the one-sided implication in Equation (2.6).) Solving Equation (2.6) is much simpler than solving Equation (2.5).

Using equations (2.2) and (2.6),

$$\left(\frac{\delta G}{\delta \phi}\right)_{c,T} \frac{\partial \phi}{\partial t} \leq 0 \iff -M_\phi \left(\frac{\delta G}{\delta \phi}\right)_{c,T}^2 \leq 0, \tag{2.7}$$

where $M_\phi > 0$ is the mobility. Thus Equation (2.2) satisfies the first of Equation (2.6). The resulting governing equation for ϕ, using Equation (2.2), is then,

$$\frac{\partial \phi}{\partial t} = M_\phi \left(\epsilon^2 \nabla^2 \phi - \frac{\partial g(\phi)}{\partial \phi}\right), \tag{2.8}$$

where $g(\phi) = g_0(\phi) + \frac{1}{2}\epsilon(\nabla\phi)^2$. Similarly, the governing equations for c and T are given as [Whe99, QW03b],

$$\frac{\partial c}{\partial t} = \nabla \cdot \left[M_c \left(\frac{\partial^2 G}{\partial c^2} \right)_{\phi,T} \nabla c \right], \tag{2.9}$$

$$\frac{\partial T}{\partial t} = \nabla \cdot \left[M_T \left(\frac{\partial^2 G}{\partial T^2} \right)_{\phi,c} \nabla T \right], \tag{2.10}$$

where M_c and M_T are mobility parameters for mass and temperature respectively. The parameters ϵ and ω are related to the half-interface width, λ, and the interfacial energy, σ, as [Whe99],

$$\epsilon^2 = \frac{3\lambda\sigma}{1.1}, \quad \omega = \frac{\lambda}{26.4\sigma}. \tag{2.11}$$

The PF method is popular in the area of materials science due to its ability to provide a visual representation of the developing microstructure without the requirement to explicitly track interfaces. This trait comes hand-in-hand with the diffuse interface description. However, one of the problems the PF method is faced with is the thickness of the interface. In reality, the resolving of interfacial features and complex shapes may require interface widths in the atomic dimensions. In order to resolve these features, one must improve lattice resolution which quickly becomes computationally cumbersome.

2.1.3 From free energy to free energy density

It is assumed that the free energy of a system can be defined by a Ginzburg-Landau free energy functional of a state function/order parameter ϕ as [CH58, Gin55],

$$F = \int_\Omega (f(\phi) + \frac{1}{2}k|\nabla\phi|^2)dx, \tag{2.12}$$

where the coefficient k is positive, f is the Helmholtz free energy density of the bulk homogeneous phases and Ω is the system domain. F is minimised at equilibrium and this solution for

ϕ satisfies $\frac{\delta F}{\delta \phi} = 0$. For Equation (2.12), this variational derivative gives [Wei74],

$$\frac{\delta F}{\delta \phi} = f'(\phi) - k\nabla^2 \phi. \tag{2.13}$$

We have that within the bulk phases, $\nabla^2 \phi = 0$ and,

$$\frac{\delta F}{\delta \phi} = 0, \quad \Rightarrow f'(\phi) = 0, \tag{2.14}$$

i.e. $f(\phi)$ is minimised.

If ϕ is to be a quantity that is not conserved, i.e. the fraction of the solidified phase in a solidification model [PF90],

$$\phi_{,t} = K(k\nabla^2 \phi - f'(\phi)). \tag{2.15}$$

If ϕ is to be a conserved quantity, i.e. the total sum of all its values across the system is constant $(\frac{d}{dt} \int_\Omega \phi dx = 0)$ [PF90],

$$\phi_{,t} = \nabla \cdot (M\nabla[f'(\phi) - k\nabla^2 \phi]), \tag{2.16}$$

where $K \equiv K(\phi, T)$ and $M \equiv M(\phi, T)$ are functions. Both equations (2.15) and (2.16) result in a monotonically decreasing F. This does not violate the 2nd Law of Thermodynamics.

Addition of governing equations for other field variables, such as temperature, is also often required to describe evolution. The following equations are derived for the case with temperature evolution [PF90],

$$\alpha\zeta^2 \phi_{,t} \quad = \zeta^2 \nabla^2 \phi + g(\phi) - T \tag{2.17}$$

$$T_{,t} \quad = \nabla^2 T + \lambda \phi_{,t}, \tag{2.18}$$

where T is temperature and ζ is a positive constant. However, equations (2.17) and (2.18) do not result in a monotonically decreasing free energy F. This is due to the method of deriving these equations. Equation (2.17) is derived assuming T is constant. Then Equation (2.18) is derived

using Fick's Law and allowing T to vary in time. Note that Equation (2.17) can be obtained from Equation (2.15) by choosing $f'(\phi) = T - g(\phi)$, $k = \zeta^2$ and $K = 1/(\alpha\zeta^2)$. Also, the notion of temperature change is closely related to the energy evolution of the system, prompting a requirement for energy conservation. If temperature is not assumed to be constant, the entropy functional becomes more suitable [PF90]. In order to write Equation (2.12) in terms of the entropy density, a relationship between the free energy density, f, and the entropy density, s, is formed as [PF90],

$$f(T, \phi) = \inf_{e}[e - Ts(e, \phi)], \tag{2.19}$$

where e is the energy density and $\inf_e$ means the infimum with respect to e. The Legendre transform (Equation (2.19)) is obtained through certain assumptions about the functions, f and s. Namely that they are concave in their variables. Equation (2.12) can now be rewritten as,

$$
\begin{aligned}
F &= \int_{\Omega} (f + \frac{1}{2}k|\nabla\phi|^2)dx \\
&= \int_{\Omega} (\inf_{e}[e - Ts] + \frac{1}{2}k|\nabla\phi|^2)dx \\
&= \int_{\Omega} (\inf_{e}[e - Ts + \frac{1}{2}k|\nabla\phi|^2])dx \\
&= \inf_{e} \int_{\Omega} (e - Ts + \frac{1}{2}k|\nabla\phi|^2)dx \\
&= \inf_{e}[\int_{\Omega} edx - \int_{\Omega} (Ts - \frac{1}{2}k|\nabla\phi|^2)dx] \\
&= \inf_{e}[E - TS], \tag{2.20}
\end{aligned}
$$

where E is the total energy and S is the total entropy,

$$E = \int_{\Omega} edx, \tag{2.21}$$

$$S = \int_{\Omega} (s - \frac{k}{2T}|\nabla\phi|^2)dx. \tag{2.22}$$

Equations (2.15) and (2.16) are then replaced by [PF90],

$$\phi_{,t} \quad = KT\frac{\delta S}{\delta \phi}, \tag{2.23}$$

$$\phi_{,t} \quad = -\nabla \cdot \{MT\nabla(\frac{\delta S}{\delta \phi})\}, \tag{2.24}$$

respectively, in the case of a variable temperature field. Analogous to these equations, the corresponding equations for e (conserved) is,

$$e_{,t} \quad = -\nabla \cdot \{K_1 T^2 \nabla(\frac{1}{T})\}$$

$$= K_1 \nabla^2 T. \tag{2.25}$$

where it was assumed $M = K_1 T^2$ with K_1 a constant. This entropy and total energy description now results in a non-decreasing entropy with respect to ϕ [PF90].

2.1.4   Application of phase-field method to solidification

Suppose that the state of the system at a particular time corresponds to the state of a single PF variable $\phi(\mathbf{r})$,

$$\phi(\vec{\mathbf{r}}, t) = \begin{cases} 0 & \vec{\mathbf{r}} \in \Omega_L(t) \\ 1 & \vec{\mathbf{r}} \in \Omega_S(t) \\ (0, 1) & \vec{\mathbf{r}} \in \Gamma(t) \end{cases}, \tag{2.26}$$

where Ω_L, Ω_S and Γ are the subsets of the points in the domain corresponding to the liquid, solid and interface respectively. Then, a Helmholtz free energy functional can be formed in terms of $\phi(\mathbf{r})$ as [PF90, OKS01] Equation (2.12),

$$F = \int_V \left[g_0(\phi, T) + \frac{1}{2}\epsilon(\nabla\phi)^2 \right] d\mathbf{r}, \tag{2.27}$$

where V is a volume of space, $\epsilon > 0$ is the gradient energy coefficient related to the interface energy and g_0 (f in Equation (2.19)) is a double well function the minima of which reflects the two existing stable phases. If the PF variable is chosen to represent the local concentration,

then the equilibrium state of the interface is found by minimising the free energy functional. In the case of solidification, Equation (2.3) gives,

$$g_0(\phi, T) = h(\phi)f^S + (1 - h(\phi))f^L + \frac{1}{4\omega}\phi^2(1 - \phi)^2, \tag{2.28}$$

where f^S and f^L are respectively the solid and liquid free energy densities. Equation (2.8) then results in,

$$\frac{\partial \phi}{\partial t} = M_\phi \left(\epsilon_\phi^2 \nabla^2 \phi - h'(\phi)(f^L - f^S) - \frac{1}{2\omega}\phi(1 - \phi)(1 - 2\phi) \right). \tag{2.29}$$

In phase-field models for binary mixtures, the phase change as a function of composition is assumed to be continuous. This means the homogeneous free energy densities are functions of composition,

$$f^L = c_S f_B^L(T) + (1 - c_S)f_A^L(T), \tag{2.30}$$

$$f^S = c_L f_B^S(T) + (1 - c_L)f_A^S(T), \tag{2.31}$$

$$c = h(\phi)c_S + (1 - h(\phi))c_L, \tag{2.32}$$

$$\mu^S(c_S(x_{int}, t)) = \mu^L(c_L(x_{int}, t)), \tag{2.33}$$

where A and B are the components, c_S and c_L are the solid and liquid compositions respectively, c is the local composition, x_{int} denotes a position within the interface, and μ^S and μ^L are their chemical potentials. Assuming $M_T \frac{\partial^2 F}{\partial T^2} = D_T$, a constant, in Equation (2.10), and adding a latent heat term gives,

$$\frac{\partial T}{\partial t} = D_T \nabla^2 T + h'(\phi)\frac{L}{c_p}\frac{\partial \phi}{\partial t}, \tag{2.34}$$

where L and c_p is the latent heat and the specific heat respectively. A solute diffusion equation may also be included in the model (Equation (2.9)),

$$\frac{\partial c}{\partial t} = \nabla \cdot \left(\frac{D_c}{g_{,cc}}\nabla g_{,c} \right), \tag{2.35}$$

where $D_c = M_c g_{,cc}$ is the solute diffusivity and can be dependent on ϕ. $g_{,c}$ and $g_{,cc}$ are the first and second derivatives of g with respect to composition.

Using this model as a base, it is possible to describe dendritic growth by introducing an anisotropy parameter (in two dimensions) which is applied to the gradient energy coefficient [Kob93, QW03b],

$$\epsilon = \bar{\epsilon}(1 + v\cos(k\theta)), \quad \tan(\theta) = \frac{\partial\phi/\partial y}{\partial\phi/\partial x}, \tag{2.36}$$

where $\bar{\epsilon}$ is a constant (the mean value of ϵ), v is the amplitude and k represents the symmetry.

The Helmholtz free energy functional (Equation (2.27)) is applied to the PF method if the temperature is assumed constant. If the temperature is a variable, Equation (2.27) is replaced with the entropy functional Equation (2.22) [WSW+93],

$$S = \int_V \left[s(\phi, e, c) - \frac{1}{2}\epsilon_\phi^2(\nabla\phi)^2 \right] dV, \tag{2.37}$$

where s is the entropy density.

Using this entropy functional instead of the free energy functional in Equation (2.2) a model for solidification can be constructed [WB95] the parameters of which can be related to material parameters such as melting temperature and interface energy.

The classical equations for the description of the solidification of a pure melt were outlined in Section 1.2.2. It was mentioned that a separate equation for each phase is required as well as equilibrium conditions across each boundary. This quickly becomes impractical when the model is pitted against multiple phases especially where complex interface shapes are involved. However, the description of the PF method given in Section 2.1 makes it ideal for overcoming computational resource barriers by requiring only a single set of equations to be solved for the entire simulation domain. Additionally, complicated interface morphologies have less impact on the efficiency.

While such PF models are applied to stationary liquid environments, which is insufficient when the aim is to simulate real life processes, it is possible to incorporate fluid flow into the

PF method by solving the Navier-Stokes equations [TA98, BDS$^+$99, TA00].

In summary, the formulation of a PF model for solidification begins with the assumption that the phase dynamics at the interface can be approximated by a smooth function ϕ, the PF variable, while taking on nearly constant values within the phases. A free energy functional or entropy functional is then formulated as a function of ϕ. The second law of thermodynamics is then applied demanding the increase of entropy and the decrease of the total free energy of the system with respect to time.

2.2 Thermodynamic properties

Calculation of microstructure evolution using the PF method requires thermodynamic quantities (e.g. free energy and chemical potential) as input parameters. This can sometimes be done by integration of the PF code with a commercial thermodynamic database. However, there are several disadvantages in doing so. One is the computational speed. A commercial thermodynamic database is aimed to produce phase-equilibrium calculations. It calculates many thermodynamic quantities that are not required in the PF method. The most efficient method is to have a code package for thermodynamic calculation for the purpose of the PF calculation. For this purpose, a code package has been developed. The thermodynamic theory and calculation methods are summarised in this section.

2.2.1 Fundamental definitions

Computations such as those used in producing phase diagrams and the possibility of spontaneous reactions require knowledge of thermodynamics since it involves a transformation of the thermodynamic system from one state to another. Thermodynamics deals with the relationships between heat, matter and different forms of energy. Over the course of the development of this branch of science, four laws have come into existence which will be helpful to predict certain behaviours of systems such as its evolution direction. These laws are given as:

Zeroth Law: If a body, A, be in thermal equilibrium with two other bodies, B and C, then B and C are in thermal equilibrium with one another [Pla45].

First Law: The energy of the universe is constant.

Second Law: The entropy of the universe tends to a maximum.

Third Law: The entropy of a perfect crystal, at absolute zero (zero kelvins), is exactly equal to zero.

The First Law given by Clausius in his 9th paper in 1865 is in the form of the equation $\Delta U = q - w$ pertaining to a closed system, where ΔU is an increment in the internal energy and q and w is the heat accumulated by the system and the work done by the system respectively. The assumption that the entropy of an isolated system (i.e. a system with no mass or energy transfer across its boundaries) never decreases, The Second Law, is important for thermodynamic evolution equations.

The total energy contained within a system is called the internal energy of the system, U. By the first law of thermodynamics, U is related to the work done by the system, w, and the heat transferred in to the system, q, in integral form by,

$$\Delta U = q - w \qquad (2.38)$$

or in differential form,

$$dU = dq - dw \qquad (2.39)$$

where work done by the system and heat given in to the system are positive. So for a system with constant pressure,

$$dU = dq - PdV. \qquad (2.40)$$

Entropy, usually denoted by S, is another thermodynamic parameter used to describe a system. The use of entropy is beneficial in that isolated systems tend to evolve towards a

state of maximum entropy. In statistical mechanics entropy is defined to be a measure of the number of configurations of its microconstituents and can be used as a measure of disorder or randomness. In thermodynamics however, it is defined on a macroscopic scale in terms of heat for a reversible process as $\Delta S = \int_A^B \frac{dq}{T}$. The entropy is related to the internal energy by the thermodynamic identity,

$$dU = TdS - PdV, \tag{2.41}$$

where T is temperature.

The enthalpy, H, of a system is defined to be,

$$H = U + PV. \tag{2.42}$$

This equation along with Equation (2.40) can now be used to describe the thermodynamics of a system as,

$$dH = dU + d(PV) = dq - PdV + d(PV). \tag{2.43}$$

Using the product rule for differentiation reduces the equation to,

$$dH = dq - VdP, \tag{2.44}$$

resulting in a more useful equation for use with a system with variable volume but constant pressure. The partial derivative of Equation (2.44) at constant pressure with respect to temperature is defined to be the specific heat capacity, C_P, of a phase at constant pressure,

$$C_P = \left(\frac{\partial H}{\partial T}\right)_P = \left(\frac{\partial q}{\partial T}\right)_P. \tag{2.45}$$

The specific heat capacity at constant volume, C_V, is defined using Equation (2.40),

$$C_V = \left(\frac{\partial U}{\partial T}\right) = \left(\frac{\partial q}{\partial T}\right)_V. \tag{2.46}$$

A change in the enthalpy of a system represents the heat absorbed by the system and the work done. So a change in the enthalpy corresponds to a possibility of a spontaneous reaction. However, some systems may undergo spontaneous reactions without a change in enthalpy. For instance, an isothermal ideal gas has $\Delta H = 0$, but upon release from a confined space (ordered state) the gas proceeds to expand towards disorder. This corresponds to an increase in entropy. Therefore, the entropy change as well as the enthalpy change of a system need to be considered when describing a system. Along these lines the Gibbs free energy, G, of a system is defined to be (for a system with constant temperature and pressure),

$$G = H - TS, \tag{2.47}$$

and the Helmholtz free energy, F, is (for a system with constant temperature and volume),

$$F = U - TS. \tag{2.48}$$

The entropy and the Gibbs and Helmholtz free energies depend only on the current state of the system and not on its history and so are called functions of state.

In chemistry, a mole (n) is used as a unit of measurement for a quantity of a substance. The equations (2.47) and (2.48) are often expressed as per mole of a substance. Consider a phase α with two constituent atoms a and b. The molar Gibbs free energy of the phase α for a multicomponent system is then a function of the free energies of the respective phases,

$$G_m^\alpha = (1-x)G_a^\alpha + xG_b^\alpha - T\Delta S^{ideal}. \tag{2.49}$$

where x is the mole fraction of component b, $1-x$ is the mole fraction of component a, and G_a^α is the Gibbs free energy of a in phase α. For an ideal solution we have the molar entropy,

$$\Delta S^{ideal} = -R((1-x)\ln(1-x) + x\ln(x)). \tag{2.50}$$

Then the molar Gibbs free energy for an ideal solution can be written as,

$$G_m^\alpha = (1-x)G_a^\alpha + xG_b^\alpha + RT((1-x)\ln(1-x) + x\ln(x)). \qquad (2.51)$$

For non-ideal systems, the ideal solution is often used as a reference solution while adding the excess components ($^E G_m = {}^E H - T{}^E S$) that contribute to its non-ideality,

$$G_m^\alpha = (1-x)G_a^\alpha + xG_b^\alpha + {}^E G_m + RT((1-x)\ln(1-x) + x\ln(x)). \qquad (2.52)$$

The free energies of equations (2.47) and (2.48) written in the form of Equation (2.52) are used to produce phase diagrams such as that in Figure 2.4. Figure 2.5 shows a common tangent method to producing the binary phase diagram. The two functions G^1 and G^2 correspond to ferrite and austenite respectively. For all total compositions lying between the two intersection points, the system can reduce it's free energy by mixing with the compositions resulting from the common tangent to the two phases. The process of constructing these functions is demonstrated in the following sections.

2.2.2 The regular solution model

A regular solution model can be used to describe the molar free energies in a solution in which the atoms of the solutions are distributed in a regular manner within the sublattices. Due to the iron and carbon atoms having different characteristics, such as their size, they occupy different sublattices. In this case it is possible to use a regular solution model under the assumption that there is random mixing within each sublattice. The possibility of multiple sublattices prompts the introduction of a new composition parameter, $Y_i^s = n_i^s/(n_{Va}^s + \sum_i n_i^s)$, known as the site fraction of component i in sublattice s with subscript Va referring to vacant sites and n_i the number of moles of component i. Since the sum of the site fractions of all the components within a sublattice must equal 1, $\sum_i Y_i^s + Y_{Va}^s = 1$ for all s. If a component is not found in a particular sublattice the corresponding site fraction is zero. For instance, the regular solution model of α-iron has two sublattices with carbon atoms not entering in to the
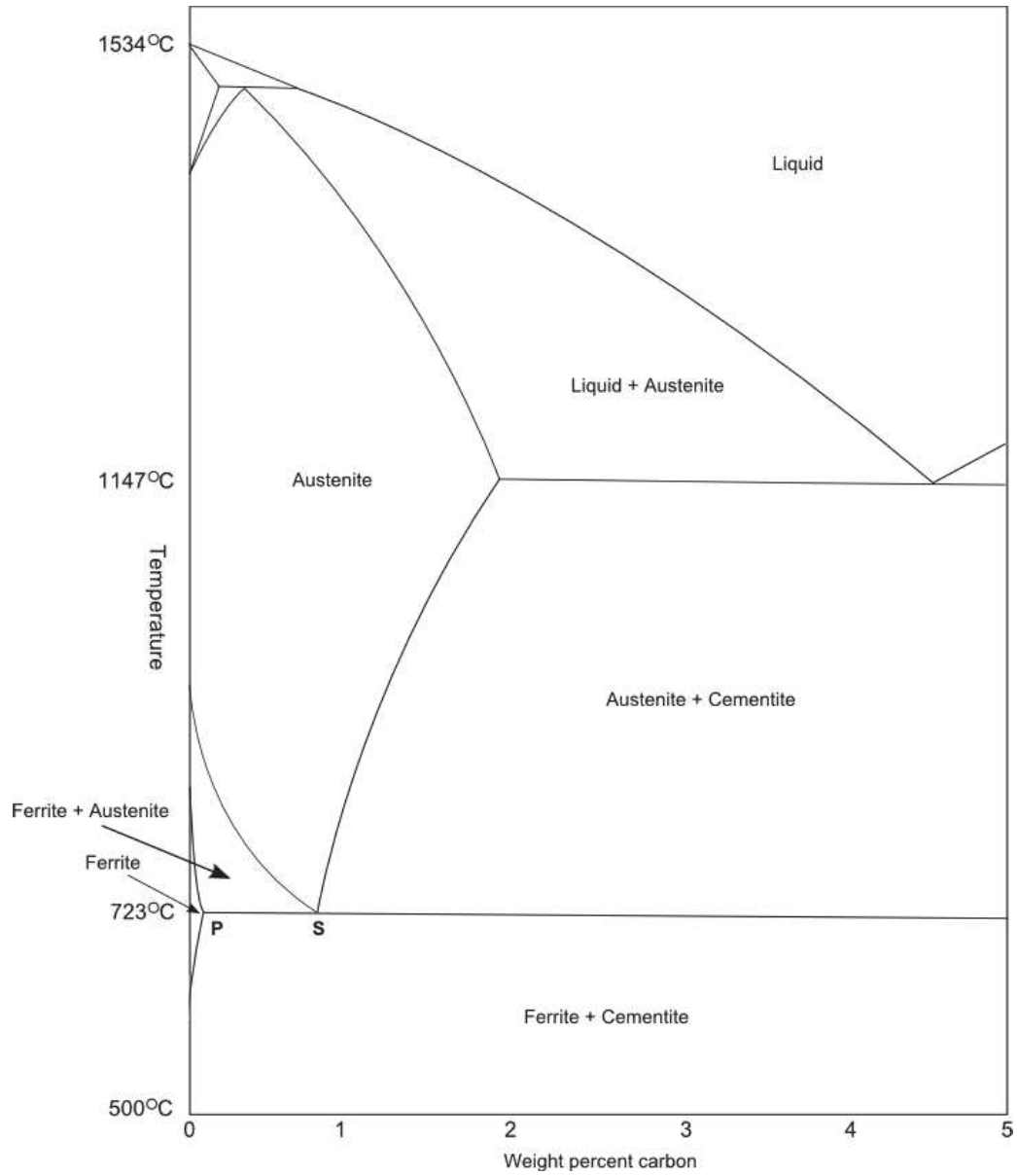
Figure 2.4: The Fe-C binary phase diagram. Adapted from [HB06]. The points S and P can be calculated as in Figure 2.5.
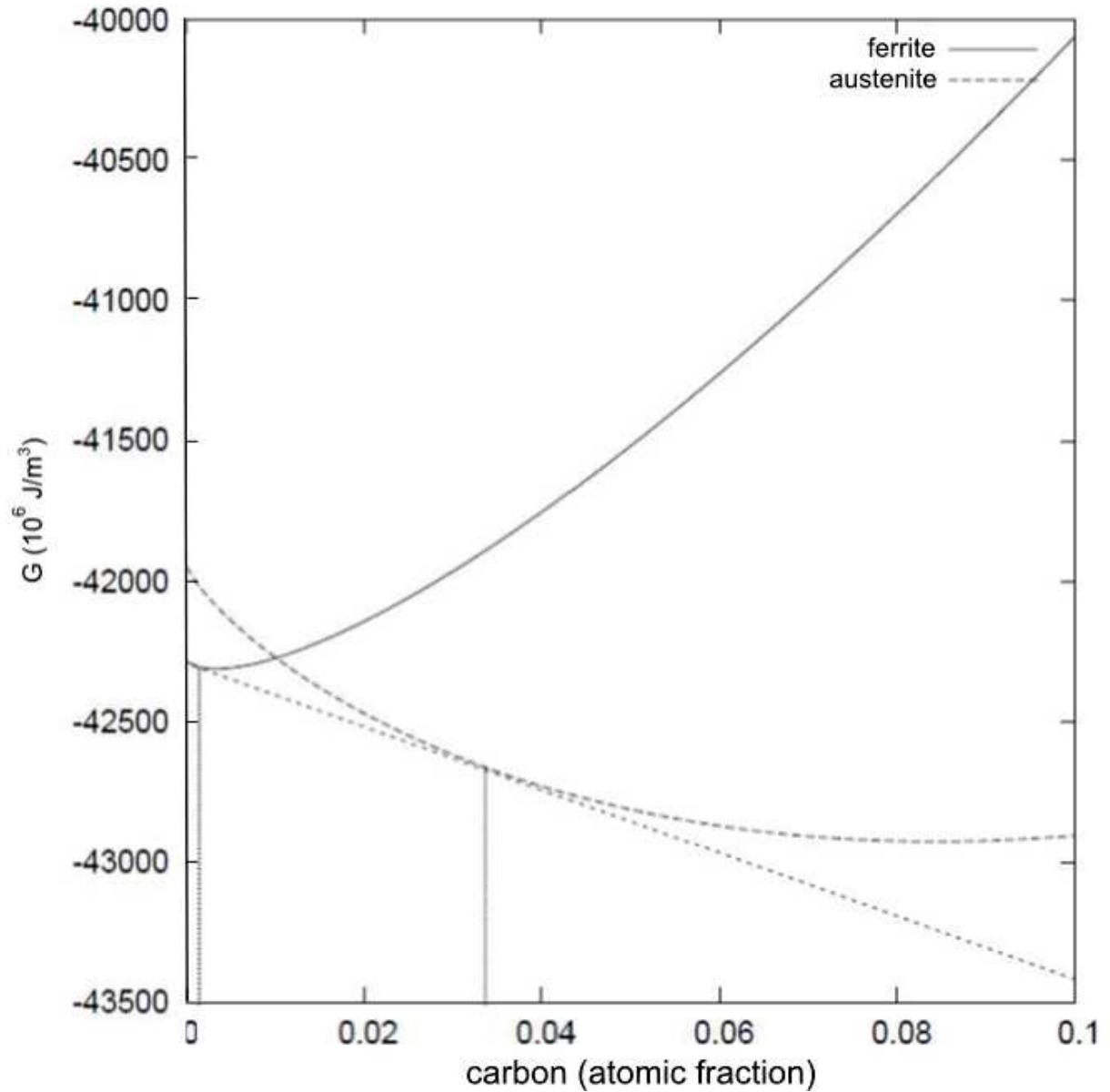
Figure 2.5: A plot of the free energies of ferrite and austenite for temperature $T = 727°C$ ($T = 1000.15K$). The common tangent approach is used to find the compositions of the two phases (the short dotted line). These points correspond to the points S and P in Figure 2.4. Repeating the process for varying T produces the whole diagram.

same sublattice as the iron atoms, hence Y_C^1 will be zero where $s = 1$ refers to the sublattice occupied by the Fe atoms.

The mole fraction X_i of component i can be calculated from the site fractions as,

$$X_i = \frac{\sum_s a^s Y_i^s}{\sum_s a^s (1 - Y_{Va}^s)}, \tag{2.53}$$

where a^s is the number of sites on sublattice s per formula units of the phase. Equation (2.53) is plausible since each atom is represented by a site and a mole is defined to be a fixed number of atoms so that it translates to a fixed number of sites. The introduction of the site fraction is based on the fact that we are dealing with multiple sublattices. The numerator of the right-hand side of Equation (2.53) is the total number of sites occupied by component i while the denominator is the total number of sites occupied by an atom. This is precisely the definition of a mole fraction.

The assumption of random mixing within each sublattice leads to the following expression for the ideal molar entropy of mixing (Equation (2.50)),

$$-\Delta S^{ideal} = R \sum_s a^s \sum_i Y_i^s \ln Y_i^s. \tag{2.54}$$

Even though iron has no ideal solutions (always has a non-zero enthalpy) its constituents are still distributed randomly and the error with respect to an ideal solution can be corrected by the introduction of an excess free energy term,

$$G_m = \sum_i X_i \,^\circ G_i - T\Delta S^{ideal} + {}^E G_m \tag{2.55}$$

where $X_i = \frac{n_i}{n}$ is the molar fraction of component i, with n_i the number of moles of component i and n the total number of moles in the solution. The term $^\circ G_i$ is the Gibbs free energy of the

pure component i and $^{E}G_m$ is the excess free energy, [Gus85]

$$^{E}G_m = \frac{1}{2}\sum_s\sum_i\sum_j\sum_k Y_i^s Y_j^s Y_k^t L_{ijk}^{sst} \qquad (2.56)$$

where L_{ijk}^{sst} represents the interaction energy between i and j which are found within the same sublattice for a two sublattice model. The interaction energies usually depend upon the components present in the other sublattices k as expressed by the superscript t which must be different from s.

2.2.3   The regular solution model applied to the Fe-C system

The molar free energies of the solid phases of the Fe-C system according to a 2 sublattice model with formula units $Fe_a(Va,C)_b$ can be expressed as, [Gus85],

$$G_m = Y_{Va}^2\,{}^{\circ}G_{Fe:Va}^h + Y_C^2\,{}^{\circ}G_{Fe:C}^h + bRT\{Y_C^2\ln(Y_C^2) + Y_{Va}^2\ln(Y_{Va}^2)\} + Y_{Va}^2 Y_C^2 L_{Fe:Va,C} + G_m^{mo} \quad (2.57)$$

where Y_i^s is the site fraction of component i on sublattice s and $s = 2$ is the interstitial sublattice not occupied by Fe. The Gibbs free energy of pure component Fe is denoted $^{\circ}G_{Fe:Va}^h$ and $^{\circ}G_{Fe:C}^h$ is the Gibbs free energy of Fe with all interstices filled with C. The enthalpy is calculated by interaction energies as $L_{Fe:Va,C}$ where the vacancies (Va) being in the same sublattice as the carbon atoms (C) are separated with a comma rather than a colon. The contribution due to magnetic ordering is expressed as G_m^{mo}.

Carbon atoms enter the octahedral sites of both the FCC and BCC structure. So the formula units for ferrite and austenite correspond to the ratio of lattice points occupied by the constituent atoms in Figure 2.6. Each Fe atom at the corner of the FCC structure contributes 1/8th of a lattice point to the total and each Fe atom at the centre of a face contributes 1/2. There are 8 corners and 6 faces giving a total of 4 lattice points. Each interstitial site at the edges contribute 1/4 of a lattice point so that 12 edges contribute toward the total of 4 lattice points occupied by interstitial sites including the interstitial site at the centre of the

FCC. Austenite then has formula units $Fe_1(Va, C)_1$ since the lattice points occupied by the two sublattices have a ratio of $1:1$. Similarly, ferrite has formula units $Fe_1(Va, C)_3$ since the lattice points occupied by the two sublattices have a ratio of $1:3$.

Considering the 2 sublattice model of ferrite with formula units $Fe_1(Va, C)_3$ we have $a^1 = 1$ and $a^2 = 3$, thus by Equation (2.54):

$$X_C = \frac{3Y_C}{1 + 3Y_C},$$

(2.58)

with $Y_{Va}^1 = 0$. Rearranging and defining the u-fraction of C as $u_C = \frac{X_C}{1 - X_C}$ gives [LAgA04],

$$Y_C = \frac{u_C}{3},$$

(2.59)

$$Y_{Va} = 1 - \frac{u_C}{3},$$

(2.60)

Similarly for austenite with constituents $Fe_1(Va, C)_1$ we have $a^1 = 1$ and $a^2 = 1$,

$$X_C \quad = \frac{Y_C}{1 + Y_C},$$

(2.61)

$$Y_C \quad = u_C,$$

(2.62)

$$Y_{Va} \quad = 1 - u_C.$$

(2.63)

While the range of values for X_C is $[0, 1]$, the range of values for u_C is $[0, \infty)$.

2.2.4   Computational thermodynamics for steels

Following Gustafson's expressions for the molar Gibbs free energy of the Fe-C system [Gus85], it is possible to compute the solubilities of carbon in the various phases using the common tangent approach. Suppose we have two smooth functions $G_m^\alpha(x)$ and $G_m^\gamma(x)$. The tangent functions $T_1(x)$ and $T_2(x)$ to these functions at points x_1 and x_2 respectively would have to
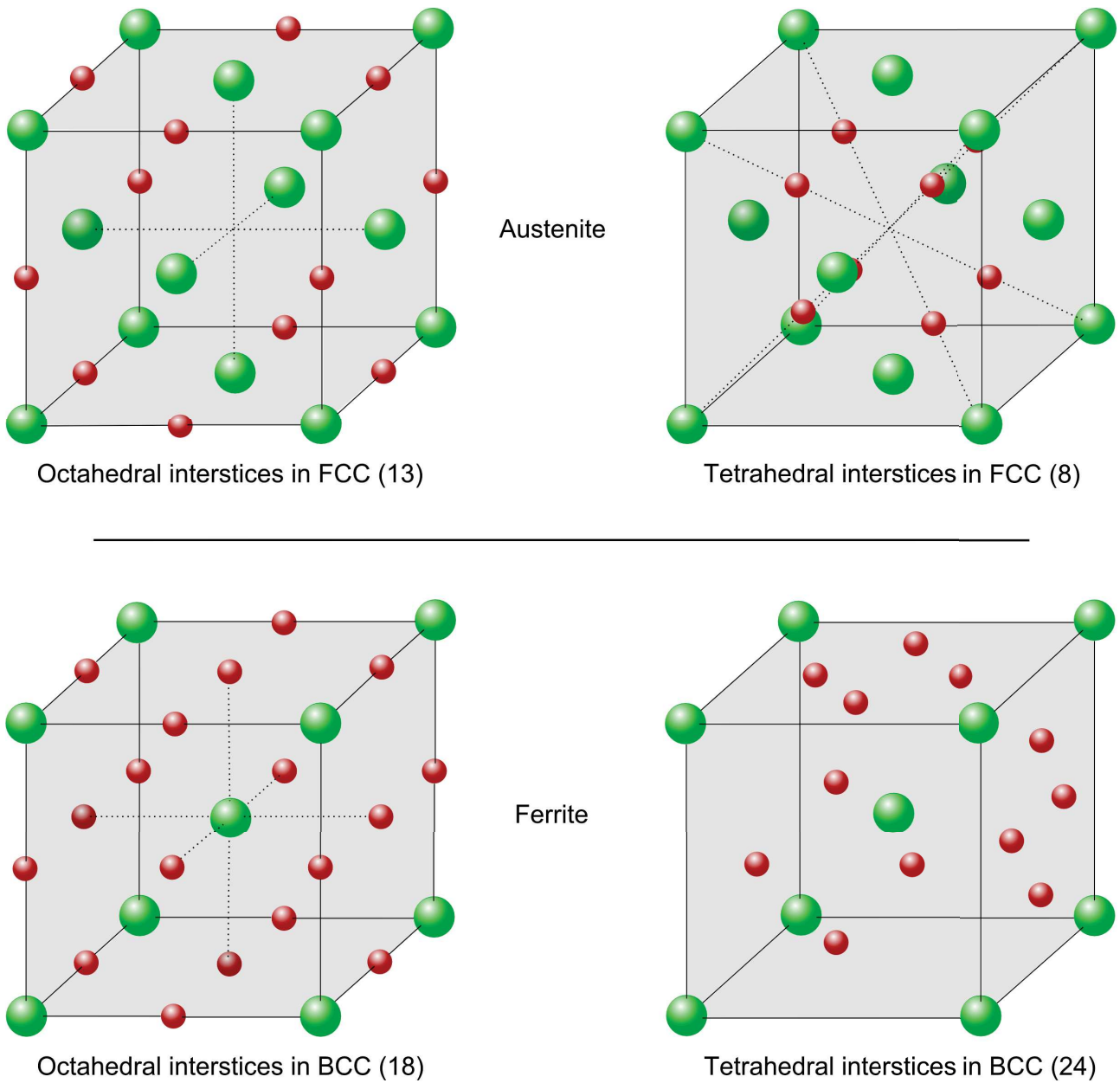
Figure 2.6: The molecular structures of austenite (FCC) and ferrite (BCC). The FCC structure has 13 octahedral and 8 tetrahedral interstices. 12 octahedral interstices are situated on the edges and 1 at the center. If the cube were to be divided in to 8 equal subcubes, a tetrahedral interstice is located at the center of each of these cubes. The BCC structure has 18 octahedral and 24 tetrahedral interstices. 6 octahedral interstices are located at the centers of the 6 faces with the remaining at the edges. The tetrahedral interstices are found at the faces of the cube mid-way between the center of the face and the edges.

satisfy the equations:

$$T_1(x) = \frac{dG_m^\alpha(x_1)}{dx}x + C_1,$$

$$T_2(x) = \frac{dG_m^\gamma(x_2)}{dx}x + C_2.$$

For these two tangents to be common we must have $T_1(x) = T_2(x)$ for all x. For $x = 0$ we have $C_1 = C_2 = C$. Since the derivative of a tangent function is the same everywhere we obtain the following equations:

$$
\begin{aligned}
T(x) &= \frac{dG_m^\alpha(x_1)}{dx}x + C, \\
T(x) &= \frac{dG_m^\gamma(x_2)}{dx}x + C, \\
\Rightarrow \frac{dG_m^\alpha(x_1)}{dx} &= \frac{dG_m^\gamma(x_2)}{dx}.
\end{aligned}
$$

Using the fact that $T(x_1) = G_m^\alpha(x_1)$ and $T(x_2) = G_m^\gamma(x_2)$, i.e. the tangent functions intersect the corresponding functions at x_1 and x_2 respectively, we have,

$$G_m^\alpha(x_1) - G_m^\gamma(x_2) = T(x_1) - T(x_2) = \frac{dG_m^\alpha(x_1)}{dx}x_1 - \frac{dG_m^\gamma(x_2)}{dx}x_2$$

and thus deriving the equations for solving for the common tangent:

$$
\begin{aligned}
\frac{dG_m^\alpha(x_1)}{dx} &= \frac{G_m^\alpha(x_1) - G_m^\gamma(x_2)}{x_1 - x_2}, \\
\frac{dG_m^\alpha(x_1)}{dx} &= \frac{dG_m^\gamma(x_2)}{dx}.
\end{aligned}
$$

A common tangent to G_m^γ and G_m^α must satisfy the above two equations which when solved give the two points corresponding to Figure 2.5. Taking $G_m^\alpha(x)$ and $G_m^\gamma(x)$ to be the molar free energies of the α and γ phases as functions of composition respectively as provided by Gustafson, we can compute the solubility of carbon in the α phase as $x_1 = x_\alpha$ and the γ phase as $x_2 = x_\gamma$. Note that G_m is a function of temperature and the above formulation for x_α and x_γ is for a particular temperature. Calculating x_α and x_γ for various temperatures in the same way as above, a section of the FeC binary phase diagram such as that in Figure 2.7 can be

computed.
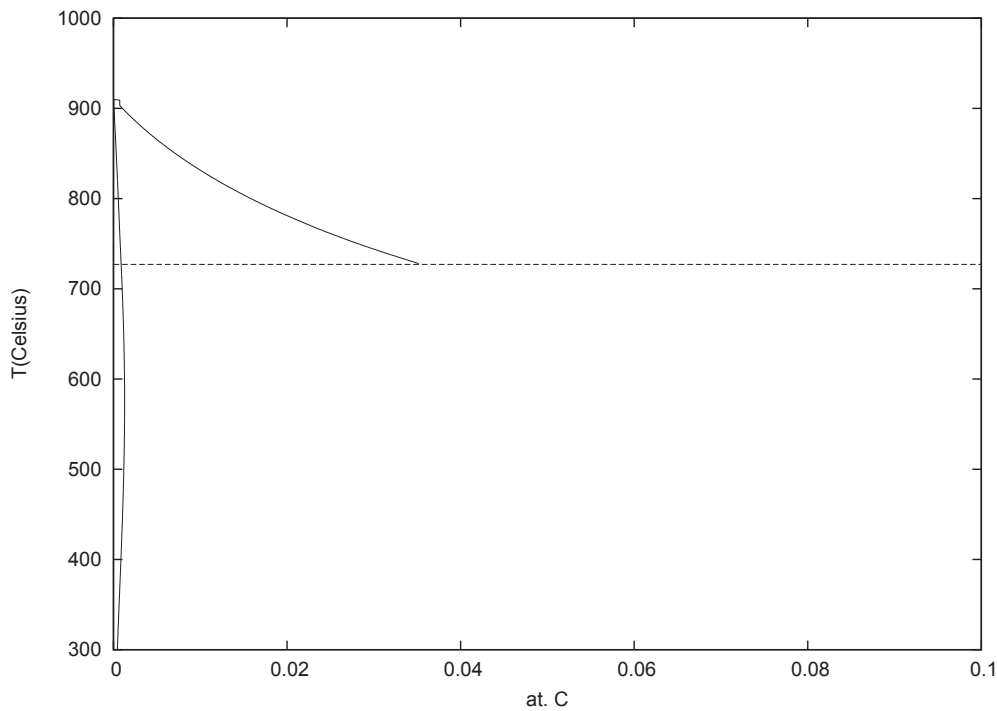
Figure 2.7: A section of the phase diagram computed using the common tangent construction giving a solubility limit of 0.091 atomic fraction carbon in the ferrite phase.

2.3 The smoothed particle hydrodynamics method

2.3.1 Introduction

Smoothed particle hydrodynamics (SPH), as a meshfree Lagrangian particle method, was originally introduced to deal with astrophysical phenomena on a large scale. Since it's inception some forty years ago independently by Lucy [Luc77] and Monaghan [Mon92] there have been significant improvements to the capabilities of SPH such as the formulation of SPH to discretize the equations of hydrodynamics while explicitly adhering to the second law of thermodynamics [EnR03]. While the focus of this thesis is on the use of SPH on mesoscale systems with the interpolation points representing volumes of material, the length scales within the scope of the capabilities of the SPH method runs from the astronomical scale to the microscale [NZ02]. The method has also been used to represent discrete particles rather than continuum mechanics. As

we shall soon see, there are many different formulations of the SPH equations. Some are better when applied to certain situations. However, the one thing common to all is the basic idea of SPH - the use of a weight function as an interpolation function to approximate the value of a field function at any given particle point. This approach enables the calculation of derivatives of the field functions to be obtained via the derivatives of the weight function only. A given particle within a system in the SPH formulations is generally regarded as a subsystem with its own variables such as mass, density and velocity representative of the material it contains. The SPH method holds many advantages over other methods and can be summarised as follows:

- The SPH method can be applied to problems of astronomical scale down to the microscale [NZ02]

- Particles representing the system are not rigidly connected to each other making large deformations easy to deal with (solving the problem faced with using the traditional Lagrangian description)

- Adapts to the system at hand thereby not being affected by initial particle distribution

- Complex geometries are easily dealt with

- Free surfaces are not a problem

- Moving interfaces are not a problem

- Can trace a discrete volume of material through space and time

- Boundary conditions are easily applied

- The particles in the SPH method not only act as interpolation points but also carry around system properties such as mass, velocity, pressure, density etc...

Using a weight function, a field property such as pressure at a particle location is calculated using the values of that field property at the locations of neighbouring particles. This can be

represented for field property $f(\mathbf{r}_i)$ at position $\mathbf{r}_i$ and weight function $W(\mathbf{r})$ as,

$$f(\mathbf{r}_i) = \sum_{j=0}^{N} W(\mathbf{r}_i - \mathbf{r}_j)f(\mathbf{r}_j). \tag{2.64}$$

This immediately implies that the accuracy and benefits of the approximation depend on the choice of the weight function. There are many choices for the weight function and these are discussed later.

2.3.2 The fundamental theory of smoothed particle hydrodynamics

In order to convey the general idea of the SPH method we derive the SPH methodology from the integral representation of a function $f(\mathbf{r})$ at position $\mathbf{r}$ using the dirac delta function $\delta(\mathbf{r})$,

$$\delta = \begin{cases} \infty, & \mathbf{r} = 0 \\ 0, & \mathbf{r} \neq 0 \end{cases}. \tag{2.65}$$

The following is true for the dirac delta function:

$$\int_{\Omega} \delta(\mathbf{r} - \mathbf{r}')d\mathbf{r}' = 1, \tag{2.66}$$

$$\int_{\Omega} f(\mathbf{r}')\delta(\mathbf{r} - \mathbf{r}')d\mathbf{r}' = f(\mathbf{r}), \tag{2.67}$$

where Ω is a region of volume containing $\mathbf{r}$. Here, Equation (2.67) is exact, however, the function δ is too rigid and too abstract to be dealt with easily. Instead, we formulate an approximation to this equation by replacing $\delta(\mathbf{r})$ with a weight function (also called a smoothing function/Kernel) $W(\mathbf{r}, h)$ with the property that,

$$\int_{\Omega} W(\mathbf{r}', h)d\mathbf{r}' = 1, \tag{2.68}$$

$$W(\mathbf{r}, h) = 0, \quad if \quad \mathbf{r} \notin B(h), \tag{2.69}$$

where h is called the smoothing length and determines the volume $(B(h))$ within which the kernel has influence and is non-zero. $B(h)$ is called the support domain and Ω is the system domain. In other words, $W(\mathbf{r}, h)$ is a smoothed approximation of $\delta(\mathbf{r})$ that does not have an infinitesimally small domain within which it is non-zero. W is visualised in Figure 2.8 where it can be seen that the field properties are *smoothed* over a region.
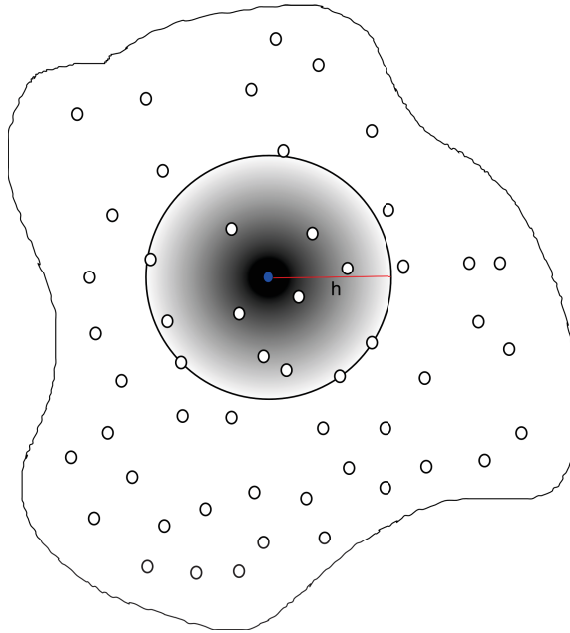
Figure 2.8: A figure of the support domain of length h of a particle (blue). Higher contrast areas correlate to larger contributions due to the weight function to the summation of Equation (2.64) from a particle in that region.

We can now re-write Equation (2.67) as,

$$f(\mathbf{r}) \approx \int_{\Omega} f(\mathbf{r}')W(\mathbf{r} - \mathbf{r}', h)d\mathbf{r}', \tag{2.70}$$

where the kernel W must adhere to certain requirements which will be specified later.

Approximation to the derivatives $\nabla f(\mathbf{r})$ and $\nabla \cdot \mathbf{f}(\mathbf{r})$ can be obtained as (where f is a scalar function in the prior case and a vector function in the latter),

$$\nabla f(\mathbf{r}) \approx \int_\Omega (\nabla f(\mathbf{r}'))W(\mathbf{r} - \mathbf{r}', h)d\mathbf{r}' \tag{2.71}$$

$$\nabla \cdot \mathbf{f}(\mathbf{r}) \approx \int_\Omega (\nabla \cdot \mathbf{f}(\mathbf{r}'))W(\mathbf{r} - \mathbf{r}', h)d\mathbf{r}'. \tag{2.72}$$

Using the identity,

$$\nabla \cdot (\mathbf{f}W) = W\nabla \cdot \mathbf{f} + \mathbf{f} \cdot \nabla W, \tag{2.73}$$

Equation (2.72) can be written as,

$$\nabla \cdot \mathbf{f}(\mathbf{r}) \approx \int_\Omega \left[\nabla \cdot (\mathbf{f}(\mathbf{r}')W) - \mathbf{f}(\mathbf{r}') \cdot \nabla W\right]d\mathbf{r}'. \tag{2.74}$$

Using the divergence theorem to convert the first term on the right-hand side of Equation (2.74) into an integral over the surface,

$$\nabla \cdot \mathbf{f}(\mathbf{r}) \approx \int_S \mathbf{f}(\mathbf{r}')W \cdot \hat{\mathbf{n}}dS - \int_\Omega \mathbf{f}(\mathbf{r}') \cdot \nabla W d\mathbf{r}', \tag{2.75}$$

where $\hat{\mathbf{n}}$ is the unit normal to surface S of the support domain. The first term on the right-hand side of Equation (2.75) vanishes since the kernel is zero everywhere except for within the support domain. Similar operations on Equation (2.71) results in,

$$\nabla f(\mathbf{r}) = -\int_\Omega f(\mathbf{r}')\nabla W d\mathbf{r}', \tag{2.76}$$

$$\nabla \cdot \mathbf{f}(\mathbf{r}) = -\int_\Omega \mathbf{f}(\mathbf{r}') \cdot \nabla W d\mathbf{r}', \tag{2.77}$$

where the gradients on the right-hand side of the equations are with respect to $\mathbf{r}'$. Re-writing the equations with the gradients with respect to $\mathbf{r}$ we can get rid of the negative sign (since

$$\frac{\partial W(\mathbf{r}_i - \mathbf{r}_j)}{\partial \mathbf{r}_j} = \frac{\partial W(\mathbf{r}_i - \mathbf{r}_j)}{\partial (\mathbf{r}_i - \mathbf{r}_j)} \frac{\partial (\mathbf{r}_i - \mathbf{r}_j)}{\partial \mathbf{r}_j} = \frac{\partial W(\mathbf{r}_i - \mathbf{r}_j)}{\partial (\mathbf{r}_i - \mathbf{r}_j)} \left(-\frac{\partial (\mathbf{r}_i - \mathbf{r}_j)}{\partial \mathbf{r}_i} \right),$$

$$\nabla f(\mathbf{r}) = \int_{\Omega} f(\mathbf{r}') \nabla W \, d\mathbf{r}', \tag{2.78}$$

$$\nabla \cdot \mathbf{f}(\mathbf{r}) = \int_{\Omega} \mathbf{f}(\mathbf{r}') \cdot \nabla W \, d\mathbf{r}'. \tag{2.79}$$

Note that this simplification is only valid if the support domain of the particle in question is entirely within the system domain. In cases where part of the support domain is outside the system domain, the first term on the right-hand side of Equation (2.75) is no longer zero. However, there are techniques that compensate for these cases as we shall see later.

2.4   Hydrodynamics

In fluid mechanics, the equations governing the evolution of the system must adhere to the conservation of certain variables such as the mass, momentum and energy. The four fundamental equations are explicitly, the conservation equations for mass, energy, momentum and angular momentum. Including the second law of thermodynamics gives the equations for describing a thermofluid. The Lagrangian form of these equations of hydrodynamics are [PHK95, PH97]:

$$\frac{d\rho}{dt} = -\rho \nabla \cdot \mathbf{v}, \tag{2.80}$$

$$\frac{d\mathbf{v}}{dt} = \frac{1}{\rho} \nabla \cdot \mathbf{P} + g, \tag{2.81}$$

$$T\rho \frac{dS}{dt} = \phi + \kappa \nabla^2 T, \tag{2.82}$$

$$\frac{dU}{dt} = \frac{1}{\rho} \mathbf{P} : \nabla \mathbf{v} - \frac{1}{\rho} \nabla \cdot q, \tag{2.83}$$

$$\mathbf{P} = -P\mathbf{I} + \sigma, \tag{2.84}$$

$$\sigma = \eta_V [\nabla \mathbf{v} + \nabla \mathbf{v}^T] + (\zeta - \frac{2}{d}\eta_V)(\nabla \cdot \mathbf{v})\mathbf{I}, \tag{2.85}$$

$$\mathbf{q} = -K\nabla T, \tag{2.86}$$

where ρ, $\mathbf{v}$, S, P and T is the density field, velocity field, entropy per unit mass, pressure field and the temperature field respectively. The coefficients η_V, ζ and κ are the shear viscosity, bulk

or dilatational viscosity and thermal conductivity respectively. The stress tensor is denoted by $\mathbf{P}$ and the viscous stress tensor is denoted by σ. ϕ is the viscous heating field and is defined by,

$$\phi = 2\eta \overline{\nabla \mathbf{v}} : \overline{\nabla \mathbf{v}} + \zeta (\nabla \cdot \mathbf{v})^2, \tag{2.87}$$

where the tensor $\overline{\nabla \mathbf{v}}$ is given for dimension d by,

$$\overline{\nabla \mathbf{v}} = \frac{1}{2}[\nabla \mathbf{v} + \nabla \mathbf{v}^T] - \frac{1}{d}\mathbf{1}\nabla \cdot \mathbf{v}. \tag{2.88}$$

$\mathbf{1}$ is the unit tensor and the expression $\mathbf{A} : \mathbf{B} = \sum_i \sum_j A_{ij} B_{ji}$ is the double dot product of two tensors with A_{ij} referring to the element found in the ith row and jth column of the tensor $\mathbf{A}$. ϕ ensures the contribution to the internal energy from the energy dissipation due to shear stresses.

In many cases, the fundamental equations describing fluid motion and evolution are insufficient for solving for the system parameters. It is therefore necessary to increase the number of equations in relation to the parameters. These equations are called constitutive equations. For instance, Fick's law of mass transfer is a constitutive equation. In this thesis, there will be many instances of a frequently used constitutive equation called the equation of state which involves thermodynamic variables such as pressure, temperature and density.

Chapter 3

Phase field models for martensitic transformations

3.1   Solid-solid phase transformations

The mobility of elements in the solid-state is much lower than that in the liquid state. In the solid state, atom diffusivity is related to the temperature as

$$D(T) = D_O \exp(-\frac{K_b}{K_B T}),$$ (3.1)

where D_o is a coefficient dependent on the atom size and atom vibration frequency. K_b is the kinetic barrier. K_B is the Boltzmann constant, and T is the temperature. This means that the diffusivity at high temperatures is greater than at low temperatures. In high temperature solid-solid phase transformations, the atom mobility is still high enough to enable diffusive transformations. Austenite to pearlite transformation, austenite to allotriomorphic ferrite transformation and austenite to idiomorphic ferrite transformation are typical diffusive solid-solid phase transformations in steels. However, when the temperature is low, atom mobility is too low to fulfill the requirements of the phase transformation. Thus displacive transformation may take pace. The latter is a cooperative displacement of atoms. An example

46

of a displacive transformation in steels is martensite which is obtained by rapidly cooling the steel to low temperatures. This particular phase transforms from a face centered cubic (FCC) structure to a body centered cubic (BCC) structure at very high speed allowing atoms (say carbon atoms) very little time to diffuse into the surrounding material. The result is a supersaturated body centered tetragonal (BCT) phase. Martensite is a highly brittle but strong phase. Due to the rapid speed of formation of these phases, experimental results, for instance during the formation of a plate, are absent and incredibly difficult if not impossible to obtain. Numerical modelling and simulation, as will be seen in the subsequent chapters, enables the study of these transformations at very small time increments.

3.2 Martensitic transformation theory

Martensitic transformation (MT) is observed in many materials, not just in steels, and at a wide range of temperatures [Bha01]. MT in steels is accompanied by a rearrangement of the crystal lattice. The transformation is displacive and so there is no atomic diffusion. The microstructure formed resembles plate-like regions where martensite has formed. There are 24 different orientation variants of the martensite plates in steels [Kun07]. Given the accommodating nature of the transformation, the microstructure tends to favour certain variants above others.

One way to model and simulate martensitic growth using the PF method is to find a free energy as a function of the order parameter, η, which produces a single minimum (at $\eta = 0$) at high temperatures corresponding to the high temperature phase and two minima at low temperatures corresponding to the low temperature phase. These two minima must be at nonzero order parameter. At intermediate temperatures, the free energy must have three minima. Landau expanded the free energy density of a system to model second order phase transitions as,

$$f(\eta, T) = f_0 + a_2(T - T_1)\eta^2 + a_4\eta^4,\qquad(3.2)$$

where the constants $a_2, a_4 > 0$. This is obtained from the original power series expansion,

$$f(\eta, T) = f_0 + a_1\eta + a_2\eta^2 + a_3\eta^3 + a_4\eta^4 + ..., \tag{3.3}$$

as follows: Let T_1 be the transition temperature. At high temperatures above T_1, the high temperature phase must be stable, i.e. the free energy must have a minimum at $\eta = 0$,

$$\frac{\partial f}{\partial \eta}\mid_{\eta=0} = [a_1 + 2a_2\eta + 3a_3\eta^2 + ...]\mid_{\eta=0} = 0, \tag{3.4}$$

$$\frac{\partial^2 f}{\partial \eta^2}\mid_{\eta=0} = [2a_2 + 6a_3\eta + ...]\mid_{\eta=0} > 0. \tag{3.5}$$

Equation (3.4) implies $a_1 = 0$. Equation (3.5) implies $a_2 > 0$. Below T_1 we should have the emergence of a new phase and the high temperature phase should be unstable, i.e. the free energy must have a maximum at $\eta = 0$,

$$\frac{\partial^2 f}{\partial \eta^2}\mid_{\eta=0} < 0 \rightarrow a_2 < 0. \tag{3.6}$$

This means a_2 depends on temperature and changes sign at the transition temperature. One simple possibility is $a(T - T_1)$, $a > 0$. For $f(\eta, T)$ to increase with $|\eta|$, i.e. continuous transition between phases, we must have $a_3 = 0$ and $a_4 > 0$. Devonshire [Dev54] devised a free energy for first order phase transitions as (called the 2-4-6 phase transition polynomial),

$$f(\eta, T) = f_0(T) + A(T)\eta^2 - B\eta^4 + C\eta^6, \tag{3.7}$$

$$A(T) = a(T - T_1),$$

where $a, B, C, T_1 > 0$. f_0 is the free energy at $\eta = 0$ (i.e. high temperature phase) as expanded by the power series. The order parameter η, may correspond to the strain or atomic shuffling. A plot of Equation (3.2) and Equation (3.7) is shown in Figure 3.1 and Figure 3.2 respectively.
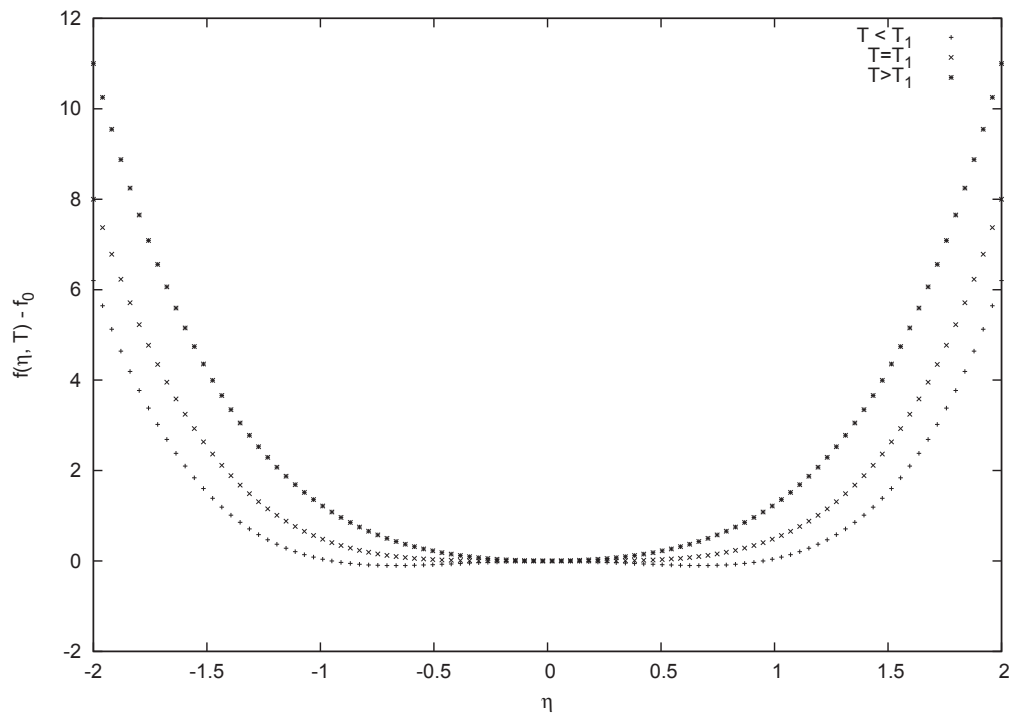
Figure 3.1: A plot of Equation (3.2) (Landau) with $a_2 = 0.05$, $a_4 = 0.5$ and $T_1 = 10$.
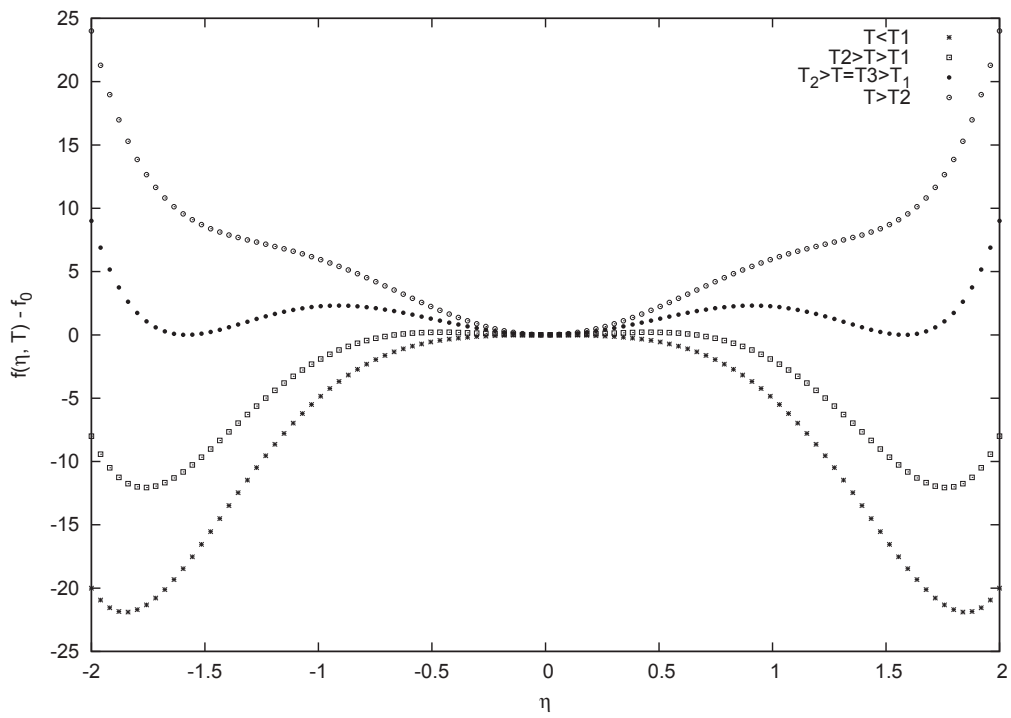
Figure 3.2: A plot of Equation (3.7) (Devonshire) with $a = C = 1$, $B = 5$ and $T_1 = 10$.

Solving $\frac{\partial f}{\partial \eta} = 0$ for Equation (3.7) gives the five roots,

$$\eta = \pm\sqrt{\frac{2B \pm \sqrt{4B^2 - 12ac(T - T_1)}}{6C}},$$

(3.8)

$$\eta = 0.$$

Let T_2 be such that $4B^2 - 12ac(T - T_1) = 0$ and T_3 be such that $f(\eta_1, T) = f(\eta_2, T) = f(0, T)$ for the minima η_1 and η_2 in Equation (3.8). This gives,

$$T_2 = \frac{B^2}{3ac} + T_1,$$

(3.9)

$$T_3 = \frac{B^2}{4ac} + T_1.$$

(3.10)

Then Equation (3.8) results in one root and one minimum for $T > T_2$, three roots and two minima for $T \leq T_1$ and five roots and three minima for $T_2 > T > T_1$. At $T = T_3$, the energy wells are of equal depth. The two minima corresponding to nonzero order parameter represent two orientation variants of the martensitic phase.

In the presence of an external field, $\tilde{\sigma}$ (external stress), the free energy is [Fal82],

$$\tilde{f}(\eta, T) = f(\eta, T) - \tilde{\sigma}\eta,$$

(3.11)

implying equilibrium at,

$$\frac{\partial \tilde{f}}{\partial \eta} = 0 \rightarrow \frac{\partial f}{\partial \eta} = \tilde{\sigma}.$$

(3.12)

Equation (3.7) is plotted again with $\tilde{\sigma} > 0$ in Figure 3.3.

It may be noticed that if one were to use Equation (3.11) to model phase transitions involving domains, equilibrium considerations of the free energy will result in infinitesimally narrow interface widths. Ginzburg-Landau free energy is the result of adding a gradient term to the
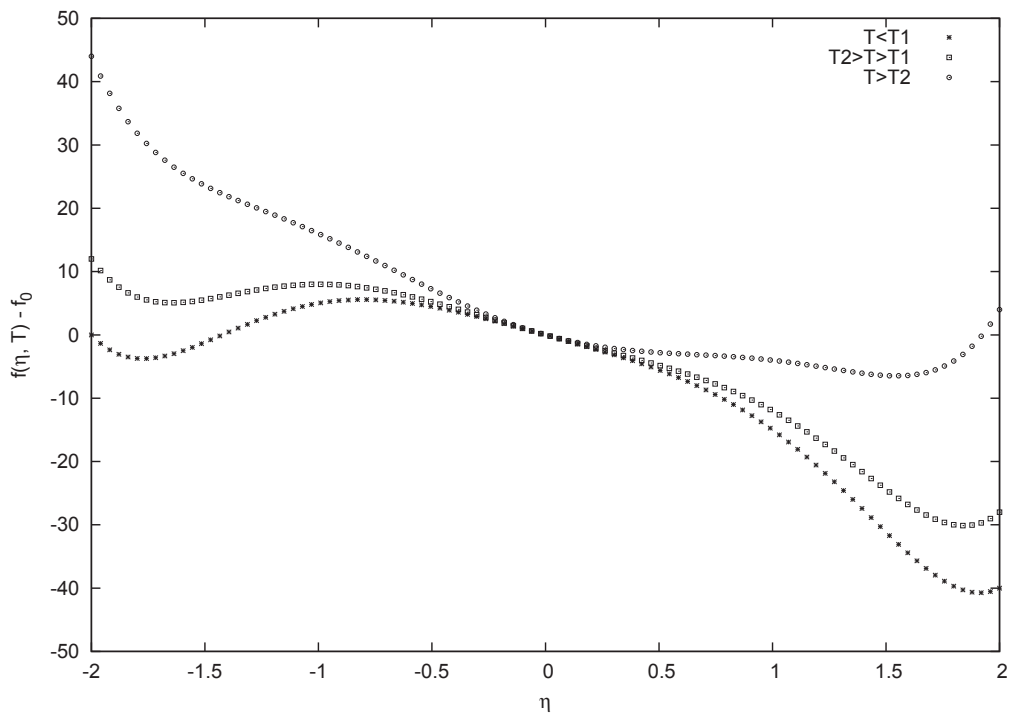
Figure 3.3: A plot of Equation (3.11) with $a = C = 1$, $B = 5$, $T_1 = 10$ and $\sigma = 10$.

homogeneous free energy density,

$$\tilde{f}(\eta, \nabla\eta, T) = \tilde{f}(\eta, T) + \epsilon(\nabla\eta)^2, \tag{3.13}$$

where $\epsilon > 0$ is the gradient energy coefficient. Thus minimising the total free energy,

$$F(\eta, \nabla\eta, T) = \int_\Omega \tilde{f}(\eta, \nabla\eta, T) dV, \tag{3.14}$$

where Ω is the system domain, V is the volume and the terms η and T now depend on position x. For cases which are not invariant under the transformation $(\eta \longrightarrow -\eta)$, a $2-3-4$ polynomial may be used,

$$f(\eta, T) = f_0 + a_1(T - T_1)\eta^2 - a_2\eta^3 + a_3\eta^4. \tag{3.15}$$

The nonsymmetric nature of Equation (3.15) can be seen in Figure 3.4. As mentioned in Section
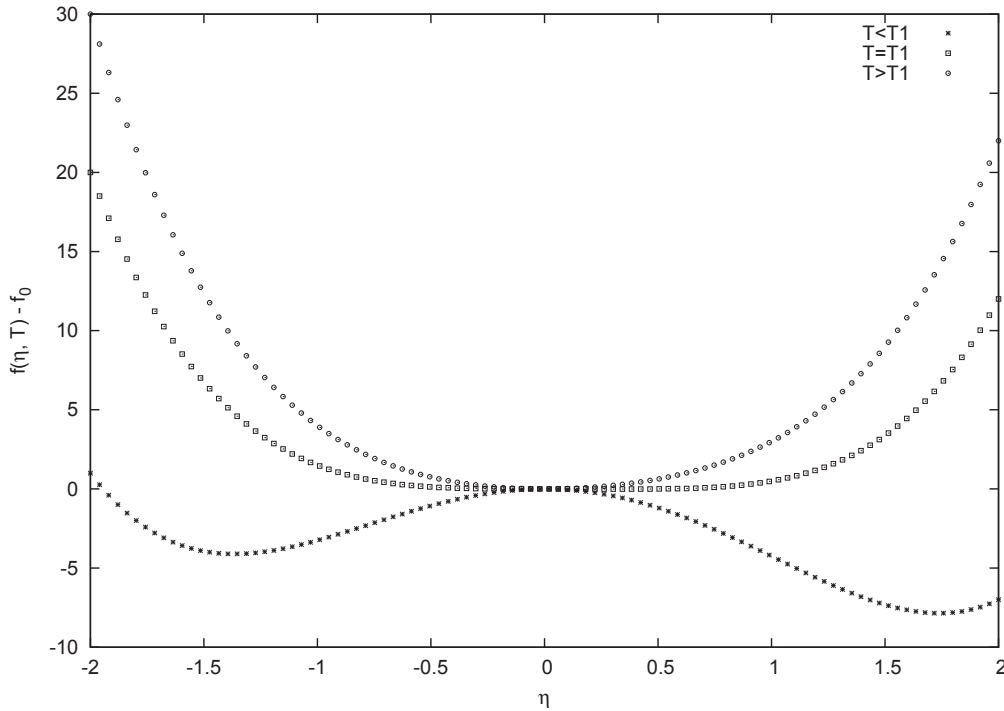
Figure 3.4: A plot of Equation (3.15) with $a_1 = 0.05$, $a_2 = 0.5$, $a_3 = 1$ and $T_1 = 10$.

2.1.3, in some PF models, secondary order parameters are employed such as temperature and

composition. For martensitic phase transitions, PF models may involve a coupling of the order parameter η with a secondary order parameter, ε, the strain. A simple free energy with coupling to ε is,

$$f(\eta, T) = a_1 \eta^2 - a_2 \eta^4 + a_3 \eta^6 + \frac{E}{2}\varepsilon^2 - F\varepsilon\eta^k, \tag{3.16}$$

with $k = 1, 2$.
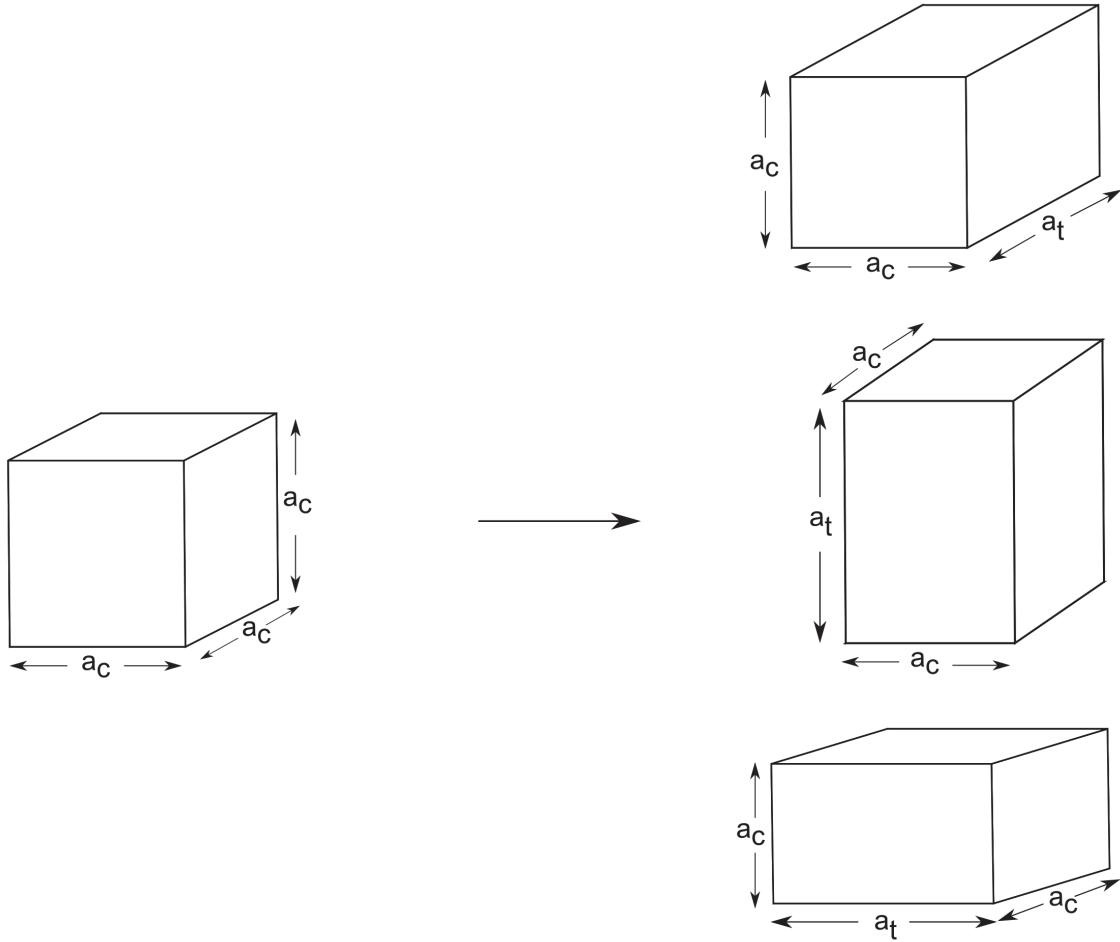
Figure 3.5: The three cubic to tetragonal transformations.

As stated above, PF models may use Equation (3.2) or (3.7) with η representing the strain [Fal82, AB65, AY81, BK84, SWL97, RLS$^+$01, CKO$^+$07, SSF12], Equation (3.2) coupled with strain with η representing the three different energy equivalent transformations from a cubic lattice to a tetragonal lattice (Figure 3.5) [WK97, JAK01, KO03, SHL$^+$03, YTT08], or a coupled Equation (3.2) with strain and an additional 2-3-4 polynomial for thermal effects. The Gibbs

free energy in this case is then formulated as,

$$G = -\sigma : \lambda : \sigma/2 : \varepsilon_t \phi(\eta) + f(\eta, T), \tag{3.17}$$

where, as in Equation (2.87), : is the double dot product of two tensors, ε_t is the transformation strain and ϕ and f are 2-3-4 polynomials in η. The strain may also be coupled to a 2-3-4-5 polynomial to model martensite-martensite transitions [LPL03]. Other works have also applied this approach [ICL08, ICL08, Ber10]. The order parameter in martensitic transformations may also take other forms such as electronic band energy levels [Bha78] and charge density waves [KS79] among others.

3.3 A phase-field formulation for martensite

Given the transformation of austenite to martensite, the free energy density of the system can be represented by [WBM92],

$$g = \frac{1}{2}\epsilon^2|\nabla\phi|^2 + \frac{1}{4\omega}\phi^2(1-\phi)^2 + h(\phi)g_{\alpha'} + [1 - h(\phi)]g_\gamma, \tag{3.18}$$

with $h(\phi) = \phi^3(6\phi^2 - 15\phi + 10)$ [WB95] where $g_{\alpha'}$ and g_γ are the homogeneous free energy densities of the martensite and austenite phases respectively. Equation (3.18) is in the form of Figure 2.3 with the α' and γ phases represented by the two energy wells with the energy barrier representing the interface between the two. The value of ϕ at any point $\vec{r}$ determines the phase present. Here, $\phi = 0$ and $\phi = 1$ corresponds to austenite and martensite respectively. Values of ϕ in the interval $(0, 1)$ correspond to the interface between austenite and martensite. The kinetic coefficient (ω) and the gradient energy coefficient (ϵ) are related to the interface energy (σ) and half-interface thickness (λ) as $\omega = \lambda/(26.4\sigma)$ and $\epsilon = \sqrt{3\lambda\sigma/1.1}$ [KKS98]. The governing equation for ϕ is then [WBM92, KKS98],

$$\phi_t = M_\phi[\epsilon^2\nabla^2\phi + \frac{1}{2\omega}\phi(1-\phi)(1-2\phi) - 30\phi^2(1-\phi)^2(g_{\alpha'} - g_\gamma)], \tag{3.19}$$

where $M_\phi > 0$ is the PF mobility. Equilibrium of the system corresponds to $g_{\alpha'\gamma} = g_{\alpha'} - g_\gamma = 0$. The driving force can be separated into the chemical free energy difference and the strain energy difference,

$$g_{\alpha'\gamma} = g_{\alpha'\gamma}^{chem} + g_{\alpha'\gamma}^{strain}. \tag{3.20}$$

The value of $g_{\alpha'\gamma}^{chem}$ may be calculated using thermodynamic computational software. This coupling of thermodynamic software and the PF method has been demonstrated in the past for solidification in reference [QW03b]. The strain energy provides a positive contribution to the free energy meaning it is unfavourable, i.e. it serves to reduce the driving force $g_{\alpha'\gamma}$. The interface between the martensite and austenite on the macroscopic scale is termed the habit plane. The formation of matensite is accompanied by a dilatation δ normal to the habit plane and a shear s lying on it. The non-shear and shear contribution to the strain energy related to this ellipsoidal inclusion shaped transformation with dimensions c_a and a is given respectively as [Chr58],

$$g_{\alpha'\gamma1}^{strain} = \frac{\mu}{1-\sigma_p}[\frac{2}{9}(1+\sigma_p)\Delta^2 + \frac{\pi c_a}{4a}\delta^2 + \frac{\pi}{3}(1+\sigma_p)\frac{c_a}{a}\Delta\delta], \tag{3.21}$$

$$g_{\alpha'\gamma2}^{strain} = \frac{\mu}{1-\sigma_p}[\frac{\pi}{8}(2-\sigma_p)\frac{c_a}{a}s^2], \tag{3.22}$$

where μ, σ_p and Δ is the shear modulus, poisson's ratio and the uniform dilatation respectively. Assuming $\Delta, \frac{c_a}{a} << 1$, Equation (3.21) may be approximated to second order in Δ and δ by [Chr58],

$$g_{\alpha'\gamma1}^{strain} = \frac{\mu}{1-\sigma_p}[\frac{\pi c_a}{4a}\delta^2]. \tag{3.23}$$

The total strain energy due to the oblate ellipsoidal inclusion is then,

$$g_{\alpha'\gamma}^{strain} = \frac{\mu\pi c_a}{4a(1-\sigma_p)}[\delta^2 + \frac{2-\sigma_p}{2}s^2]. \tag{3.24}$$

Choosing the coordinate system such that $\vec{s}_x$, $\vec{s}_y$ and $\vec{\delta}$ correspond to the x, y and z directions (martensite coordinate system),

$$\vec{\delta} = \phi_{,z}\hat{k}, \quad \vec{s} = \vec{s}_x + \vec{s}_y = \phi_{,x}\hat{i} + \phi_{,y}\hat{j}, \tag{3.25}$$

where $\phi_{,m} = \frac{\partial \phi}{\partial m}$ and $\hat{i}$, $\hat{j}$ and $\hat{k}$ are the unit vectors in the x, y and z directions respectively. Equation (3.24) can then be written in terms of the PF variable as,

$$g_{\alpha'\gamma}^{strain} = \frac{\mu \pi c}{4a(1 - \sigma_p)}[\phi_{,z}^2 + \frac{2 - \sigma_p}{2}(\phi_{,x}^2 + \phi_{,y}^2)]. \tag{3.26}$$

In order for the correct macroscopic shape change to be observed, the chemical free energy change is required to be a function of second order in the PF variable. Consideration of symmetry as in Appendix A gives,

$$g_{\alpha'\gamma}^{chem} = k_1\phi_{,x}^2 + k_2\phi_{,y}^2 + k_3\phi_{,z}^2, \tag{3.27}$$

where the k_i are constants. The chemical free energy change is dependent on the amount of phase transformed and not on orientation, thus $k_1 = k_2 = k_3 = K$ and,

$$g_{\alpha'\gamma}^{chem} = K(\nabla \phi)^2. \tag{3.28}$$

In this way, the total driving force due to the strain and chemical energy difference is expressed as,

$$g_{\alpha'\gamma} = g_{\alpha'\gamma}^{strain} + g_{\alpha'\gamma}^{chem} = \frac{1}{d}[(f_1 + dk_1)\phi_{,x}^2 + (f_2 + dk_2)\phi_{,y}^2 + (1 + dk_3)\phi_{,z}^2], \tag{3.29}$$

with $f_1 = f_2 = \frac{2 - \sigma_p}{2}$ and $d = \frac{4a(1 - \sigma_p)}{c_a \mu \pi}$ and $k_1 = k_2 = k_3 = K$. In order to determine the favoured growth shape of Equation (3.29), note that within the composition-temperature range within which MT is favourable, K is negative. From the definition of f_1 and f_2 and that $\sigma_p > 0$ we have $0 < f_1, f_2 < 1$. This results in the coefficients of $\phi_{,x}^2$ and $\phi_{,y}^2$ in Equation (3.29) being smaller (more energetically favourable) than that of $\phi_{,z}$, e.g. $f_1 + dK = f_2 + dK < 1 + dK$. The resulting macroscopic shape change is an oblate ellipsoid. Equation (3.29) is with respect to the martensite coordinate system. The required format should be with respect to the austenite coordinate system. Letting $[\gamma, \vec{v}]$ and $[\alpha', \vec{v}]$ be the column vector $\vec{v}$ in the austenite and martensite coordinate system respectively, there exists a transformation matrix

$(\gamma J\alpha')$ from the martensite coordinate system to the austenite coordinate system such that,

$$[\gamma, \vec{v}] = (\gamma J\alpha')[\alpha', \vec{v}], \tag{3.30}$$

and for polycrystalline steels an orientation matrix for different austenite grains is introduced as $[\gamma, \vec{v}] = (SJ\gamma)(\gamma J\alpha')[\alpha', \vec{v}]$ where $(SJ\gamma)$ is a rotation matrix from the austenite coordinate system to the sample coordinate system. The matrix $(\gamma J\alpha')$ is available for many steels. The works here use the transformation matrix for $Fe - 30Ni - 0.3C$ [Kun07] as,

$$\begin{pmatrix} 0.575371 & 0.542097 & 0.097510 \\ -0.550726 & 0.568476 & 0.089244 \\ -0.008855 & -0.131888 & 0.785465 \end{pmatrix}$$

. Letting the elements of the 3×3 matrix $(\gamma J\alpha')$ be represented by H_{ij}, and applying the transformation to the vector $\nabla\phi$,

$$\begin{pmatrix} H_{11} & H_{12} & H_{13} \\ H_{21} & H_{22} & H_{23} \\ H_{31} & H_{32} & H_{33} \end{pmatrix} \begin{pmatrix} \phi_{,x} \\ \phi_{,y} \\ \phi_{,z} \end{pmatrix} = \begin{pmatrix} H_{11}\phi_{,x} + H_{12}\phi_{,y} + H_{13}\phi_{,z} \\ H_{21}\phi_{,x} + H_{22}\phi_{,y} + H_{23}\phi_{,z} \\ H_{31}\phi_{,x} + H_{32}\phi_{,y} + H_{33}\phi_{,z} \end{pmatrix},$$

gives the driving force as,

$$g_{\alpha'\gamma} = \frac{1}{d}\sum_{i=1}^{3}(f_i + dK)(H_{i1}\phi_{,x} + H_{i2}\phi_{,y} + H_{i3}\phi_{,z})^2. \tag{3.31}$$

There are 24 variants of martensite plate growth in steels. This is due to the equivalent symmetry variants of the cubic structure. Letting each of the 6 faces of the cube take position as the bottom face and applying rotations (4 rotations) about the z-axis through this face results in $6 \times 4 = 24$ symmetry operations. Applying these operations to $(\gamma J\alpha')$ gives another 23 matrices.

Individual plates are produced using Equation (3.31) and the following parameters: $M_\phi = 100$ (PF mobility, qualitatively unimportant here), $\sigma = 0.6J/m^2$, $\lambda = 14.3nm$ [QB09, QW03a, WBM93, KR98], $\sigma_p = 0.285$ (real values are in the range 0.27-0.3), $\mu = 72 \times 10^9 Pa$ by using the equation [Ban05],

$$\mu(T) = \mu_0 - \frac{D}{exp(298/T) - 1},$$ (3.32)

where T is temperature in Kelvin, $\mu_0 = 85GPa$, $D = 10$GPa and $T = 250°C$ (523.15 Kelvin). $K = 3.6 \times 10^9 J/m^3$ is chosen and is in the same order of magnitude as that in reference [YTT10]. The parameter c_a/a is the observed dimensions of the oblate ellipsoid. This ratio should be reflected in the coefficients of the various directions in Equation (3.31), by solving the following equation for c_a/a,

$$\frac{1 + dK}{f_1 + dK} = \frac{c_a}{a}.$$ (3.33)

For the chosen parameters, $c_a/a = 0.045197387$. Using these parameters, the 24 plate variants are shown in Figure 4 in Appendix D. During growth, each variant is given a unique ID which is only for identification purposes and does not require governing equations. This way, the nucleation and growth of multiple martensite grains within multiple austenite grains is possible. This is shown in Figure 3.17. Figure 3.6 Shows the PF variable profile of a simulation of a single variant by nucleation on a grain boundary. Figure 3.7 shows a simulation of 30 nuclei randomly nucleated at the system boundary. New nucleations are performed every 20 timesteps until a maximum of 30 nuclei is reached.

The formulations above do not consider externally applied stress. Given an externally applied stress, the system is no longer in a stress free state. The first term in Equation (3.19) is responsible for the energy contribution of the interface. The second term is responsible for the energy barrier between two stable states. The effect of an applied stress must then be reflected by the driving force term, i.e. an applied stress effects the driving force for growth [Kun07]. Again, requirement of symmetry results in only the second order terms [Kun07],

$$U = \sigma_N \delta^2 + \tau s^2 = \sigma_N \phi_{,z}^2 + \tau(\phi_{,x}^2 + \phi_{,y}^2),$$ (3.34)

where U is in units of Pa, due to an applied stress and σ_N and τ is the stress components resolved normal and parallel to the habit plane respectively. Applying this to Equation (3.29) in a similar manner to reference [Kun07],

$$
\begin{aligned}
g_{\alpha'\gamma} &= g_{\alpha'\gamma}^{chem} + g_{\alpha'\gamma}^{strain} \\
&= \frac{1}{d}[(0.85 + dK - d\tau)(\phi_{,x}^2 + \phi_{,y}^2) + (1 + dK - d\sigma_N)\phi_{,z}^2.
\end{aligned}
\tag{3.35}
$$

The condition inferred by Equation (3.33) is then transformed to,

$$
\frac{1 + dK - d\sigma_N}{f_1 + dK - d\tau} = \frac{c_a}{a}.
\tag{3.36}
$$

Given an applied stress of

$$
\sigma = \begin{pmatrix} 1 & 0 & 0 \\ 0 & 1 & 0 \\ 0 & 0 & 1 \end{pmatrix}
$$

the value of c_a/a is 0.0576. In the case for a uniaxial applied stress, a simulation of all variants is shown in Figure 12 in Appendix D. Figure 8 in Appendix D shows the effect of applied stress on c_a/a. This agrees well with references [Kun07, GR86] where it is shown that a general applied stress results in a larger c_a/a ratio. It is seen from Figure 8 in Appendix D that an applied stress of around 200MPa increases the ratio of the plates by around 5% for this steel within the range given in [GR86]. In Figure 12 there are 16 out of 24 variants that are able to grow, 12 of which have a favourable interaction with the applied stress. This is also shown in Tables (3.4) and (3.5) in reference [Kun07].

3.4 Phase-field simulation of bainitic transformation

One such case of martensitic transformation where structures must be distinguished from each other is bainite. The method has been used to simulate the evolution of bainite formation using a criteria for autocatalytic nucleation based on driving force values at each point across
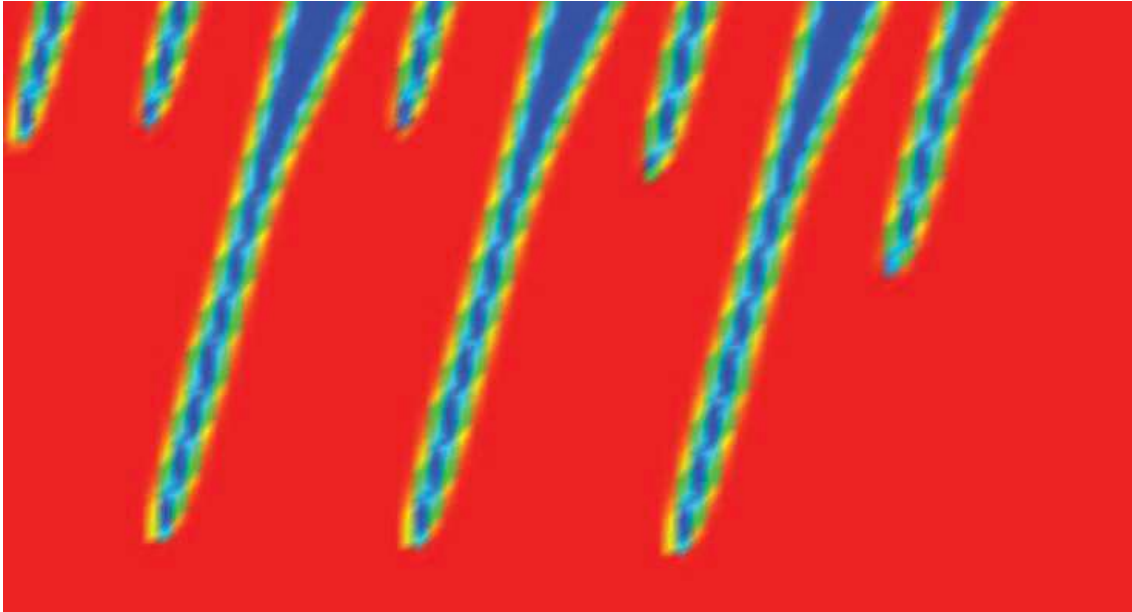
Figure 3.6: The phase-field variable profile of 8 martensite nuclei nucleated at the boundary. The image is of a cross section of the domain.
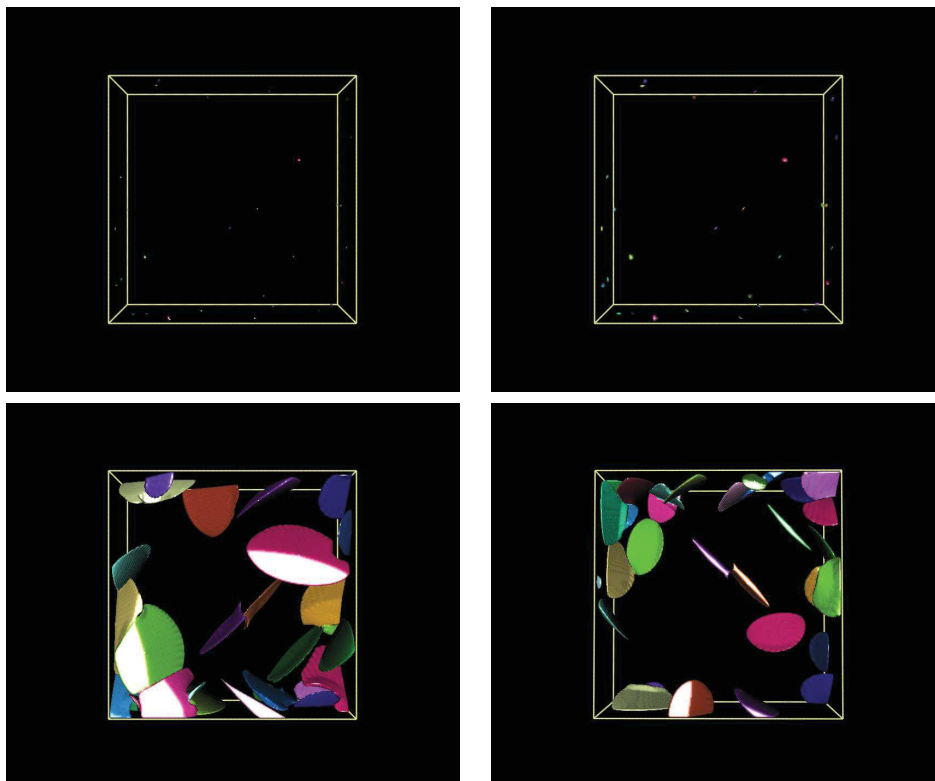
Figure 3.7: The growth of 30 martensitic nuclei at time step 1000 (top left), 2000 (top right), 24000 (bottom left and bottom right).

the domain. Even so, the method could be employed given any nucleation criteria that may arise from recent studies involving bainite. For the γ to bainite (α_B) transformation, unlike the γ to α' transformation, the composition is no longer constant in time during the growth of the phase [Bha92]. This means a governing equation for composition must also be considered as well as the presence of composition terms in the free energy density. Equation (3.18) becomes Equation (A.9),

$$g = \frac{1}{2}\epsilon_\phi^2|\nabla\phi|^2 + \frac{1}{2}\epsilon_c^2|\nabla c|^2 + \frac{1}{4\omega}\phi^2(1-\phi)^2 + h(\phi)g_{\alpha_B} + [1-h(\phi)]g_\gamma, \qquad (3.37)$$

where ϵ_ϕ and ϵ_c are the gradient energy coefficient associated with the PF variable and the composition respectively with the governing equation as that in Equation (3.19). A governing equation for c is derived as [CH58],

$$\frac{\partial c}{\partial t} = \nabla \cdot (M_c \nabla \frac{\delta G}{\delta c}), \qquad (3.38)$$

$$G = \int_\Omega g \, dv, \qquad (3.39)$$

where M_c is the concentration mobility and $\frac{\delta G}{\delta c}$ is the functional derivative of the total free energy G. We have,

$$\frac{\delta G}{\delta c} = \frac{\partial g}{\partial c} - \nabla \cdot \frac{\partial g}{\partial \nabla c}, \qquad (3.40)$$

giving,

$$\frac{\partial c}{\partial t} = \nabla \cdot (D \nabla c), \qquad (3.41)$$

with the diffusivity $D = M_c \frac{\partial^2 g}{\partial c^2}$. This term is calculated using Equation (2.57) for both phases as,

$$\frac{\partial^2 g}{\partial c^2} = h(\phi)\frac{\partial^2 g_{\alpha_B}^{chem}}{\partial c^2} + [1-h(\phi)]\frac{\partial^2 g_\gamma^{chem}}{\partial c^2}. \qquad (3.42)$$

An increase in carbon content translates to a decrease in the aspect ratio of the bainitic subunits [WZYF00]. In the previous work on the PF modelling of bainite (see Appendix E), the function $l(c) = -h_4 tan^{-1}(h_1 c + h_2) + h_3$, where h_1, h_2, h_3 and h_4 are constants, was used to fit available data on the carbon concentration dependence of the aspect ratio of bainite plates. The existence

of Equation (3.33) to determine the aspect ratio means that this is now not necessary. To show that there is a general reduction of the aspect ratio for an increase in carbon concentration, Equation (3.33) is solved for $T = 400°C$ (673.15 Kelvin), $\mu = 67 \times 10^9 Pa$ and $\sigma_p = 0.285$ at carbon concentrations $c = 0.0111$ and $c = 0.0211$ atom fraction. This gives $K = -1.8 \times 10^9$ Pa and $K = -1.4 \times 10^9$ Pa respectively using the regular solution method from Section 2.2.3. Solutions of Equation (3.33) for these values give,

$$\frac{c_a}{a} = \frac{(-d\frac{c_a}{a}K + 1) \pm \sqrt{(-d\frac{c_a}{a}K + 1)^2 + 4(d\frac{c_a}{a}K)0.8575}}{2(0.8575)},$$

$$\frac{c_a}{a}(c = 0.0111) = 0.0244$$

$$\frac{c_a}{a}(c = 0.0211) = 0.019,$$

i.e. an increase of c results in a reduction of $\frac{c_a}{a}$. Equation (3.29) results in energy favourable for growth only if $1 + dK < 0$. For $T = 400°C$ this gives a carbon concentration less than $c = 0.051$ and an aspect ratio for the individual subunits as small as $\frac{c_a}{a} = 0.03$.

Using the same parameters as in Section 3.3 but with $T = 400°C$, $\mu = 67 \times 10^9$ Pa and $c = 0.0111$, a single bainitic subunit in the subunit coordinate system is shown using the PF method in Figure 3.9 on a 100^3 grid. The growth of a single subunit is stopped after 7000 time steps or if the subunit encounters a grain boundary. The carbon concentration from the center of the subunit is plotted in Figure 3.8. It can be seen that, due to Equation (3.41), the carbon diffuses out of the subunit to the adjacent austenite. More figures can be seen on this from Figure 4 in Appendix E.

In order to reproduce autocatalytic behaviour, a random number generator is used in the vicinity of the existing subunits. The possibility of a nucleation is gauged by the driving force at that location. It can be seen from Figure 3.8 (see also Figure 2 and Figure 4 in Appendix E) that the carbon concentration around the subunit increases. This corresponds to a lower driving force in that region. This can be seen in Figure 3.10 of the driving force profile across the subunit in Figure 3.9. This nucleation criteria results in a higher possibility to nucleate
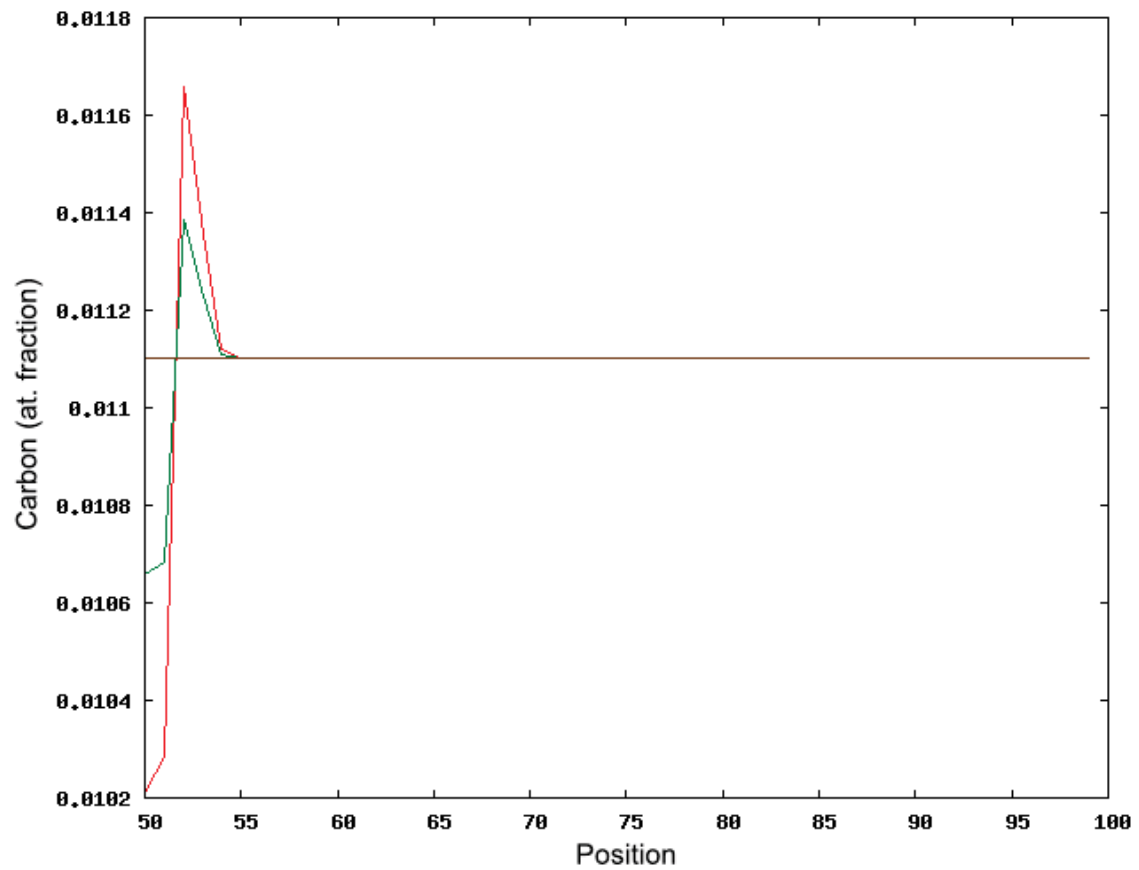
Figure 3.8: The concentration profile across the bainitic subunit in Figure 3.9. Position 50 corresponds to the centre of the plate with the measured direction advancing vertically in Figure 3.9.

near the tips of existing subunits as seen experimentally [RB92a].
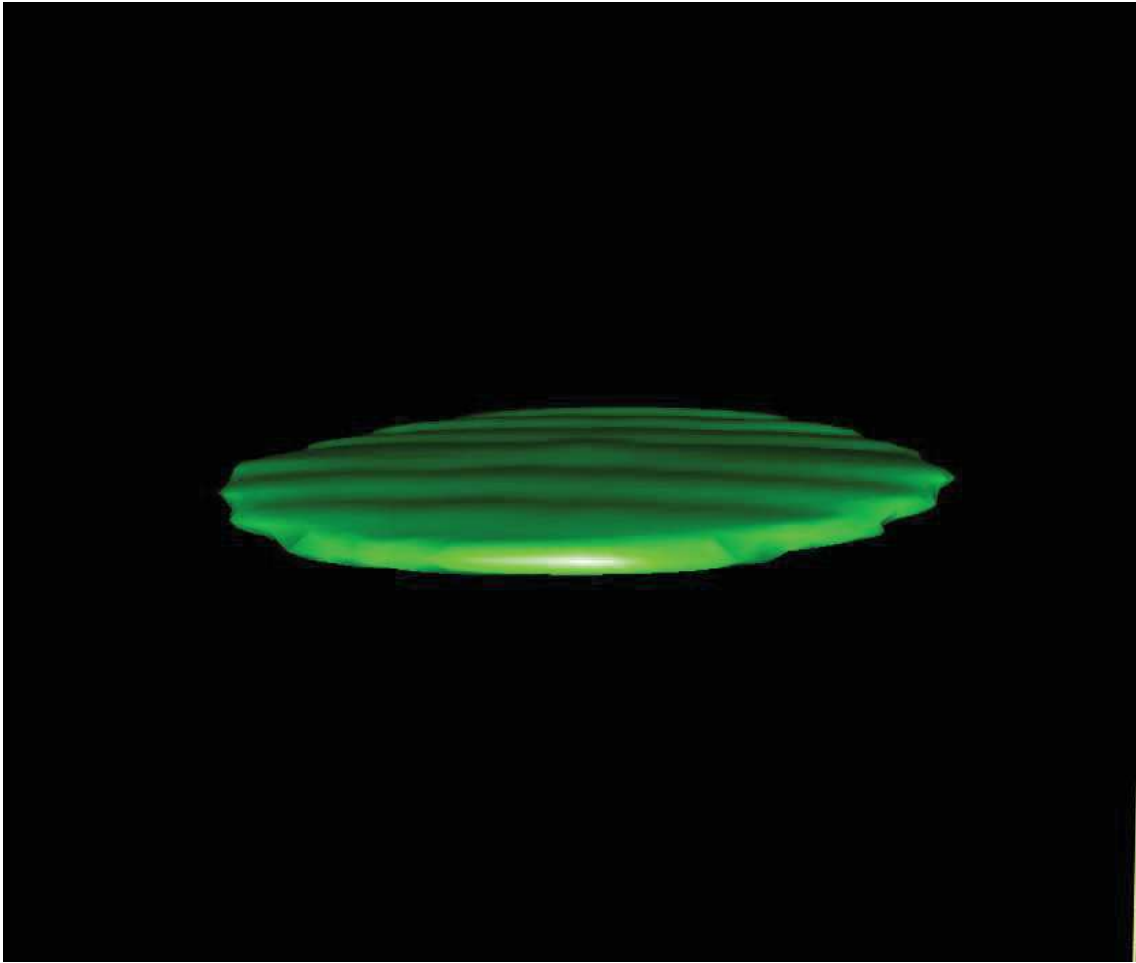
Figure 3.9: A simulation of a single bainitic subunit on a 100^3 grid using the PF model described in Section 3.3.

In this manner, autocatalytic behaviour is demonstrated in Figure 3.11 and Figure 3.12. Here, a single bainitic subunit is nucleated at the grain boundary with three subsequent autocatalytic nucleations. An entire sheaf is shown in Figure 3.13 growing through a grain from one side to the other. The concentration profile across the width of the sheaf is shown in Figure 3.14 with regions of high concentration corresponding to the carbon build up between subunits (see also Figure 6 in Appendix E).

A system domain consisting of two austenite grains on a 100^3 lattice is shown in Figure 3.16. This is obtained by randomly nucleating two austenite grains, assigning them random rotation matrices ($(SJ\gamma)$ in Section 3.3) and letting them grow spherically. The lattice points in which
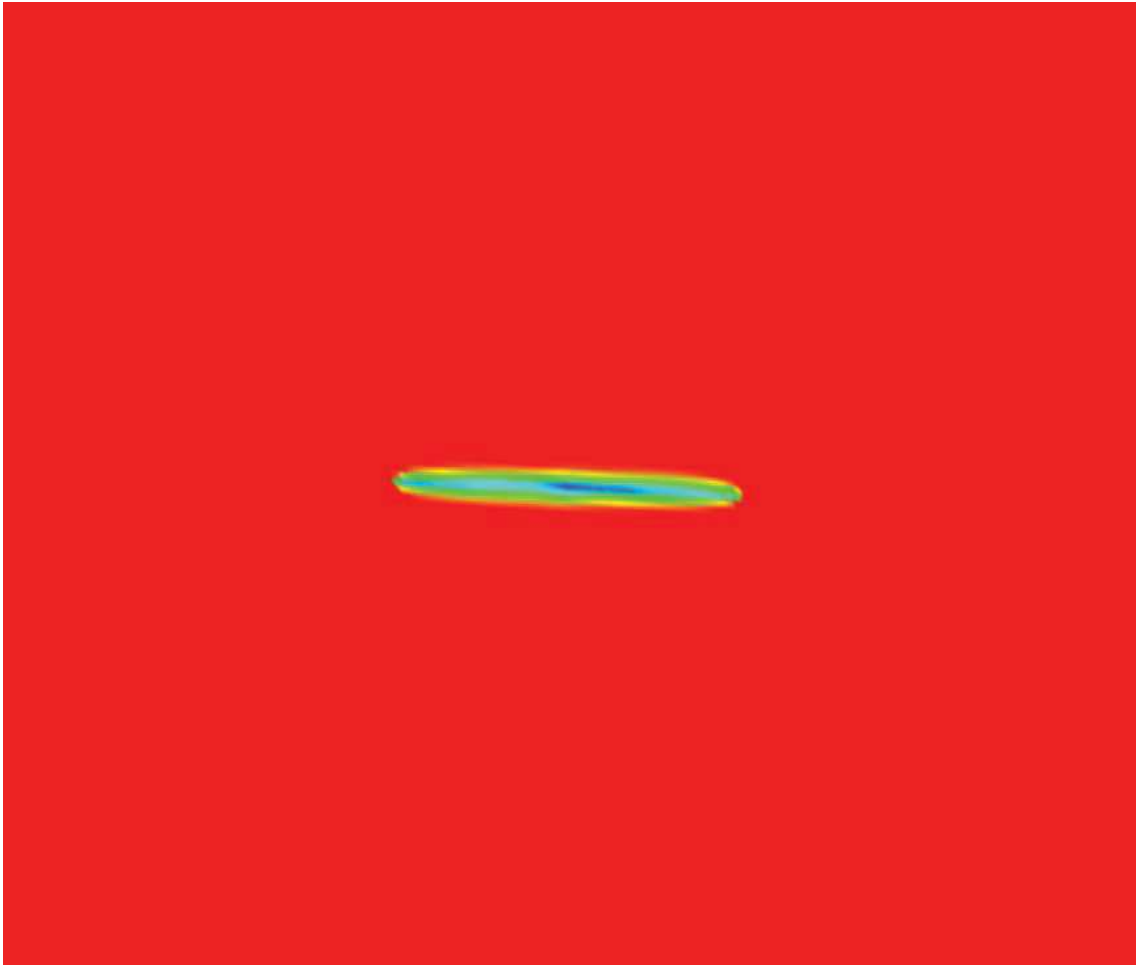
Figure 3.10: The driving force profile of the subunit in Figure 3.9. The red regions correspond to high driving forces while blue regions indicate low driving forces.

the two grains meet is identified as a grain boundary as are the system domain boundaries. Six subunits are nucleated randomly at the grain boundaries within this domain. Subsequent autocatalytic growth generates the microstructure shown in Figure 3.17. Finally, on a similar two-austenite domain but with 200^3 lattice points, multiple grain boundary nucleations and autocatalytic nucleations form a microstructure with its cross section shown in Figure 3.15 (see also Figure 3 in Appendix F).
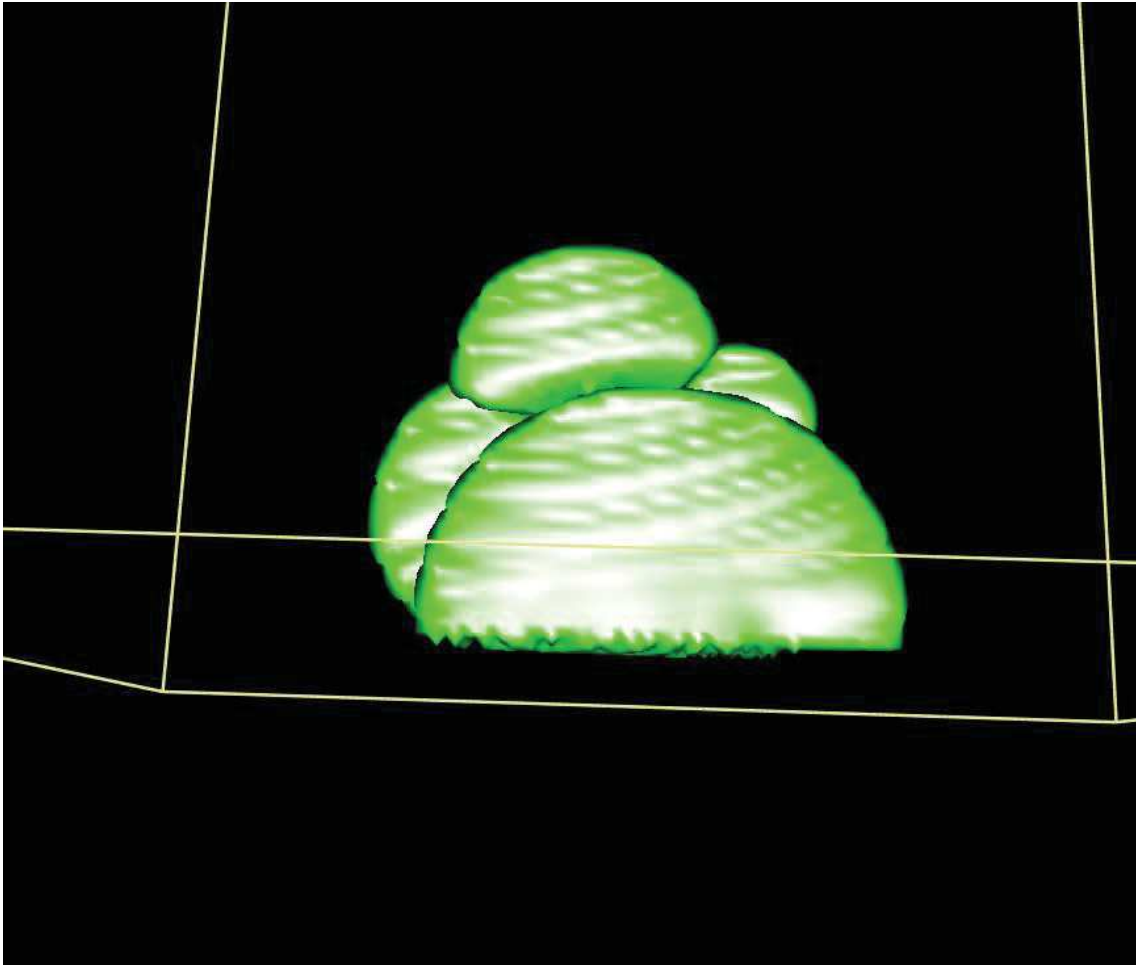
Figure 3.11: A simulation of a bainitic sheaf via autocatalytic subunit nucleation on a 100^3 grid using the PF model described in Section 3.3.

3.5 Summary and discussion

The developed model for martensite plate growth is unlike previous studies of PF modelling of martensite in that only a single PF variable is used for the growth of multiple plates. The
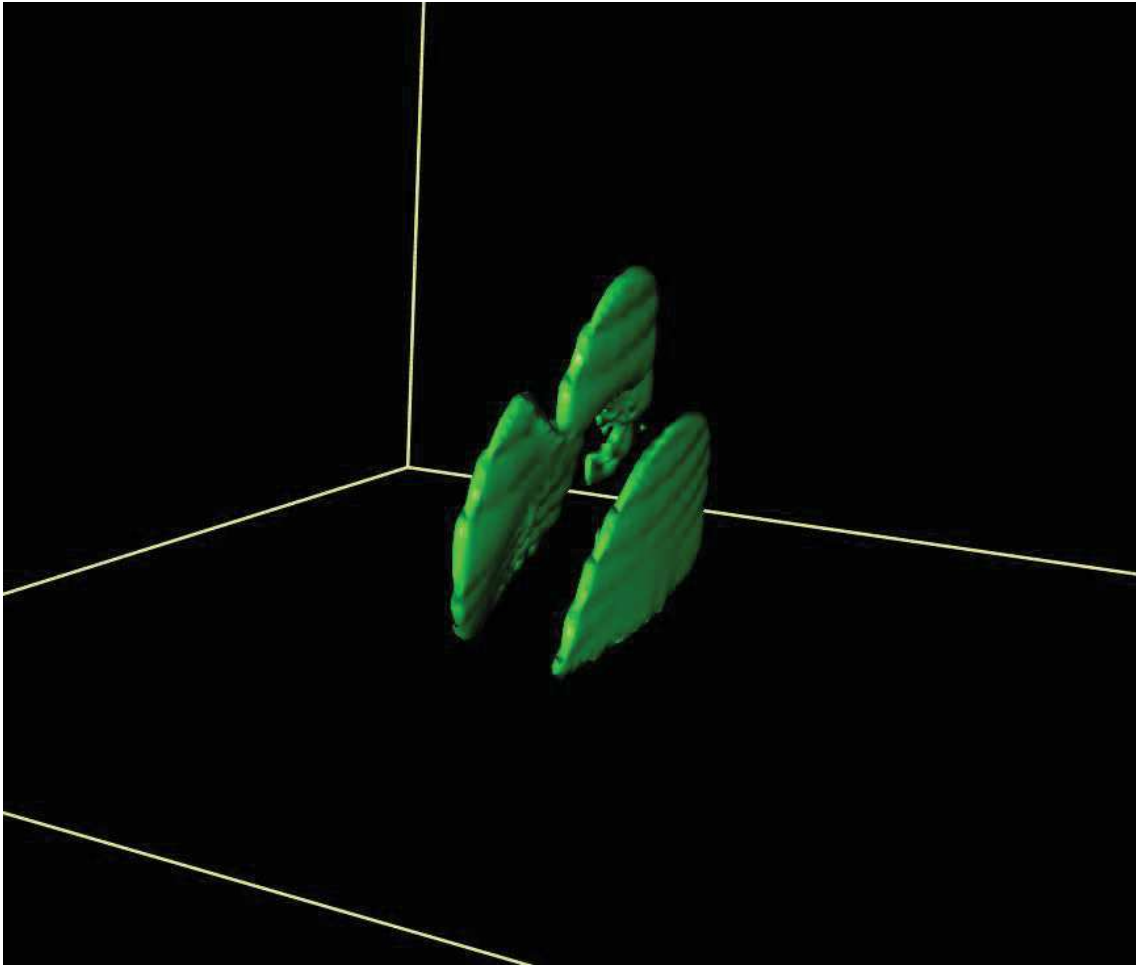
Figure 3.12: A simulation of a bainitic sheaf via autocatalytic subunit nucleation on a 100^3 grid using the PF model described in Section 3.3.
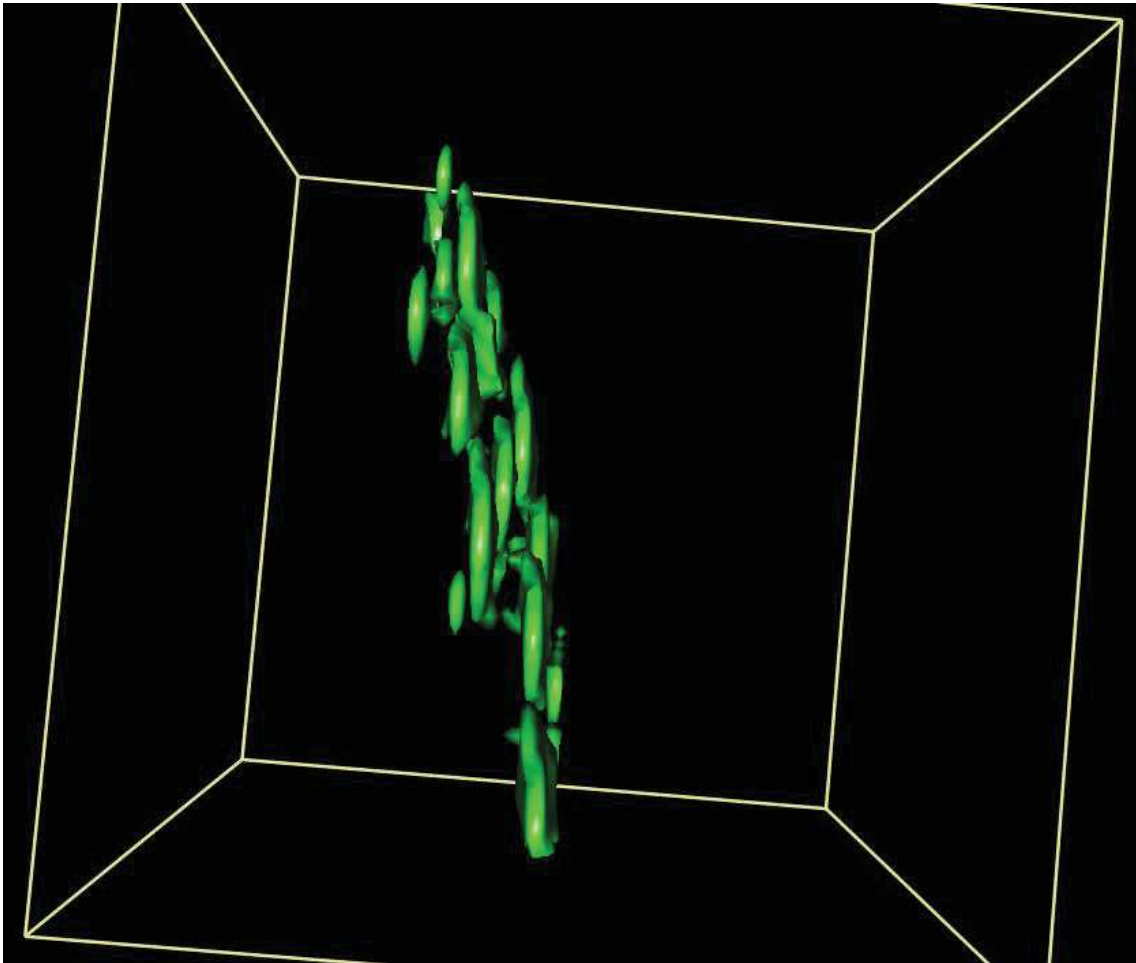
Figure 3.13: A simulation of a bainitic sheaf via autocatalytic subunit nucleation on a 100^3 grid using the PF model described in Section 3.3.
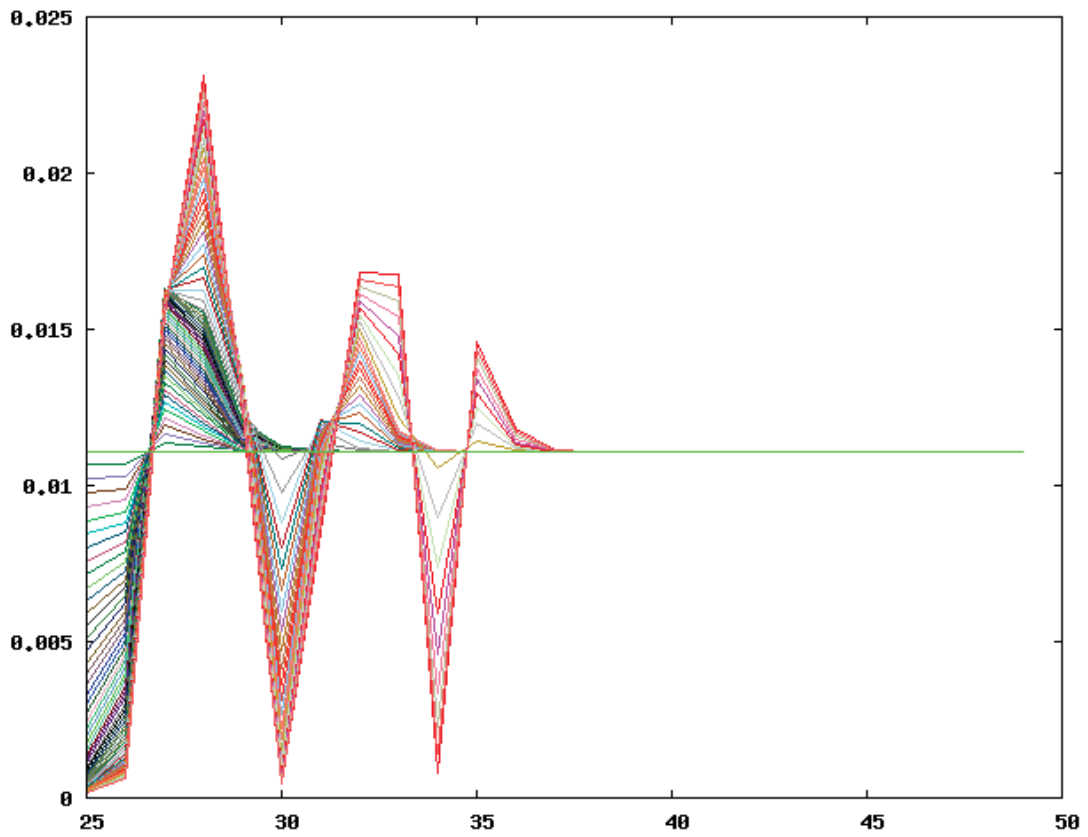
Figure 3.14: The concentration profile across the domain of Figure 3.13. The high peaks in concentration lie in the regions between the subunits whereas the smallest concentration values are at the centres of the subunits.
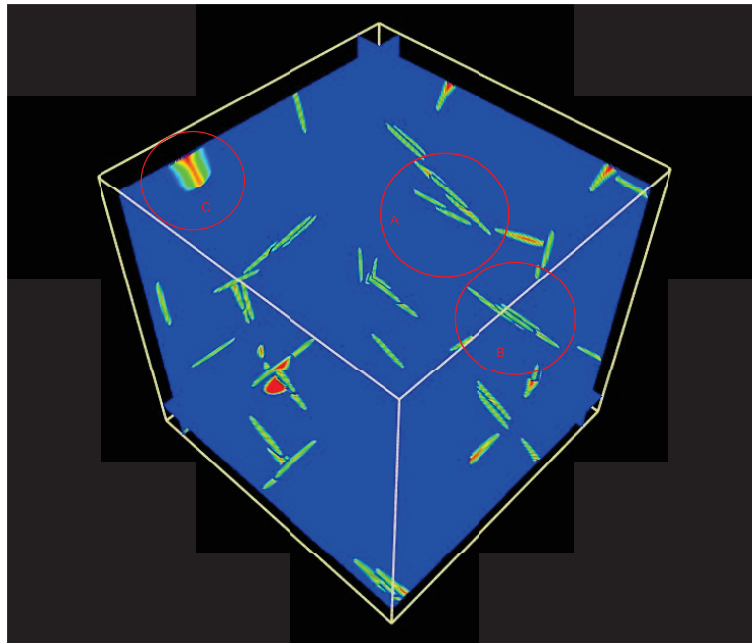
Figure 3.15: The cross section of a simulation of bainite growth on a 200^3 fixed grid showing two bainite sheaves (indicated as A and B). C is an intersection of the slice section and a larger cross section of a subunit.
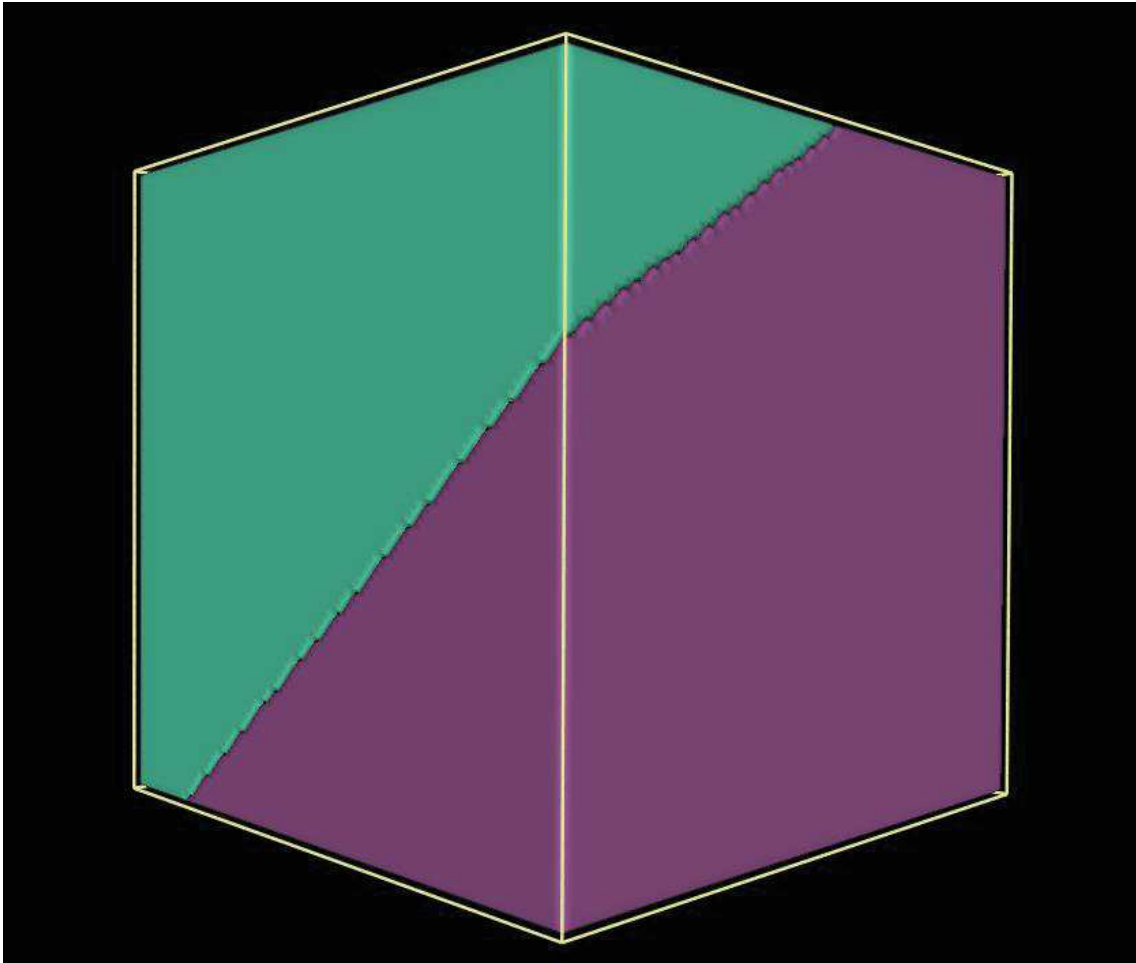
Figure 3.16: A system domain of size 100^3 composed of two austenite grains.
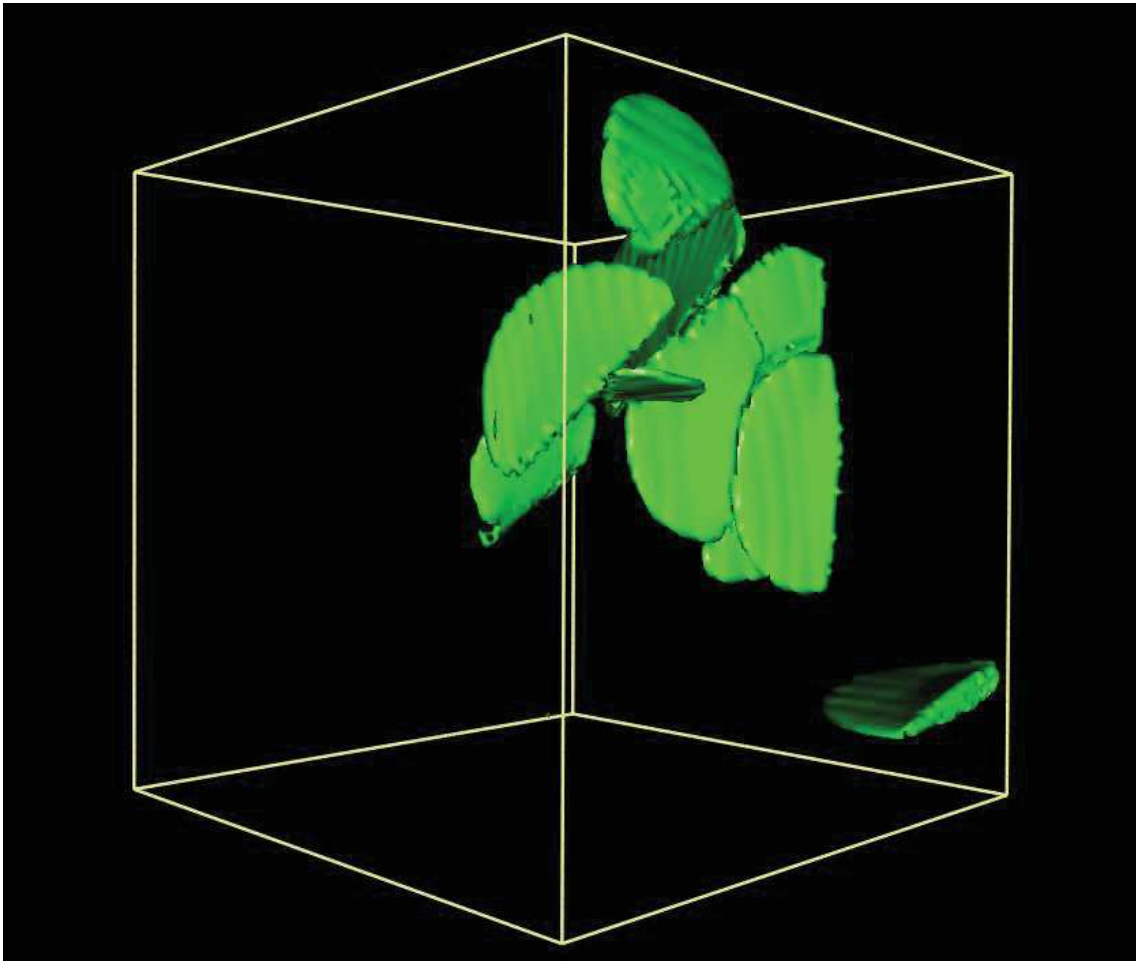
Figure 3.17: A PF simulation of bainitic autocatalytic growth on the system domain described in Figure 3.16.

evolution is free energy driven within which is contained the contribution due to the strain energy from the phenomenological theory of ellipsoidal inclusions. Each plate is assigned a unique identifier in order to distinguish it from other plates. Thus the orientation influence in the governing equation for each plate is dependent on this identifier in order to produce correct orientation by application of a transformation matrix. This transformation matrix is known for many steels.

The use of a single PF variable reduces computation time greatly. Also, due to the more phenomenological nature of the model, the microstructure produced will be more macroscopically realistic. The model is able to reproduce all 24 variants with and without applied stress with the use of transformation matrices which is an input parameter. This enables the reproduction of variant selection which is influenced by applied stress. The thickness and shape of the martensitic plates are determined clearly by the chemical free energy term K, applied stress σ and temperature T.

It was previously shown possible to employ a more fundamental PF approach to the modelling of martensite using elastic energy minimisation [SMKU13]. As in atomistic calculations, this approach provides information about the transformation which the current model can not. However, this occurs at a great computational cost. These methods utilise a PF order parameter which not only is a vector, but the number of which scales with the number of present phases. Not only does this result in higher loads on memory but also impacts computation time due to the additional equations that must be solved for elastic energy minimisation. One can argue that recent increased computational capabilities enable such simulations of martensitic growth within a domain, however, today models are required to perform in unison with other models or at least have the ability to be made use of in order to describe the evolution of multiple complex phases through time. This makes any improvement upon computation load significant.

The previous paragraph may appear to imply that the elastic field of the growing structures is completely ignored. This is far from the truth. Phenomenological theory has previously

been applied to the growth of inclusions [Esh57, Chr58]. This work has then linked this phenomenological theory with the growing martensite grains and their size. It is these resulting expressions that have been minimised in the evolution of the PF variable. It is also the myriad of data on variant selection on the martensite phase that enables this approach to be fruitful while still remaining relatively simple.

Much like how atomistic simulations, while unable to be utilised for length scales above the nanometer, are able to provide information about the actual atomic rearrangement during martensitic transformations [SU09], the PF method is able to render system size almost unimportant as far as the calculation time is concerned. Also, it is well known that a finer lattice spacing in the simulation domain results in a more accurate representation of complex interface structures. The PF method given here then has the ability to be applied to large systems while not presenting much extra load on computation due to the increased number of phases

The developed PF model has been shown to be able to simulate bainite growth. The bainitic subunits are described using the PF model for martensite growth adapted to incorporate a nonconstant concentration. A Cahn-Hilliard governing equation for the diffusion is also used in order to evolve concentration levels. This approach reproduces the carbon build up in the austenite films between the subunits and also enables autocatalytic nucleation based on the reduction of the driving force caused by the diffusion of carbon. Further application of this model will enable the reproduction of the incomplete transformation phenomenon [RB92b].

Chapter 4

The SPH model of complex reactive fluids

4.1 Introduction

In Section 1.4, the areas in the simulation of steel processing that require further attention were detailed. One of those areas is displacive transformations. In Chapter 3, a model for displacive transformations was developed in order to describe martensite and bainite transformations. This presents us with the tools to simulate solid state phase transformations arising from the heat treatment and deformation of steel. However, the treatment process as shown in Figure 1.1 involves a stage within which a coupling of fluid dynamics as well as solidification is required. In order to develop the tools required to simulate such dynamics with the goal of SPH working alongside the phase-field modelling of solid state mechanics, the SPH method is analysed in this chapter. The theory of the method is introduced leading to some applications to the complex cases mentioned in Chapter 1.2, such as complex boundaries, free surfaces and large density ratios. Then an application of SPH to vdW fluids is given. This is a case requiring a larger presence of thermodynamics showing that SPH has the capability to represent thermodynamical parameters such as entropy.

4.2   Theory

The essence of SPH lies in the identity,

$$f(\mathbf{r}_i) = \int_\Omega f(\mathbf{r}')W(\mathbf{r}_i - \mathbf{r}')d\mathbf{r}', \tag{4.1}$$

where $\mathbf{r} = \mathbf{r}_i$ denotes the position of particle i, $f(\mathbf{r}_i)$ is the value of a field variable f approximated at particle i and $W(\mathbf{r}_i - \mathbf{r})$ is the kernel as in Equation (2.70). In 3 dimensions this is an integral over a volume. Explicitly specifying the volume element of a particle as $d\mathbf{r}' = \Delta V_j$ and noting that the mass m_j and density ρ_j of that particle are related to its volume element by $\Delta V_j = m_j/\rho_j$, Equation (4.1) can be approximated as,

$$
\begin{aligned}
f(\mathbf{r}_i) \ &= \sum_{j=0}^{N} f(\mathbf{r}_j)W(\mathbf{r}_i - \mathbf{r}_j, h)\Delta V_j \\
&= \sum_{j=0}^{N} \frac{m_j}{\rho_j} f_j W_{ij},
\end{aligned} \tag{4.2}
$$

where $f_i = f(\mathbf{r}_i)$ and $W_{ij} = W(\mathbf{r}_i - \mathbf{r}_j, h)$. The summation in Equation (4.2) includes the case where $i = j$ (self contribution). Note that the consideration of a volume element ΔV_j is an approximation to the integral. Thus the smaller the volume element with respect to h, the better the approximation. Similarly, equations (2.78) and (2.79) become,

$$\nabla f_i \ = \sum_{j=0}^{N} \frac{m_j}{\rho_j} f_j \nabla_i W_{ij}, \tag{4.3}$$

$$\nabla \cdot \mathbf{f}_i \ = \sum_{j=0}^{N} \frac{m_j}{\rho_j} \mathbf{f}_j \cdot \nabla_i W_{ij}, \tag{4.4}$$

where it has been explicitly stated that $\nabla_i W_{ij}$ is a spatial derivative with respect to particle i.

One of the most recognised and widely used SPH equations is the estimation of the density $\rho(\mathbf{r}_i) = \rho_i$ at particle i. By simply replacing ρ_i as the field function f_i in Equation (4.2) we obtain,

$$\rho_i = \sum_{j=0}^{N} m_j W_{ij}. \tag{4.5}$$

While equations (4.3) and (4.4) are sufficient to perform an SPH approximation, it is preferred to have both particles involved in the summation. Consider Equation (4.2) and suppose that particle i and j are within the support domains of each other. Then the contribution of i and j to this summation for i is the same as that for j, i.e.

$$
\begin{aligned}
\sum_{k=i,j} f_k W_{ik} &= f_i W_{ii} + f_j W_{ij} \\
&= f_i W_{jj} + f_j W_{ji} \\
&= \sum_{k=i,j} f_k W_{jk},
\end{aligned}
\tag{4.6}
$$

since W is an even function and $\mathbf{r}_i - \mathbf{r}_i = \mathbf{r}_j - \mathbf{r}_j = 0$. Now consider Equation (4.3). The contribution of i and j to the summation for i is given as,

$$
\sum_{k=i,j} \frac{m_k}{\rho_k} f_k \nabla_i W_{ik}.
\tag{4.7}
$$

However, due to the symmetric and differentiable nature of W, even though $W(0, h) \neq 0$, we have $\nabla_i W(0, h) = 0$ such that the surviving term of Equation (4.7) is the $\mathbf{r}_i \neq \mathbf{r}_j$ term,

$$
\frac{m_j}{\rho_j} f_j \nabla_i W_{ij},
\tag{4.8}
$$

which is not necessarily equal in magnitude to the counterpart for the summation for j,

$$
\frac{m_i}{\rho_i} f_i \nabla_j W_{ji} = -\frac{m_i}{\rho_i} f_i \nabla_i W_{ij}.
\tag{4.9}
$$

This means that forces arising from interparticle interactions may not experience the same repelling/attracting force. This gives rise to asymmetry and thus the aforementioned presence of both i and j on the right-hand side is preferred. Symmetric forms of these equations are derived in Appendix B and seen in the following.

Given a system of governing equations (such as Eq.'s (2.80) - (2.88)), we now take steps to discretize the gradients and time derivatives involved in order to form representative SPH

equations for the system. Focusing on particle i, these equations are given as,

$$
(\frac{d\rho}{dt})_i \quad = -\rho_i(\nabla \cdot \mathbf{v})_i, \tag{4.10}
$$

$$
(\frac{d\mathbf{v}}{dt})_i \quad = \frac{1}{\rho_i}(\nabla \cdot \mathbf{P})_i + g, \tag{4.11}
$$

$$
T_i\rho_i(\frac{dS}{dt})_i \quad = \phi_i + \kappa(\nabla^2 T)_i, \tag{4.12}
$$

$$
(\frac{dU}{dt})_i \quad = \frac{1}{\rho_i}\mathbf{P}_i : (\nabla\mathbf{v})_i - \frac{1}{\rho_i}(\nabla \cdot q)_i, \tag{4.13}
$$

$$
\mathbf{P}_i \quad = -P_i\mathbf{I} + \sigma_i, \tag{4.14}
$$

$$
\sigma_i \quad = \eta[(\nabla\mathbf{v})_i + (\nabla\mathbf{v}^T)_i] + (\zeta - \frac{2}{d}\eta)(\nabla \cdot \mathbf{v})_i\mathbf{I}, \tag{4.15}
$$

$$
\mathbf{q}_i \quad = -K(\nabla T)_i, \tag{4.16}
$$

$$
\phi_i \quad = 2\eta(\overline{\nabla\mathbf{v}})_i : (\overline{\nabla\mathbf{v}})_i + \zeta(\nabla \cdot \mathbf{v})_i^2, \tag{4.17}
$$

$$
(\overline{\nabla\mathbf{v}})_i \quad = \frac{1}{2}[(\nabla\mathbf{v})_i + (\nabla\mathbf{v}^T)_i] - \frac{1}{d}\mathbf{1}(\nabla \cdot \mathbf{v})_i. \tag{4.18}
$$

Using Equation (4.4), the divergence of the velocity can be calculated as,

$$
(\nabla \cdot \mathbf{v})_i = \sum_{j=1}^{N} \frac{m_j}{\rho_j}\mathbf{v}_j \cdot \nabla_i W_{ij}, \tag{4.19}
$$

or with the presence of both terms on the right-hand side (Equation (B.2) in Appendix B),

$$
(\nabla \cdot \mathbf{v})_i = \sum_{j=1}^{N} \frac{m_j}{\rho_{ij}}\mathbf{v}_{ji} \cdot \nabla_i W_{ij}, \tag{4.20}
$$

where $\rho_{ij} = \frac{1}{2}(\rho_i + \rho_j)$ and $\mathbf{v}_{ji} = \mathbf{v}_j - \mathbf{v}_i$, giving an expression for the time rate of change of the density,

$$
\dot{\rho}_i = -\rho_i(\nabla \cdot \mathbf{v})_i = -\rho_i \sum_{j=1}^{N} \frac{m_j}{\rho_{ij}}\mathbf{v}_{ji} \cdot \nabla_i W_{ij}. \tag{4.21}
$$

Similarly, the temperature gradients are [EnR03],

$$
(\nabla T)_i \quad = \sum_{j=0}^{N} \frac{m_j}{\rho_{ij}}T_{ji}\nabla_i W_{ij}, \tag{4.22}
$$

$$
(\nabla^2 T)_i \quad = 2\sum_{j=0}^{N} m_j \frac{\mathbf{r}_{ij}\nabla_i W_{ij}}{\rho_j r^2}\mathbf{T}_{ij}. \tag{4.23}
$$

The interpolant of the pressure field is given by,

$$P(\mathbf{r}_i) = \sum_j \frac{m_j}{\rho_j} P(\mathbf{r}_j) W_{ij} \tag{4.24}$$

and its gradient by (given in Appendix B),

$$(\nabla P(\mathbf{r}))_i = -\rho_i \sum_j m_j \left[\frac{P_j}{\rho_j^2} + \frac{P_i}{\rho_i^2} \right] \nabla W_{ij}. \tag{4.25}$$

Some other forms for these discretizations are given in Appendix B.

4.3 Numerical algorithm

The numerical simulation then proceeds as follows:

- 1 - Set up the particle representation giving the particles appropriate mass, velocity etc...

- 2 - Apply a pairing procedure in order to pair the SPH particles

- 3 - Calculate the density (Equation (4.5) if using the summation density approach instead of Equation (4.10))

- 4 - Calculate the stress tensor using the velocities and other properties of the particles (Equation (4.14) using Equation (4.15) and the pressure from a suitable equation of state, i.e. Equation (4.59))

- 5 - Determine the acceleration of each particle using the stress tensor (Equation (4.11))

- 6 - Calculate the velocity at each particle using their accelerations

- 7 - Apply velocity restrictions according to maximum velocity

- 8 - Calculate the new positions of the particles using their velocities

- 9 - Apply boundary conditions

- 10 - Repeat steps 2-9

4.4   Assessment of Kernels and their accuracy

The accuracy and the dynamics observed during the numerical evolution of a system solved using the SPH method is directly related to the form of the kernel. There are many possible kernels that are constructed according to the following constraints:

- 1 - Unity condition

$$\int_\Omega W(\mathbf{r}, h) dr = 1$$

- 2 - Compact condition

$$|\mathbf{r}| > h \implies W(\mathbf{r}, h) = 0$$

- 3 - Positivity condition

$$W(\mathbf{r}, h) \geq 0 \ \forall \ \mathbf{r}$$

- 4 - Monotonic condition

$$\frac{\partial W(\mathbf{r}, h)}{\partial r} \leq 0 \ \forall \ r \geq 0$$

- 5 - Delta function limit condition

$$\lim_{h \to 0} W(\mathbf{r}, h) = \delta(\mathbf{r})$$

- 6 - Even function condition

$$W(\mathbf{r}, h) = W(-\mathbf{r}, h)$$

- 7 - Smooth condition

The first condition is related to the accuracy of the approximation. The compact condition enables the application of the interpolation over a small portion of the system domain rather

than the entire domain, which clearly benefits efficiency. The monotonic condition ensures that closer particles will have more of an effect compared to particles further away. An even kernel ensures all particles at the same distance will contribute equally in magnitude. The smoothness condition states that a kernel should be sufficiently smooth. The Delta function limit condition is a resulting condition of the enforcement of conditions 1-4. To informally see this, as $h \to 0$, due to the compact condition, $W(\mathbf{r}) = 0$ everywhere but in the infinitesimally small volume $d\mathbf{r}$. Due to the monotonic and positivity conditions, the largest contribution is always at $\mathbf{r} = 0$. Given this information, the only function to satisfy the unity condition is by definition the Delta function.

The following are just some kernel functions that are popular for SPH simulations:

$$W_L(\mathbf{r} - \mathbf{r}', h) \quad = \alpha_L \times \begin{cases} (1 + 3\frac{r}{h})(1 - \frac{r}{h})^3 & 0 \leq r < h \\ 0 & r \geq h \end{cases}, \qquad (4.26)$$

$$W_{cs}(\mathbf{r} - \mathbf{r}', h) \quad = \alpha_{cs} \times \begin{cases} (2 - \frac{r}{h})^3 - 4(1 - \frac{r}{h})^3 & 0 \leq r < h \\ (2 - \frac{r}{h})^3 & h \leq r < 2h \\ 0 & r \geq 2h \end{cases}, \qquad (4.27)$$

$$W_{hs}(\mathbf{r} - \mathbf{r}', h) \quad = \alpha_{hs} \times \begin{cases} (\frac{r}{h})^3 - 6\frac{r}{h} + 6 & 0 \leq r < h \\ (2 - \frac{r}{h})^3 & h \leq r < 2h \\ 0 & r \geq 2h \end{cases}, \qquad (4.28)$$

and their gradients are:

$$\nabla_i W(\mathbf{r} - \mathbf{r}', h) \quad = \frac{\partial W}{\partial \mathbf{r}_i} = \frac{\partial W}{\partial r}\frac{\partial r}{\partial \mathbf{r}_i} = \frac{\partial W}{\partial r}\frac{\mathbf{r}_{ij}}{r},$$

$$\nabla_i W_L(\mathbf{r} - \mathbf{r}', h) \quad = \frac{-12\alpha_L}{h^3} \times \begin{cases} \mathbf{r}_{ij}(1 - \frac{r}{h})^2 & 0 \le r < h \\ \\ 0 & r \ge h \end{cases}, \qquad (4.29)$$

$$\nabla_i W_{cs}(\mathbf{r} - \mathbf{r}', h) \quad = \frac{-3\alpha_{cs}}{h} \times \begin{cases} \frac{\mathbf{r}_{ij}}{r}(2 - \frac{r}{h})^2 - \frac{4\mathbf{r}_{ij}}{r}(1 - \frac{r}{h})^2 & 0 \le r < h \\ \frac{\mathbf{r}_{ij}}{r}(2 - \frac{r}{h})^2 & h \le r < 2h \\ 0 & r \ge h \end{cases}, \qquad (4.30)$$

$$\nabla_i W_{hs}(\mathbf{r} - \mathbf{r}', h) \quad = \frac{-\alpha_{hs}}{h} \times \begin{cases} \frac{6\mathbf{r}_{ij}}{r} - 3\frac{\mathbf{r}_{ij}r}{h^2} & 0 \le r < h \\ 3\frac{\mathbf{r}_{ij}}{r}(2 - \frac{r}{h})^2 & h \le r < 2h \\ 0 & r \ge 2h \end{cases}, \qquad (4.31)$$

where $\mathbf{r}_{ij} = \mathbf{r}_i - \mathbf{r}_j$, $r = |\mathbf{r}_{ij}|$ and W_L, W_{cs} and W_{hs} are respectively the Lucy function, the cubic spline kernel and the hyperbolic spline kernel. The constants α_L, α_{cs} and α_{hs} are scaling constants determined by the unity condition,

$$\int_\Omega W dV = 1, \qquad (4.32)$$

where the integral is taken over a volume Ω with volume element dV. In Appendix C, the constants are calculated as follows: $\alpha_L = 5/(4h)$, $\alpha_{cs} = 1/(6h)$ and $\alpha_{hs} = 1/(7h)$ in one dimension, $\alpha_L = 5/(\pi h^2)$, $\alpha_{cs} = 5/(14\pi h^2)$ and $\alpha_{hs} = 1/(3\pi h^2)$ in two dimensions and $\alpha_L = 105/(16\pi h^3)$, $\alpha_{cs} = 1/(4\pi h^3)$ and $\alpha_{hs} = 15/(62\pi h^3)$ in three dimensions.

By the definition of the kernel functions, the compact condition is satisfied. The positivity condition is satisfied by the fact that each of the kernel functions are functions of $r = |\mathbf{r}_i - \mathbf{r}_j|$. In order to see that the monotonic condition also holds, we note that the function $\frac{\partial W_{ij}}{\partial r}$ is the same as $\nabla_i W$ with $\mathbf{r}_{ij}$ replaced by r. The even condition is satisfied similar to the positivity condition in that the kernel functions are functions of r. For the Delta limit condition, as the smoothing length h tends to zero, the value of the kernel within this compact domain

approaches infinity. To see this consider Lucy's function with $h > r = \epsilon h$ with $\epsilon < 1$,

$$\lim_{h \to 0} W_L = \lim_{h \to 0} \alpha_L (1 + 3\epsilon)(1 - \epsilon)^3 = \infty, \tag{4.33}$$

since $(1 + 3\epsilon)(1 - \epsilon)^3 < 1$ is bounded and $\alpha_L \propto 1/h^d$ with dimension d. The kernel functions and their derivatives are plotted in Figures 4.1 - 4.3.
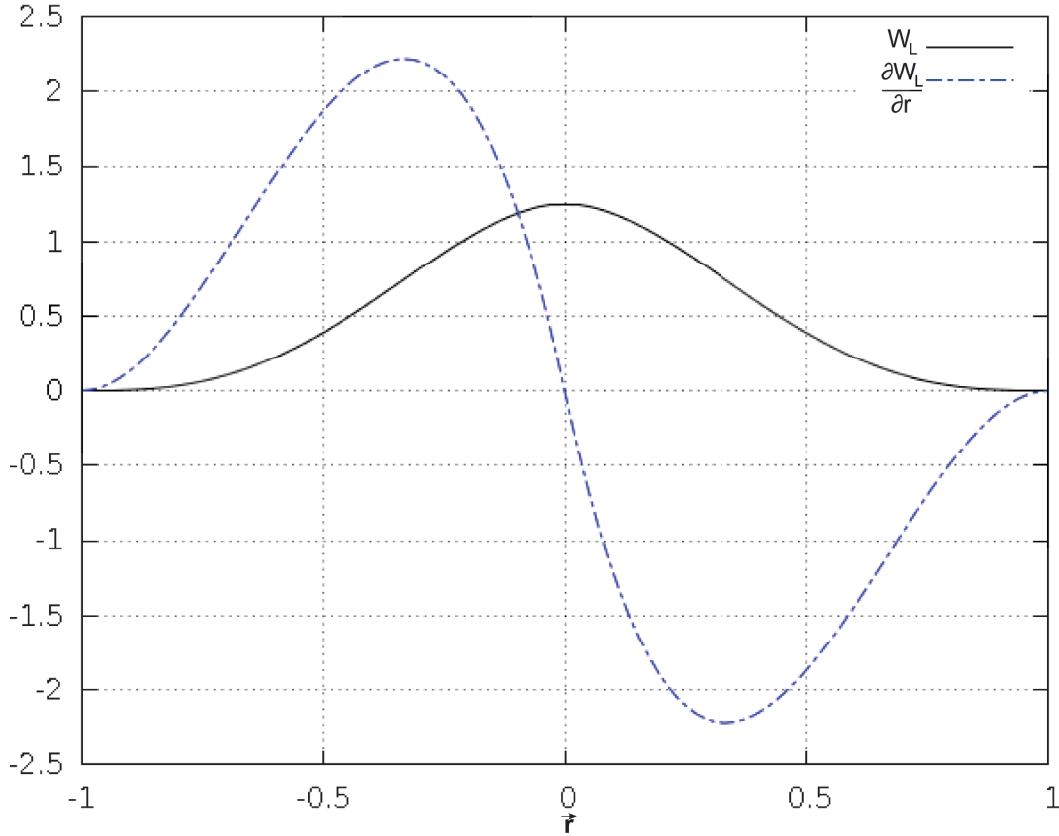
Figure 4.1: The Lucy kernel and its derivative with $h = 1$ in 1 dimension. $\vec{r}$ is a 1 dimensional vector. In higher dimensions the functions are scaled due to α_L but the features are analogous to the 1 dimensional case.

One immediate observation from the kernels is that the hyperbolic spline is discontinuous at $\vec{r} = \vec{0}$. In fact this is not the only kernel function to exhibit such a feature. The quadratic spline is also discontinuous at this point [JSB96]. The reason such a discontinuity is unavoidable is due to the instability condition [SHA95]. A kernel function will result in instability in certain cases if its second derivative is negative within some region. This immediately imposes the restriction that not only the kernel function itself but its first derivative must also be monotonic. In particular, the first derivative must be monotonically increasing. Such a function cannot
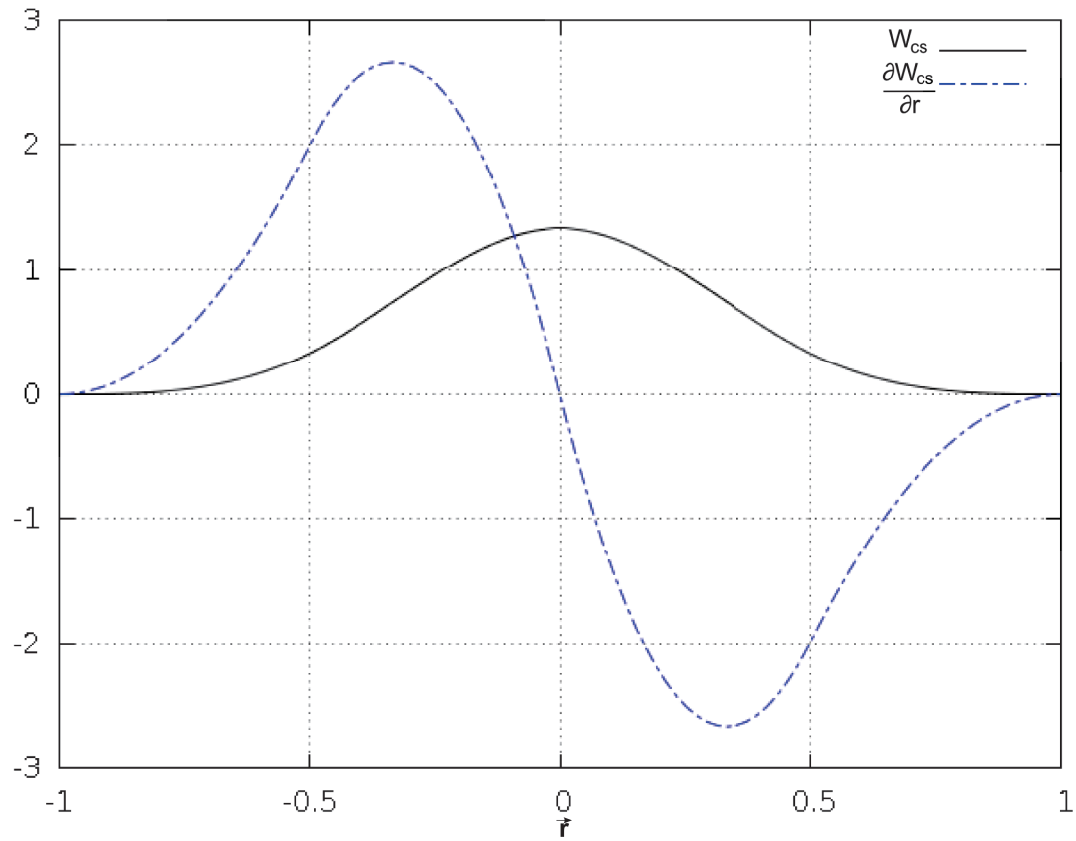
Figure 4.2: The cubic spline kernel and its derivative with $h = 0.5$ in 1 dimension. $\vec{r}$ is a 1 dimensional vector. In higher dimensions the functions are scaled due to α_{cs} but the features are analogous to the 1 dimensional case.
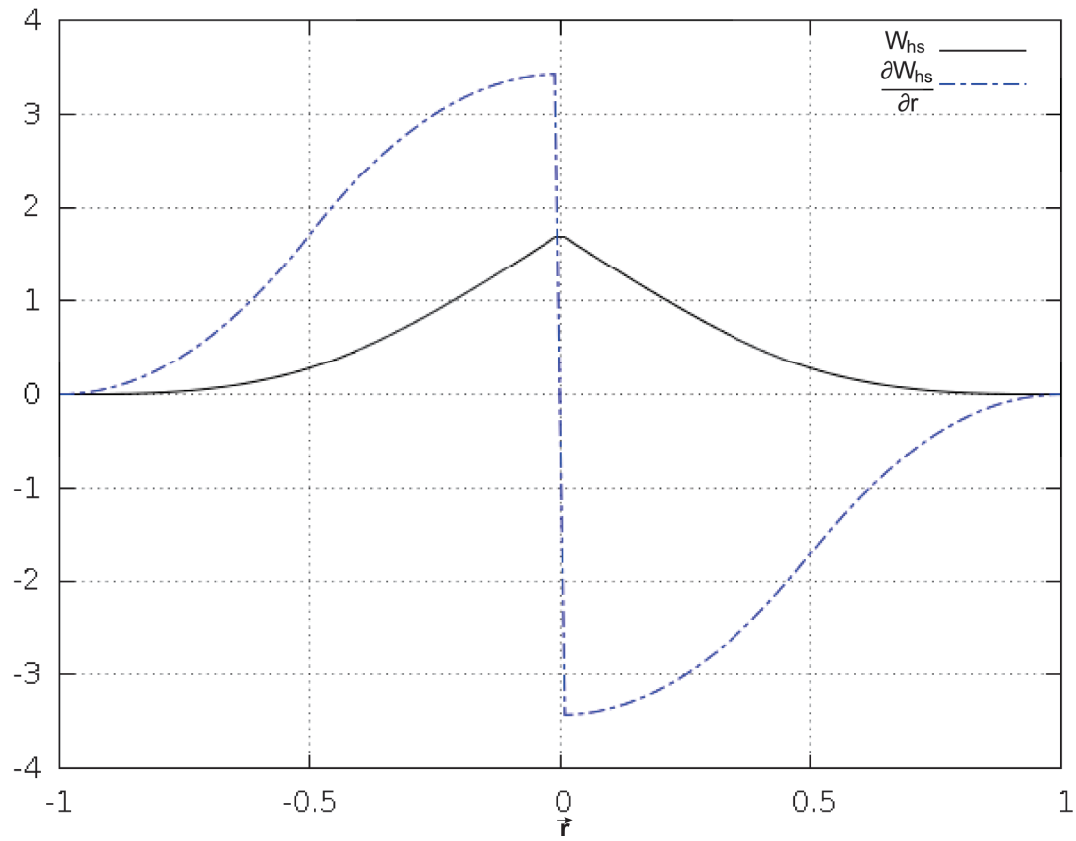
Figure 4.3: The hyperbolic spline kernel and its derivative with $h = 0.5$ in 1 dimension. $\vec{r}$ is a 1 dimensional vector. In higher dimensions the functions are scaled due to α_{hs} but the features are analogous to the 1 dimensional case.

be continuous over the entire domain as follows. Suppose such a function existed. Then the following conditions for the right and left-handed limits are true,

$$\forall \quad \epsilon_1 > 0 \quad \exists \quad \delta_1 > 0 \quad \text{such} \quad \text{that} \quad \forall \quad \mathbf{r},$$

$$0 < \mathbf{r} < \mathbf{r} + \delta_1 \Rightarrow |\nabla W(\mathbf{r}) - L_1| < \epsilon_1, \tag{4.34}$$

and,

$$\forall \quad \epsilon_2 > 0 \quad \exists \quad \delta_2 > 0 \quad \text{such} \quad \text{that} \quad \forall \quad \mathbf{r},$$

$$\mathbf{r} - \delta_2 < \mathbf{r} < 0 \Rightarrow |\nabla W(\mathbf{r}) - L_2| < \epsilon_2. \tag{4.35}$$

Due to the monotonic condition we have that $\nabla W(\mathbf{r}) \leq 0$ for $\mathbf{r} \geq 0$ giving $L_1 \leq 0$ and $\nabla W(\mathbf{r}) \geq 0$ for $\mathbf{r} \leq 0$ (a smooth function with compact condition at some $\mathbf{r} = h > 0$) giving $L_2 \geq 0$. This means that the limit of such a function can only exist at 0 if $L_1 = L_2 = 0$. Along with the monotonic condition, the only smooth function to satisfy this is $\nabla W(\mathbf{r}) = 0 \quad \forall \quad \mathbf{r}$.

Suppose a field function $f(\mathbf{r})$ exists which is differentiable over the system domain. Let us expand the field function $f(\mathbf{r}')$ as a Taylor series,

$$
\begin{aligned}
f(\mathbf{r}') \quad &= f(\mathbf{r}) + f'(\mathbf{r})(\mathbf{r}' - \mathbf{r}) + \cdots + R(\mathbf{r} - \mathbf{r}') \\
&= f(\mathbf{r}) - f'(\mathbf{r})(\mathbf{r} - \mathbf{r}') + \cdots + R(\mathbf{r} - \mathbf{r}') \\
&= \sum_{k=0}^{n} \frac{(-1)^k (\mathbf{r} - \mathbf{r}')^k}{k!} f^k(\mathbf{r}) + R_n(\mathbf{r} - \mathbf{r}'),
\end{aligned}
\tag{4.36}
$$

where f' is the derivative of f with respect to $\mathbf{r}$ and $R_n(\mathbf{r} - \mathbf{r}')$ is the remainder term of terms of order $> n$. Placing this expansion into Equation (2.70) leads to,

$$f(\mathbf{r}) = \sum_{k=0}^{n} \frac{(-1)^k f^k(\mathbf{r})}{k!} \int_{\Omega} (\mathbf{r} - \mathbf{r}')^k W(\mathbf{r} - \mathbf{r}', h) d\mathbf{r}' + R_n(\mathbf{r} - \mathbf{r}'). \tag{4.37}$$

Only the $k = 0$ term survives in the equality (since the coefficient of $f(\mathbf{r})$ should be 1 and the coefficients of $f^k(\mathbf{r})$ should be zero for $k > 0$). This gives,

$$\frac{(-1)^k}{k!} \int_\Omega (\mathbf{r} - \mathbf{r}')^k W(\mathbf{r} - \mathbf{r}', h) d\mathbf{r}' = \begin{cases} 1 & k = 0 \\ 0 & k > 0 \end{cases}. \tag{4.38}$$

This immediately results in the unity condition. In addition to this, the case with $k = 1$,

$$-\int_\Omega (\mathbf{r} - \mathbf{r}') W(\mathbf{r} - \mathbf{r}', h) d\mathbf{r}' = 0, \tag{4.39}$$

is translated as the symmetric condition. Given these 2 conditions, first order accuracy is guarenteed leaving a remainder $R_1(\mathbf{r} - \mathbf{r}')$. Subsequently, second order accuracy is obtained only if the following condition for $k = 2$ holds,

$$\int_\Omega (\mathbf{r} - \mathbf{r}')^2 W(\mathbf{r} - \mathbf{r}', h) d\mathbf{r}' = 0. \tag{4.40}$$

This is unfortunate since this implies that the kernel must be negative in some parts of its domain. Given that this aspect of a kernel often results in unphysical evolution such as negative density values, non-positive kernels are often avoided.

Again, taylor expansion of $f(\mathbf{r}')$ about $\mathbf{r}$ results in,

$$f(\mathbf{r}') = f(\mathbf{r}) + f'(\mathbf{r})(\mathbf{r}' - \mathbf{r}) + R((\mathbf{r}' - \mathbf{r})^2),$$

where f' is the derivative of f with respect to $\mathbf{r}$ and R is a function of the higher terms or the residual of the taylor expansion. Substituting this into Equation (2.70) and expanding,

$$f(\mathbf{r}) \quad = \int_\Omega f(\mathbf{r})W(\mathbf{r}' - \mathbf{r}, h)d\mathbf{r}' + \int_\Omega f'(\mathbf{r})(\mathbf{r} - \mathbf{r}')W(\mathbf{r} - \mathbf{r}', h)d\mathbf{r}' \tag{4.41}$$

$$+ \int_\Omega R((\mathbf{r}' - \mathbf{r})^2)W(\mathbf{r} - \mathbf{r}', h)d\mathbf{r}' \tag{4.42}$$

$$= f(\mathbf{r})\int_\Omega W(\mathbf{r}' - \mathbf{r}, h)d\mathbf{r}' + f'(\mathbf{r})\int_\Omega (\mathbf{r}' - \mathbf{r})W(\mathbf{r} - \mathbf{r}', h)d\mathbf{r}' \tag{4.43}$$

$$+ \int_\Omega R((\mathbf{r}' - \mathbf{r})^2)W(\mathbf{r} - \mathbf{r}', h)d\mathbf{r}'. \tag{4.44}$$

Using the even function condition and letting,

$$g(\mathbf{r}') = (\mathbf{r}' - \mathbf{r})W(\mathbf{r} - \mathbf{r}', h),$$

and $\mathbf{r}_1 - \mathbf{r} = -(\mathbf{r}_2 - \mathbf{r})$ such that a straight line drawn from point $\mathbf{r}_1$ to point $\mathbf{r}_2$ in space, goes through the point $\mathbf{r}$. We have,

$$g(\mathbf{r}_1) \quad = (\mathbf{r}_1 - \mathbf{r})W(\mathbf{r} - \mathbf{r}_1, h)$$

$$= (\mathbf{r}_1 - \mathbf{r})W(-(\mathbf{r} - \mathbf{r}_1), h)$$

$$= -(\mathbf{r}_2 - \mathbf{r})W(\mathbf{r} - \mathbf{r}_2, h) = -g(\mathbf{r}_2). \tag{4.45}$$

So that $g(\mathbf{r}')$ is an odd function with respect to $\mathbf{r}$. Thus, over a symmetric region about $\mathbf{r}$ (each point $\mathbf{r}_1$ having an equivalent $\mathbf{r}_2$ with a line going through $\mathbf{r}$),

$$\int_\Omega (\mathbf{r}' - \mathbf{r})W(\mathbf{r} - \mathbf{r}', h)d\mathbf{r}' = 0.$$

Using the unity condition we have,

$$f(\mathbf{r}) \quad \leq f(\mathbf{r}) + O(h^2)\int_\Omega W d\mathbf{r}$$

$$= f(\mathbf{r}) + O(h^2). \tag{4.46}$$

This implies that, subject to conditions 1 and 6, the kernel approximation of Equation (2.70) is of second order accuracy in h.

The accuracy analysis of the kernel approximation made above considers the accuracy of the approximation of the integral representation using the kernel function [LL03]. It does not say anything about the accuracy when this form is discretized using interpolation points. Consider the particle approximations of Equations (4.38) for $k = 0$ and $k = 1$,

$$\sum_{j=0}^{N} \frac{m_j}{\rho_j} W_{ij} = 1, \qquad (4.47)$$

$$\sum_{j=0}^{N} \frac{m_j}{\rho_j} (\mathbf{r}_i - \mathbf{r}_j) W_{ij} = 0. \qquad (4.48)$$
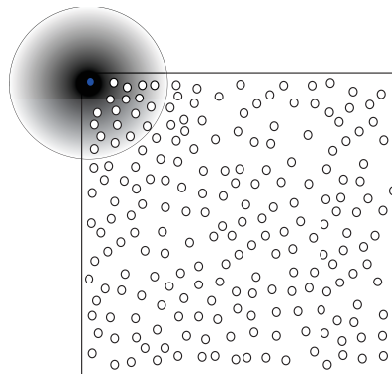
Figure 4.4: Figure of the support domain of a particle (blue) close to the boundary of the system domain.

It can be seen from Figure 4.4 that Equations (4.47) and (4.48) will not be satisfied. In some cases this is beneficial to reproduce boundary and interfacial effects (such as in vdW droplet formation discussed in Section 4.10.4). Nevertheless, in cases where boundary deficiencies such as this are undesirable, approximation may be improved by using kernel adjustments at the boundary particles [LL03, LJZ95, LNW02, LG04]. However, these methods are computationally exhaustive and will not be considered in this work.

Notice that from figures 4.1 - 4.3, that the centre peak of the kernels differ. One may ask what effect this has on the approximation. To answer this, we begin by assuming a kernel can be written in the form [LL03],

$$W(r, h) = a_0 + a_1 \frac{r}{h} + a_2 \frac{r^2}{h^2} + a_3 \frac{r^3}{h^3} + \cdots .$$

Then the unity condition in one dimension gives,

$$
\begin{aligned}
\int_{-h}^{h} W(r, h) d\mathbf{r} \quad &= 2h[a_0 + \frac{a_1}{2} + \frac{a_2}{3} + \frac{a_3}{4} + \frac{a_4}{5} + \cdots] \\
&= 1 \\
\implies a_0 &= \frac{1}{2h} - [\frac{a_1}{2} + \frac{a_2}{3} + \frac{a_3}{4} + \frac{a_4}{5} + \cdots] \\
\implies a_0 &= \frac{1}{2h} - f(a_1, a_2, a_3, \cdots),
\end{aligned}
\tag{4.49}
$$

where f is a positive function since at h, $W(r = 0, h) > W(r = h, h)$ gives $a_0 > a_0 + f$ which results in $f < 0$. The larger a_0 is the smaller f is. The absolute value of the remainder term, R_1, in Equation (4.37) tells us about the approximation. Namely, the smaller this term is in magnitude, the better the approximation to second order.

$$
\begin{aligned}
R_1 \quad &= 2 \int_0^h r^2 W(r, h) d\mathbf{r} \\
&= 2[\int_0^h r^2 a_0 d\mathbf{r} + \frac{1}{h} \int_0^h r^3 a_1 d\mathbf{r} + \frac{1}{h^2} \int_0^h r^4 a_2 d\mathbf{r} + \cdots] \\
&= 2[\int_0^h r^2 a_0 d\mathbf{r} + \sum_{k=1}^{\infty} \frac{1}{h^k} \int_0^h r^{k+2} a_k d\mathbf{r}] \\
&= 2 \int_0^h r^2 [\frac{1}{2h} - \frac{a_1}{2} - \frac{a_2}{3} - \frac{a_3}{4} - \cdots] d\mathbf{r} + \sum_{k=1}^{\infty} \frac{1}{h^k} 2 \int_0^h r^{k+2} a_k d\mathbf{r} \\
&= 2 \int_0^h \frac{r^2}{2h} d\mathbf{r} + 2 \sum_{k=1}^{\infty} a_k \int_0^h [\frac{r^{k+2}}{h^k} - \frac{r^2}{k+1}] d\mathbf{r} \\
&= 2 \int_0^h \frac{r^2}{2h} d\mathbf{r} + 2 \sum_{k=1}^{\infty} a_k h^3 [\frac{1}{k+3} - \frac{1}{3k+3}].
\end{aligned}
\tag{4.50}
$$

We see that the coefficient of each a_k term in Equation (4.50) for $k > 0$ is positive. This means smaller values for all $\{a_k : k > 0\}$ will result in a smaller remainder. On the other hand,

Equation (4.49) states that smaller values for these constants results in a larger a_0, i.e. a larger center peak value. However, the other direction of this statement is not true since given a set of values $\{a_k\}$, suppose we pick a new set $\{a'_k\}$ with $a'_3 = a_3 + 1$ and $a'_4 = a_4 - 1$. This reduces f by 0.05 and increases Equation (4.50) by $\frac{2h^3}{140}$. Thus in this case an increase of a_0 does not result in a reduction in the remainder term.

We can calculate the value of the remainder term for each kernel in order to determine which is a better approximation. For Lucy's function, the cubic spline kernel and the hyperbolic spline, the remainder term, R_1, is calculated in 1 dimensions to be $2(2h)^2/21$, $h^2/3$ and $31h^2/105$ respectively. So the accuracy improves in that order. The $(2h)^2$ in the remainder term for Lucy's function is present because this kernel has domain $[0, h]$ instead of $[0, 2h]$ so that for comparison, this must be scaled.

4.5   Artificial viscosity

In cases of high velocity impacts, or simply where particles penetrate each other due to high velocities, an artificial viscosity addition to the momentum equation is employed. The most popular form of artificial viscosity is given by Monaghan and Gingold [MG83],

$$\Pi_{ij} = \begin{cases} \frac{-\alpha_\Pi \bar{c}_{ij} \phi_{ij} + \beta_\Pi \phi_{ij}^2}{\rho_{ij}} & \mathbf{v}_{ij} \cdot \mathbf{r}_{ij} < 0 \\ 0 & \mathbf{v}_{ij} \cdot \mathbf{r}_{ij} \geq 0 \end{cases} \tag{4.51}$$

where $\rho_{ij} = (\rho_i + \rho_j)/2$, $\phi_{ij} = (h_{ij} \mathbf{v}_{ij} \cdot \mathbf{r}_{ij})/(|\mathbf{r}_{ij}|^2 + 0.1 h_{ij})$, $h_{ij} = (h_i + h_j)/2$, $\bar{c}_{ij} = (c_i + c_j)/2$ and c_i is the speed of sound of particle i. α_Π is the bulk viscosity and β_Π is the antipenetration parameter. The artificial viscosity term is placed in the pressure term. It can be seen from the pressure term in Equation (4.14) that the artificial viscosity would result in a negative contribution to the momentum equation which is translated as a repulsion between particles. Equation (4.51) is plotted in Figure 4.5 with the part of the domain with $\mathbf{v}_{ij} \cdot \mathbf{r}_{ij} < 0$ shown.

Particles close to each other with velocities such that they are on a collision course will generate a repulsion from this artificial viscosity.
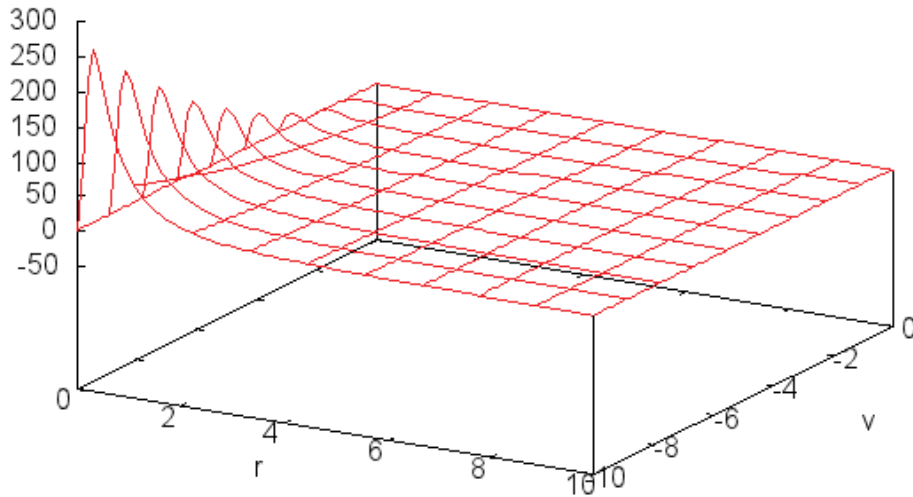
Figure 4.5: The Monaghan type artificial viscosity. Equation (4.51) with $\alpha_\Pi = 1$, $\beta_\Pi = 1$, $h_{ij} = 1$, $\bar{c}_{ij} = 1$ and $\rho_{ij} = 1$.

4.6   Artificial compressibility and the time step

The approach to modelling theoretically incompressible flows using the SPH method usually assumes that the fluid has a small amount of compressibility. This relaxes the conditions imposed on the system by the equation of state and allows for larger time steps [Mon94]. The assumption that a theoretically incompressible flow can be approximated as a weakly compressible flow is the result of an artificial compressibility approach. A weakly compressible equation of state relating density changes to the pressure is given as [Mon94],

$$P = B((\frac{\rho}{\rho_0})^\gamma - 1), \tag{4.52}$$

where ρ is the density, ρ_0 is the reference density and γ and B are constants. This equation is used to simulate common flows in the following sections. It can be seen from this pressure equation that the gradient of the pressure is dependent on a change in density. It can also be seen that the acceleration of the SPH particles in Equation (4.11) is determined by the pressure gradient. Since the time step for the simulation should be chosen depending on the maximum velocity each SPH particle can travel within a single time step, it is ultimately related to a density change. Analysing a change in density [Mon94],

$$\frac{\Delta\rho}{\rho} = \frac{v^2}{c^2} = M^2, \tag{4.53}$$

where c is the speed of sound in the material and M is known as the Mach number. It is seen that for an incompressible material, c is very large. However, choosing c to be a constant less than the actual speed of sound in the material to allow a small density variation, say 1% (i.e. $M^2 < 0.01$), the flow can be approximated by a weakly compressible condition. As mentioned before, the equation of state in Equation (4.52) is a function of the change in density. The coefficient B is chosen to be related to the maximum velocity of the material as [Mon05],

$$B = \frac{c^2 \rho_0}{\gamma} = \frac{v_{max}^2 \rho_0}{\gamma(\frac{\Delta\rho}{\rho})} = \frac{v_{max}^2 \rho_0}{\gamma(0.01)} = \frac{100 v_{max}^2 \rho_0}{\gamma}, \tag{4.54}$$

since $v^2/c^2 < v_{max}^2/c^2 = 0.01$ where v_{max} is the maximum expected velocity of the SPH particles. This should result in a density change of less than 1%.

To determine the time step, Δt, the condition is to set it to be proportional to the smallest particle spacing for movement. To ensure that the effects of particle presence on neighboring particles are captured during each time step, we require the spatial movement to be less that the smallest smoothing distance [LL03],

$$\Delta t = \min_i(\frac{h_i}{c_i}), \tag{4.55}$$

where h_i and c_i are the smoothing length and speed of sound of particle i respectively. To include the effects of viscous dissipation and external forces such as gravity [Mon92],

$$\Delta t_1 = \min_i \left(\frac{h_i}{c_i + 0.6(\alpha_\Pi c_i + \beta_\Pi max(\phi_{ij}))} \right),$$
$$\Delta t_2 = \min_i \left(\frac{h_i}{|f_i|} \right),$$

where f_i is the acceleration due to the external force on particle i. Then the time step is chosen as,

$$\Delta t = \min(\lambda_1 \Delta t_1, \lambda_2 \Delta t_2), \tag{4.56}$$

where λ_1 and λ_2 are safety parameters ($\lambda_1 = 0.4$ and $\lambda_2 = 0.25$ in [Mon92]). Determining the time step in this manner enables the numerical time integration to be stable.

4.7 Average velocity

In cases where the particles are too disorderly and the velocity profile is too erratic, the velocity is adjusted by an extra term which averages velocity values over an area determined by the smoothing length h [Mon92],

$$\tilde{\mathbf{v}}_i = v_i + \epsilon \sum_{j=0}^{N} \frac{m_j}{\rho_{ij}} \mathbf{v}_{ji} W_{ij}, \tag{4.57}$$

where $\rho_{ij} = (\rho_i + \rho_j)/2$ and $\epsilon < 1$ is a constant and determines the extend of averaging. An SPH variant using Equation (4.57) is called XSPH. If this approach is to be used along with the continuity calculation of density then Equation (4.21) should be calculated using $\tilde{\mathbf{v}}_i$ instead of $\mathbf{v}_i$. In this thesis, the XSPH variant will be utilised when needed.

4.8   The equations of state

The dynamics of an evolving system heavily depends on the equations of state governing fluid motion. The equations of state relate state variables. Consider a system on a relatively large scale such as water flow around a dam. Thermodynamic effects such as temperature and internal energy changes will be minimal. This means internal energy and temperature changes need not be modelled. Thus we only require an equation of state determining pressure such as Equation (4.59). However, some situations such as droplet formation call for the calculation of other variables such as internal energy and temperature. In this case, equations of state relating these variables are required. These may be given as equations relating pressure, density, internal energy and temperature such as in equations (4.71) and (4.72).

Mutliple equations of state are used in the susequent sections to describe different cases. In short, the variables of interest are determined for the evolution of a system, equations of state are then formed using equilibrium conditions relating them in order to close the system of equations.

4.9   Boundary conditions and virtual particles

There are four types of boundary conditions that will be applied in this work: No boundary conditions, periodic boundary conditions, reflective boundary conditions and virtual particles. While in some cases, such as within a vacuum environment, no boundary conditions are applied to represent the fact that there is no force imposed due to the environment, in most cases the boundary conditions need to be treated with care. Figure 4.6 shows the starting conditions for drop formation within a vacuum environment. The particles at the sides and edges do not interact with particles on the other side of the simulation domain. Periodic boundary conditions however, assumes the domain is looped such that particles on the edges interact with particles on the opposite edges. If periodic boundary conditions are applied to a homogeneous system such as that in Figure 4.6, the system should not evolve without creating a small inhomogeneity

or disturbance. Reflective boundary conditions involve putting a particle which has escaped the domain back into the simulation domain to the point it escaped (its position at the previous time step) then reflecting the directional properties, such as its velocity, across the boundary. In some cases, such as when walls and impenetrable boundaries are involved, virtual particles are placed at the boundaries with strong repelling properties. Take Figure 4.7 for instance, the green particles are virtual particles. They are not actual particles in the sense that they are not considered in some interactions such as equation of state calculations. They are mainly considered for repulsion calculations. On the other hand, other types of virtual particles may be employed at the boundaries to solve, to some extent, the boundary particle deficiency resulting from the kernel being cut off by the boundary (Figure 4.4).
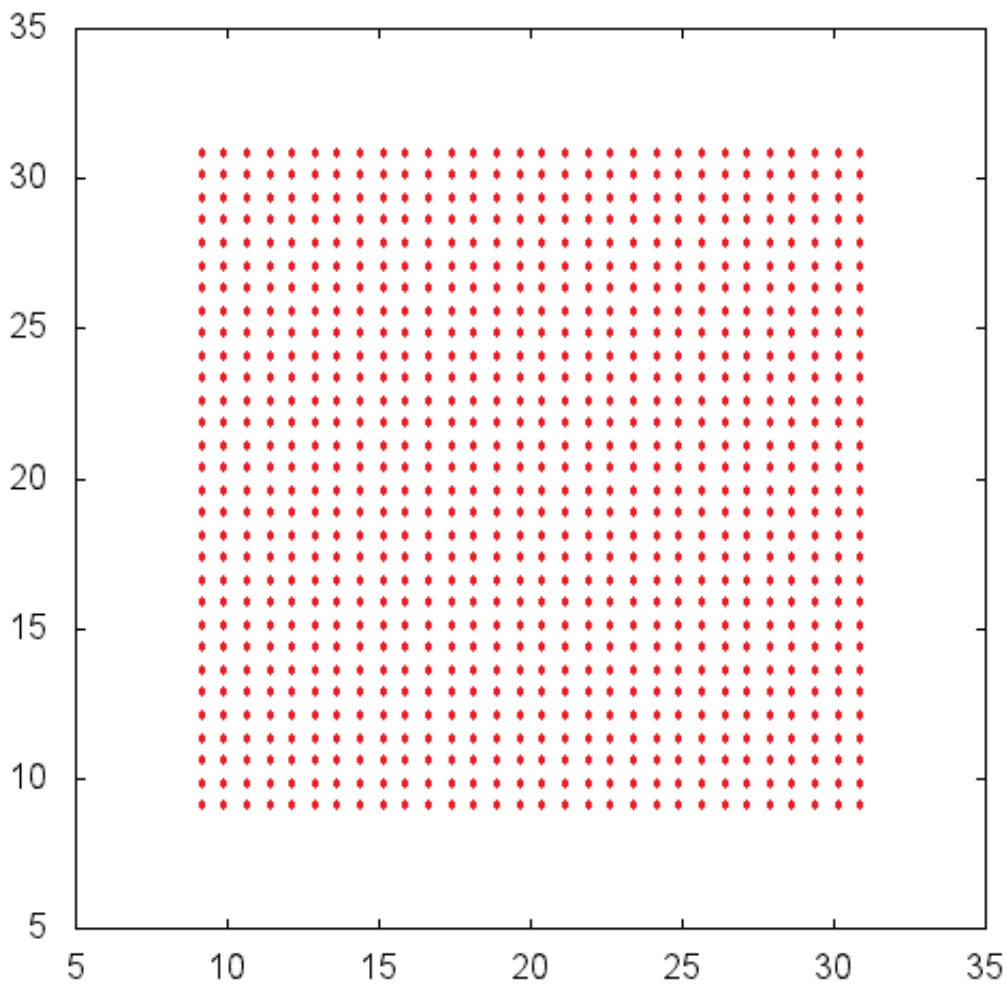
Figure 4.6: 30 × 30 particles on a square grid. Starting point for drop formation simulations.
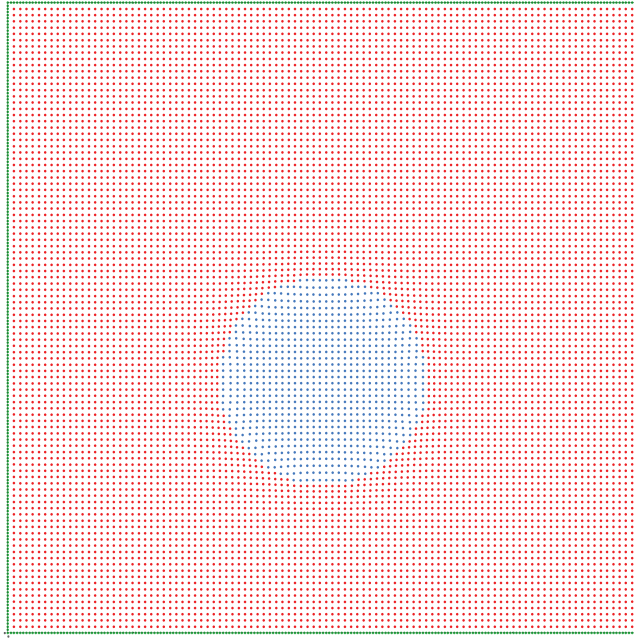
Figure 4.7: Particles on a square grid with virtual particles (green). Starting point for bubble rising simulations.

A popular potential for virtual particle repulsion is the Lennard-Jones potential,

$$V_{LJ} = \frac{D_L((\frac{r_0}{r})^{12} - (\frac{r_0}{r})^6)\mathbf{r}_{ij}}{r^2},$$
(4.58)

where D_L is related to the maximum permitted velocity $D_L = v_{max}^2$ and r_0 is some specified influence range. Figure 4.8 shows what this force looks like. It can be seen that the force approaches infinity as the distance goes to zero. While in the continuous sense this will guarantee that the boundary is not penetrated, the boundary application should still be approached with care. Often in SPH simulations a constant speed of sound is defined to limit the space an SPH particle can cover in a single time step (velocity). If this does not match with other aspects of the simulation such as the boundary conditions one may find the SPH particle on the other side of the virtual particles. Also, the speed of sound limiting the particle velocities should be applied after the boundary conditions. Since otherwise a particle may be given a large velocity due to traveling too close to the virtual particles. As seen in Figure 4.9, an SPH particle has traveled too close over the r_0 distance for the Lennard-Jones potential. If the resulting force is not limited, this particle will be flung into the simulation domain with great velocity. Some numerical techniques, such as the predictor-corrector method [VSMS08], enable calculations at
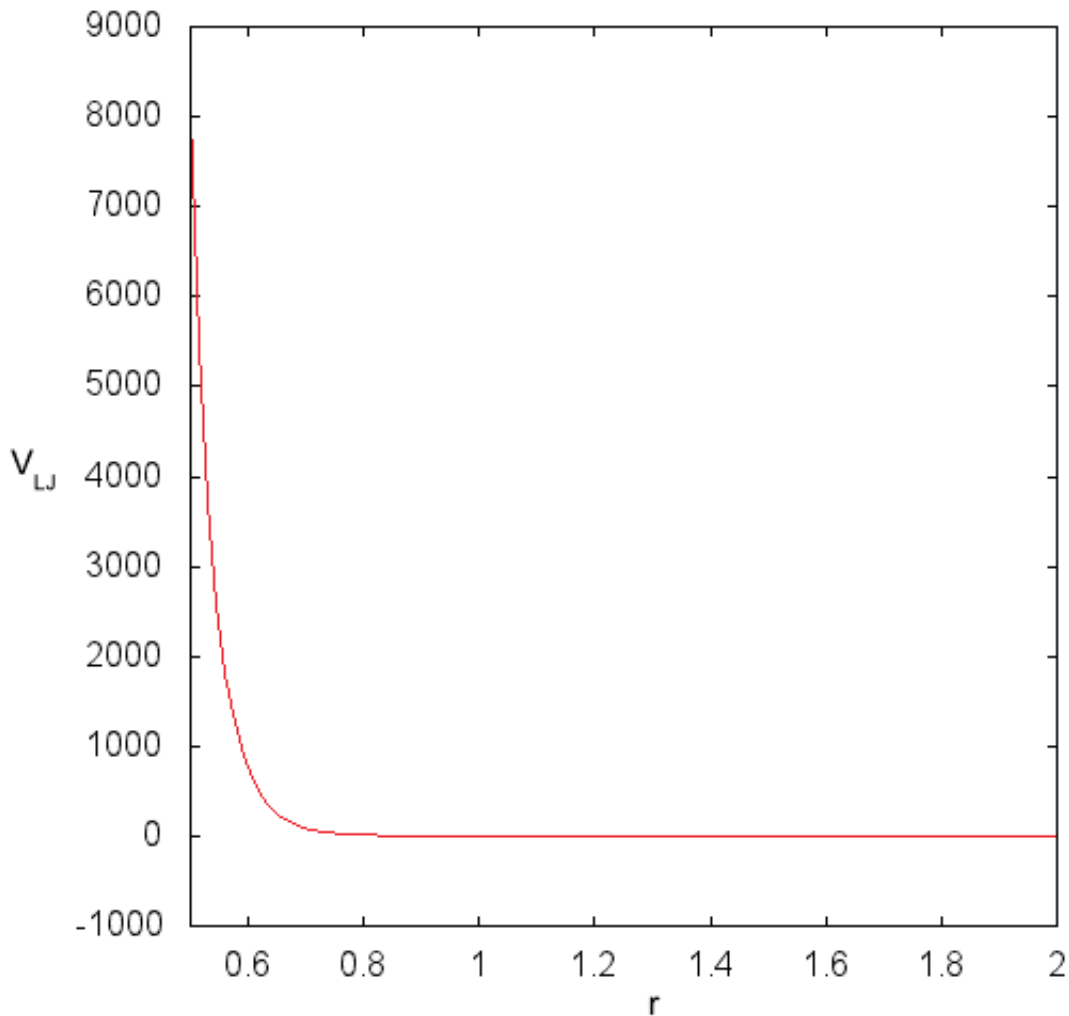
Figure 4.8: Lennard-Jones potential for $D_L = 1$ and $r_0 = 1$ in Equation (4.58).

half time steps to be taken into account reducing such effects.

4.10   Numerical calculation and results

4.10.1   Heat diffusion, the collapsing dam and parameter selection

First we apply the SPH to demonstrate simple heat diffusion (Equation (4.16)). 900 SPH particles are used with a heat diffusion coefficient of $K = 1$. The particles are fixed in position and the time step $dt = 0.005$. After 1000 time steps the temperature profile of the system is shown in Figure 4.10. Next we apply the SPH method to some fluid dynamics cases. However, a suitable equation of state must first be specified. The equation of state relating pressure and
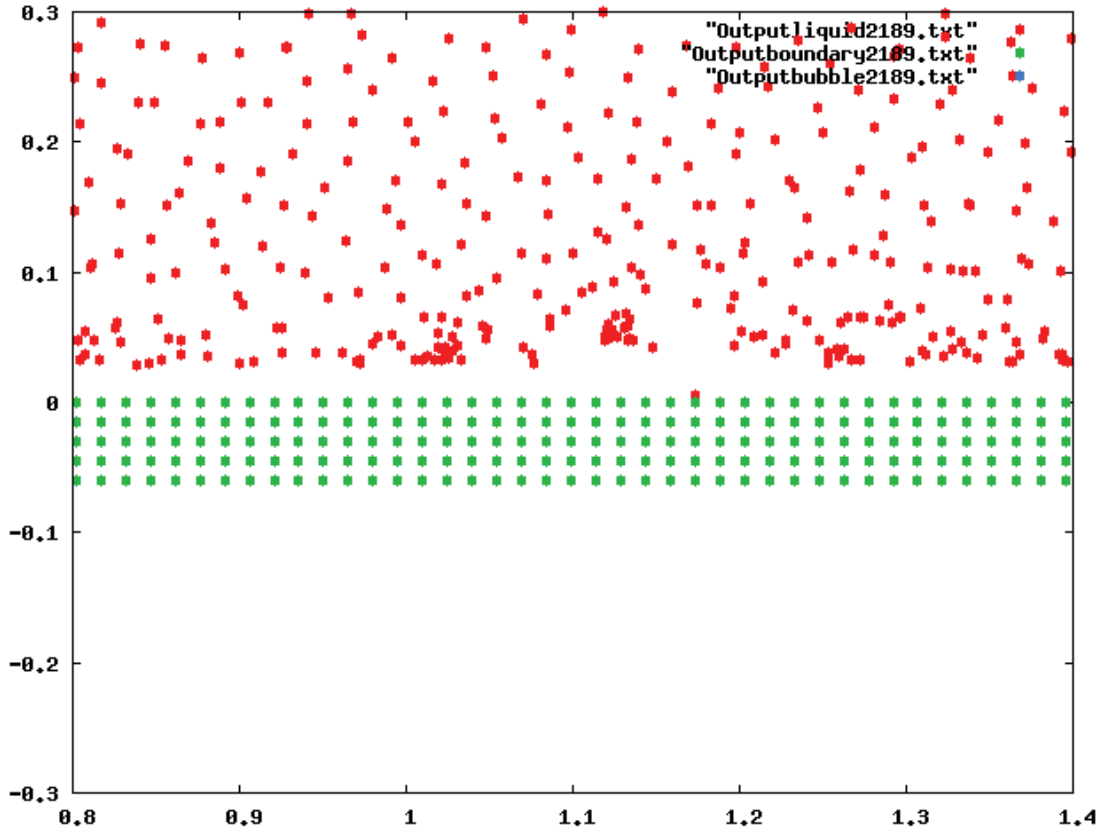
Figure 4.9: An SPH simulation using multiple rows of virtual particles. An SPH particle comes too close to the virtual particles.

density used here will be [Mon94],

$$P = b((\frac{\rho}{\rho_0})^\gamma - 1) + \chi, \tag{4.59}$$

where ρ_0 is some initial reference density and b, γ and χ are constants. Another equation of state would also be required relating temperature and internal energy (such as Equation (4.72)) if these variables play a substantial role in the dynamics. The first term on the right hand side is affected by a change in density such as compression and so b is a constant related to the compressibility of the fluid. Even when dealing with theoretically incompressible flows, some compressibility is assumed. The constant χ is not related to the evolution of the fluid. Considering two different fluids, the pressure of one is indefinitely elevated due to a higher χ term and so this term is related to the interface length of the fluid with other fluids. The values used here are $\gamma_d = 7$, $\rho_{d0} = 1000$, $b_d = 28000$ and $\chi_d = 0$ for the dense liquid and $\gamma_l = 1.4$, $\rho_{l0} = 500$, $b = 5000$ and $\chi = 30000$ for the lighter liquid in the case for a rising bubble
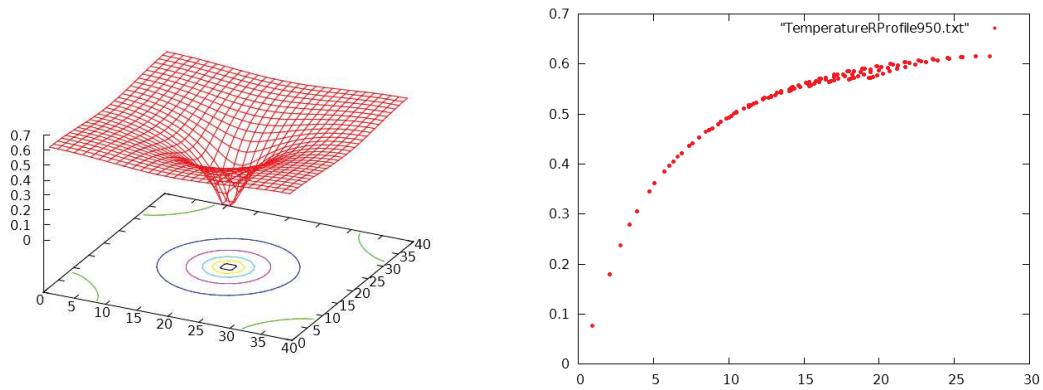
Figure 4.10: A simulation of heat diffusion using the SPH method. A contour plot (left) and the temperature profile with respect to the origin (right).

Figure 4.11: Dam collapse simulation with 10000 particles at time steps 30 (top), 1620 (middle) and 3990 (bottom). No boundary particles were used in this SPH simulation, instead a simple bounce back algorithm was applied at the boundaries (invisible). This corresponds to the absence of friction.

Figure 4.12: Dam raise simulation with 10000 particles at time steps 30 (top), 990 (second down), 2490 (third down) and 3990 (bottom). Virtual boundary particles (green) were used. Friction exists in the form of particle-boundary interaction.

[VSMS08]. It is important to note that since the equations for internal energy increase the computational impact they are not applied to these flows allowing the use of a larger number of particles. Figure 4.11 shows a simulation of a collapsing dam. The initial condition is to order 10000 particles into a square. The bottom and left side of the square is considered a wall with reflective boundary conditions. The force of gravity is then allowed to influence the movement of the fluid reproducing the effect of suddenly removing the right wall. Another wall is placed a small distance to the right with a gap in the bottom in order to demonstrate the dynamics that occur in such a situation. All boundary conditions in this collapsing dam simulation is reflective and friction is not included. The walls are invisible since there are no particles placed there.

Figure 4.12 shows a simulation of a dam raise. 10000 particles are placed inside a square box and the wall one the right side is lifted to reveal a small gap at the bottom. A small ramp is also placed a small distance to the right. Here, virtual boundary conditions are applied. Friction exists in the sense that the virtual particles are included in average velocity calculations (Equation (4.57)). The virtual particles are given a constant velocity of 0 and their effect on the averaging will be to drag the SPH particles. Notice the different flow dynamics when compared

to the dam collapse simulation. Figure 4.11 shows particles gliding along a frictionless surface.
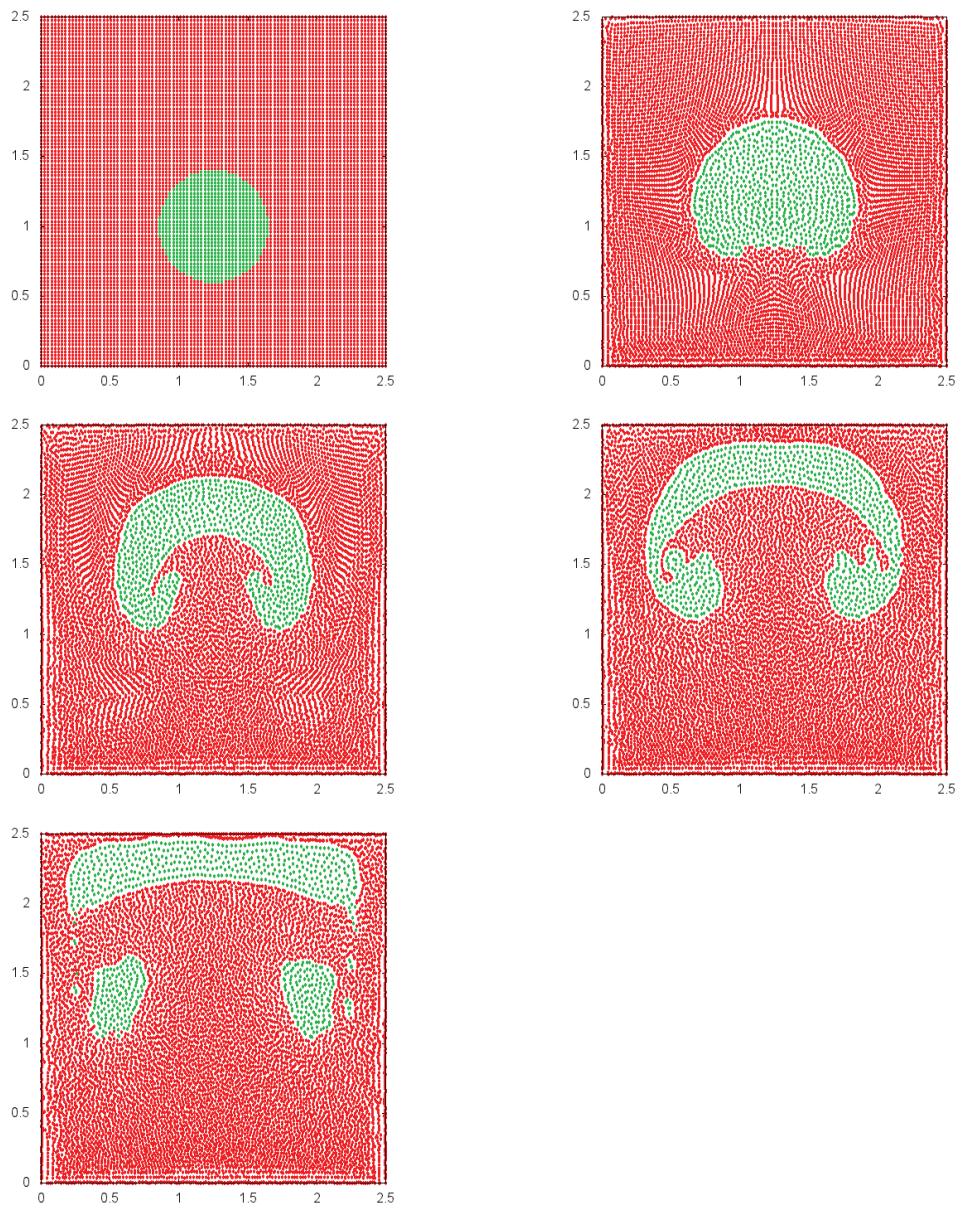
Figure 4.13: A simulation of a rising bubble of fluid within a heavier more viscous fluid at time step 0 (top left), 1000 (top right), 2000 (middle left), 3000 (middle right) and 4000 (bottom left). 10000 particles were used along with reflective boundary conditions.

4.10.2   Rising bubble

Figures 4.13 and 4.14 show a bubble of lighter fluid rising within a denser fluid using reflective boundary conditions and virtual particles respectively. The density of the denser fluid is 1000 and that of the lighter fluid is 500. The lighter fluid rises to the top of the simulation domain
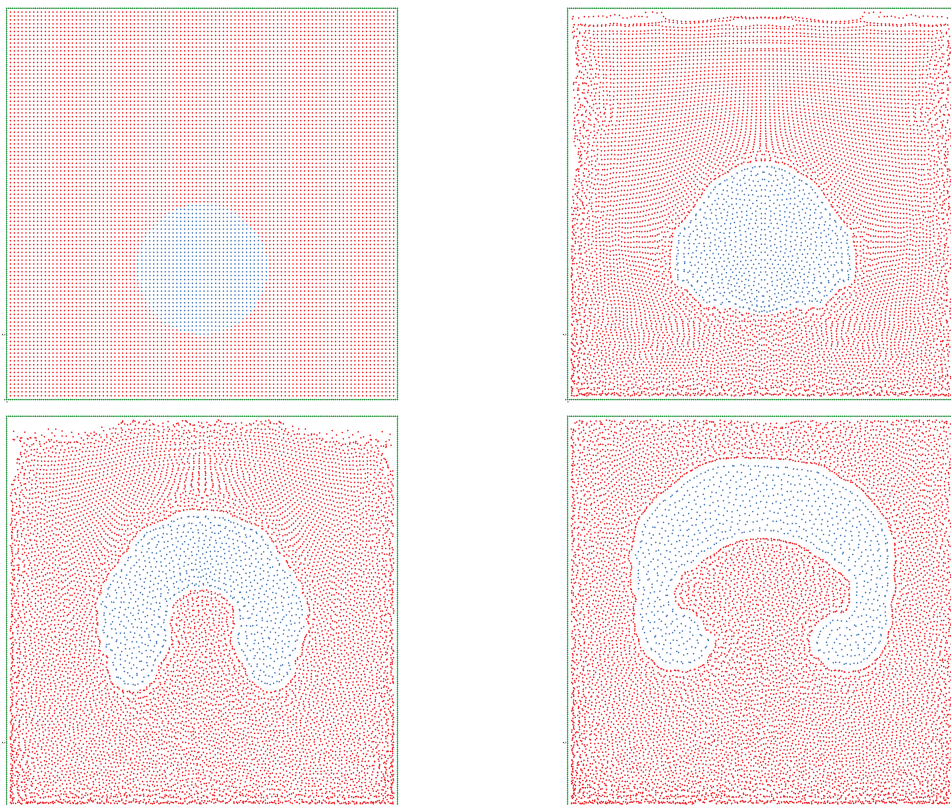
Figure 4.14: A simulation of a rising bubble of fluid within a heavier more viscous fluid at time step 0 (top left), 1000 (top right), 2000 (bottom left) and 3000 (bottom right). 10000 particles were used along with virtual particles.
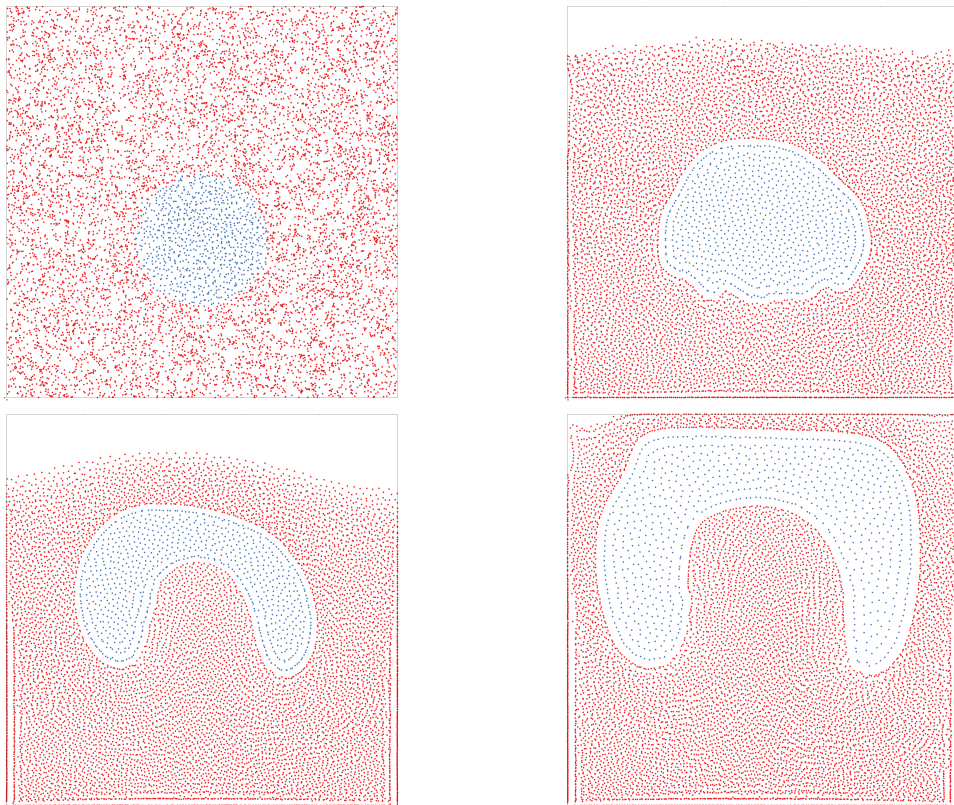
Figure 4.15: A simulation of a rising bubble of fluid within a heavier more viscous fluid at time step 0 (top left), 1000 (top right), 2000 (middle left), 3000 (middle right). 10000 particles were placed randomly with reflective boundary conditions.

due to the influence of gravity [VSMS08]. This is an important example of how easily SPH can deal with small phases breaking away from larger phases and producing complex boundaries. Figure 4.15 shows a bubble in a fluid where instead of placing particles with equal distances, the points are randomly scattered. Then all points within a certain circular area are designated the lighter fluid with the rest being the heavier fluid. This demonstrates how SPH deals with and adapts to the system conditions at hand.

4.10.3   Shock tube

An example involving discontinuities (in density) is that of the shock tube simulation [HK89, Mon05]. The system is set up with two regions of high and low density seperated by a membrane (Figure 4.16). This membrane is then removed creating a discontinuity in density across the interface between the two regions [HK89, LL03]. The subsequent shock wave dynamics is then captured using the standard SPH method. The regions attributed to the shock tube are shown in Figure 4.17. For the 2D simulation, the number of high density (red) particles is 40000 giving a particle distance of 0.00375 and the number of low density (green) particles is 10000 giving a particle distance of 0.0075. For the 1D simulation, the number of high density (red) particles is 640 giving a particle distance of 0.001172 and the number of low density (green) particles is 160 giving a particle distance of 0.00469. The mass of each particle is set as $m = 0.000014072$ for the 2D simulation and $m = 0.00117075$ in order to satisfy $\rho_{left} = 1$ for both cases. The equation of state is given as [BFP07],

$$P_i = (\gamma - 1)U_i\rho_i, \tag{4.60}$$

where U_i is the internal energy of each particle and $\gamma = 1.4$ is the specific heat ratio. The initial internal energy is $U_i = 2.5$ for the high density region and $U_i = 1.795$ for the low density region. This gives initial conditions for the pressure as $P_{left} = 1$ and $P_{right} = 0.1795$. The initial density for the low density fluid is $\rho_{right} = 0.25$. The domain size is given as $0 \leq x \leq 1.5$ and $0 \leq y \leq 0.75$. The support range of each particle is 0.02. All particles are initially stationary.
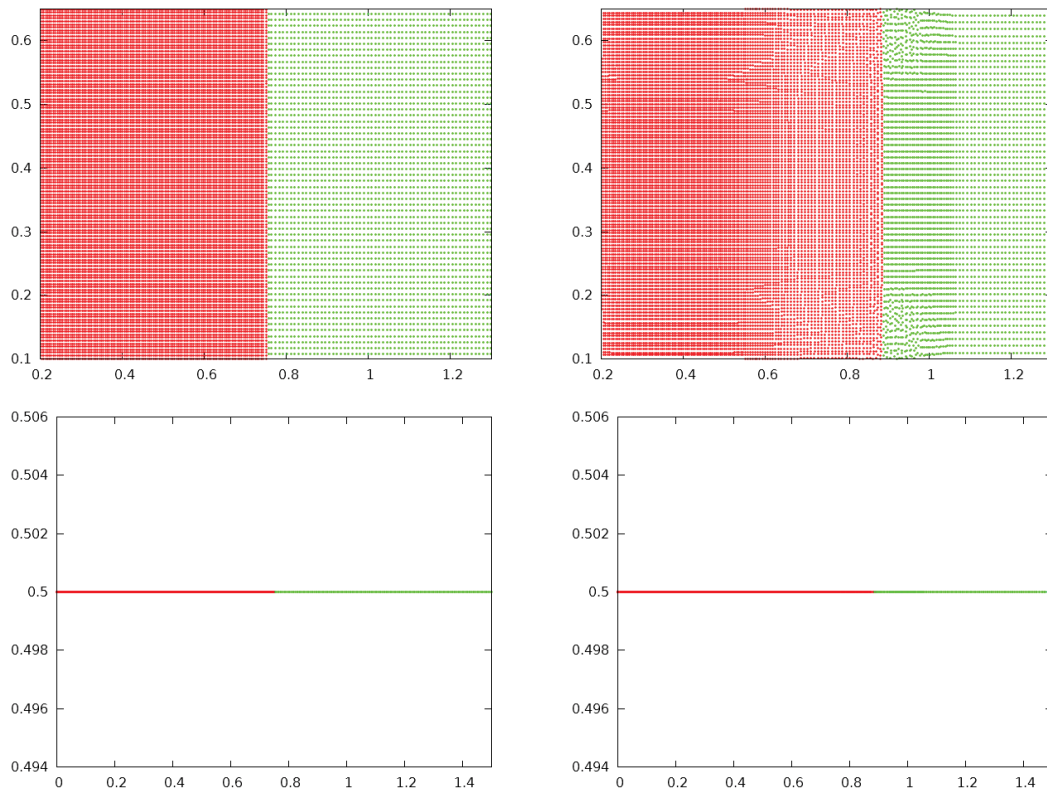
Figure 4.16: The initial particle positions (left) and at t=0.2s (right) for the shock tube simulation. The top and bottom figures represent the 2D and 1D simulations resprectively.
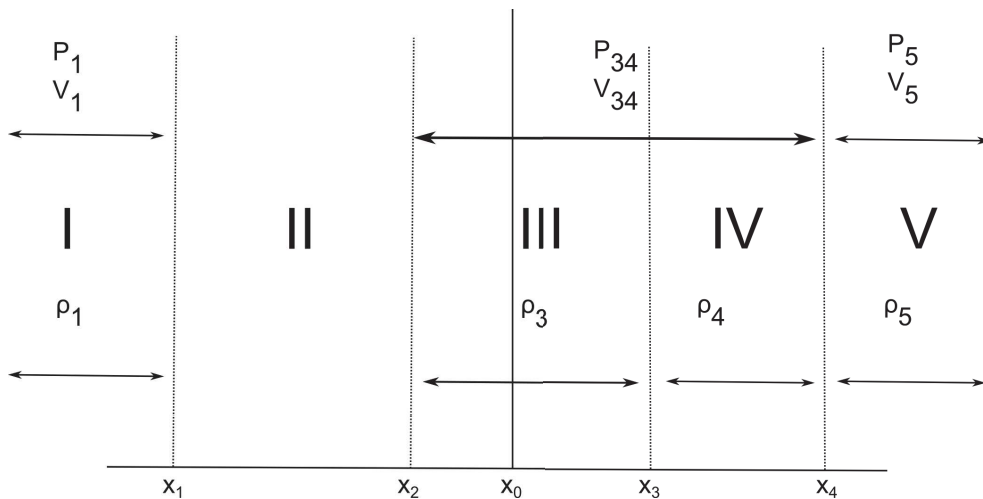
Figure 4.17: The regions of interest in the shock tube system. The subscripts 1, 3, 34, 5 denote the corresponding values in the left, middle, post shock, and right regions of the domain respectively. Region II is the rarefaction section.

For the analytic solution, the pressure for the regions III and IV (P_{34}) is found by solving the following equation for P [Sod78],

$$\frac{2\sqrt{\gamma}}{\gamma-1}\left[1-P^{\frac{\gamma-1}{2\gamma}}\right] = (P-P_5)\left[\frac{(1-\mu^2)^2}{\rho_5(P+\mu^2 P_5)}\right]^{1/2}, \tag{4.61}$$

where $\mu^2 = (\gamma-1)/(\gamma+1)$. The velocity of the fluid in this region is then calculated using P_{34} as

$$V_{34} = \frac{2\sqrt{\gamma}}{\gamma-1}\left[1-P_{34}^{\frac{\gamma-1}{2\gamma}}\right]. \tag{4.62}$$

The velocity of the shock wave V_{shock} and ρ_3 and ρ_4 are now calculated as,

$$V_{shock} = V_{34}\frac{\frac{\rho_{34}}{\rho_5}}{\frac{\rho_{34}}{\rho_5}-1}, \tag{4.63}$$

$$\rho_3 = \rho_1\left(\frac{P_{34}}{P_1}\right), \tag{4.64}$$

$$\rho_4 = \rho_5\frac{\frac{P_{34}}{P_5}+\mu^2}{1+\mu^2\frac{P_{34}}{P_5}}. \tag{4.65}$$

The speed of sound in region II, c_2, is then calculated as,

$$c_2(x) = \mu^2\left[\frac{x_0-x}{t}\right]+(1-\mu^2)c_1, \tag{4.66}$$

where $c_1 = \sqrt{\gamma P_1/\rho}$ is the speed of sound in region I. The state variables in region II are then calculated as,

$$V_2(x) = (1-\mu^2)\left[\frac{-x_0+x}{t}+c_1\right], \tag{4.67}$$

$$\rho_2(x) = \rho_1\left(\frac{c_2(x)}{c_1}\right)^{\frac{2}{\gamma-1}}, \tag{4.68}$$

$$P_2(x) = P_1\left(\frac{\rho_2(x)}{\rho_1}\right)^{\gamma}. \tag{4.69}$$

The locations of the regions and the internal energy, $U(x)$, are then

$$x_1 = x_0 - c_1 t, \quad x_3 = x_0 + V_{34}t, \quad x_4 = x_0 + V_{shock}t, \quad U(x) = \frac{P(x)}{(\gamma-1)\rho}. \tag{4.70}$$

The location of x_2 is the x value where we have the equality $P_2(x) = P_{34}$.

For the initial conditions given above, the variables are calculated to be as follows: $\mu^2 = 1/6$, $x_0 = 0.75$, $c_1 = 1.183$, $V_{shock} = 1.5$, $x_1 = 0.5134$, $x_2 = 0.668$, $x_3 = 0.885$, $x_4 = 1.05$, $P_{34} = 0.427$, $V_{34} = 0.677$, $\rho_3 = 0.545$ and $\rho_4 = 0.456$. The analytic solution is compared to the SPH solutions in Figure 4.18. Figure 4.19 is an additional plot of the pressure profile since the exceptional agreement of the cubic spline results is not obvious from Figure 4.18. It can be seen that the cubic spline gives results more comparable to the analytical solution.
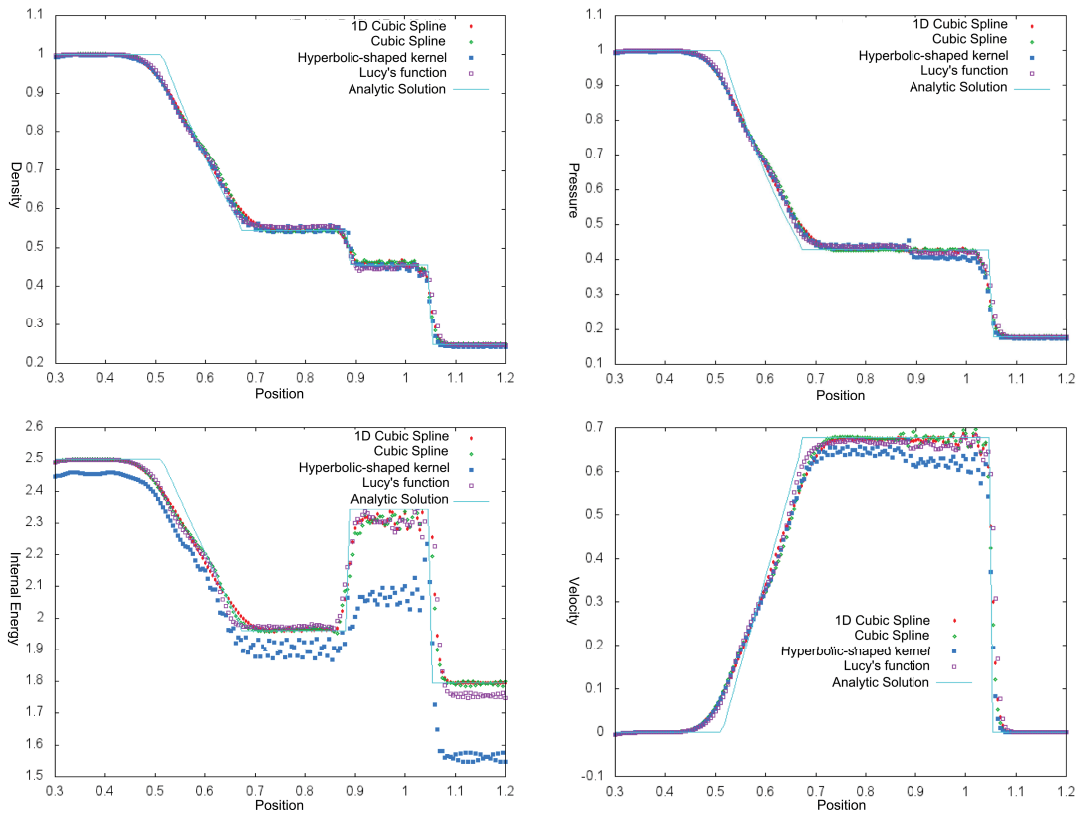
Figure 4.18: The shock tube results with $h = 0.01$ for the cubic spline and the hyperbolic-shaped kernel and $h = 0.02$ for Lucy's function. The plots include the analytical solution and results from all three kernels including an additional 1 dimensional simulation using the cubic spline.

4.10.4   Droplet formation in non-ideal fluids

The use of the SPH method for the simulation of some hydrodynamic simulations is now possible using equations (4.10) - (4.18). However, a suitable equation of state for droplet
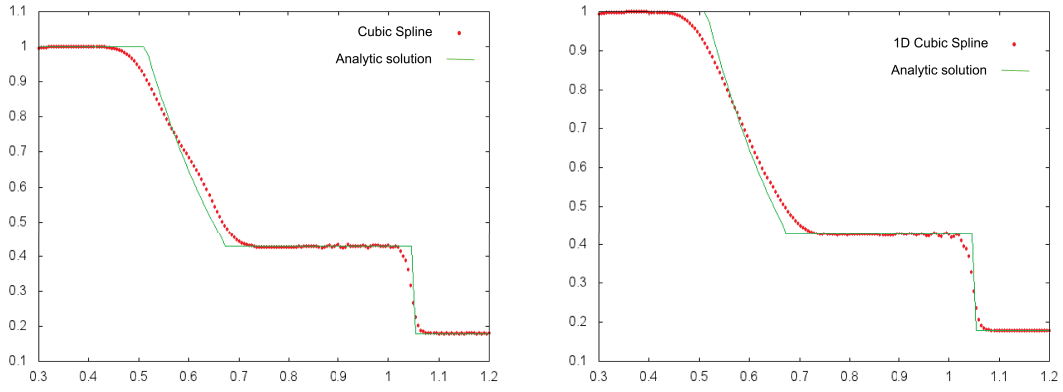
Figure 4.19: The shock tube results for the pressure for the 2 dimensional (left) and 1 dimensional (right) cubic spline kernel.

formation must first be specified. The equation of state used here will be the van der Waals equation of state,

$$P = \frac{\rho \bar{k} T}{1 - \rho \bar{b}} - \bar{a}\rho^2, \tag{4.71}$$

where $\bar{k} = k_B/m$ is the scaled Boltzmann constant and $\bar{a} = a/m$ and $\bar{b} = b/m$ are the scaled van der Waals parameters. $\bar{a}$ is related to the strength of attraction of the particles whereas $\bar{b}$ is related to the occupied volume per mole of the hard spheres. The equation of state relating the internal energy U to temperature T is given as,

$$U = \frac{d}{2}\bar{k}T - \bar{a}\rho, \tag{4.72}$$

where d is the dimension of the problem. Unless explicitly specified, the general process for the simulations is to begin with a domain with homogeneously dispersed particles with equal distances from each other. The mass is set to be constant for all the particles and remains constant in time (apart from mass fluctuations). This immediately results in a view of the model as considering a single particle to represent a fixed amount of fluid. The particle density d_i (and subsequently the mass density ρ_i) of particle i can then change depending on the locations of the particles. Unfortunately, such a treatment for a vdW droplet does not yield stable results. The reason for this was found to be due to the assumption that the vdW attraction force acts on the same scale as the repulsion due to pressure differences. Nugent and Posch [NP00] introduced a larger smoothing length, $H \geq h$, over which to impose the effects of

the second term on the right-hand side of Equation (4.71). This results in the following terms
to be considered seperately,

$$\left(\frac{d\mathbf{v}}{dt}\right)_i^a = 2\bar{a}\sum_{j=0}^{N} m_j \nabla_i W ij^H, \tag{4.73}$$

$$\left(\frac{d\mathbf{u}}{dt}\right)_i^a = \bar{a}\sum_{j=0}^{N} m_j (\mathbf{v}_j - \mathbf{v}_i) \cdot \nabla_i W ij^H, \tag{4.74}$$

where the superscript ^{a} denotes the long range contribution acting over smoothing length
$H > h$. Given a symmetric kernel and a symmetric treatment for the smoothing lengths
(which is the case here since the smoothing lengths do not differ from particle to particle),
it can be seen that Equations (4.73) and (4.74) are symmetric in space. This means that
the contribution due to these long range forces cancel within the bulk of the vdW droplet.
The boundary of the droplet however, experiences a change in density and other parameters
disturbing the symmetricity of the long range contributions. The resolved attractive force is in
the direction of the normal to the curvature, towards the center of the droplet. This naturally
gives rise to surface tension [NP00, LS06].

The boundary conditions are periodic. Applying fluid dynamics to this exactly homogeneous
system will not evolve it in any particular manner and thus an inhomogeneity needs to be
introduced. This is done by introducing random mass fluctuations throughout the system.

Figure 4.20 shows a vdW simulation using 61×61 SPH particles each given a mass of 0.6 with
temperature 0.8. The smoothing length is set to $h = 2$ and $H = 1.6 \times h$. The bulk viscosity is
$\zeta = 0.1$ and the shear viscosity is $\eta = 1$. The artificial viscosity parameters are $\alpha_\Pi = 0.1$ and
$\beta_\Pi = 1$. The heat conduction coefficient is $K = 5$. The vdW parameters are $\bar{a} = 1.018226$,
$\bar{b} = 0.3$ and $\bar{k} = 1$. These vdW parameters are taken from a similar simulation using Lattice
Boltzmann [Qin06] and the resulting high-low density values shown in Figure 4.21 agree for
this temperature (roughly 0.3 and 2.1).
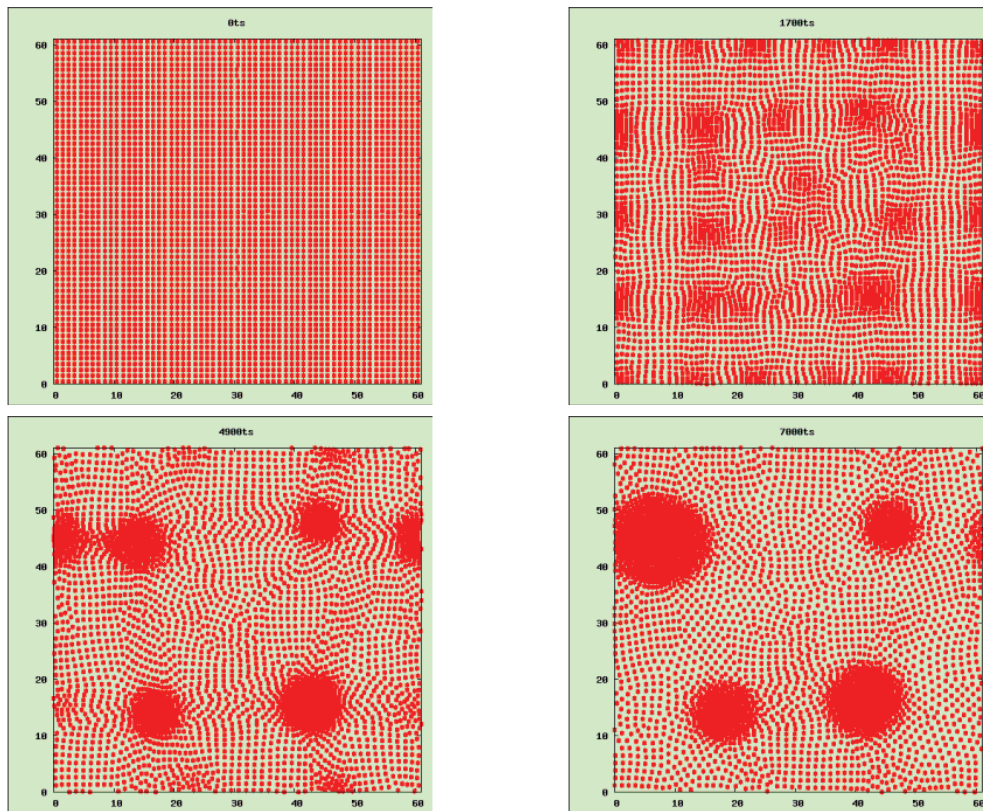
Figure 4.20: A simulation of vdW drop coalescence using 61×61 SPH particles. Periodic boundary conditions with random mass fluctuations was employed.
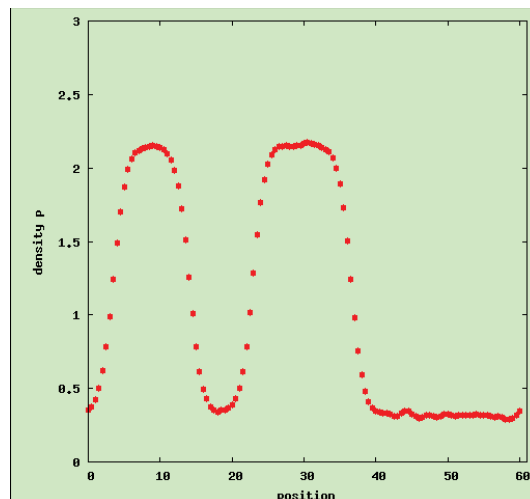
Figure 4.21: The density profile across two of the coalesced drops from the simulation in Figure 4.20.

The previous simulation was done using a single fluid type. Suppose now that we introduce a system with two fluid types. Fluid A and fluid B. The vdW interactions between different pairs of fluid volumes should now be different. Let us define the vdW parameters as $\bar{a}_{ij}$ and $\bar{b}_{ij}$ where the subscript represents the combinations {AA,AB,BB}. For the first simulation we set $\bar{a}_{ij} = 1.018226$ if $i = j = B$ and $\bar{a}_{ij} = 0$ otherwise and $\bar{b}_{ij} = 0.3$ as before. The result is shown in Figure 4.22. The green SPH particles are of type B. It can be seen that the sizes of the high density regions are quite small. Introducing the right amount of velocity gradients (stirring, mixing etc...) may lead to the formation of larger high density regions. Figure 4.23 is a simulation with the same parameters but with a positive velocity given to particles near the top and bottom of the domain and a negative velocity given to those near the horizontal center line. The velocities of the particles are increased gradually. This way different vdW scenarios can be simulated.
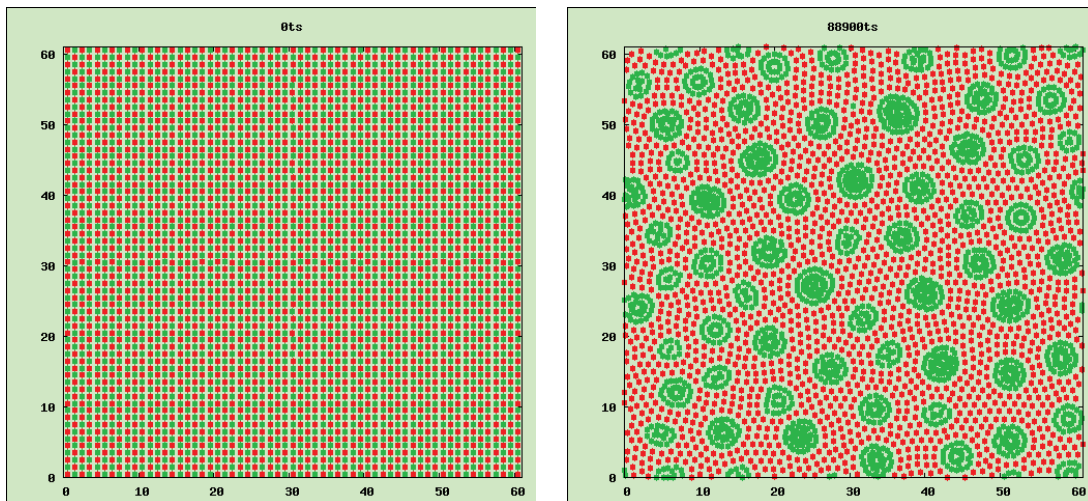
Figure 4.22: A simulation of vdW drop coalescence using 61×61 SPH particles (1861 type A and 1860 type B particles). Periodic boundary conditions with random mass fluctuations was employed.

4.11   Smoothing length dependence of the results obtained from van der Waals simulations

It has been seen that the smoothing length effects the accuracy of the results when applying the SPH method to describe natural phenomena. In this chapter, we explore the effects on the
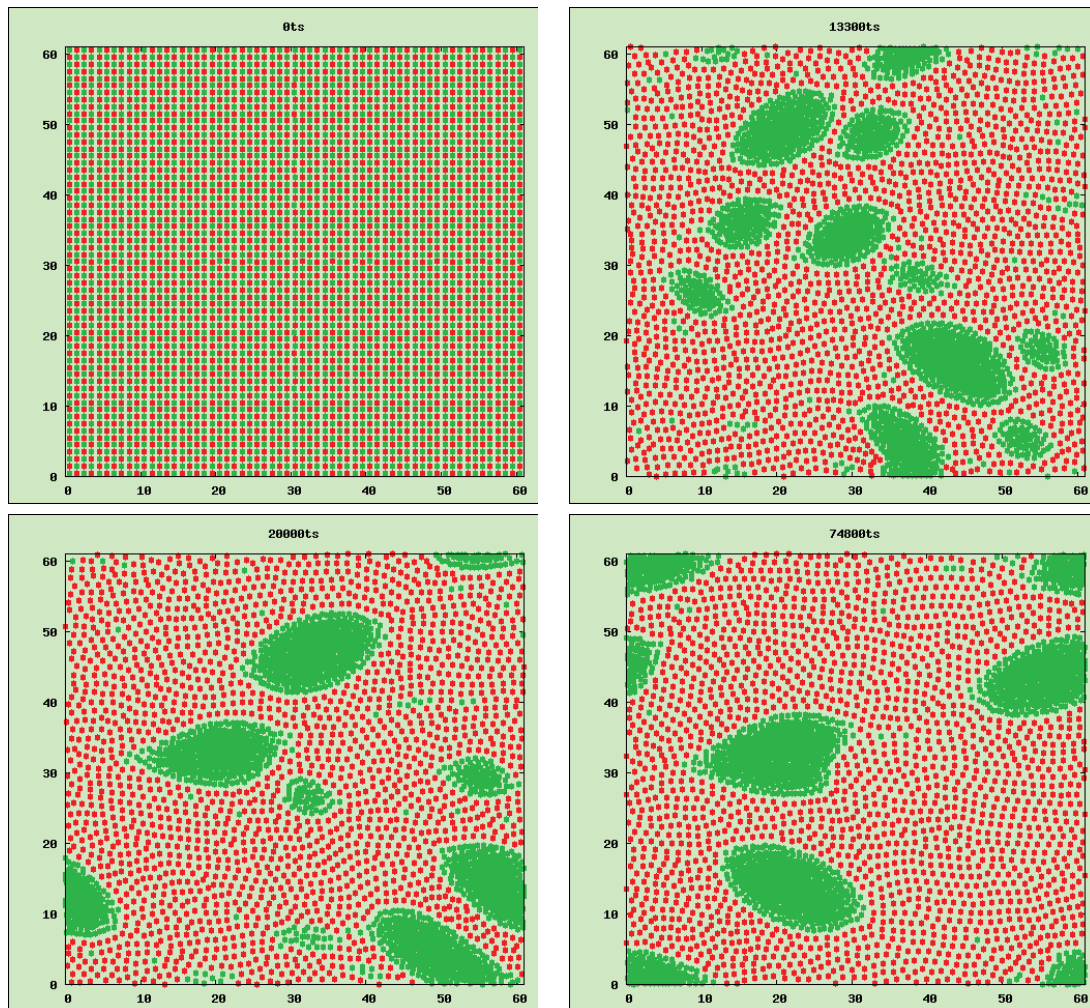
Figure 4.23: A simulation of vdW drop coalescence using 61×61 SPH particles (1861 type A and 1860 type B particles). Periodic boundary conditions with random mass fluctuations and a velocity gradient was employed.

consistency of the results of systems governed by forces such as van der Waals forces due to a change in smoothing length. This consistency is of great importance when communicating or sharing system states between models cooperating in order to describe an entire system. One important quantity is entropy. If the entropy of a system depends upon the accuracy parameters used such as the smoothing length in the SPH method, this makes it increasingly difficult to obtain correct results when models running in tandem with the SPH method depend upon the information being consistent.

Multiple simulations are performed on a system with initial state consisting of 30×30 SPH particles as in Figure 4.6. The smoothing length is varied while using Lucy's function as the kernel. The evolution of the velocity and internal energy are evolved as in Section 4.10.4, i.e. using Equations (4.11) and (4.73) for the velocity and Equations (4.13) and (4.74) for the internal energy. The tensor form of Equation (4.20) is used for $(\nabla v)_i$ and Equations (4.22) and (4.23) are used for $(\nabla T)_i$ and $(\nabla^2 T)_i$ respectively. The vector form of Equation (4.25) is used to calculate $(\nabla \cdot P)_i$ and the entropy evolution is calculated according to Equation (4.12). The density is calculated according to the summation density equation, Equation (4.5). The reason this is used instead of evolving density according to the continuity equation, Equation (4.10), is because the summation density equation conserves mass. The traditional evolution equation for heat conduction is (analogous to that for pressure),

$$(\nabla \cdot q)_i = \rho_i K \sum_{j=0}^{N} m_j \left(\frac{q_i}{\rho_i^2} + \frac{q_j}{\rho_j^2} \right) \cdot \nabla_i W_{ij}, \tag{4.75}$$

however, reports of a more consistent form of heat conduction is given as [YLP14, Mon05],

$$(\nabla \cdot q)_i = -\rho_i K \sum_{j=0}^{N} \frac{2 m_j r_{ij} \cdot \nabla_i W_{ij}}{\rho_i \rho_j (r_{ij}^2 + 0.01 h^2)} (T_j - T_i). \tag{4.76}$$

The initial temperature is set as $T = 0.02$, heat conductivity $K = 5$ and particle distance $\Delta x = 0.75$. A time step of $\Delta t = 0.005$ is used. The forces involved in the path towards equilibrium of a vdW fluid involves oscillations about equilibrium. The amplitude of these

oscillations in the simulations tend towards zero as time goes to infinity. It is therefore more practical to assign a logical point at which sufficient evolution toward equilibrium is assumed. This point is assumed here to be the point at which the entropy change is as $\Delta S < 0.0001$. Due to the presence of velocity and temperature gradients in the evolution of the entropy change, an entropy change tending toward zero translates as a decrease in system activity.

The SPH particle positions as well as the pressure profiles for the cases for Lucy's function with $h = 3$ with and without the application of average velocity are shown in Figure 4.24. Table (1) and Table (2) in Appendix G show the total entropy change in each of these cases with and without the average velocity technique respectively. One immediately notices clumping behaviour of SPH particles for smoothing lengths larger than 2. It is seen that a kernel with a negative second derivative will exhibit tensile instability for distances within the region where its second derivative is negative [SHA95, YLP14]. Lucy's function has a negative second derivative. Given the initial conditions which result in particle distance $\Delta x = 0.75$, using a smoothing length value $h > 2$, will result in calculations lying in the negative second derivative region hence the clumping of SPH particles within this region. The simulations with and without average velocity show that the average velocity technique greatly improves the entropy consistency, especially for Lucy's function.

4.12 Summary

The SPH method is a tool that has been developed from an initial simple integral identity (Equation (4.1)) into a method fully capable of describing complex fluid systems. Given hydrodynamic evolution equations, the SPH method can be used to discretise a system of equations (equations (4.10) - (4.13)) in order to predict fluid environments. An essential component to the SPH method is the use of a smoothing function or a kernel to enable the possibility to represent discrete points as continuous regions. This is the reason it is possible to approximate gradients of physical state variables. There are multiple candidates for kernels, three of which are given in Section 4.4. These are chosen since they cover three categories of kernels: piece-
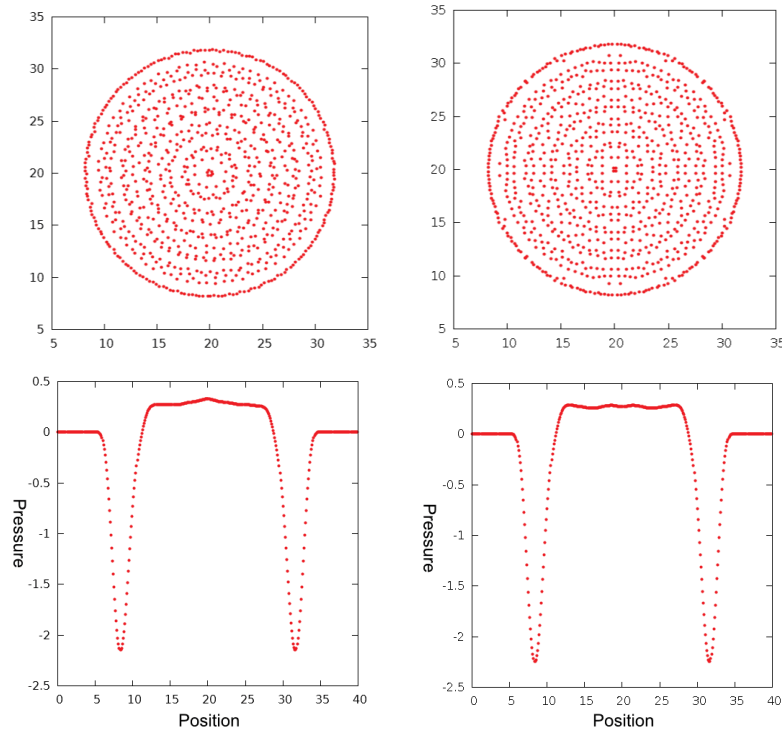
Figure 4.24: A simulation of a vdW droplet using the SPH method. The figure shows the particle positions and pressure profiles for Lucy's function with $h = 3$ using average velocity (right column) and without average velocity (left column).

wise kernels with negative second derivatives (cubic spline, Equation (4.27), Figure 4.2), single function kernels with negative second derivatives (Lucy's function, Equation (4.26), Figure 4.1) and kernels with positive second derivatives (hyperbolic shaped kernel, Equation (4.28), Figure 4.3).

It is fortunate that the errors produced using the SPH method are bounded. This is because given a set of governing equations representing a physical system, along with the equations of state, the direction and magnitude of evolution is always dependent on the current state of the system. This means that if it is accepted that the SPH method used incurs some approximation errors, these errors do not carry from one time step to the next [LL03]. This ability to adapt to the current state of the system is seen in Figure 4.15, in which the SPH points are randomly placed within the system domain.

Some techniques can be utilised in order to make SPH a more stable and robust method. These include the inclusion of artificial viscosity (Section 4.5) to remedy particle penetration,

the average velocity technique (Section 4.7) in order to produce a smoother velocity profile and the inclusion of virtual particles at the boundary of the system (Section 4.9) in order to minimise errors in approximation due to part of the smoothing range of particles close to the boundary lying outside of the system (Figure 4.4). The SPH method is applied to heat diffusion, flow through obstacles, rising bubbles of less dense material within a more dense material, the shock tube and droplet formation (Section 4.10). The smoothing length is shown to have influence on the results obtained for the van der Waals simulations. In particular, the obtained entropy change is inconsistent and erratic. Applying the average velocity technique is shown to reduce entropy change variations by forming a smoother velocity profile. Also, instead of simply increasing the smoothing length in order to obtain better accuracy, it is seen to be better to increase the number of SPH points while keeping the total mass constant.

Chapter 5

Conclusion and discussion

The phase-field (PF) method and the smoothed particle hydrodynamics (SPH) method are seen to be more than capable of dealing with complex phenomena in materials science. The PF method is popular in describing phase transformations due to its ability to describe interfacial regions implicitly without requiring the locating of these structures explicitly during computation. The SPH method is exceptional in describing fluid mechanics situations. Due to the method being meshfree, it has received much attention for its capability in simulating situations involving high velocity impact, irregular boundaries and large deformations.

Concerning the solid state regions of Figure 1.1, the developed PF model for martensite and bainite formation has the capability to reproduce orientation variants of martensitic plates observed in steels. The phenomenological theory of strain energy is incorporated into the model which uses a governing equation for a single PF variable for phase growth. The growth of different orientations are then dependent upon the orientation matrices obtained from literature. Effects of different applied stresses on variant selection is also within the capabilities of the model. Application to bainite formation by including carbon diffusion has reproduced the trapping of carbon within the films of austenite between bainite subunits. It is also capable of reproducing the incomplete transformation phenomenon experimentally observed in bainitic steels. While sufficient for describing many bainitic steels, future development of the model

would typically involve incorporating carbide precipitation within these supersaturated austenite regions. The nucleation and growth of martensitic plates are influenced by the growth of prior plates. The strain energy far away from an ellipsoidal inclusion is given by Eshelby [Esh57]. Consideration of this in the model to reproduce this long distance strain energy along with the interaction energy between nucleations and the stress field [MRH06] will enable autocatalytic nucleations seen in martensite nucleation.

The SPH method has the ability to model many fluid dynamics situations for treatment of the region in Figure 1.1 involving hydrodynamics. The method is very flexible to initial and boundary conditions. Virtual particles may be placed at the boundary in order to simulate impenetrable walls with and without friction. Alternatively, the absence of any boundary conditions aid in simulating systems in a vacuum environment. By applying some techniques it is capable of generating a consistent entropy production in droplet formation. The same system will result in approximately the same entropy regardless of a change in the accuracy parameters such as the number of particles. It is seen that the some kernels such as Lucy's function respond better to this treatment than others. Application of SPH to modelling surface tension in real fluids requires the adjustment of parameters for those of the fluids as well as vdW parameters governing the interaction between different types of fluids [LVCT14].

The final region in Figure 1.1 to be studied adequately involves both hydrodynamics and solidification. This calls for a coupling of the methods SPH and PF. When it comes to the merging of the PF method with the SPH method, Lagrangian and Eulerian methods have been successfully coupled to solve complex natural phenomena [Ben92, HAC74, WWGB09]. An important requirement here is the mode of communication between the two methods. The PF method relies on a fixed grid and so is unable to interpret data obtained at random locations within the system domain. The nature of the SPH interpolation makes this cooperation between models possible. Within the SPH framework, interpolation is performed at particle locations whereas the output properties in the figures in Section 4.10 are performed at discrete points in the system domain where no particle resides. This means that an evolutionary property

to be communicated between the PF and SPH methods can be translated from grid points to meshfree particles and vice versa. In this way, cases involving the solidification in the presence of flow can be treated with high Reynolds numbers and conditions deemed too complex for traditional computing methods to handle.

A free floating solid particle within a fluid material is arguably one of the most complex cases to be modelled. Not only does this particle, in the most general case, have complex boundaries and movement, it also rotates. We have seen that the models mentioned in this work have no trouble with complex interfaces. The solid particle can be represented in the SPH calculations as a cluster of spaced SPH particles fixed together. These particles can then interact with the fluid particles to calculate forces. The movement of the solid particle should be governed by the hydrodynamics capabilities of the SPH method by calculating linear and angular momentum due to drag forces.

The capability of the particle to rotate would be affected by the motion of SPH fluid particles against the impenetrable boundary of the solid particle as well as collisions of solid particles subjected to a contact force. This contact force (e.g. linear spring dashpot contact force [RRL14]) appears as a force in the acceleration equation. The effect of the fluid on the solid particles is to inflict a drag force (e.g. Stokes drag force). The effect of the drag force on SPH solid particle i is related to the difference in average velocities of the solid particles and the velocity of particle i. This means that in order to calculate the drag force, summations are required over same phase particles. Once this force is determined, it must be equal in magnitude to the force on the surrounding fluid. Thus resulting in a net force acting upon the fluid particles. When applying an SPH summation for each fluid particle over the surrounding solid particles, care must be taken in order to ensure the forces match. A similar treatment for the boundary inconsistency may be applied here (Equation (B.7)). This way, the drag force on each solid particle is translated as a drag force on each fluid particle. Identifying the centre of mass of the solid particle and the susequent translational and angular velocity determines the motion of the solid. The PF method governs the evolution of the solid-liquid interface. After

movement of the solid particle has been completed, the variables are mapped back onto the PF mesh. The motion of the liquid particles near the solid-liquid interface require careful attention ensuring heat conduction and material transport are adequately modelled.

Bibliography

[AB65]   PW Anderson and EI Blount. Symmetry Considerations on Martensitic Trans-
           formations: "Ferroelectric" Metals? *Physical Review Letters*, 14(7):217–219,
           1965.

[AY81]   JD Axe and Y Yamada. Cubic-tetragonal elastic phase transformations in solids.
           Physical Review B, 24(5):2567–2569, 1981.

[Ban05]   B Banerjee. The mechanical threshold stress model for various tempers of AISI
           4340 steel. *International journal of solids and structures*, pages 1–44, 2005.

[BCB03]   VE Badalassi, HD Ceniceros, and S Banerjee. Computation of multiphase sys-
           tems with phase field models. *Journal of Computational Physics*, 190(2):371–
           397, September 2003.

[BDS⁺99]   C Beckermann, HJ Diepers, I Steinbach, A Karma, and X Tong. Modeling Melt
           Convection in Phase-Field Simulations of Solidification. *Journal of Computa-
           tional Physics*, 154(2):468–496, September 1999.

[Ben92]   DJ Benson. Computational methods in Lagrangian and Eulerian hydrocodes.
           Computer Methods in Applied Mechanics and Engineering, 99(2-3):235–394,
           September 1992.

[Ber10]   V Berti. Hysteresis and phase transitions for 1D and 3D models in shape memory
           alloys. *Journal of Mathematical Physics*, 51:062901–1, 2010.

[Bes14]   D Bestion. The difficult challenge of a two-phase CFD modelling for all flow regimes. *Nuclear Engineering and Design*, 279:116–125, November 2014.

[BFP07]   Y Busegnies, J François, and G Paulus. Unidimensional SPH simulations of reactive shock tubes in an astrophysical perspective. *Shock Waves*, 16(4-5):359–389, March 2007.

[Bha78]   RN Bhatt. Structural transition in A-15 compounds: Possible Landau theory descriptions. *Physical Review B*, 17(7), 1978.

[Bha92]   HKDH Bhadeshia. *Bainite in steels*. Cambridge, 1992.

[Bha01]   HKDH Bhadeshia. *Worked examples in the Geometry of Crystals Second edition*. Institute of Materials, London, 2001.

[BK84]   GR Barsch and JA Krumhansl. Twin boundaries in ferroelastic media without interface dislocations. *Physical Review Letters*, 53(11):1069–1072, 1984.

[CH58]   JW Cahn and JE Hilliard. Free energy of a nonuniform system. I. Interfacial free energy. *J. Chem. Phys.*, 28:258–266, 1958.

[CH59]   JW Cahn and JE Hilliard. Free Energy of a Nonuniform System. III. Nucleation in a Two-Component Incompressible Fluid. *The Journal of Chemical Physics*, 31(3):688–699, 1959.

[CH71]   JW Cahn and JE Hilliard. Spinodal decomposition: A reprise. *Acta Metallurgica*, 19(2), 1971.

[Chr58]   JW Christian. Accommodation strains in martensite formation, and the use of a dilatation parameter. *Acta Metallurgica*, 6:377–379, 1958.

[CKO+07]   Y Cui, T Koyama, I Ohnuma, K Oikawa, R Kainuma, and K Ishida. Simulation of hexagonalorthorhombic phase transformation in polycrystals. *Acta Materialia*, 55(1):233–241, January 2007.

[CYY01]   PR Cha, DH Yeon, and JK Yoon. A phase field model for isothermal solidifica-
           tion. *Acta Materialia*, 49:3295–3307, 2001.

[Dev54]   AF Devonshire. Theory of ferroelectrics. *Advances in Physics*, 3(10):85–130,
           April 1954.

[EnR03]   P Español and M Revenga. Smoothed dissipative particle dynamics. *Physical
           Review E*, 67(2):026705, February 2003.

[Esh57]   JD Eshelby. The determination of the elastic field of an ellipsoidal inclusion,
           and related problems. *Proc. R. Soc. London Sect. A*, 241:376, 1957.

[Fal82]   F Falk. Landau theory and martensitic phase transitions. *Le Journal de Physique
           Colloques*, 43, 1982.

[Gin55]   VL Ginzburg. On the Theory oI Superconductivity . *Il Nuovo Cimento*, II(5),
           1955.

[GLAR15]   S Goel, X Luo, A Agrawal, and RL Reuben. Diamond machining of silicon: A
           review of advances in molecular dynamics simulation. *International Journal of
           Machine Tools and Manufacture*, 88:131–164, January 2015.

[GR86]   G Ghosh and V Raghavan. The Dimensions of Isothermally Formed Martensitic
           Plates in an FeNiMn Alloy. *Materials Science and Engineering*, 79:223–231,
           1986.

[Gus85]   P Gustafson. A Thermodynamic Evaluation of the Fe–C System. *Scand. J.
           Metall.*, 1985.

[HAC74]   CW Hirt, AA Amsden, and JL Cook. An arbitrary Lagrangian-Eulerian comput-
           ing method for all flow speeds. *Journal of Computational Physics*, 14:227–253,
           1974.

[HB06]   RWK Honeycombe and HKDH Bhadeshia. *Steels: Microstructure and
           Properties-Third Edition*. Heinemann, Butterworth, 2006.

[HBTQ04]   DM Heyes, J Baxter, U Tüzün, and RS Qin. Discrete-element method simulations: from micro to macro scales. *Philosophical transactions. Series A, Mathematical, Physical, and Engineering Sciences*, 362(1822):1853–65, September 2004.

[HK89]   L Hernquist and N Katz. TREESPH-A unification of SPH with the hierarchical tree method. *The Astrophysical Journal Supplement Series*, 70:419–446, 1989.

[ICL08]   AV Idesman, JY Cho, and VI Levitas. Finite element modeling of dynamics of martensitic phase transitions. *Applied Physics Letters*, 93(4):043102, 2008.

[JAK01]   YM Jin, A Artemev, and AG Khachaturyan. Three-dimensional phase field model of low-symmetry martensitic transformation in polycrystal: simulation of zeta 2 martensite in AuCd alloys. *Acta Materialia*, 49:2309–2320, 2001.

[JSB96]   GR Johnson, RA Stryk, and SR Beissel. SPH for high velocity impact computations. *Computer Methods in Applied Mechanics and Engineering*, 139(1-4):347–373, December 1996.

[KKS98]   S Kim, W Kim, and T Suzuki. Interfacial compositions of solid and liquid in a phase-field model with finite interface thickness for isothermal solidification in binary alloys. *Physical Review E*, 58(3):3316–3323, September 1998.

[KO03]   T Koyama and H Onodera. Phase-field simulation of microstructure changes in Ni 2 MnGa ferromagnetic alloy under external stress and magnetic fields. *Materials Transactions*, 44(12):2503–2508, 2003.

[Kob93]   R Kobayashi. Modeling and numerical simulations of dendritic crystal growth. *Physica D: Nonlinear Phenomena*, 63:410–423, 1993.

[KP04]   JM Kim and RJ Phillips. Dissipative particle dynamics simulation of flow around spheres and cylinders at finite Reynolds numbers. *Chemical Engineering Science*, 59(20):4155–4168, October 2004.

[KR98]   A Karma and WJ Rappel. Quantitative phase-field modeling of dendritic growth in two and three dimensions. *Physical Review E*, 57(4):4323–4349, April 1998.

[KS79]   MJ Kelly and WM Stobbs. A simple order parameter for reversible martensitic transformations? *Scripta Metallurgica*, 13(c):919–921, 1979.

[Kun07]   S Kundu. *Transformation strain and crystallographic texture in steels*. PhD thesis, University of Cambridge London, 2007.

[LAgA04]   I Loginova, J Å gren, and G Amberg. On the formation of Widmanstätten ferrite in binary FeC phase-field approach. *Acta Materialia*, 52(13):4055–4063, August 2004.

[LG04]   GR Liu and YT Gu. Boundary meshfree methods based on the boundary point interpolation methods. *Engineering Analysis with Boundary Elements*, 28(5):475–487, May 2004.

[LJZ95]   WK Liu, S Jun, and YF Zhang. Reproducing kernel particle methods. *International Journal for Numerical Methods in Fluids*, 20:1081–1106, 1995.

[LL03]   GR Liu and MB Liu. *Smoothed particle hydrodynamics: a meshfree particle method*. 2003.

[LNW02]   KM Liew, TY Ng, and YC Wu. Meshfree method for large deformation analysisa reproducing kernel particle approach. *Engineering Structures*, 24(5):543–551, May 2002.

[LPL03]   V Levitas, D Preston, and DW Lee. Three-dimensional Landau theory for multivariant stress-induced martensitic phase transformations. III. Alternative potentials, critical nuclei, kink solutions, and dislocation theory. *Physical Review B*, 68(13):134201, October 2003.

[LS06]   H López and L Sigalotti. Oscillation of viscous drops with smoothed particle hydrodynamics. *Physical Review E*, 73(5):051201, May 2006.

[Luc77]   LB Lucy. A numerical approach to the testing of the fission hypothesis. *The Astronomical Journal*, 82(12):1013–1024, 1977.

[LVCT14]   EQ Li, IU Vakarelski, DYC Chan, and ST Thoroddsen. Stabilization of thin liquid films by repulsive van der Waals force. *Langmuir: The ACS Journal of Surfaces and Colloids*, 30(18):5162–9, May 2014.

[MBW08]   N Moelans, B Blanpain, and P Wollants. An introduction to phase-field modeling of microstructure evolution. *Calphad*, 32(2):268–294, June 2008.

[MDPPTK13] N Mai-Duy, D Pan, N Phan-Thien, and BC Khoo. Dissipative particle dynamics modeling of low Reynolds number incompressible flows. *Journal of Rheology*, 57(2):585, 2013.

[MG83]   JJ Monaghan and RA Gingold. Shock simulation by the particle method SPH. *Journal of Computational Physics*, 389:374–389, 1983.

[Mil60]   DG Miller. Thermodynamics of Irreversible Processes. The Experimental Verification of the Onsager Reciprocal Relations. *Chemical Reviews*, 60:15–37, 1960.

[MMSV06]   M Militzer, M Mecozzi, J Sietsma, and S Vanderzwaag. Three-dimensional phase field modelling of the austenite-to-ferrite transformation. *Acta Materialia*, 54(15):3961–3972, September 2006.

[Mon92]   J Monaghan. Smoothed Particle Hydrodynamics. *Annual Review of Astronomy and Astrophysics*, 30(1):543–574, January 1992.

[Mon94]   JJ Monaghan. Simulating free surface flows with SPH.pdf. *Journal of computational physics*, 110:399–406, 1994.

[Mon05]   JJ Monaghan. Smoothed particle hydrodynamics. *Reports on Progress in Physics*, 68(8):1703–1759, August 2005.

[MRH06]   QP Meng, YH Rong, and TY Hsu. Effect of internal stress on autocatalytic nucleation of martensitic transformation. *Metallurgical and Materials Transactions A*, 37(5):1405–1411, 2006.

[MZE13] M Mamivand, MA Zaeem, and H El Kadiri. A review on phase field modeling of martensitic phase transformation. *Computational Materials Science*, 77:304–311, September 2013.

[NC11] B Nestler and A Choudhury. Phase-field modeling of multi-component systems. *Current Opinion in Solid State and Materials Science*, 15(3):93–105, June 2011.

[NP00] S Nugent and H Posch. Liquid drops and surface tension with smoothed particle applied mechanics. *Physical review. E, Statistical physics, plasmas, fluids, and related interdisciplinary topics*, 62(4 Pt A):4968–75, October 2000.

[NZ02] LC Nitsche and W Zhang. Atomistic SPH and a link between diffusion and interfacial tension. *AIChE Journal*, 48(2):201–211, February 2002.

[OKS01] M Ode, SG Kim, and T Suzuki. Recent advances in the phase-field model for solidification. *ISIJ International*, 41(10):1076–1082, 2001.

[Ons31] L Onsager. Reciprocal relations in irreversible processes. I. *Physical Review*, 37:405–426, 1931.

[PF90] O Penrose and PC Fife. Thermodynamically consistent models of phase-field type for the kinetics of phase transitions.pdf. *Physica D: Nonlinear Phenomena*, 43:44–62, 1990.

[PH97] HA Posch and WG Hoover. Simulation of two-dimensional Kolmogorov flow with smooth particle applied mechanics. *Physica A*, 240:286–296, 1997.

[PHK95] HA Posch, WG Hoover, and O Kum. Steady-state shear flows via nonequilibrium molecular dynamics and smooth-particle applied mechanics. *Physical Review E*, 52(2):1711–1720, 1995.

[Pla45] M Planck. *Treatise on thermodynamics*. Dover Publications, New York, 1945.

[PPTMDK13] D Pan, N Phan-Thien, N Mai-Duy, and BC Khoo. Numerical investigations on the compressibility of a DPD fluid. *Journal of Computational Physics*, 242:196–210, 2013.

[QB09]   RS Qin and HKDH Bhadeshia. Phase-field model study of the effect of inter-
           face anisotropy on the crystal morphological evolution of cubic metals. *Acta
           Materialia*, 57(7):2210–2216, April 2009.

[Qin06]   R Qin. Mesoscopic interparticle potentials in the lattice Boltzmann equation
           for multiphase fluids. *Physical Review E*, 73(6):066703, June 2006.

[QW03a]   RS Qin and ER Wallach. A method to compute the migration rate of planar
           solidliquid interfaces in binary alloys. *Journal of Crystal Growth*, 253(1-4):549–
           556, June 2003.

[QW03b]   RS Qin and ER Wallach. A phase-field model coupled with a thermodynamic
           database. *Acta Materialia*, 51(20):6199–6210, December 2003.

[RB92a]   GI Rees and H Bhadeshia. Bainite transformation kinetics Part 1 Modified
           model. *Materials Science and Technology*, 8(November):985–993, 1992.

[RB92b]   GI Rees and H Bhadeshia. Bainite transformation kinetics Part 2 Non-uniform
           distribution of carbon. *Materials Science and Technology*, 8(November):994–
           1003, 1992.

[RL96]   PW Randles and LD Libersky. Smoothed particle hydrodynamics: some recent
           improvements and applications. *Computer Methods in Applied Mechanics and
           Engineering*, 139:375–408, 1996.

[RLS+01]   K Rasmussen, T Lookman, A Saxena, A Bishop, R Albers, and S Shenoy.
           Three-Dimensional Elastic Compatibility and Varieties of Twins in Martensites.
           Physical Review Letters, 87(5):055704, July 2001.

[RRL14]   M Robinson, M Ramaioli, and S Luding. Fluidparticle flow simulations using
           two-way-coupled mesoscale SPHDEM and validation. *International Journal of
           Multiphase Flow*, 59:121–134, February 2014.

[SHA95]   JW Swegle, DL Hicks, and SW Attaway. Smoothed particle hydrodynamics
           stability analysis. *Journal of Computational Physics*, 134:123–134, 1995.

[SHL⁺03]   DJ Seol, SY Hu, YL Li, LQ Chen, and KH Oh. Cubic to tetragonal martensitic transformation in a thin film elastically constrained by a substrate. *Metals and Materials International*, 9(3):221–226, June 2003.

[SMKU13]   R Schmitt, R Müller, C Kuhn, and HM Urbassek. A phase field approach for multivariant martensitic transformations of stable and metastable phases. *Archive of Applied Mechanics*, 83(6):849–859, January 2013.

[Sod78]   GA Sod. A survey of several finite difference methods for systems of nonlinear hyperbolic conservation laws. *Journal of Computational Physics*, 27(1):1–31, 1978.

[SSF12]   O Shchyglo, U Salman, and A Finel. Martensitic phase transformations in NiTi-based shape memory alloys: The Landau theory. *Acta Materialia*, 60(19):6784–6792, November 2012.

[SU09]   L Sandoval and HM Urbassek. Transformation pathways in the solid-solid phase transitions of iron nanowires. *Applied Physics Letters*, 95(19):191909, 2009.

[SWL97]   A Saxena, Y Wu, and T Lookman. Hierarchical pattern formation in elastic materials. *Physica A*, 239:18–34, 1997.

[TA98]   R Tönhardt and G Amberg. Phase-field simulation of dendritic growth in a shear flow. *Journal of Crystal Growth*, 194(3-4):406–425, December 1998.

[TA00]   R Tönhardt and G Amberg. Dendritic growth of randomly oriented nuclei in a shear flow. *Journal of Crystal Growth*, 213:161–187, 2000.

[VSMS08]   A Valizadeh, M Shafieefar, JJ Monaghan, and SAA Salehi Neyshaboori. Modeling Two-Phase Flows Using SPH Method. *Journal of Applied Sciences*, 8:3817–3826, 2008.

[WB95]   JA Warren and WJ Boettinger. Prediction of dendritic growth and microsegregation patterns in a binary alloy using the phase-field method. *Acta Metallurgica et Materialia*, 43(2):689–703, 1995.

[WBM92] AA Wheeler, WJ Boettinger, and GB McFadden. Phase-field model for isothermal phase transitions in binary alloys. *Physical Review A*, 45(10):7424–7440, 1992.

[WBM93] AA Wheeler, WJ Boettinger, and GB McFadden. Phase-field model of solute trapping during solidification. *Physical review E*, 47(3), 1993.

[Wei74] R Weinstock. *Calculus of Variations: with Applications to Physics and Engineering.* Dover Publications, New York, 1974.

[Whe99] AA Wheeler. CahnHoffman ξ-Vector and its relation to diffuse interface models of phase transitions. pages 1245–1280, 1999.

[WK97] Y Wang and AG Khachaturyan. Three-dimensional field model and computer modeling of martensitic transformations. *Acta Materialia*, 45(2):759–773, February 1997.

[WSW$^+$93] SL Wang, RF Sekerka, AA Wheeler, BT Murray, SR Coriell, RJ Braun, and GB McFadden. Thermodynamically-consistent phase-field models for solidification. *Physica D: Nonlinear Phenomena*, 69(1-2):189–200, November 1993.

[WWGB09] HP Wang, CT Wu, Y Guo, and ME Botkin. A coupled meshfree/finite element method for automotive crashworthiness simulations. *International Journal of Impact Engineering*, 36(10-11):1210–1222, October 2009.

[WZYF00] J Wang, S Zwaag, Z Yang, and HS Fang. Aspect ratio of bainite in steels. *Materials Letters*, 45:228–234, 2000.

[YL03] WA Yong and LS Luo. Nonexistence of H theorems for the athermal lattice Boltzmann models with polynomial equilibria. *Physical Review E*, 67(5):051105, May 2003.

[YLP14] X Yang, M Liu, and S Peng. Smoothed particle hydrodynamics modeling of viscous liquid drop without tensile instability. *Computers & Fluids*, (January), January 2014.

[YTT08]   A Yamanaka, T Takaki, and Y Tomita. Elastoplastic phase-field simulation of self- and plastic accommodations in martensitic transformation. *Materials Science and Engineering: A*, 491(1-2):378–384, September 2008.

[YTT10]   A Yamanaka, T Takaki, and Y Tomita. Elastoplastic phase-field simulation of martensitic transformation with plastic deformation in polycrystal. *International Journal of Mechanical Sciences*, 52(2):245–250, February 2010.

[ZTVO05]   B Zhao, BG Thomas, SP Vanka, and RJ O'malley. Transient fluid flow and superheat transport in continuous casting of steel slabs. *Metallurgical and Materials Transactions B*, 36:801–823, 2005.

Appendix A

Phase-field free energy

Consider an isothermal system at constant pressure. The state variable to be considered is the Gibbs free energy of the system. The Gibbs free energy density of a heterogeneous system per unit volume is assumed to be able to be expressed in terms of the phase-field variable , composition, temperature, and their gradients, $g(\phi, c, T, \nabla\phi, \nabla c, \nabla T, ...)$, where c is composition and T is temperature. The Gibbs free energy density is written as a Taylor series about the Gibbs free energy of its homogeneous description (all gradients equal to zero) [CH71, CH59],

$$
\begin{aligned}
g(\phi, c, T, ...) \quad &= g_0 + \frac{\partial g_0}{\partial \nabla\phi}(\nabla\phi) + \frac{1}{2}\frac{\partial^2 g_0}{\partial(\nabla\phi)^2}(\nabla\phi)^2 + \frac{1}{6}\frac{\partial^3 g_0}{\partial(\nabla\phi)^3}(\nabla\phi)^3... \\
&+ \frac{\partial g_0}{\partial \nabla c}(\nabla c) + \frac{1}{2}\frac{\partial^2 g_0}{\partial(\nabla c)^2}(\nabla c)^2 + \frac{1}{6}\frac{\partial^3 g_0}{\partial(\nabla c)^3}(\nabla c)^3... \\
&+ \frac{\partial g_0}{\partial \nabla T}(\nabla T) + \frac{1}{2}\frac{\partial^2 g_0}{\partial(\nabla T)^2}(\nabla T)^2 + \frac{1}{6}\frac{\partial^3 g_0}{\partial(\nabla T)^3}(\nabla T)^3... \\
&+ \frac{\partial g_0}{\partial \nabla^2\phi}(\nabla^2\phi) + \frac{1}{2}\frac{\partial^2 g_0}{\partial(\nabla^2\phi)^2}(\nabla^2\phi)^2 + \frac{1}{6}\frac{\partial^3 g_0}{\partial(\nabla^2\phi)^3}(\nabla^2\phi)^3... \\
&+ \frac{\partial g_0}{\partial \nabla^2 c}(\nabla^2 c) + \frac{1}{2}\frac{\partial^2 g_0}{\partial(\nabla^2 c)^2}(\nabla^2 c)^2 + \frac{1}{6}\frac{\partial^3 g_0}{\partial(\nabla^2 c)^3}(\nabla^2 c)^3... \\
&+ \frac{\partial g_0}{\partial \nabla^2 T}(\nabla^2 T) + \frac{1}{2}\frac{\partial^2 g_0}{\partial(\nabla^2 T)^2}(\nabla^2 T)^2 + \frac{1}{6}\frac{\partial^3 g_0}{\partial(\nabla^2 T)^3}(\nabla^2 T)^3... \\
&\quad\vdots
\end{aligned}
\tag{A.1}
$$

where the subscript denotes $g_0 = g(\phi, c, T, \nabla\phi = 0, \nabla c = 0, \nabla T = 0, \nabla^2\phi = 0, ...)$ and g_0 is the Gibbs free energy density of the homogeneous phase. Thus we are considering a small

displacement of the gradient terms from homogeneity. The free energy must be symmetric about the origin, thus the coefficients of odd power or order terms are zero. In addition to this, truncating to omit third and higher order terms we obtain a simplified description of the free energy density,

$$
\begin{aligned}
g(\phi, c, T, ...) \quad &= g_0 + \frac{1}{2}\frac{\partial^2 g_0}{\partial(\nabla\phi)^2}(\nabla\phi)^2 + \frac{1}{2}\frac{\partial^2 g_0}{\partial(\nabla c)^2}(\nabla c)^2 + \frac{1}{2}\frac{\partial^2 g_0}{\partial(\nabla T)^2}(\nabla T)^2 \\
&+ \frac{\partial g_0}{\partial\nabla^2\phi}\nabla^2\phi + \frac{\partial g_0}{\partial\nabla^2 c}\nabla^2 c + \frac{\partial g_0}{\partial\nabla^2 T}\nabla^2 T.
\end{aligned}
\tag{A.2}
$$

It is obvious that the variables involving the squared terms are symmetric about the origin. An even derivative of a function with respect to spatial coordinates is also an even function. To see this, consider a function $f(\mathbf{r})$. We have,

$$
\nabla f = \frac{\partial f}{\partial\mathbf{r}} = \frac{\partial f}{\partial(-\mathbf{r})}\frac{\partial(-\mathbf{r})}{\partial\mathbf{r}} = -\frac{\partial f}{\partial(-\mathbf{r})},
\tag{A.3}
$$

$$
\frac{\partial^2 f}{\partial(-\mathbf{r})^2} = \frac{\partial\frac{\partial f}{\partial(-\mathbf{r})}}{\partial(-\mathbf{r})} = -\frac{\partial\frac{\partial f}{\partial(-\mathbf{r})}}{\partial\mathbf{r}} = \frac{\partial\frac{\partial f}{\partial\mathbf{r}}}{\partial(\mathbf{r})} = \frac{\partial^2 f}{\partial\mathbf{r}^2} = \nabla^2 f,
\tag{A.4}
$$

so that ∇f is not an even function of $\mathbf{r}$ but $\nabla^2 f$ is. For the second step in Equation (A.4) we used the result from Equation (A.3) and then applied the product rule for differentiation for the step after that.

For simplicity let us write $g(\phi, c, T, \nabla\phi, ...)$ as $g(\alpha_i, \nabla\alpha_i, \nabla^2\alpha_i) : i \in \{1, 2, 3\}$ so that $\alpha_1 = \phi$, $\alpha_2 = c$ and $\alpha_3 = T$. The total free energy over the volume V of the system is then,

$$
\begin{aligned}
\int_V g(\alpha_i, \nabla\alpha_i, \nabla^2\alpha_i)dr \quad &= \int_V \Big[g_0(\alpha_i) + \sum_{i=1}^{3}\Big(\frac{1}{2}\frac{\partial g_0}{\partial(\nabla\alpha_i)^2}(\nabla\alpha_i)^2 \\
&+ \frac{\partial g_0}{\partial\nabla^2\alpha_i}\nabla^2\alpha_i\Big)\Big]dr.
\end{aligned}
\tag{A.5}
$$

Using integration by parts on the term involving the Laplace operator,

$$
\begin{aligned}
\int_V \frac{\partial g_0}{\partial \nabla^2 \alpha_i} \nabla^2 \alpha_i dr \quad &= \frac{\partial g_0}{\partial \nabla^2 \alpha_i} \int_V \nabla^2 \alpha_i dr - \int_V \left(\frac{\partial}{\partial r} \frac{\partial g_0}{\partial \nabla^2 \alpha_i} \int_V \nabla^2 \alpha_i dr \right) dr \\
&= \frac{\partial g_0}{\partial \nabla^2 \alpha_i} \int_V \nabla^2 \alpha_i \hat{\mathbf{r}} d\mathbf{r} - \int_V \left(\frac{\partial}{\partial r} \frac{\partial g_0}{\partial \nabla^2 \alpha_i} \int_V \nabla^2 \alpha_i \hat{\mathbf{r}} d\mathbf{r} \right) dr \\
&= \frac{\partial g_0}{\partial \nabla^2 \alpha_i} \left[\hat{\mathbf{r}} \cdot \nabla \alpha_i - \int_V \nabla \alpha_i \cdot \frac{d\hat{\mathbf{r}}}{d\mathbf{r}} d\mathbf{r} \right] \\
&\quad - \int_V \frac{\partial}{\partial r} \frac{\partial g_0}{\partial \nabla^2 \alpha_i} \left[\hat{\mathbf{r}} \nabla \alpha_i - \int_V \nabla \alpha_i \frac{d\hat{\mathbf{r}}}{d\mathbf{r}} d\mathbf{r} \right] dr \\
&= \frac{\partial g_0}{\partial \nabla^2 \alpha_i} \hat{\mathbf{r}} \cdot \nabla \alpha_i - \int_V \frac{\partial}{\partial r} \frac{\partial g_0}{\partial \nabla^2 \alpha_i} \hat{\mathbf{r}} \cdot \nabla \alpha_i dr \\
&= \frac{\partial g_0}{\partial \nabla^2 \alpha_i} \hat{\mathbf{r}} \cdot \nabla \alpha_i - \int_V \frac{\partial}{\partial \alpha_i} \frac{\partial g_0}{\partial \nabla^2 \alpha_i} \frac{\partial \alpha_i}{\partial \mathbf{r}} \frac{d\mathbf{r}}{dr} \hat{\mathbf{r}} \cdot \nabla \alpha_i dr \\
&= \frac{\partial g_0}{\partial \nabla^2 \alpha_i} \hat{\mathbf{r}} \cdot \nabla \alpha_i - \int_V \frac{\partial}{\partial \alpha_i} \frac{\partial g_0}{\partial \nabla^2 \alpha_i} (\nabla \alpha_i)^2 \hat{\mathbf{r}}^2 dr \\
&= \frac{\partial g_0}{\partial \nabla^2 \alpha_i} \hat{\mathbf{r}} \cdot \nabla \alpha_i - \int_V \frac{\partial}{\partial \alpha_i} \frac{\partial g_0}{\partial \nabla^2 \alpha_i} (\nabla \alpha_i)^2 dr \qquad \text{(A.6)}
\end{aligned}
$$

where $\hat{\mathbf{r}}$ is the unit vector in the coordinate direction. The first term is of odd order and the same reasoning as before results in the coefficient of the first term being zero. The following have been used in the derivation of Equation (A.6):

$$
\mathbf{r} = \hat{\mathbf{r}} r \implies \frac{d\mathbf{r}}{dr} = \hat{\mathbf{r}} \implies d\mathbf{r} = \hat{\mathbf{r}} dr \qquad \text{(A.7)}
$$

$$
0 = \frac{d(1)}{d\mathbf{r}} = \frac{d(\hat{\mathbf{r}}) \cdot \hat{\mathbf{r}}}{d\mathbf{r}} = 2 \frac{d\hat{\mathbf{r}}}{d\mathbf{r}} \cdot \hat{\mathbf{r}} \implies \frac{d\hat{\mathbf{r}}}{d\mathbf{r}} = 0. \qquad \text{(A.8)}
$$

Equation (A.5) then becomes,

$$
\begin{aligned}
\int_V g(\alpha_i, \nabla \alpha_i, \nabla^2 \alpha_i) dr \quad &= \int_V \left[g_0 + \sum_{i=1}^{3} \left(\frac{1}{2} \frac{\partial g_0}{\partial (\nabla \alpha_i)^2} (\nabla \alpha_i)^2 - \frac{\partial}{\partial \alpha_i} \frac{\partial g_0}{\partial \nabla^2 \alpha_i} (\nabla \alpha_i)^2 \right) \right] dr \\
&= \int_V \left[g_0 + \sum_{i=1}^{3} \left(\frac{1}{2} \left[\frac{\partial g_0}{\partial (\nabla \alpha_i)^2} - 2 \frac{\partial}{\partial \alpha_i} \frac{\partial g_0}{\partial \nabla^2 \alpha_i} \right] (\nabla \alpha_i)^2 \right) \right] dr \\
&= \int_V \left[g_0 + \sum_{i=1}^{3} \frac{1}{2} \epsilon_i (\nabla \alpha_i)^2 \right] dr \qquad \text{(A.9)}
\end{aligned}
$$

where $\epsilon_i = \frac{\partial g_0}{\partial (\nabla \alpha_i)^2} - 2 \frac{\partial}{\partial \alpha_i} \frac{\partial g_0}{\partial \nabla^2 \alpha_i}$.

Appendix B

SPH equations

Density

The continuity equation is given as,

$$\dot{\rho}_i = -\rho_i(\nabla \cdot \mathbf{v})_i. \tag{B.1}$$

Using Equations (4.3) and (4.4) we have,

$$
\begin{aligned}
\dot{\rho}_i \quad &= -\rho_i(\nabla \cdot \mathbf{v})_i + 0 \\
&= -\rho_i(\nabla \cdot \mathbf{v})_i + \rho_i \mathbf{v}_i \cdot \nabla 1 \\
&= -\rho_i \sum_j \frac{m_j}{\rho_j} \mathbf{v}_j \cdot \nabla_i W_{ij} + \rho_i \mathbf{v}_i \cdot \sum_j \frac{m_j}{\rho_j} \nabla_i W_{ij} \\
&= \rho_i \sum_j \frac{m_j}{\rho_j} \mathbf{v}_{ij} \cdot \nabla_i W_{ij}, \tag{B.2}
\end{aligned}
$$

where we used the fact that $\nabla 1 = \mathbf{0}$. One may argue that instead of $\nabla 1$, we may use an SPH approximation to $\nabla C = 0$ with any constant C. This is true and the continuity equation still holds, however, the evolution towards equilibrium will have a steeper gradient if $C > 1$ or the sensitivity of the density to velocity changes will be different.

————————

If we use the identity,

$$-\rho_i(\nabla \cdot \mathbf{v})_i = \mathbf{v}_i \cdot (\nabla \rho)_i - (\nabla \cdot (\rho \mathbf{v}))_i, \tag{B.3}$$

and apply Equations (4.3) and (4.4), we obtain another approximation to the continuity equation,

$$
\begin{aligned}
\dot{\rho}_i \quad &= -\rho_i(\nabla \cdot \mathbf{v})_i = \mathbf{v}_i \cdot (\nabla \rho)_i - (\nabla \cdot (\rho \mathbf{v}))_i \\
&= \mathbf{v}_i \sum_j m_j \nabla_i W_{ij} - \sum_j m_j \mathbf{v}_j \cdot \nabla_i W_{ij} \\
&= \sum_j m_j \mathbf{v}_i \cdot \nabla_i W_{ij} - \sum_j m_j \mathbf{v}_j \cdot \nabla_i W_{ij} \\
&= \sum_j m_j \mathbf{v}_{ij} \cdot \nabla_i W_{ij}, \tag{B.4}
\end{aligned}
$$

where $\mathbf{v}_{ij} = \mathbf{v}_i - \mathbf{v}_j$.

The summation density (Equation (4.5)) is obtained from Equation (4.2) as,

$$\rho = \sum_j m_j W_{ij}. \tag{B.5}$$

Using Equation (4.2), the SPH approximation of 1 can be found as,

$$1 = \sum_j \frac{m_j}{\rho_j} W_{ij}. \tag{B.6}$$

Multiplying this approximation to 1 by ρ_i and subtracting it from Equation (4.5)) gives an approximation to ρ_i suitable for the treatment of free surfaces and phase boundaries [RL96],

$$\rho = \frac{\sum_j m_j W_{ij}}{\sum_j \frac{m_j}{\rho_j} W_{ij}}. \tag{B.7}$$

Pressure gradient

In order to find the gradient of the pressure field, rather than take the derivative of Equation (4.24), we proceed with the approximation to the integral representation of the field variable,

$$
\begin{aligned}
\nabla P(\mathbf{r}) \quad &= \int_\Omega \nabla P(\mathbf{r}')W(\mathbf{r}-\mathbf{r}',h)d\mathbf{r} \\
&= \int_\Omega \left[\rho(\mathbf{r})\nabla\frac{P(\mathbf{r}')}{\rho(\mathbf{r}')} + \frac{P(\mathbf{r})}{\rho(\mathbf{r})}\nabla\rho(\mathbf{r}') \right]W\,d\mathbf{r}' \\
&= \int_\Omega \rho(\mathbf{r})\nabla\frac{P(\mathbf{r}')}{\rho(\mathbf{r}')}W\,d\mathbf{r}' + \int_\Omega \frac{P(\mathbf{r})}{\rho(\mathbf{r})}\nabla\rho(\mathbf{r}')W\,d\mathbf{r}' \\
&= \rho(\mathbf{r})\int_\Omega \left[\nabla\left(\frac{P(\mathbf{r}')}{\rho(\mathbf{r}')}W \right) - \frac{P(\mathbf{r}')}{\rho(\mathbf{r}')}\nabla W \right]d\mathbf{r}' \\
&\quad + \frac{P(\mathbf{r})}{\rho(\mathbf{r})}\int_\Omega \left[\nabla\left(\rho(\mathbf{r}')W \right) - \rho(\mathbf{r}')\nabla W \right]d\mathbf{r}' \\
&= -\rho(\mathbf{r})\int_\Omega \frac{P(\mathbf{r}')}{\rho(\mathbf{r}')}\nabla W\,d\mathbf{r}' - \frac{P(\mathbf{r})}{\rho(\mathbf{r})}\int_\Omega \rho(\mathbf{r}')\nabla W\,d\mathbf{r}' \\
&= -\rho(\mathbf{r})\int_\Omega \left[\frac{P(\mathbf{r}')}{\rho(\mathbf{r}')} + \frac{P(\mathbf{r})}{\rho(\mathbf{r})^2}\rho(\mathbf{r}') \right]\nabla W\,d\mathbf{r}' \\
&= -\rho(\mathbf{r})\sum_j \left[\frac{m_j P_j}{\rho_j^2} + \frac{P(\mathbf{r})m_j}{\rho(\mathbf{r})^2} \right]\nabla W_{ij} \\
\implies \nabla P(\mathbf{r}_i) \quad &= -\rho_i\sum_j m_j \left[\frac{P_j}{\rho_j^2} + \frac{P_i}{\rho_i^2} \right]\nabla W_{ij}.
\end{aligned}
\tag{B.8}
$$

The following product rule applications were used in the above derivation,

$$
\nabla P(\mathbf{r}') \quad = \rho(\mathbf{r})\nabla\frac{P(\mathbf{r}')}{\rho(\mathbf{r}')} + \frac{P(\mathbf{r})}{\rho(\mathbf{r})}\nabla\rho(\mathbf{r}')
\tag{B.9}
$$

$$
\nabla\frac{P(\mathbf{r}')}{\rho(\mathbf{r}')} \quad = \nabla\left[\frac{P(\mathbf{r}')}{\rho(\mathbf{r}')}W \right] - \frac{P(\mathbf{r}')}{\rho(\mathbf{r}')}\nabla W
\tag{B.10}
$$

$$
W\nabla\rho(\mathbf{r}') \quad = \nabla\left[\rho(\mathbf{r}')W \right] - \rho(\mathbf{r}')\nabla W,
\tag{B.11}
$$

and from line 4 to line 5 of Equation (B.8) we use the divergence theorem from a volume Ω to a surface S,

$$
\int_\Omega \nabla(FW)dV = \int_S FW\cdot\hat{n}dS
\tag{B.12}
$$

along with the fact that the kernel is zero everywhere but within the support domain making the right-hand side of Equation (B.12) equal to zero.

Direct SPH approximation of the pressure tensor results in,

$$(\nabla P)_i = \sum_j \frac{m_j}{\rho_j} P_j \nabla_i W_{ij}. \tag{B.13}$$

Adding zero to this results in,

$$
\begin{aligned}
(\nabla P)_i &= \sum_j \frac{m_j}{\rho_j} P_j \nabla_i W_{ij} + P_i \nabla 1 \\
&= \sum_j \frac{m_j}{\rho_j} P_j \nabla_i W_{ij} + P_i \sum_j \frac{m_j}{\rho_j} \nabla_i W_{ij} \\
&= \sum_j m_j \frac{P_i + P_j}{\rho_j} \nabla_i W_{ij}.
\end{aligned} \tag{B.14}
$$

For the Navier-Stokes equations, the pressure P can be directly replaced with the more general stress tensor $\mathbf{P} = \mathbf{I}P + \sigma$ where $\mathbf{I}$ is the unit tensor and σ is the viscous stress tensor.

Divergence of the velocity

The particle density is defined as,

$$d_i = \sum_j W_{ij}, \tag{B.15}$$

and for the mass density in terms of the particle density,

$$\rho_i = m_i d_i. \tag{B.16}$$

The derivative of ρ can be calculated using Equation (B.15) as,

$$\dot{\rho} = m_i \dot{d}_i = m_i \sum_j \frac{\partial W_{ij}}{\partial t} = m_i \sum_j \frac{\partial W_{ij}}{\partial \mathbf{r}_{ij}} \frac{\partial \mathbf{r}_{ij}}{\partial t} = m_i \sum_j \mathbf{v}_{ij} \nabla W_{ij}. \tag{B.17}$$

where $\dot{\rho} \equiv \frac{\partial \rho}{\partial t}$. Comparing Equations (B.17) and (4.10) gives an expression for the divergence of the velocity,

$$
\begin{aligned}
-\rho_i (\nabla \cdot \mathbf{v})_i \quad &= m_i \sum_j \nabla \mathbf{v}_{ij} W_{ij}, \\
\implies (\nabla \cdot \mathbf{v})_i \quad &= -\frac{m_i}{\rho_i} \sum_j \nabla \mathbf{v}_{ij} W_{ij} = -\frac{1}{d_i} \sum_j \mathbf{v}_{ij} \nabla W_{ij}.
\end{aligned}
\tag{B.18}
$$

Appendix C

SPH unity condition

The constants of the Lucy function, the cubic spline kernel and the hyperbolic-shaped kernel denoted respectively as α_L, α_{cs} and α_{hs} are scaling constants determined by the unity condition,

$$\int_\Omega W \, dV = 1 \qquad (C.1)$$

where the integral is taken over a volume Ω in three dimensions.

For Lucy's kernel we have,

$$\int_\Omega W \, dV = \alpha_L \int_\Omega [1 - 6\frac{r^2}{h^2} + 8\frac{r^3}{h^3} - 3\frac{r^4}{h^4}] dV. \qquad (C.2)$$

In one dimension (two sides of 0 where $|r| \le h$ on the real line),

$$\int_\Omega W \, dV = \alpha_L \int_{-h}^{h} [1 - 6\frac{r^2}{h^2} + 8\frac{r^3}{h^3} - 3\frac{r^4}{h^4}] dr = \alpha_L \frac{4}{5} h \qquad (C.3)$$

giving $\alpha_L = 5/(4h)$. In two dimensions,

$$\int_\Omega W \, dV = \alpha_L \int_0^h \int_0^{2\pi} [1 - 6\frac{r^2}{h^2} + 8\frac{r^3}{h^3} - 3\frac{r^4}{h^4}] r \, d\theta dr = \alpha_L \frac{\pi}{5} h^2 \qquad (C.4)$$

giving $\alpha_L = 5/(\pi h^2)$. In three dimensions,

$$\int_\Omega W\,dV = \alpha_L \int_0^h \int_0^\pi \int_0^{2\pi} [1 - 6\frac{r^2}{h^2} + 8\frac{r^3}{h^3} - 3\frac{r^4}{h^4}]r^2 \sin\phi\,d\phi\,d\theta\,dr = \alpha_L \frac{16\pi}{105} h^3 \qquad \text{(C.5)}$$

giving $\alpha_L = 105/(16\pi h^3)$.

For the cubic spline kernel we have,

$$\int_\Omega W\,dV = \alpha_{cs} [\int_{\mathbf{r}\in\Omega:r\leq h} [(2 - \frac{r}{h})^3 - 4(1 - \frac{r}{h})^3]dV + \int_{\mathbf{r}\in\Omega:h\leq r\leq 2h} (2 - \frac{r}{h})^3 dV]. \qquad \text{(C.6)}$$

In one dimension,

$$\int_\Omega W\,dV = \alpha_{cs} [2\int_0^h [(2 - \frac{r}{h})^3 - 4(1 - \frac{r}{h})^3]dr + 2\int_h^{2h} (2 - \frac{r}{h})^3 dr] = 6h\alpha_{cs} \qquad \text{(C.7)}$$

giving $\alpha_{cs} = 1/(6h)$. In two dimensions,

$$\int_\Omega W\,dV = \alpha_{cs} [\int_0^h \int_0^{2\pi} [(2 - \frac{r}{h})^3 - 4(1 - \frac{r}{h})^3]r\,d\theta\,dr + \int_h^{2h} \int_0^{2\pi} (2 - \frac{r}{h})^3 r\,d\theta\,dr] = \frac{14\pi}{5} h^2 \alpha_{cs} \quad \text{(C.8)}$$

giving $\alpha_{cs} = 5/(14\pi h^2)$. In three dimensions,

$$\begin{aligned}
\int_\Omega W\,dV \quad &= \alpha_{cs} [\int_0^h \int_0^{2\pi} \int_0^\pi [(2 - \frac{r}{h})^3 - 4(1 - \frac{r}{h})^3]r^2 \sin\phi\,d\phi\,d\theta\,dr \\
&+ \int_h^{2h} \int_0^{2\pi} \int_0^\pi (2 - \frac{r}{h})^3 r^2 \sin\phi\,d\phi\,d\theta\,dr] = 4\pi h^3 \alpha_{cs}
\end{aligned} \qquad \text{(C.9)}$$

giving $\alpha_{cs} = 1/(4\pi h^3)$.

For the hyperbolic spline kernel we have,

$$\int_\Omega W\,dV = \alpha_{hs} [\int_{\mathbf{r}\in\Omega:r\leq h} (\frac{r^3}{h^3} - 6\frac{r}{h} + 6)dV + \int_{\mathbf{r}\in\Omega:h\leq r\leq 2h} (2 - \frac{r}{h})^3 dV]. \qquad \text{(C.10)}$$

In one dimension,

$$\int_\Omega W dV = \alpha_{hs}[2\int_0^h (\frac{r^3}{h^3} - 6\frac{r}{h} + 6)dr + 2\int_h^{2h} (2 - \frac{r}{h})^3 dr] = 7h\alpha_{hs} \qquad (C.11)$$

giving $\alpha_{hs} = 1/(7h)$. In two dimensions,

$$\int_\Omega W dV = \alpha_{hs}[\int_0^h \int_0^{2\pi} (\frac{r^3}{h^3} - 6\frac{r}{h} + 6)rd\theta dr + \int_h^{2h} \int_0^{2\pi} (2 - \frac{r}{h})^3 rd\theta dr] = 3\pi\alpha_{hs}h^2 \qquad (C.12)$$

giving $\alpha_{hs} = 1/(3\pi h^2)$. In three dimensions,

$$\int_\Omega W dV = \alpha_{hs}[\int_0^h \int_0^{2\pi} \int_0^\pi (\frac{r^3}{h^3} - 6\frac{r}{h} + 6)r^2 \sin\phi d\phi d\theta dr$$
$$+ \int_h^{2h} \int_0^{2\pi} \int_0^\pi (2 - \frac{r}{h})^3 r^2 \sin\phi d\phi d\theta dr] = \frac{62}{15}\pi h^3 \alpha_{hs} \qquad (C.13)$$

giving $\alpha_{hs} = 15/(62\pi h^3)$.

Appendix D

A phenomenological phase-field model for martensite formation

A phenomenological phase-field model for martensite formation

T. T. Arif[a,*], R. S. Qin[a,*]

[a]*Department of Materials, Imperial College London, Exhibition Road, London SW7 2AZ, UK*

Abstract

A phase-field model for the computation of microstructure and texture evolution of plate formation under applied stress during martensite transformation (MT) has been developed. The model is based on the phenomenological MT theory and the symmetric analysis of cubic crystals, and has reproduced realistic martensite grain morphology and accurate crystallographic orientation. The free energy has been constructed according to the established strain energy expression and cubic symmetry. The theoretical framework is consistent with classical phase-field schemes. The model is applicable to MT in a wide range of real materials and processing, e.g. variant selection and texture formation in stress-affected MT in polycrystalline materials. The comparison between the present and existing phase-field models is addressed.

Keywords: `Phase-field`, martensite, solid-state phase transformation, phenomenological theory

1. Introduction

Martensite transformation (MT) is a displacive phase transition where atom mobility is too slow to fulfil the structural transformation. MT can take place in various materials at a wide range of temperatures, e.g. from 1200 K in ZrO_2

---
*Corresponding author
Email addresses: `t.arif11@imperial.ac.uk` (T. T. Arif), `r.qin@imperial.ac.uk` (R. S. Qin)

to 30 K in Ar-40N$_2$ [1]. Modelling and simulation of MTs have attracted significant attention for many years. More recently, the formation of martensite during deformation at high strain rates has been studied using modelling techniques [2], modelling the behaviour of stress assisted MT [3] and TRIP steels using a phenomenological mean-field approach [4, 5, 6, 7], reproducing the elastic and plastic deformations of metallic materials [8], the coupling of MT and plasticity [9] etc... Martensite in steels is considered one of the strongest but most brittle of phases. Its excellent strength is favourable in the design of a new generation of advanced high strength steels, but its poor toughness is detrimental to the mechanical properties. The aim of the phase-field study of MT is to provide information on microstructure evolution in MT so as to improve the understanding of its microstructure-property relationship.

Symmetry preservation is one of the most important restrictions in the description of crystalline materials. According to Landau-Ginzburg-Devonshire theory, the free energy density of a bulk phase with cubic crystallographic symmetry (g_b) can be represented by the following generic format [10]

$$
\begin{aligned}
g_b \quad &= a_1(\phi_x^2 + \phi_y^2 + \phi_z^2) + a_{11}(\phi_x^2 + \phi_y^2 + \phi_z^2)^2 \\
&+ a_{12}(\phi_x^2\phi_y^2 + \phi_y^2\phi_z^2 + \phi_z^2\phi_x^2) + a_{123}\phi_x^2\phi_y^2\phi_z^2 \\
&+ a_{111}(\phi_x^2 + \phi_y^2 + \phi_z^2)^3 + a_{112}[\phi_x^4(\phi_y^2 + \phi_z^2) \\
&+ \phi_y^4(\phi_z^2 + \phi_x^2) + \phi_z^4(\phi_x^2 + \phi_y^2)],
\end{aligned}
\tag{1}
$$

where a_i, a_{ij} and a_{ijk} are coefficients. ϕ_x, ϕ_y and ϕ_z are the order parameters along the x, y and z directions in a Cartesian coordinate system, respectively. For ferroelectric materials such as BaTiO$_3$, ϕ_α represents the polarization along the α direction [10]. Eq. (1) preserves cubic symmetry because applying all the O_h(or $m\bar{3}m$) symmetry operations to the right hand size of Eq. (1) give the same value of g_b. Within the interface of a cubic crystal, the free energy density

(g_i) is suggested to take the following expression [11]

$$
\begin{aligned}
g_i \quad &= b_{11}(\phi_{x,x}^2 + \phi_{y,y}^2 + \phi_{z,z}^2) \\
&+ b_{12}(\phi_{x,x}\phi_{y,y} + \phi_{y,y}\phi_{z,z} + \phi_{z,z}\phi_{x,x}) \\
&+ b_{44}(\phi_{x,y}^2 + \phi_{x,z}^2 + \phi_{y,z}^2 + \phi_{y,x}^2 + \phi_{z,x}^2 + \phi_{z,y}^2),
\end{aligned}
\tag{2}
$$

where b_{11}, b_{12} and b_{44} are coefficients. The suffixes preceded by a comma denote partial differentiation: $\phi_{x,y} = \partial\phi_x/\partial y$. Eq. (2) also preserves cubic symmetry. It is worth emphasising that Eq. (2) represents the general free energy density within the interface rather than just the conventional interface energy. The expressions for the anisotropic interface energies, such as those proposed by Karma and Rappel [12], Haxhimali et al. [13] and Qin and Bhadeshia [14] for cubic crystals, and Böttger et al. [15] and Qin and Bhadeshia [16] for hexagonal close-packed crystals, all preserve the symmetrical properties of crystals. The bulk free energy formula utilized in the computational thermodynamics, such as the Redlich-Kister equation [17], contains no vectors but scalars (e.g. temperature, composition and pressure) and therefore does not violate the symmetric properties of the crystal.

The phase-field models based on Eq. (1) have been developed by Ma et al. [18] and Li and Chen [19] for the simulation of the precipitations in zirconium and Al-Cu alloys, respectively. Li et al. have developed a phase-field model based on Eq. (1) and a simplified format of Eq. (2) and applied this to the domain morphological evolution of PbZrTiO$_3$ ferroelectric grains [20]. The phase-field model of Zhang et al. is based on a simplified format of both Eq. (1) and Eq. (2) and has simulated the BiFeO$_3$ thin film [21]. Hu et al. has coupled a much simplified format of Eq. (1) and Eq. (2) with an elastic field and used the phase-field scheme for the investigation of the phase transition in Pu-Ga alloys [22]. The phase-field model proposed by Moelans et al. was based on the first three terms in Eq. (1) and described grain growth in anisotropic polycrystalline materials [23]. Chen reviewed the application of the extended format of Eq. (1) in phase-field models to the simulation of ferroelectric materials where the crystal symmetry may be affected by the applied electric field

and stress field [24].

There are a number of phase-field models published already in the simulation of MT and displacive transformation. Wang and Khachaturyan have reviewed a number of phase-field models based on Eq. (1) for the simulation of MT [25]. Levitas et al. have developed a phase-field model and studied the stress-induced MT [26, 27, 28], where a Landau type potential has been derived to include the large rotation and elastic strains [26]. The interface profile and velocity are found to be a function of temperature and the stress tensor in their solutions [27]. Recently, Yeddu et al. developed a new phase-field model for MT in steel which used the 1st, 2nd and 5th terms in Eq. (1) to represent chemical free energy while also considering the anisotropic elastic property in the MT. Their simulation reproduced the autocatalysis and morphological mirror image formation [29, 30].

The PF model of Kundin et al. [31] caters for plastic accommodation and relaxation effects during MT. A dislocation density field is introduced and evolved seperately and used to simulate the evolution of butterfly-type martensite. Within this work, the energy of interaction between two martensitic plates is also considered. An order parameter for each martensitic variant is evolved as a set of governing equations. The total free energy of the system is the sum of the elastic energy and the chemical energy which does not explicitly depend on composition. Instead, the dependence is on the equilibrium transformation temperature T_0 and an anisotropic function which in turn has a dependence on plate width. Once the elastic component of the driving force and the equilibrium shape of a martensitic plate is estimated, the evolution of the order paramters may commence.

The works of Levitas et al. [32] and the references within on the application of the PF method to martensite transformation is notable for their advancement in the area. The model is demonstrated on the material NiAl with elastic strains considered small to simplify equations which involves plastic relaxation in the surrounding bulk during plate formation. While the method also incorporates plastic deformation, it is also applied to deduce the interface energy and

4

width between two martensitic variants. This not only enables their model to have the ability to represent martensite - martensite transformations, but also multiple twinning. A single radial order parameter, Υ, is applied to represent all matrix to martensite transformations along with n additional angular order parameters, $v_i : i = 1, 2, .., n$, where n is the number of twinning systems. The parameter Υ alone is not sufficient in determining the variant and orientation of the resulting martensitic variant, but is simply used to determine the region that is a martensitic phase. The variant and orientation are determined by the additional order parameters v_i. The authors state that it is not possible to represent two simple shears between two martensitic variants with a single order parameter using the classic application of the PF method to martensitic transformation. The elastic field is solved completely for the sample in order to deduce the values of the order parameters. The selling point of the model is that the number of order parameters are sufficient in describing the myriad of variant-variant twinning.

Yeddu et al. [33] have developed a PF model in order to determine the effect of martensite embryo size on the subsequent transformation in steel. The chemical energy density is expressed as a function of three martensitic domains (η_1, η_2, η_3) as [34]

$$G_v^{chem}(\eta_1, \eta_2, \eta3) \quad = \frac{1}{V_m} \left[\frac{1}{2} A(\eta_1^2 + \eta_2^2 + \eta_3^2) \right. \tag{3}$$

$$\left. - \frac{1}{3} B(\eta_1^3 + \eta_2^3 + \eta_3^3) + \frac{1}{4} C(\eta_1^2 + \eta_2^2 + \eta_3^2)^2 \right], \tag{4}$$

where V_m is the molar volume and A, B and C are coefficients. Their model incorporates elastic and plastic strain effects by evolving the strain field throughout the system.

MT with self accommodation and plastic accommodation has been incorporated by Yamanaka et al. [35] with three order parameters while considering the form of the chemical free energy the same as that in Eqn. (4) with the constants: $A = 0.15$, $B = 3A + 12$ and $C = 2A + 12$. The point at which plastic deformation takes place depends upon the comparison between the shear and

5

yield stresses of the material. The plastic strain as well as the order parameters are then evolved according to the time dependent Ginzburg-Landau equation. The plastic accommodation is shown to reduce the elastic strain energy considerably. The resulting crystallographic information is reported to agree with phenomenological crystallography theories.

MT is driven by the chemical free energy difference between martensite and austenite. The morphology of martensite, however, is affected significantly by the strain energy. Based on this consideration, many existing phase-field models have been coupled with the precise calculation of the strain and stress fields. These models possess many advantages over the phenomenological and coarse-scaled approximations, e.g. being able to reveal the fundamental interactions between mechanical properties and phase transitions in materials. The disadvantages include the excess demand in computational resources, difficulties in the addition of more sophisticated factors and poor agreement with experimental observations. For example, the computational microstructure for MT is hardly comparable to what is seen experimentally. The composition-dependent orientation of the habit plane in MT has not been reproduced so far. The variant selection under external stress, the texture formation and evolution in martensitic steels and many other important phenomena have not been covered by many existing phase-field models.

The aim of the present work was to develop a phenomenological phase-field model to study the MT in steels. The phenomenological description of MT is easier to understand and has the ability to be scaled up to simulate more sophisticate phenomena in the thermo-mechanical processing of steels. The phase-field model developed in the present work is consistent with the MT theory in steels, and is able to produce realistic microstructure and correct texture information. Particularly, the model is capable of producing the differences in the microstructure and texture of MT in various steels and under versatile processing conditions. For example, it is easy to predict the differences between MT in 304 stainless steels, Fe-3Mn-2Si-0.4C wt% steel and Fe-31Ni-0.23C wt%, and to predict the variant selection and texture formation in stress-affected MT

6

in polycrystalline steels.

As has been shown, there are many PF models on MT with a microscopic theme, however, to the authors' knowledge there are no PF models of the type used in this paper applied to MT.

2. The theoretical consideration and the phase-field model

The MT in steels transforms face-centered-cubic (fcc) austenite (denoted as γ) to body-centered-cubic (bcc) martensite (denoted as α') crystals. From a thermodynamic point of view, the transition can be described by a double-well potential with the asymmetry representing the thermodynamic driving force and the height of the peak representing the kinetic barrier [36]. The free energy density of a steel containing austenite, martensite and the interface can be represented by the following [37, 38]

$$
\begin{aligned}
g \quad &= \frac{1}{2}\epsilon^2|\nabla\phi|^2 + \frac{1}{4\omega}\phi^2(1-\phi)^2 \\
&+ h(\phi)g_{\alpha'} + [1-h(\phi)]g_{\gamma},
\end{aligned}
\tag{5}
$$

where ϕ is the phase-field order parameter with $\phi = 0$ representing the austenite, $\phi = 1$ the martensite and $0 < \phi < 1$ the interface between austenite and martensite. ϵ is the gradient energy coefficient and ω is a coefficient associated with the kinetic barrier. $h(\phi) = \phi^3(6\phi^2 - 15\phi + 10)$ can be understood to be the local volume fraction of martensite. It has $h(\phi) = 1$ when $\phi = 1$ and $h(\phi) = 0$ when $\phi = 0$. The bulk free energies of the martensite and austenite phases are denoted by $g_{\alpha'}$ and g_{γ}, respectively. The parameters ϵ and ω are determined by $\epsilon^2 = 3\lambda\sigma/1.1$ and $\omega = \lambda/(26.4\sigma)$ [38], where σ is the interface energy and λ is the half-thickness of the interface. The interface energy is small due to the coherency of the austenite-martensite interface. There are a limited number of interface orientations meeting the lattice coherence.

The governing equation for the phase-field order parameter can be derived

7

from the second law of thermodynamics and has the following format [37, 38]

$$\frac{\partial \phi}{\partial t} = M_\phi [\epsilon^2 \nabla^2 \phi + \frac{1}{2\omega} \phi (1 - \phi)(1 - 2\phi) \\ - 30\phi^2 (1 - \phi)^2 (g_{\alpha'} - g_\gamma)], \tag{6}$$

where $M_\phi > 0$ is called the phase-field mobility which is related to the growth rate of a martensite grain. The third term within the square bracket on the right hand side of Eq. (6) is non-zero only within the interface (where $\phi \neq 0$ and $\phi \neq 1$) and at non-equilibrium (where $g_{\alpha'\gamma} = g_{\alpha'} - g_\gamma \neq 0$). Therefore $g_{\alpha'\gamma}$ is the driving force for MT and the equilibrium corresponds to $g_{\alpha'} = g_\gamma$. This is different from reconstructive transformation where the equilibrium corresponds to the common tangent of the chemical potential rather than the equivalence of the free energy. The reason is that MT does not involve the partitioning of chemical compositions. The following consideration on $g_{\alpha'\gamma}$ is for the martensite-austenite interface only where the aim is to solve Eq. (6). This has

$$g_{\alpha'\gamma} = g_{\alpha'\gamma}^{chem} + g_{\alpha'\gamma}^{strain}, \tag{7}$$

where $g_{\alpha'\gamma}^{chem} = g_{\alpha'}^{chem} - g_\gamma^{chem}$ is the chemical free energy difference and $g_{\alpha'\gamma}^{strain} = g_{\alpha'}^{strain} - g_\gamma^{strain}$ is the strain energy difference between the martensite and the austenite phases. $g_{\alpha'\gamma}^{chem}$ should be negative in MT according to the second law of thermodynamics. If there is no external stress acting on the steel, then $g_{\alpha'\gamma}^{strain} = 0$ before the MT. Equation (7) does not include the interface energy since this has been included and represented by the first term within the square bracket on the right hand side of Eq. (6). $g_{\alpha'\gamma}^{chem}$ is associated with the chemical constitution, temperature and pressure of the steel. This value can be obtained directly from a commercial computational thermodynamic database such as Thermo_Calc or MTDATA.

A martensite grain is in an oblate ellipsoidal shape. The shear and dilatation components of the strain energy contribution to the free energy can be assumed independent. The overall free energy change due to the transformation is dependent on the dilatation normal to the habit plane, δ, and the shear lying on

8

the habit plane, s. Eshelby analysed the strain energy of an ellipsoidal inclusion in a homogeneous matrix [39]. The strain energy contribution to the free energy is given by Christian as [40],

$$
\begin{aligned}
g_{\alpha'\gamma}^{strain1} \quad &= \frac{\mu}{1-\sigma_p}[\frac{2}{9}(1+\sigma_p)\Delta^2 \\
&+ \frac{\pi c}{4a}\delta^2 + \frac{\pi}{3}(1+\sigma_p)\frac{c}{a}\Delta\delta] \quad (8)\\
g_{\alpha'\gamma}^{strain2} \quad &= \frac{\mu}{1-\sigma_p}[\frac{\pi}{8}(2-\sigma_p)\frac{c}{a}s^2]. \quad (9)
\end{aligned}
$$

where μ, σ_p, Δ, δ and s are the shear modulus, Poisson's ratio, lattice dilatation, uniaxial expansion and the amount of shear, respectively. The $g_{\alpha'\gamma}^{strain1}$ and $g_{\alpha'\gamma}^{strain2}$ are the non-shear and shear components of the contribution respectively. The constants a and c are the dimensions of the oblate ellipsoid. $g_{\alpha'\gamma}$ achieves minimum when $\Delta = 0$ and c/a goes to minimum. In other words, the overall change from a bcc cell to a martensite cell involves no uniaxial dilatation. The minimum value of c/a affects the nucleation of martensite. The non-shear contribution can be written as,

$$
g_{\alpha'\gamma}^{strain1} = \frac{\mu}{1-\sigma_p}\frac{\pi c}{4a}\delta^2, \quad (10)
$$

and the shear component as,

$$
g_{\alpha'\gamma}^{strain2} = \frac{\mu}{1-\sigma_p}[\frac{\pi}{8}(2-\sigma_p)\frac{c}{a}s^2]. \quad (11)
$$

185 The total energy due to strain is then,

$$
\begin{aligned}
g_{\alpha'\gamma}^{strain} \quad &= g_{\alpha'\gamma}^{strain1} + g_{\alpha'\gamma}^{strain2} \\
&= \frac{\mu\pi c}{4a(1-\sigma_p)}[\delta^2 + \frac{2-\sigma_p}{2}s^2]. \quad (12)
\end{aligned}
$$

Equation (12) shows the strain contribution to the free energy from a dilatation of δ normal to the habit plane and a shear s lying on the habit plane. Writing this equation in terms of small increments we obtain,

$$
\Delta g_{\alpha'\gamma}^{strain} = \frac{\mu\pi c}{4a(1-\sigma_p)}[(\Delta\delta)^2 + \frac{2-\sigma_p}{2}(\Delta s)^2], \quad (13)
$$

where Δ refers to a small change and not the uniaxial dilatation parameter. In the PF method, a small change in location of the interface is translated as a

9

small change in the PF variable ϕ at that location, $\phi_{,x} = \frac{\partial \phi}{\partial x}$, $\phi_{,y} = \frac{\partial \phi}{\partial y}$ and $\phi_{,z} = \frac{\partial \phi}{\partial z}$ in the x, y and z directions respectively. In the coordinate system of the martensite plate, δ corresponds to the z axis. The shear direction lies on the habit plane normal to the z axis and so the shear vector can be divided into two orthogonal vectors as $\vec{s} = \vec{s}_x + \vec{s}_y$. In small displacement form, these correspond to,

$$\Delta\vec{\delta} = \phi_{,z}\mathbf{k}, \quad \Delta\vec{s} = \Delta\vec{s}_x + \Delta\vec{s}_y = \phi_{,x}\mathbf{i} + \phi_{,y}\mathbf{j}, \tag{14}$$

where $\mathbf{i}$, $\mathbf{j}$ and $\mathbf{k}$ are unit vectors in the x, y and z directions respectively. Considering the fact that the total strain contribution from Eq. (12) in the untransformed matrix is zero, Eq. (12) can now be written in terms of the PF variable as,

$$g_{\alpha'\gamma}^{strain} = \frac{\mu\pi c}{4a(1-\sigma_p)}[\phi_{,z}^2 + \frac{2-\sigma_p}{2}(\phi_{,x}^2 + \phi_{,y}^2)]. \tag{15}$$

In addition to the strain energy, the chemical free energy contribution, K, to the total free energy must also be considered. This depends on the local composition and temperature. In other words, the affinity of the material to transform at a given location is gauged by the contribution through the strain energy and the chemical free energy due to the local composition and temperature. The chemical free energy is related to the rate of change of the PF variable as,

$$g_{\alpha'\gamma}^{chem} = k_1\phi_{,x}^2 + k_2\phi_{,y}^2 + k_3\phi_{,z}^2. \tag{16}$$

The total free energy contribution is therefore,

$$
\begin{aligned}
g_{\alpha'\gamma} \quad &= g_{\alpha'\gamma}^{strain} + g_{\alpha'\gamma}^{chem} \\
&= \frac{\mu\pi c}{4a(1-\sigma_p)}[(\frac{2-\sigma_p}{2} + \frac{4a(1-\sigma_p)}{\mu\pi c}k_1)\phi_{,x}^2 \\
&+ (\frac{2-\sigma_p}{2} + \frac{4a(1-\sigma_p)}{\mu\pi c}k_2)\phi_{,y}^2 \\
&+ (1 + \frac{4a(1-\sigma_p)}{\mu\pi c}k_3)\phi_{,z}^2].
\end{aligned}
\tag{17}
$$

The parameter μ is the shear modulus and is temperature dependent. The aspect ratio c/a is dependent on composition as well as temperature. Equation

10

(17) is written as the total free energy per unit volume. Let $f_1 = f_2 = (2-\sigma_p)/2$ and $d = 4a(1 - \sigma_p)/\mu\pi\sigma_p$ to give,

$$\begin{aligned} g_{\alpha'\gamma} \quad &= \frac{1}{d}[(f_1 + dk_1)\phi_{,x}^2 + (f_2 + dk_2)\phi_{,y}^2 \\ &\quad +(1 + dk_3)\phi_{,z}^2]. \end{aligned} \tag{18}$$

Since $f_1, f_2 < 1$ and the chemical driving force is a negative value during MT, the direction normal to the habit plane will naturally be less favoured in an energy reduction sense.
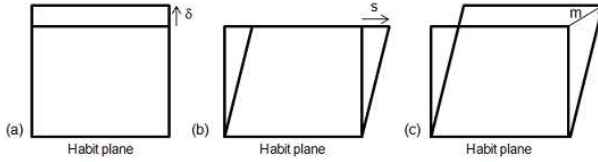
Figure 1: Two-dimensional schematic diagrams showing the three invariant-plane strains of: (a) the uniaxial dilatational strain δ; (b) the simple shear strain s; (c) the general displacement strain m.
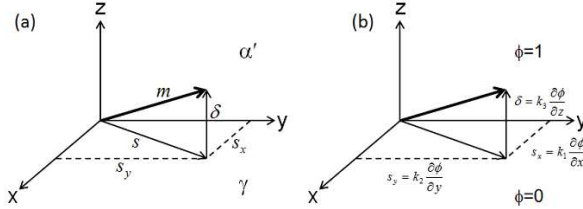
Figure 2: Schematic diagrams showing: (a) martensite transformation with shear, expansion and deformation; (b) phase-field interpretation of the martensite transformation.

Equation (16) does not imply that the chemical free energy is orientation dependent. This is achieved through specifying the k_i. In this work, all the k_i are equal inferring an isotropic chemical free energy. The main meaning behind Eq. (16) is that the driving force due to the chemical free energy change at a location is related to the amount of phase present or more precisely, the amount of phase to be formed in a given evolution time. Given that $k_1 = k_2 = k_3 = K$, Eq. (18)

11

does not preserve cubic symmetry unless $f_1 = f_2 = 1$. The latter is clearly not possible in MT in steels because $s \gg \delta$. However, the coordinate system defined in Fig. 2 is with respect to the martensite grain while the symmetry analysis should be based on the austenite grain within which MT is taking place. Figure 3 demonstrates the relation between the austenite coordinate system $(x_\gamma y_\gamma z_\gamma)$ and the martensite coordinate system (xyz). Following the notation set by Bowles and MacKenzie [41], the deformation vector $\vec{m} = \vec{s} + \vec{\delta}$ in the austenite coordinate system can be obtained by multiplying its representation in the martensite coordinate system by a coordinate transformation matrix. This operation is represented as

$$[\gamma,\, m] = (\gamma\, \mathbf{J}\, \alpha')[\alpha'\, m], \tag{19}$$

where the square bracket represents a 3×1 column matrix and $(\gamma\, \mathbf{J}\, \alpha')$ is a 3×3 matrix. The real value of $(\gamma\, \mathbf{J}\, \alpha')$ is available for many steels and can be calculated according to crystallographic theory for any steel. For example, the $(\gamma\, \mathbf{J}\, \alpha')$ matrix for the 304 stainless steels has been described in reference [42].
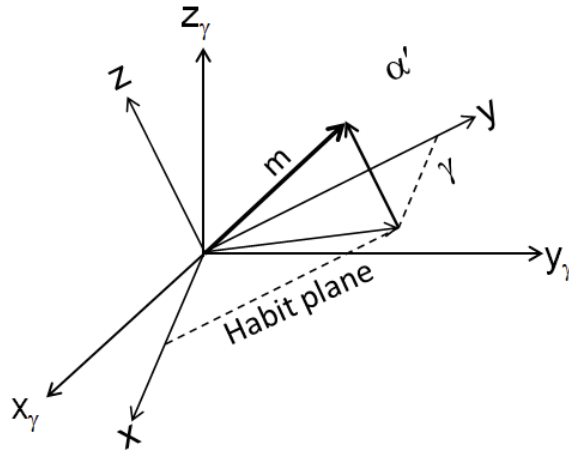
Figure 3: A schematic diagram of the coordinate systems in the austenite and the martensite grains.

Applying the cubic symmetry operations O_h (or $m\bar{3}m$) to $(\gamma\, \mathbf{J}\, \alpha')$ will pro-

duce another 23 formats of $(\gamma \mathbf{J} \alpha')$. These 24 formats represent the 24 grain variants in MT. Let H_{ij} represent the elements of the $(\gamma \mathbf{J} \alpha')$ matrix. Substituting this into Eq. (19) gives the total free energy in the austenite coordinate system as

$$
\begin{aligned}
g_{\alpha'\gamma} &= \frac{1}{d} \sum_{i=1}^{3} (f_i + dk)(H_{i1}\phi_{,x} + H_{i2}\phi_{,y} \\
&\quad + H_{i3}\phi_{,z})^2,
\end{aligned}
\tag{20}
$$

where $f_3 = 1$. The selection of f_i will be discussed later in this work. Eq. (20) preserves cubic symmetry. Substituting Eq. (20) into Eq. (6) leads to the governing equation for the phase-field order parameter in MT as,

$$
\begin{aligned}
\frac{\partial \phi}{\partial t} &= M_\phi[\epsilon^2 \nabla^2 \phi + \frac{1}{2\omega}\phi(1-\phi)(1-2\phi) - 30\phi^2(1-\phi)^2 \\
&\quad \times \frac{1}{d}\sum_{i=1}^{3}(f_i + dk)(H_{i1}\phi_{,x} + H_{i2}\phi_{,y} + H_{i3}\phi_{,z})^2].
\end{aligned}
\tag{21}
$$

3. Numerical calculation and discussion

To validate the proposed phase-field model, Eq. (21) is solved numerically using a 6-neighbour explicit finite difference method on a three dimensional uniform grid with the following parameters: $M_\phi = 100$, $\lambda = 14.3$ nm, $\sigma = 0.6$ J/m^2. The parameters ϵ and ω are obtained according to $\epsilon^2 = 3\lambda\sigma/1.1$ and $\omega = \lambda/(26.4\sigma)$. We have also chosen Poisson's ratio as $\sigma_p = 0.285$. All input parameters, except for the mobility M_ϕ, have been obtained from realistic expected values in martensite transformation in steels. Parameter selection has taken into account the following considerations:

M_ϕ - The phase-field mobility is proportional to the migration rate of the martensite-austenite interface in MT [36]. The latter has been proven to be very high and is comparable to the speed of sound in steel. However, a larger value of M_ϕ requires a smaller computing time step to retain the numerical stability. The value of M_ϕ in the majority of the phase-field simulations for diffusional phase-transitions is less than 50 [43], thus one can choose $M_\phi = 100$ to reflect the high speed martensite growth. It should be pointed out that the selection

13

of the value of M_ϕ does not affect these numerical results in any sense because no other mechanism is competing with the growth of the martensite grains in the present simulation.

$\lambda = 14.3$ nm has been used in a number of papers when the Eq. (5) approach is used for the free energy density [14, 36, 44, 12]. Following on those references, the grid size is defined as $\Delta x = 0.5\lambda$ so that the interface covers 4 grid points. The time step is defined according to the mathematical theory on the stability of the explicit finite difference method.

σ_p - Poisson's ratio is between $0.27 - 0.3$ for steels. The average value of 0.285 has been chosen.

σ - The interface energy between martensite and austenite is small due to coherence. The value used in the present work is chosen according to experimental data for the fcc-bcc interface energy of pure iron [45].

H_{ij} - The elements of the $(\gamma \, \mathbf{J} \, \alpha')$ coordinate transformation matrix are different for MT in different materials. Table 1 lists their values for several iron-alloys [1, 46]. The calculations in the present work utilized the value for Fe-30Ni-0.3C wt.% alloys. The approximate habit plane indices for this alloy is $\{3\,15\,10\}_\gamma$.

For a typical steel, the chemical free energy change is chosen as $K = 3.6 \times 10^9 \, J/m^3$. There is a range of choices for K over which growth is possible ($\sim 10^8 - 10^9$), i.e. Yamanaka et al. [35] have chosen to use a chemical driving force of $1.29 \times 10^8 \, J/m^3$ for an Fe-Ni alloy. We assume athermal growth without diffusion and so we use this value for the purpose of demonstration. Using the MTS shear modulus model for a 4340 steel [47],

$$\mu(T) = \mu_0 - \frac{D}{\exp(298/T) - 1},$$

for $\mu_0 = 85$, $D = 10$ and $T = 250°$C we obtain $\mu = 72 \times 10^9$ Pa. The term dK can now be calculated as

$$dK = \frac{4(1 - \sigma_p)}{\mu \pi \frac{c}{a}} K = \frac{-0.045518313}{\frac{c}{a}}. \tag{22}$$

14

Composition (wt.%)	Coordinate transformation matrix		
Fe-30Ni	$\begin{bmatrix} 0.579632 & 0.102883 & 0.5426071 \\ -0.552075 & 0.086760 & 0.5732948 \\ -0.014871 & 0.789220 & -0.133758 \end{bmatrix}$		
Fe-1.8C	$\begin{bmatrix} 0.575191 & 0.542067 & 0.097283 \\ -0.550660 & 0.568276 & 0.089338 \\ -0.008610 & -0.131800 & 0.785302 \end{bmatrix}$		
Fe-30Ni-0.3C	$\begin{bmatrix} 0.575371 & 0.542097 & 0.097510 \\ -0.550726 & 0.568476 & 0.089244 \\ -0.008855 & -0.131888 & 0.785465 \end{bmatrix}$		
Fe-8Cr-1C	$\begin{bmatrix} 0.584634 & 0.519305 & 0.119189 \\ -0.529661 & 0.583719 & 0.059597 \\ -0.046858 & -0.118861 & 0.813418 \end{bmatrix}$		
Fe-18Cr-8Ni	$\begin{bmatrix} 0.579356 & 0.542586 & 0.102537 \\ 0.014470 & 0.133650 & -0.788984 \\ -0.552000 & 0.572979 & 0.086936 \end{bmatrix}$		

Table 1: The coordinate transformation matrix of various iron-alloys [1, 46].
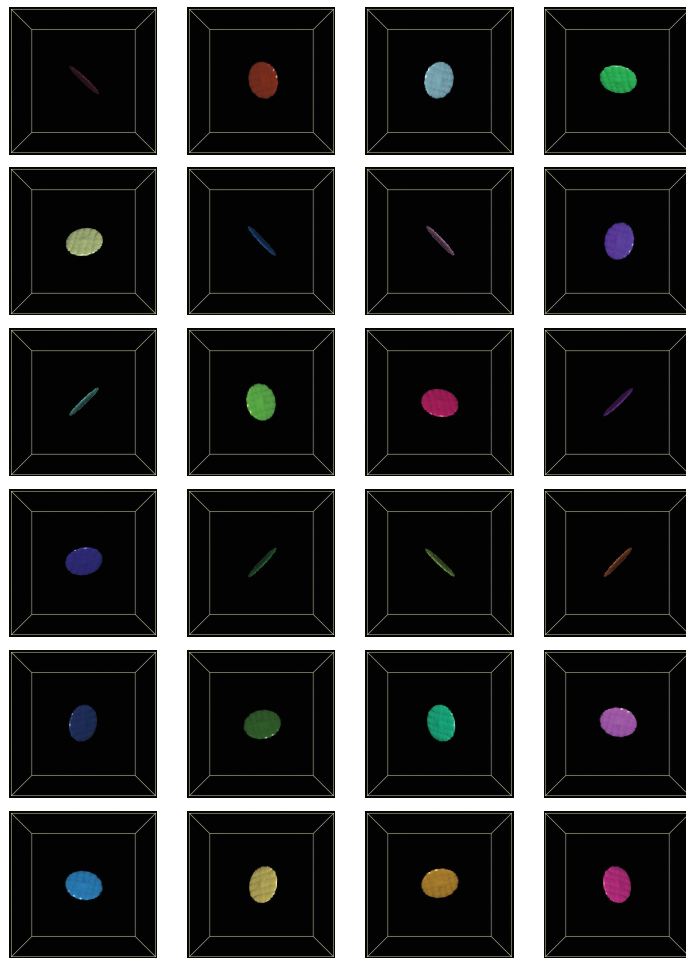
Figure 4: The 24 variants of the martensite grains at 10,000 time steps.

16

For favourable growth, Eq. (18) implies

$$dK < -1 \implies \frac{c}{a} < 0.045518313.$$

This gives an aspect ratio well within what is experimentally observed. In fact, the model must reproduce this same aspect ratio. In other words, writing Eq. (18) as three separate directions $\phi_{,x} = \phi^*$, $\phi_{,y} = \phi^*$ and $\phi_{,z} = \phi^*$, where ϕ^* is some constant value, in the separate systems respectively, we obtain the total energy contribution due to Equation (18) as,

$$(0.85 - dK)\phi^* \qquad \text{in system 1 and 2} \qquad (23)$$

$$(1 - dK)\phi^* \qquad \text{in system 3.} \qquad (24)$$

The resulting ratio will be $(1-dK)/(0.85-dK)$. This must be equal to c/a. The subsequent quadratic equation gives only a single solution $c/a = 0.045197387$ for $dK < -1$. This value is used in the subsequent simulations unless stated otherwise.

Figure 6 demonstrates the numerical results based on the earlier selected parameter values. The austenite-martensite boundary is defined as the center of diffuse interface, i.e. $\phi = 0.5$. The calculations were performed on a 100^3 grid and the time steps for growing the demonstrated martensite plates was $10,000$ steps. The initial condition was to put a spherical martensite seed at the center of the logistic frame with the phase-field order parameter configured for a single time step as

$$f(x) = \begin{cases} \phi(r, t = 0) = 1, & for \quad r \leq \Delta x \\ \phi(r, t = 0) = \frac{2}{1 + exp(r-1)}, & for \quad \Delta x < r < 4\Delta x \\ \phi(r, t = 0) = 0, & for \quad r \geq 4\Delta x \end{cases}.$$

It can be seen that the martensite grains have developed into oblate ellipsoidal shapes. There are 24 variants, and each grain has the grain orientation the same as that predicted by the crystallographic theory.

To simulate MT in polycrystalline steels, a sample coordinate system should be chosen, as demonstrated in Fig. 5. The matrix to convert a vector from

17

austenite to sample coordinates, $(s\,\mathbf{J}\,\gamma)$ can be calculated according to the orientation of the austenite grains. Eq. (19) in the sample coordinates is changed into the following format

$$[s;\,m] = (s\,\mathbf{J}\,\gamma)(\gamma\,\mathbf{J}\,\alpha')[\alpha';\,m]. \tag{25}$$

The expression for the strain energy in the sample coordinate system can be obtained directly from Eq. (25) and Eq. (20) using matrix algebra. The phase-field model presented in the present work can therefore be used to study MT in polycrystalline steels.
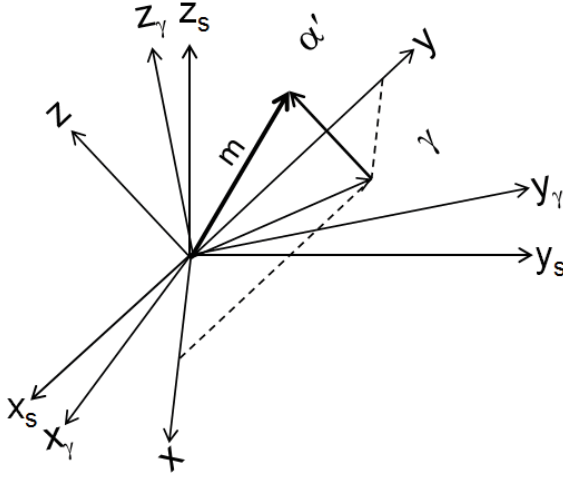
Figure 5: The schematic diagram of the martensite (xyz), austenite $(x_\gamma y_\gamma z_\gamma)$ and sample $(x_s y_s z_s)$ coordinate systems.

In steels, the nucleation of the martensite phase takes place at either the austenite grain boundary or around the inclusions/dislocations inside the austenite grain. Figure 6 demonstrates the numerical results of 50 martensite grains nucleated and then grown within the computational frame containing 200^3 lattice points and 2 austenite grains. The austenite grains have been grown from random locations and have met at the diagonal plane within the cube. Their orientations, in terms of Euler angles, are (0.298854, 0.811461, 0.646287) and

18

(0.292141, 0.408522, 0.477327). A global grain identity number (gg_id) is intro-
duced to represent the grain property. For example, the austenite grain bound-
ary is denoted by $gg\_id = 0$. The two austenite grains are denoted by $gg\_id = 1$
and $gg\_id = 2$. The martensite grains are denoted by $gg\_id = 3, 4, ...52$. Marten-
site nucleation is randomly selected in a position with $gg\_id = 0$. The growth
of martensite with $gg\_id = i > 2$ is only possible from the austenite grain and
only if at least one of the nearest lattice points possesses the same gg_id num-
ber. This ensures that the growth of one martensite grain will be unable to
grow when it meets another martensite grain or enter into another austenite
grain. A case where two martensite plates meet is given in Figure 7. The
justification for applying this procedure is that the governing equations used
here provide the strain energy representation for the transition of phase from
austenite to martensite. A strain energy representation for the transition of
phase from martensite to martensite is not yet implemented into the model and
is assumed unfavourable here for steels. The morphologies and orientations of
the martensite grains at t=2000, 7000, 10000, 13000, 16000 and 19000 are shown
in Figure 6. The figures are plotted using the in-house three-dimensional visu-
alization software - MatVisual. Since all the 24 variants have equal possibilities
to nucleate and grow, the steel after MT will not incur the preferred texture.

If an external stress is applied to the steel during MT, martensite grains with
different orientations will have different possibilities to nucleate and grow [42].
Combining the orientation-related nucleation theory with the present phase-
field model will make it possible to simulate the texture formation in stress-
induced MT in steels. Alternatively, suppose that the sample is subjected to an
externally applied stress field $\sigma_{\mathbf{ij}}$. The works of Patel and Cohen [48] show that
the energy term resulting from an applied stress can be added algebraically to
the chemical free energy of the transformation, and subsequently in this model,
to the strain energy. It is known that the interaction energy of a martensitic
plate with the applied stress field is composed of a component directed normal
to the plate (and so is a function of δ) and a component directed along the habit
plane (and so is a function of s) [46]. However, the algebraic representation

19
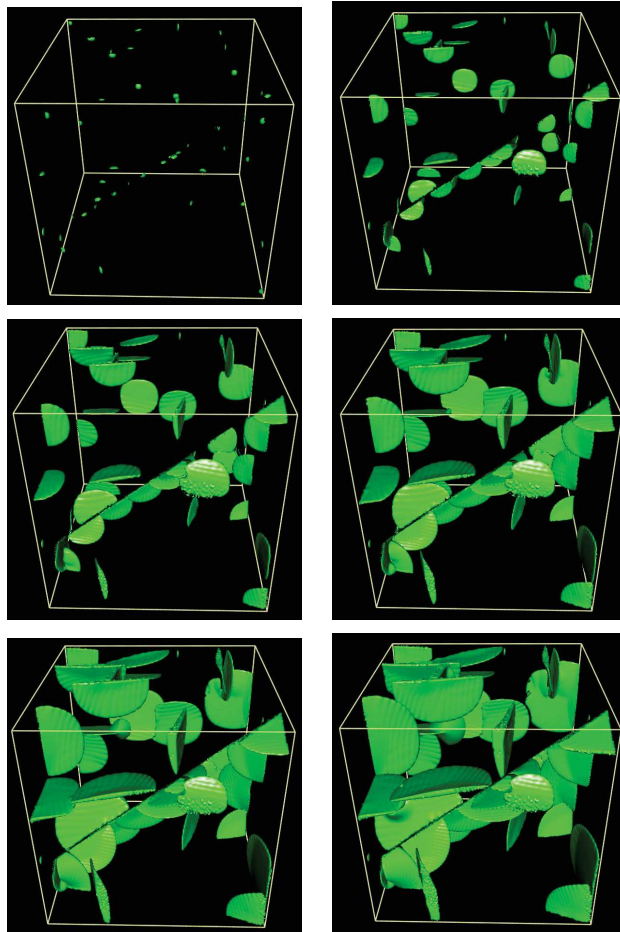
Figure 6: Growth of 50 martensite seeds in 2 austenite grains at t = 2000, 7000, 10000, 13000, 16000 and 19000 time steps.
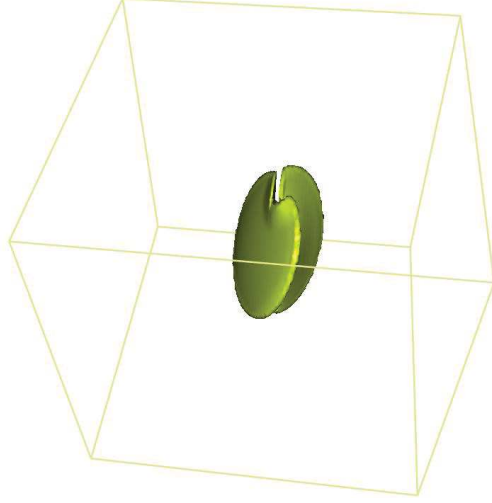
Figure 7: A figure of the case where two plates meet. Uniquely identifying each phase gives the model the ability to differentiate between them.

is not specified. Here we represent this energy in the following form so as to comply with the form of Eq. (12) and be equally dependent on δ and s,

$$U = \sigma_N \delta^2 + \tau s^2, \tag{26}$$

where σ_N and τ is the stress component resolved normal and on the habit plane respectively. Writing this in terms of the variable ϕ as before Eq. (18) now becomes,

$$
\begin{aligned}
g_{\alpha'\gamma} &= \frac{1}{d}[(0.85 + dk_1)\phi_{,x}^2 + (0.85 + dk_2)\phi_{,y}^2 \\
&\quad +(1 + dk_3)\phi_{,z}^2] - U, \\
U &= \sigma_N(\phi_{,z}^2) + \tau(\phi_{,x}^2 + \phi_{,y}^2)
\end{aligned}
\tag{27}
$$

where $f_1 = f_2 = 0.85$ due to the selection of σ_p and $U > 0$ is translated as a favourable contribution to the energy. As before, we solve the following equation in order to determine c/a:

$$\frac{\frac{1}{d}(1 + dK) - \sigma_N}{\frac{1}{d}(0.85 + dK) - \tau} = \frac{c}{a}. \tag{28}$$

21

Figure 8 is obtained by plotting Eq. (28) in order to see the effect of applied stress on the thickness of the plates. It can be seen that an applied stress normal to the habit plane causes a larger influence on the thickness whereas stress along the habit plane has little effect.
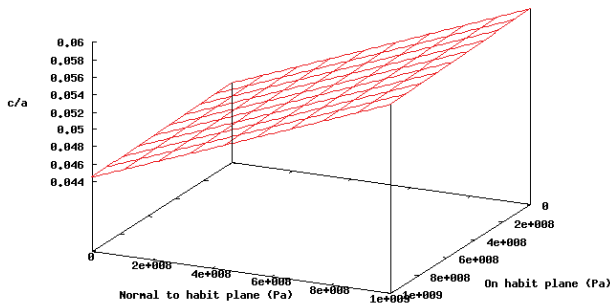
Figure 8: 3-Dimensional plot of the plate thickness dependence on the applied stress.

310 Figure 9 is obtained by investigating the effect of the applied stress on the normal component of Eq. (27). It can be seen that an applied stress on the habit plane results in a large reduction in the transformation energy for growth normal to the habit plane. Figure 10 is obtained by investigating the effect of the applied stress on the habit component of Eq. (27). It can be seen

315 that an applied stress on the habit plane results in a large reduction in the transformation energy for growth along the habit plane. Since the magnitude of increase of the transformation energy due to applied stress in the normal direction is less than the reduction caused by stress on the habit plane, and vice versa for the thickness, from these plots it is seen that for general applied stress,

320 the free energy of formation is reduced (for appropriately oriented variants) and the thickness is increased. This is the same conclusion arrived by Ohtsuka et al. [49]. Of course, some orientation variants will have an unfavourable interaction with the applied stress field. This can be seen from the two figures that force

22

resolved normal to the habit plane is unfavourable in terms of energy reduction.
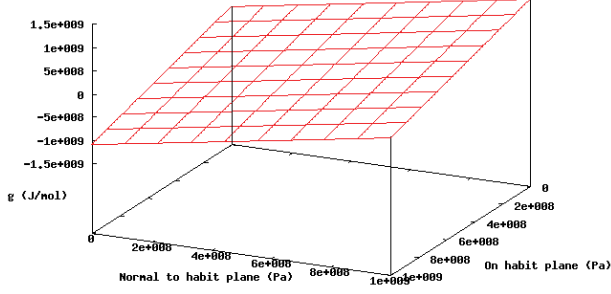
Figure 9: 3-Dimensional plot of the transformation energy normal to the habit plane and its dependence on the applied stress.

It is seen from Eq. (27) that if $U > 0$, the interaction of that particular martensitic variant with the applied stress field is favourable. For the simulations of the effects of applied stress on the growth of a single plate, the following conditions are chosen:

Case 1: $\vec{\sigma}_{ij} = \mathbf{0}$,

Case 2: $\vec{\sigma}_{ij} = \begin{pmatrix} 1 & 0 & 0 \\ 0 & 0 & 0 \\ 0 & 0 & 1 \end{pmatrix}$,

Case 3: $\vec{\sigma}_{ij} = \begin{pmatrix} 1 & 0 & 0 \\ 0 & 1 & 0 \\ 0 & 0 & 1 \end{pmatrix}$,

where the applied stresses have units of GPa and no rotation matrix is applied to the plate for demonstration purposes.

Case 1: Eq. (28) is solved giving $c/a = 0.0452$

Case 2: Eq. (28) is solved giving $c/a = 0.0576$

Case 3: Eq. (28) is solved giving $c/a = 0.0576$.

The results for all cases are given in Figure 11.

23
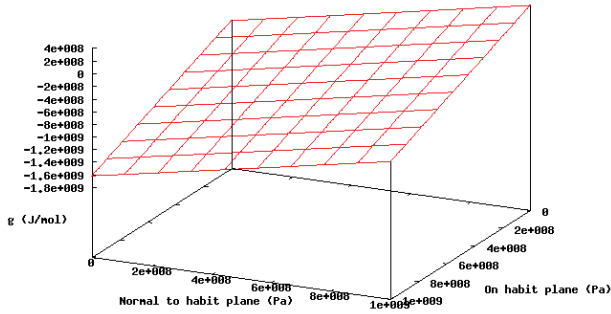
Figure 10: 3-Dimensional plot of the transformation energy in a direction lying on the habit plane and its dependence on the applied stress.

The method implies that for some cases the nucleated variant has an unfavourable interaction with the applied stress field and thus, if the unfavourable ³⁴⁰ interaction is large enough, is unable to evolve. To demonstrate this, all 24 variants are nucleated and subjected to growth under the same applied stress field. The results are given in Figure 12. The number of martensitic plates having a favourable interaction with the applied stress field is 12. The number of plates having unfavourable interactions but are still able to evolve due to this ³⁴⁵ interaction being weak are 4. Tables 3.4 and 3.5 in the works of Kundu [46] show results which agree with this very well. Aspect ratios of martensite plates formed in the absence of prior plates were shown to increase with applied stress [50]. This feature is reproduced in Figures 11 and 12.

It is well known that the total formed martensite volume fraction is a func-³⁵⁰ tion of various parameters such as temperature and applied stress. This indicates the existence of an equilibrium mechanism. The theory developed by Eshelby [39] provides the necessary contribution to the elastic field at a point close to and far away from an ellipsoidal inclusion. Due to the complication of the case for intermediate distances from the inclusion, this is not available as a

24
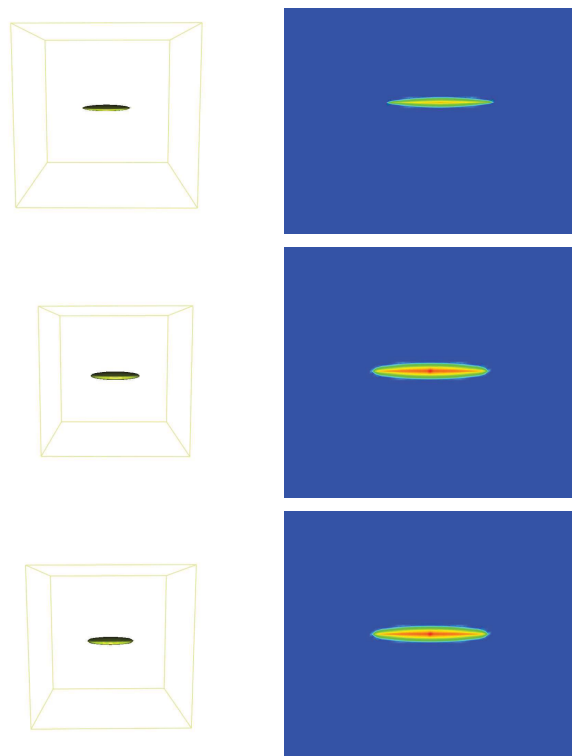
Figure 11: The 3-Dimensional growth of the plate and the 2-Dimensional contour plot of the value of ϕ under no applied stress (top), $\sigma_{11} = \sigma_{33} = 1\text{GPa}$ (middle), and $\sigma_{11} = \sigma_{22} = \sigma_{33} = 1\text{GPa}$ (bottom).
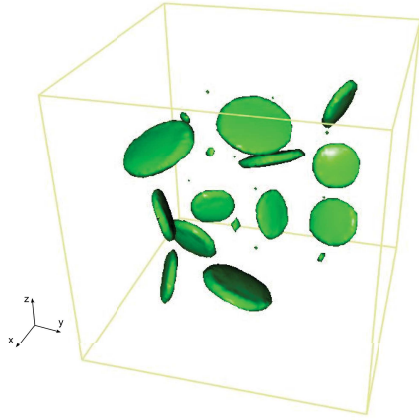
Figure 12: 3-Dimensional plot of the 24 grain variants under a uniaxial applied stress of 1GPa.

simple phenomenological model. Rather than resolving the elastic stress tensor throughout the sample at each location, the model can diffuse elastic properties during plate growth in such a manner as to reproduce the phenomenological model of Eshelby's inclusion at large distances. Similar treatment has been applied to the evolution of the plastic strain energy in the past [35]. Application of this procedure will enable the present model to both reproduce variant selection due to formed martensitic plates and to predict the final volume fraction of martensite due to the elastic field effect of prior formed plates. This problem is not tackled in the present work and will be revisited by future work.

4. Conclusion and remarks

A phenomenological phase-field model has been developed. The model is different from existing phase-field models for martensite transformation in many aspects:

a) The model developed in the present work has introduced only one phase-field order parameter, while other phase-field models for MT utilise three order parameters. This has reduced the computing time in the simulation of MT

26

by two-thirds. The meaning of the phase-field order parameter in the present work is associated with the volume fraction of the martensite phase. The order parameters in some of the other phase-field models are related to the Bain strain in three directions. The present model is easy to scale up to deal with a much larger domain and include additional factors in the growth mechanics.

b) The phase-field model developed in the present work utilises the phenomenological strain energy description associated with MT directly. Most other phase-field models are based on the elastic field analysis in martensite transformation, which require the calculation of elastic distortion in steels. Due to the phenomenological description, the present phase-field model enables the reproduction of a more realistic steel microstructure formed by the martensite phase transition.

c) The model proposed in the present work is able to produce 24 variants with accurate crystallographic orientations. This provides opportunities to simulate texture formation and evolution in steel processing.

d) It is straightforward to expand the current phase-field model to the simulation of the stress-induced martensite transformation within polycrystalline steels. The method can be used directly to simulate MT in some real steels since the input parameters for the present phase-field model, such as the crystallographic data, are available for most steels.

e) The phase-field model has been shown to be able to incorporate the effects of applied stress to the resulting strain energy change and subsequently on variant selection. In addition, the models ability does not end at uniaxially applied stresses but also those with arbitrary direction vectors.

f) It has been shown to be relatively simple, both due to the ease of the comprehension of the model and due to the reduced computational effort, to include mechanisms that effect the evolution of martensite as long as phenomenological formulae for the effect of the mechanism is accessible.

g) Due to the progressive nature of the model, the size and shape of a plate need not be checked at all throughout the simulation.

h) The effects of temperature and composition on the morphology of formed

27

plates are incorporated directly throught the term K. This enables the part of autocatalysis which is influenced by local driving force changes such as that seen in bainite formation due to local composition changes [51].

Due to the phenomenological description, some of the microscopic phenomena in martensite phase transitions have not been addressed in the present work, for example, the effect of the dislocation density on the morphology and orientation of martensite grains and the crack formation in the martensite grain. These problems will be addressed in future works.

References

[1] H. Bhadeshia, Worked examples in the Geometry of Crystals Second edition, Institute of Materials, London, 2001.

[2] R. Zaera, J. Rodríguez-Martínez, a. Casado, J. Fernández-Sáez, a. Rusinek, R. Pesci, A constitutive model for analyzing martensite formation in austenitic steels deforming at high strain rates, International Journal of Plasticity 29 (2012) 77–101. `doi:10.1016/j.ijplas.2011.08.003`. URL `http://linkinghub.elsevier.com/retrieve/pii/S0749641911001434`

[3] M. Fischlschweiger, T. Antretter, G. Cailletaud, Transformation hardening and kinetics for stress assisted and temperature driven martensitic transformation in steels, Mechanics Research Communications 47 (2013) 84–88. `doi:10.1016/j.mechrescom.2012.09.007`.

URL   http://linkinghub.elsevier.com/retrieve/pii/
S0093641312001620

[4] P. Thamburaja, A finite-deformation-based phenomenological theory for shape-memory alloys, International Journal of Plasticity 26 (8) (2010) 1195–1219. doi:10.1016/j.ijplas.2009.12.004.
URL   http://linkinghub.elsevier.com/retrieve/pii/
S074964190900165X

[5] R. Kubler, M. Berveiller, P. Buessler, Semi phenomenological modelling of the behavior of TRIP steels, International Journal of Plasticity 27 (3) (2011) 299–327. doi:10.1016/j.ijplas.2010.05.002.
URL   http://linkinghub.elsevier.com/retrieve/pii/
S0749641910000677

[6] M. Fischlschweiger, G. Cailletaud, T. Antretter, A mean-field model for transformation induced plasticity including backstress effects for non-proportional loadings, International Journal of Plasticity 37 (2012) 53–71. doi:10.1016/j.ijplas.2012.04.001.
URL   http://linkinghub.elsevier.com/retrieve/pii/
S0749641912000563

[7] B. Klusemann, T. Yalçinkaya, Plastic deformation induced microstructure evolution through gradient enhanced crystal plasticity based on a non-convex Helmholtz energy, International Journal of Plasticity 48 (2013) 168–188. doi:10.1016/j.ijplas.2013.02.012.
URL   http://linkinghub.elsevier.com/retrieve/pii/
S0749641913000570

[8] T. Hirouchi, T. Takaki, Y. Tomita, Development of numerical scheme for phase field crystal deformation simulation, Computational Materials Science 44 (4) (2009) 1192–1197. doi:10.1016/j.commatsci.2008.08.001.
URL   http://linkinghub.elsevier.com/retrieve/pii/
S092702560800373X

29

[9] S. Manchiraju, P. Anderson, Coupling between martensitic phase transformations and plasticity: A microstructure-based finite element model, International Journal of Plasticity 26 (10) (2010) 1508–1526. doi:10.1016/j.ijplas.2010.01.009.
URL http://linkinghub.elsevier.com/retrieve/pii/S0749641910000100

[10] A. Devonshire, Theory of barium titanate, Philos. Mag. 40 (309) (1949) 1040.

[11] W. Cao, Constructing Landau-Ginzburg-Devonshire type models for ferroelectric systems based on symmetry, Ferroelectrics 375 (2008) 28–39.
URL http://www.tandfonline.com/doi/abs/10.1080/00150190802437845

[12] A. Karma, W.-J. Rappel, Quantitative phase-field modeling of dendritic growth in two and three dimensions, Physical Review E 57 (4) (1998) 4323–4349. doi:10.1103/PhysRevE.57.4323.
URL http://link.aps.org/doi/10.1103/PhysRevE.57.4323

[13] T. Haxhimali, A. Karma, F. Gonzales, M. Rappaz, Orientation selection in dendritic evolution., Nature materials 5 (8) (2006) 660–4. doi:10.1038/nmat1693.
URL http://www.ncbi.nlm.nih.gov/pubmed/16845416

[14] R. Qin, H. Bhadeshia, Phase-field model study of the effect of interface anisotropy on the crystal morphological evolution of cubic metals, Acta Materialia 57 (7) (2009) 2210–2216. doi:10.1016/j.actamat.2009.01.024.
URL http://linkinghub.elsevier.com/retrieve/pii/S1359645409000512

[15] B. Bottger, J. Eiken, I. Steinbach, Phase field simulation of equiaxed solidification in technical alloys, Acta Materialia 54 (10) (2006) 2697–2704. doi:10.1016/j.actamat.2006.02.008.

30

URL http://linkinghub.elsevier.com/retrieve/pii/
S1359645406001340

[16] R. Qin, H. Bhadeshia, Phase-field model study of the crystal morpholog-
ical evolution of hcp metals, Acta Materialia 57 (11) (2009) 3382–3390.
doi:10.1016/j.actamat.2009.04.001.
URL http://linkinghub.elsevier.com/retrieve/pii/
S1359645409002080

[17] O. Redlich, A. Kister, Algebraic representation of thermodynamic proper-
ties and the classification of solutions, Industrial & Engineering Chemistry
40 (2) (1948) 345–348.
URL http://pubs.acs.org/doi/abs/10.1021/ie50458a036

[18] X. Q. Ma, S. Q. Shi, C. H. Woo, L. Q. Chen, Effect of applied load on
nucleation and growth of gamma-hydrides in zirconium, Computational
Materials Science 23 (2002) 283–290.

[19] D. Li, L. Chen, Computer simulation of stress-oriented nucleation and
growth of Îâ precipitates inAlCu alloys, Acta materialia 46 (8) (1998)
2573–2585.
URL http://www.sciencedirect.com/science/article/pii/
S1359645497004783

[20] Y. L. Li, S. Y. Hu, L. Q. Chen, Ferroelectric domain morphologies of
(001) PbZr[sub 1x]Ti[sub x]O[sub 3] epitaxial thin films, Journal of Ap-
plied Physics 97 (3) (2005) 034112. doi:10.1063/1.1849820.
URL http://link.aip.org/link/JAPIAU/v97/i3/p034112/s1&Agg=doi

[21] J. X. Zhang, Y. L. Li, S. Choudhury, L. Q. Chen, Y. H. Chu, F. Zavaliche,
M. P. Cruz, R. Ramesh, Q. X. Jia, Computer simulation of ferroelectric
domain structures in epitaxial BiFeO[sub 3] thin films, Journal of Applied
Physics 103 (9) (2008) 094111. doi:10.1063/1.2927385.
URL http://link.aip.org/link/JAPIAU/v103/i9/p094111/s1&Agg=
doi

[22] S. Y. Hu, M. I. Baskes, M. Stan, J. N. Mitchell, J. X. Zhang, L. Q. Chen, Effect of Elastic Anisotropy and Inhomogeneity on Coring Structure Evolution in Pu-Ga Alloys Phase-field modeling, Journal of Computer-Aided Materials Design 14 (3) (2007) 389–402. `doi:10.1007/s10820-007-9050-4`.
URL `http://www.springerlink.com/index/10.1007/s10820-007-9050-4`

[23] N. Moelans, B. Blanpain, P. Wollants, Quantitative Phase-Field Approach for Simulating Grain Growth in Anisotropic Systems with Arbitrary Inclination and Misorientation Dependence, Physical Review Letters 101 (2) (2008) 025502. `doi:10.1103/PhysRevLett.101.025502`.
URL `http://link.aps.org/doi/10.1103/PhysRevLett.101.025502`

[24] L.-Q. Chen, Phase-Field Method of Phase Transitions/Domain Structures in Ferroelectric Thin Films: A Review, Journal of the American Ceramic Society 91 (6) (2008) 1835–1844. `doi:10.1111/j.1551-2916.2008.02413.x`.
URL `http://doi.wiley.com/10.1111/j.1551-2916.2008.02413.x`

[25] Y. Wang, A. G. Khachaturyan, Multi-scale phase field approach to martensitic transformations, Materials Science and Engineering: A 438-440 (2006) 55–63. `doi:10.1016/j.msea.2006.04.123`.
URL `http://linkinghub.elsevier.com/retrieve/pii/S0921509306005892`

[26] V. Levitas, V. Levin, K. Zingerman, E. Freiman, Displacive Phase Transitions at Large Strains: Phase-Field Theory and Simulations, Physical Review Letters 103 (2) (2009) 025702. `doi:10.1103/PhysRevLett.103.025702`.
URL `http://link.aps.org/doi/10.1103/PhysRevLett.103.025702`

[27] V. I. Levitas, D.-W. Lee, D. L. Preston, Interface propagation and microstructure evolution in phase field models of stress-induced martensitic

32

phase transformations, International Journal of Plasticity 26 (3) (2010) 395–422. `doi:10.1016/j.ijplas.2009.08.003`.
URL `http://linkinghub.elsevier.com/retrieve/pii/` `S0749641909000989`

[28] V. I. Levitas, Phase-field theory for martensitic phase transformations at large strains, International Journal of Plasticity 49 (2013) 85–118. `doi:10.1016/j.ijplas.2013.03.002`.
URL `http://linkinghub.elsevier.com/retrieve/pii/` `S0749641913000727`

[29] H. K. Yeddu, A. Malik, J. Å gren, G. Amberg, A. Borgenstam, Three-dimensional phase-field modeling of martensitic microstructure evolution in steels, Acta Materialia 60 (4) (2012) 1538–1547. `doi:10.1016/j.actamat.2011.11.039`.
URL `http://linkinghub.elsevier.com/retrieve/pii/` `S1359645411008299`

[30] H. K. Yeddu, A. Borgenstam, P. Hedström, J. Å gren, A phase-field study of the physical concepts of martensitic transformations in steels, Materials Science and Engineering: A 538 (2012) 173–181. `doi:10.1016/j.msea.2012.01.026`.
URL `http://linkinghub.elsevier.com/retrieve/pii/` `S0921509312000482`

[31] J. Kundin, D. Raabe, H. Emmerich, A phase-field model for incoherent martensitic transformations including plastic accommodation processes in the austenite, Journal of the Mechanics and Physics of Solids 59 (10) (2011) 2082–2102. `doi:10.1016/j.jmps.2011.07.001`.
URL `http://linkinghub.elsevier.com/retrieve/pii/` `S0022509611001335`

[32] V. I. Levitas, A. M. Roy, D. L. Preston, Multiple twinning and variant-variant transformations in martensite: Phase-field approach, Physical Re-

view B 88 (5) (2013) 054113. `doi:10.1103/PhysRevB.88.054113`.
URL `http://link.aps.org/doi/10.1103/PhysRevB.88.054113`

[33] H. K. Yeddu, A. Borgenstam, J. Å gren, Effect of martensite embryo potency on the martensitic transformations in steelsA 3D phase-field study, Journal of Alloys and Compounds 577 (2013) S141–S146. `doi:10.1016/j.jallcom.2012.01.087`.
URL `http://linkinghub.elsevier.com/retrieve/pii/S0925838812001594`

[34] Y. Wang, a.G. Khachaturyan, Three-dimensional field model and computer modeling of martensitic transformations, Acta Materialia 45 (2) (1997) 759–773. `doi:10.1016/S1359-6454(96)00180-2`.
URL `http://linkinghub.elsevier.com/retrieve/pii/S1359645496001802`

[35] A. Yamanaka, T. Takaki, Y. Tomita, Elastoplastic phase-field simulation of martensitic transformation with plastic deformation in polycrystal, International Journal of Mechanical Sciences 52 (2) (2010) 245–250. `doi:10.1016/j.ijmecsci.2009.09.020`.
URL `http://linkinghub.elsevier.com/retrieve/pii/S0020740309001696`

[36] R. Qin, E. Wallach, A method to compute the migration rate of planar solidliquid interfaces in binary alloys, Journal of Crystal Growth 253 (1-4) (2003) 549–556. `doi:10.1016/S0022-0248(03)01042-X`.
URL `http://linkinghub.elsevier.com/retrieve/pii/S002202480301042X`

[37] A. Wheeler, W. Boettinger, G. McFadden, Phase-field model for isothermal phase transitions in binary alloys, Physical Review A 45 (10) (1992) 7424–7440.
URL `http://pra.aps.org/abstract/PRA/v45/i10/p7424_1`

34

[38] S. Kim, W. Kim, T. Suzuki, Interfacial compositions of solid and liquid in a phase-field model with finite interface thickness for isothermal solidification in binary alloys, Physical Review E 58 (3) (1998) 3316–3323. `doi:10.1103/PhysRevE.58.3316`.
URL `http://link.aps.org/doi/10.1103/PhysRevE.58.3316`

[39] J. Eshelby, The determination of the elastic field of an ellipsoidal inclusion, and related problems, Proc. R. Soc. London Sect. A 241 (1957) 376.
URL `http://rspa.royalsocietypublishing.org/content/241/1226/376.short`

[40] J. Christian, Accommodation strains in martensite formation, and the use of a dilatation parameter, Acta Metallurgica 6 (1958) 377–379.
URL `http://scholar.google.com/scholar?hl=en&btnG=Search&q=intitle:Accommodation+strains+in+martensite+formation,+and+the+use+of+a+dilatation+parameter#0`

[41] J. Bowles, J. Mackenzie, The crystallography of martensite transformations I, Acta Metallurgica 2 (1954) 129.
URL `http://www.sciencedirect.com/science/article/pii/0001616054901029`

[42] S. Kundu, H. Bhadeshia, Crystallographic texture and intervening transformations, Scripta Materialia 57 (9) (2007) 869–872. `doi:10.1016/j.scriptamat.2007.06.056`.
URL `http://linkinghub.elsevier.com/retrieve/pii/S1359646207004940`

[43] T. Takaki, T. Fukuoka, Y. Tomita, Phase-field simulation during directional solidification of a binary alloy using adaptive finite element method, Journal of Crystal Growth 283 (1-2) (2005) 263–278. `doi:10.1016/j.jcrysgro.2005.05.064`.
URL `http://linkinghub.elsevier.com/retrieve/pii/S0022024805007074`

[44] A. Wheeler, W. Boettinger, G. McFadden, Phase-field model of solute trapping during solidification, Physical review E 47 (3).
URL http://pre.aps.org/abstract/PRE/v47/i3/p1893_1

[45] Z. Yang, R. Johnson, An EAM simulation of the alpha-gamma iron interface, Modelling and Simulation in Materials Science and Engineering 1 (1993) 707.
URL http://iopscience.iop.org/0965-0393/1/5/010

[46] S. Kundu, Transformation strain and crystallographic texture in steels, Ph.D. thesis, University of Cambridge London (2007).
URL http://ethos.bl.uk/OrderDetails.do?uin=uk.bl.ethos.541810

[47] B. Banerjee, The mechanical threshold stress model for various tempers of AISI 4340 steel, International journal of solids and structures (2005) 1–44.
URL http://www.sciencedirect.com/science/article/pii/S002076830600182X

[48] J. Patel, M. Cohen, Criterion for the action of applied stress in the martensitic transformation, Acta Metallurgica 1 (5) (1953) 531–538.
URL http://www.sciencedirect.com/science/article/pii/0001616053900832

[49] H. Ohtsuka, G. Ghosh, H. Wada, Size and aspect ratio of martensite in FeNiC alloys formed under applied magnetic field and tensile elastic stress at 4.2 K, Materials Science and Engineering: A 273-275 (1999) 342–346. doi:10.1016/S0921-5093(99)00426-8.
URL http://linkinghub.elsevier.com/retrieve/pii/S0921509399004268

[50] G. Ghosh, V. Raghavan, The dimensions of isothermally formed martensitic plates in an FeNiMn alloy, Materials Science and Engineering 79 (2) (1986) 223–231. doi:10.1016/0025-5416(86)90407-6.
URL http://linkinghub.elsevier.com/retrieve/pii/0025541686904076

[51] T. Arif, R. Qin, A phase-field model for bainitic transformation, Computational Materials Science 77 (2013) 230–235. doi:10.1016/j.commatsci.2013.04.044.
URL http://linkinghub.elsevier.com/retrieve/pii/S0927025613002164

660

Appendix E

A phase-field model for bainitic transformation

Computational Materials science 77 (2013) 230-235

A phase-field model for bainitic transformation

T.T. Arif, R.S. Qin *

Department of Materials, Imperial College London, Exhibition Road, London SW7 2AZ, UK

ABSTRACT

A phase-field model for the computation of microstructure evolution for the bainite transformation has been developed. The model has a classical phase-field foundation, incorporates the phenomenological displacive transformation theory and the symmetric analysis of cubic crystals, and is able to reproduce realistic grain morphology and crystal orientation after adequate calibration. Using the free energy expression for the shape change of displacive transformations along with the free energy formula for the chemical free energy change of the two phases derived from established regular solution models, the current model is able to deal with autocatalysis.

© 2013 Elsevier B.V. All rights reserved.

1. Introduction

The phase-field (PF) method is used in the domain of materials science for simulating microstructure evolution on the mesoscale. The locations, sizes and shapes of the grains involved are represented by the PF variables. The evolution of the PF variables is then governed by a set of partial differential equations. They have nearly constant values within the grains but vary continuously over the interfaces between them. This means that the interface has a width and is not infinitesimally thin. Thus the method is said to have a diffuse-interface description. Unlike sharp interface methods, the diffuse-interface nature enables the computation of complex microstructures without explicitly tracking the interfaces. The method has been reviewed extensively, such as that in Refs. [1,2].

A PF model involves the formulation of a free energy functional of the PF variables and their gradients. - A form of the free energy functional includes the PF variable ϕ as a means of distinguishing coexisting phases along with the composition field C and temperature T as [3]

$$G = \int_V \left[g_0(\phi, C, T) + \frac{1}{2}\varepsilon_C^2(\vec{\nabla}C)^2 + \frac{1}{2}\varepsilon_\phi^2(\vec{\nabla}\phi)^2 \right] d\vec{r} \qquad (1)$$

where ε_C and ε_ϕ are the gradient energy coefficients and $g_0(\phi, C, T)$ is the free energy density over the volume V. The governing equation for ϕ is derived from G in a thermodynamically consistent manner adhering to the second law of thermodynamics. Eq. (1) can be coupled with a thermodynamic database [4–7] and used for the simu-

lation of solidification [8], grain growth [9], solute drag [10] and many other processes. The method has thus gained momentum in microstructure formation and evolution. In solid state phase transformations there have been PF models that consider displacive transformations [11] and those that consider diffusive transformations [9,12].

Considered within the present work is a PF model able to utilise both diffusive and displacive mechanisms in its treatment of microstructure evolution. The microstructure focussed upon is bainite. Bainite is a microstructure resulting from the decomposition of austenite usually found to occur at a temperature between the pearlite reaction and the martensite start temperature (Ms). Initially detected as a unique microstructure in the early 1900s [13,14], interest in this multi-phase product of austenite grew once its benefits were realised. Bainitic steels boast improved strength without the expense of weldability and toughness and have applications in the railway, automotive industries and structural engineering [15–19]. The time-consuming process of producing bainitic steels prompted the desire to understand and formulate models for the kinetics and formation of bainite.

Following the kinetic model of Bhadeshia [20] the supersaturated ferrite sub-units form in austenite via a displacive mechanism. The ferrite sub-units form martensitically without the partitioning of alloying elements. Due to the higher temperatures when compared to martensite, the partitioning of the interstitial carbon from the supersaturated ferrite into the residual austenite follows soon after. Upon carbide precipitation in the austenite, the upper bainite microstructure forms. As the temperature is reduced, this diffusion process is slowed down which results in carbon precipitation within the bainitic ferrite giving lower bainite

* Corresponding author. Tel.: +44 207 5946803; fax: +44 207 5946757.
E-mail address: r.qin@imperial.ac.uk (R.S. Qin).

[21]. The transformation strains are accommodated plastically with the growth of the sub-unit limited by the dislocation debris [20,22–24]. The repeated nucleation and growth of these supersaturated bainitic ferrite sub-units gives the overall sheaf structure.

There have been efforts to model Bainitic phase transformation using a multiple order parameter phase-field model [25], in which both displacive transformation and carbon diffusion are considered. However, their work considers the entire sheaf as a single structure. This is opposed to the experimental fact that a sheaf consists of many individual sub-units. In the present work, a single order parameter phase-field model will be developed and the sub-units in bainite will be considered.

2. The phase-field model and the transformation theory

The governing equation for the phase-field order parameter, ϕ, derived from Eq. (1) using the second law of thermodynamics is given as [3,26]

$$\frac{\partial \phi}{\partial t} = M_\phi \left[\varepsilon^2 \nabla^2 \phi + \frac{1}{2\omega} \phi(1-\phi)(1-2\phi) - 30\phi^2(1-\phi)^2(g_{\alpha B} - g_\gamma) \right] \tag{2}$$

where $0 < \phi < 1$ is the interface between austenite and supersaturated ferrite with $\phi = 0$ representing the austenite and $\phi = 1$ the supersaturated ferrite. ε is the gradient energy coefficient and the coefficient ω is related to the kinetic barrier. $g_{\alpha B}$ and g_γ are the bulk free energies of the supersaturated ferrite and austenite, respectively. The parameters are related by the equations $\varepsilon^2 = 3\lambda\sigma/1.1$ and $\omega = \lambda/(26.4\sigma)$ [27], where σ and λ is the interface energy and half-thickness of the interface, respectively. $g_{\alpha B} - g_\gamma$ is the driving force for microstructure evolution.

Bhadeshia expressed the strain energy of an ellipsoidal inclusion for the example of a martensitic grain as [28]

$$g_{\alpha B \gamma}^{strain} = \frac{a_1}{a_2} \mu \cdot m^2 = \frac{a_1}{a_2} \mu (s_x^2 + s_y^2 + \delta^2) \tag{3}$$

where m is the total deformation and is the sum of the shear strains along the x direction s_x and along the y direction s_y, and the uniaxial dilatation strain δ. a_1 and a_2 are the dimensions of the ellipsoid and μ is the shear modulus. In the current phase-field model, the supersaturated ferrite can be considered as an ellipsoidal inclusion. The orientation of the interface is represented by the gradient of the phase-field order parameter

$$\hat{n} = \frac{\nabla \phi}{|\nabla \phi|} = \frac{1}{|\nabla \phi|} \left(\frac{\partial \phi}{\partial x} \hat{x} + \frac{\partial \phi}{\partial y} \hat{y} + \frac{\partial \phi}{\partial z} \hat{z} \right) \tag{4}$$

Phase transformation takes place at the interface. For an interface with surface area δs and migration rate $\vec{v}(t)$, the volume of the new phase formed in the transformation within time duration δt is $\delta s \cdot \vec{v}(t) \cdot \hat{n} \delta t$. The dimension of the newly formed phase along the x direction is therefore represented as

$$\frac{\delta s \cdot |\vec{v}(t)| \cdot \delta t}{|\nabla \phi|} \cdot \frac{\partial \phi}{\partial x} \propto \frac{\partial \phi}{\partial x} \tag{5}$$

The growth of the new phase along different directions causes different amounts of strain. Therefore, one has $s_x \propto f_1 \frac{\partial \phi}{\partial x}$, $s_y \propto f_2 \frac{\partial \phi}{\partial y}$ and $\delta \propto f_3 \frac{\partial \phi}{\partial z}$. Eq. (3) is hence represented as

$$g_{\alpha B \gamma}^{strain} = f_1^2 \phi_x^2 + f_2^2 \phi_y^2 + f_3^2 \phi_z^2 \tag{6}$$

where $\phi_{x_i} = \partial \phi / \partial x_i$ is the rate of change of ϕ in the x_i direction. The change of chemical free energy only depends on the amount of new phase formed, and the free energy density difference between the new and parent phases.

The driving force is then

$$g_{\alpha B\gamma} = g_{\alpha B} - g_\gamma = (g_{\alpha B}^{strain} - g_\gamma^{strain}) + (g_{\alpha B}^{chem} - g_\gamma^{chem})$$
$$= (f_1^2 \phi_x^2 + f_2^2 \phi_y^2 + f_3^2 \phi_z^2) + g_{\alpha B\gamma}^{chem} \tag{7}$$

The chemical free energy density difference can be obtained from a thermodynamic database and is usually isotropic [1,4], meaning $k_1 = k_2 = k_3 = k$ in the following equation:

$$g_{\alpha B\gamma}^{chem} = k_1 \phi_x^2 + k_2 \phi_y^2 + k_3 \phi_z^2 \tag{8}$$

It should be pointed out that f_i and k_i are unspecified coefficients so far and that the squares of the f_i can been omitted since the square of an unspecified constant remains an unspecified constant. Eq. (7) is therefore reduced to

$$g_{\alpha B\gamma} = (f_1 + k_1)\phi_x^2 + (f_2 + k_2)\phi_y^2 + (f_3 + k_3)\phi_z^2 \tag{9}$$

Given a transformation matrix from the growing crystal coordinate system to the parent crystal coordinate system with elements represented by H_{ij}, the final form of the driving force becomes for an isotropic chemical free energy ($k_1 = k_2 = k_3 = k$)

$$g_{\alpha B\gamma} = \sum_{i=1}^{3} (f_i + k)(H_{i1}\phi_x + H_{i2}\phi_y + H_{i3}\phi_z)^2 \tag{10}$$

The phase transition from the parent phase to the new phase requires that $g_{\alpha B\gamma} < 0$. The f_i are specified as $f_1 = f_2$ and $f_3 = c_1 f_1$ according to the experimental observation of the morphology of the new phase. c_1 is a shape factor in the anisotropic driving force and related to the equilibrium aspect ratio of the bainite sub-unit. In displacive phase transformation, solute composition of the new phase is the same as that for the matrix due to its diffusionless nature. The volume change between the new phase and the parent phase is incorporated in the strain and the transformation matrix H_{ij}.

The width of the bainitic sub-units depend upon alloying elements. In particular, an increase in carbon concentration translates to a decrease in the aspect ratio of the sub-units [29]. This means that the shape factor $c_1 \equiv c_1(c)$ is a function of the carbon concentration c. Due to the shape change we must have that $c_1 f_1 + k \geqslant f_1 + k \, \forall \, c_1, k$. Since $k < 0$ we immediately have that $c_1 \geqslant 1 \cdot c_1$ is a monotonic decreasing function of c. Also at the equilibrium between bainitic ferrite and austenite (i.e. at T_0' and c^*), we have zero driving force for bainite growth giving $c_1(c^*)f_1 + k(c^*) = f_1 + k(c^*) = 0$. Since $k(c^*) = -f_1$, we have that $f_1 + k(c^*) = 0$ holds. In order for $c_1(c^*)f_1 + k(c^*) = 0$ to be true we must have $c_1(c^*) = 1$.

Given a function $l(c)$ describing the aspect ratio of bainitic sub-units, we can impose the requirement that at a carbon composition c

$$c_1(c)f_1 + k(c) = \beta(l(c))(f_1 + k(c)) \tag{11}$$

where β is a function relating the coefficient of the right hand side of Eq. (11) to the resulting aspect ratio. To clarify Eq. (11), $c_1(c)$ is the previously mentioned shape factor and $l(c)$ is the experimentally observed aspect ratio. However, observing Eq. (2) it is not obvious that the resulting aspect ratio of the bainite sub-units in the models output has a simple relation to $c_1(c)$. In other words, a shape factor of c_1 does not necessarily result in an aspect ratio of c_1. Therefore, β is introduced to establish the connection between $c_1(c)$ and the resulting aspect ratio. For instance Fig. 1 shows that the evolution of the resulting aspect ratio given an input coefficient of 0.05 (i.e. $0.05(f_1 + k(c))$) tends to a limit (approximately 0.125). This would then mean that $\beta(0.125) = 0.05$.

Given reports that an aspect ratio of 0.025 is most frequently observed with 0.008 being the minimum, we require that $l(c^*) = 0.008$ and at the initial average composition of $\bar{c}$, $(l\bar{c}) = 0.025$. Then c_1 can be calculated as

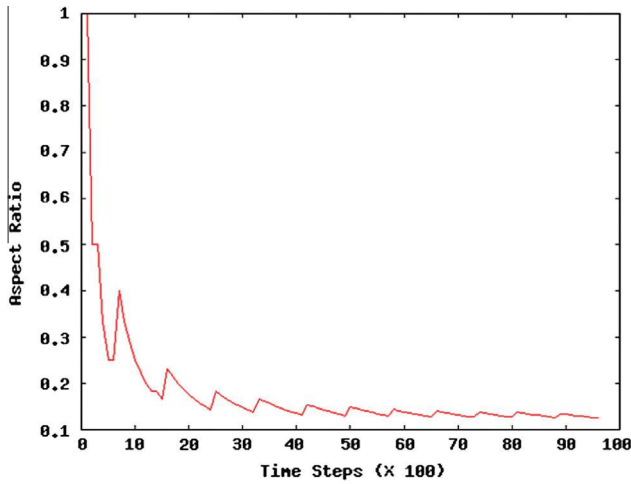$$c_1(c) = \frac{\beta(l(c))(f_1 + k(c)) - k(c)}{f_1} \tag{12}$$

Fig. 1. The evolution of the aspect ratio with time for an input coefficient of 0.05. In the figure the discrete steps are due to the lattice spacing while the system evolves toward the limiting aspect ratio.

Note that it gives $c_1(c^*) = 1$ and for $c < c^*$, $c_1(c) > 1$. Since austenite enrichment will only serve to provide the nucleation of bainite in a higher carbon enriched environment, the local composition will not drop below $\bar{c}$.

Within this work we assume $l(c)$ to be a function of the form,

$$l(c) = -h_4 \tan^{-1}(h_1 c + h_2) + h_3 \tag{13}$$

with the conditions that

    (a) $l(c) = 0.008$ at $c = c^*$.
    (b) $l(c) = 0.025$ at $c = \bar{c}$.
    (c) $l(c) \to 0$ as $c \to \infty$.
    (d) $\int_{c=\bar{c}}^{c=c^*} l(c)\, dc > \int_{x=\bar{c}}^{x=c^*} \left[\left(\frac{-0.017}{c^* - \bar{c}} \right)(x - \bar{c}) + 0.025 \right] dx$.

Eq. (13) is visualised along with the conditions in Fig. 2. Using (a–c), Eq. (13) can be written in terms of h_4 which can then be specified using condition (d). By imposing the last condition we cater for the observation that some aspect ratios are more common than others. The choice of Eq. (13) is due to its monotonic decreas-
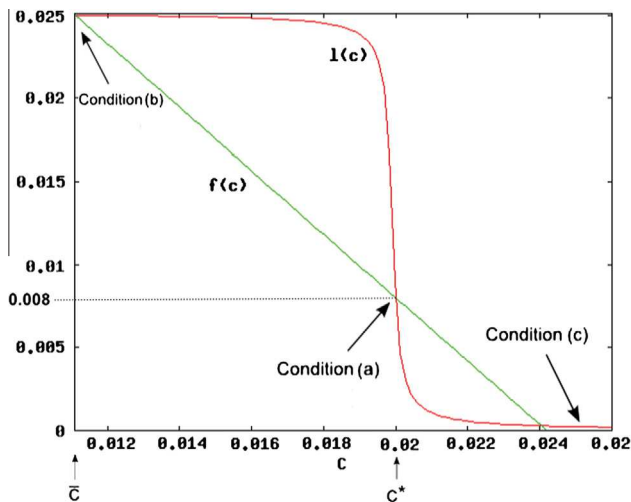

Fig. 2. A plot of $l(c)$ with $h_1 = 6843.168$, $h_2 = -136.22$, $h_3 = 0.012566$, $h_4 = 0.008$, $c^* = 0.02$ and $\bar{c} = 0.0111$. The implications of the conditions of Eq. (13) are shown in the figure. Condition (d) implies that $\int l(c)dc > \int f(c)dc$ within the range $\bar{c} \leqslant c \leqslant c^*$. It can be seen from the figure that for the majority of the c range, $l(c)$ returns an aspect ratio close to 0.025 .

ing nature and that it can be made to satisfy condition (d). The integral on the right hand side of condition (d) is the area beneath a linear equation from coordinates $(\bar{c}, 0.025)$ to $(c^*, 0.008)$. The four conditions ensure that the majority of the aspect ratios observed are close to 0.025. In reality, $l(c)$ will be determined from more thorough experimental evidence so that sub-units with accurate aspect ratios are observed for corresponding carbon enrichment. Note that it has been assumed that the majority of the c range consists of 0.025 aspect ratios and the larger ratios lie below $\bar{c}$.

After the displacive transformation, carbon in supersaturated ferrite starts to precipitate away from the ferrite and forms cementite. Both the ferrite and the cementite form the bainite. The formation of the supersaturated ferrite is formed by displacive transformation. But the formation of the cementite phase is a reconstructive transformation and is controlled by the diffusion. The governing equation for solute concentration is determined using the Cahn–Hilliard diffusion equation [30]

$$\frac{\partial c}{\partial t} = \nabla \cdot \left[M_C \nabla \frac{\delta G}{\delta c} \right] \tag{14}$$

and conserves mass. The free energy density (the expression within the integral) of Eq. (1) is written as

$$g = h(\phi)g_{\alpha B} + [1 - h(\phi)]g_\gamma + \frac{1}{4\omega}\phi^2(1-\phi)^2 + \frac{1}{2}\varepsilon^2 |\nabla \phi|^2 \tag{15}$$

The interpolation function [31] $h(\phi) = \phi^3(6\phi^2 - 15\phi + 10)$ is translated as the local volume fraction of the phase. M_C is the concentration mobility and $\frac{\delta G}{\delta c} = \frac{\partial g}{\partial c} - \nabla \cdot \frac{\partial g}{\partial \nabla c}$ is the functional derivative. To determine M_C, Eq. (14) is expanded into

$$\frac{\partial c}{\partial t} = \nabla \cdot [D \nabla c] \tag{16}$$

where $D = M_C \frac{\partial^2 g}{\partial c^2}$ and D is the diffusivity. The form of g^{chem} for the binary Fe–C system with two sublattices and a^1 and a^2 sites with site 1 occupied by Fe and site 2 occupied by C and Va (vacant sites) is given as [32,33]

$$g^{chem} = Y_{Va}^2 {}^0 G_{Fe:Va} + Y_C^2 {}^0 G_{Fe:C} + RT[a^2(Y_C^2 \ln Y_C^2 + Y_{Va}^2 \ln Y_{Va}^2)]$$
$$+ Y_{Va}^2 Y_C^2 L_{Fe:Va,C} + G_m^{mo} \tag{17}$$

where Y_i^s denotes the site fraction of component i on sublattice s, $L_{Fe:Va,C}$ is an interaction parameter with the comma separating two components in the same sublattice and a colon separating two in different sublattices. The relation between the site fraction and molar fraction x_i of component i is given as $x_i = \frac{\sum_s a^s Y_i^s}{\sum_s a^s(1 - Y_{Va}^s)}$ and $Y_{Va} = 1 - Y_C$. G_m^{mo} is the contribution due to magnetic ordering, ${}^0 G_{Fe:Va}$ is the Gibbs free energy of pure Fe and along with ${}^0 G_{Fe:C}$ and $L_{Fe:Va,C}$ is given in [32]. We have $a = 3$, $a^1 = 1$ and $a^2 = 3$ for ferrite and $a = 1$ and $a^1 = a^2 = 1$ for austenite. Note that here Eq. (17) corresponding to ferrite is used to approximate $g_{chem}^{\alpha B}$. Thus, using Eq. (17), the functional derivative in Eq. (14) can be calculated as $\frac{\delta G}{\delta c} = \frac{\partial g}{\partial c}$, which is just the chemical potential. This is calculated both in ferrite α and austenite γ and takes the form

$$\frac{\partial g}{\partial c} = h(\phi)\frac{\partial g_{chem}^{\alpha B}}{\partial c} + [1 - h(\phi)]\frac{\partial g_{chem}^\gamma}{\partial c}$$
$$\frac{\partial^2 g}{\partial c^2} = h(\phi)\frac{\partial^2 g_{chem}^{\alpha B}}{\partial c^2} + [1 - h(\phi)]\frac{\partial^2 g_{chem}^\gamma}{\partial c^2} \tag{18}$$

where the volume fraction $h(\phi)$ takes on the value 1 in ferrite and 0 in austenite. D in Eq. (16) is then calculated via Eq. (18).

For autocatalytic nucleation, a random number generator is used around the ferrite tip area of previous sub-units with the nucleation probability being calculated according to the driving force at that lattice point. During the transformation there will be carbon enrichment of the residual austenite reducing the

driving force available for the nucleation and growth of subsequent sub-units. The condition for growth is $\Delta G^{\gamma \to \alpha} < -400\,\mathrm{J\,mol^{-1}}$, where $\Delta G^{\gamma \to \alpha}$ is the chemical free energy change for the transformation [34]. This equation is simply the locus of points for which the free energies of bainite and austenite are equal (T'_0 in [35]). At the points above this line the driving force is insufficient to compensate for the strain energy involved in the plastically accommodated bainite transformation [15,35]. The effect of carbon enrichment in austenite is to reduce the magnitude of the k term in Eq. (10) until eventually growth is no longer favoured.

3. Results and simulations

An explicit finite difference method is used in solving Eqs. (2) and (14). The phase-field mobility is chosen as $M_\phi = 100$ to reflect the speed of bainite transformation when compared to diffusional transformations and the concentration mobility is $M_C = 0.00046$ in order to be slower than the displacive growth of the sub-units. The half-interface thickness and interface energy are $\lambda = 14.3$ nm [3,26–28] and $\sigma = 0.72\,\mathrm{J/m^2}$ [36], respectively. The grid point spacing is defined as $\Delta x = 0.5\lambda$ giving the width of the interface as 4 grid points [3,27,37]. k is related to the chemical free energy at 500 °C and is determined using Eq. (17). The following numerical results are obtained with 0.241 wt% carbon initially distributed homogeneously over the entire system.

The simulations are set up as follows: the simulation grid is set up with a given set of dimensions. The lattice points at the sides and edges of the grid are not part of the domain and are simply there to contain the system domain. In the case of a single austenite grain, an austenite grain is grown spherically from the centre until the entire grid is austenite (except for the previously mentioned lattice points at the sides and edges). When a bainite sub-unit is nucleated at the boundary, the nucleation actually occurs a single lattice point away from the austenite grain boundary
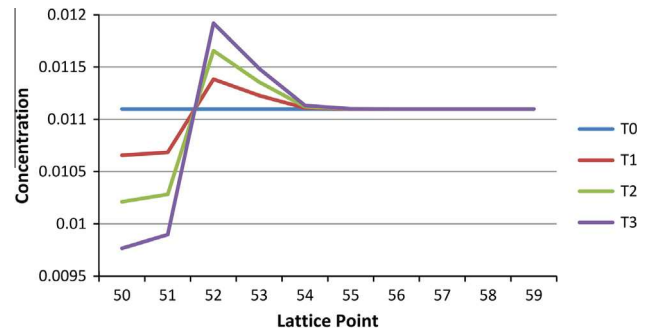
Fig. 3. Concentration profile of carbon across the bainitic ferrite/austenite interface at increasing time steps.

and two lattice points from the grid sides and edges. In the case of multiple austenite grains, the grains are grown spherically from multiple locations within the grid. When two austenite grains meet, there will be two adjacent lattice points consisting of austenite grain boundary and no growth will occur here.

A single sub-unit was nucleated at the centre of the logistic domain of dimension 100^3. The sub-unit grows to a limited size before its growth is stopped. Carbon is segregated out of the ferrite during the sub-unit growth but at a much slower speed than the growth of the sub-unit itself. Fig. 3 represents the carbon distribution evolution across a sub-unit and shows that the concentration within the sub-unit approaches minimum while the carbon content approaches the average concentration with increasing distance from the centre of the sub-unit. Fig. 4 shows the carbon profile and the driving force across a sub-unit.

A second simulation with the same parameters was performed in order to demonstrate autocatalysis. Fig. 5 is the result from the nucleation of a sub-unit at the austenite grain boundary with subsequent autocatalytic events while Fig. 6 shows a single autocatalytic

Fig. 4. Images of (a) carbon composition distribution and (b) driving force distribution across a sub-unit.

Fig. 5. Autocatalysis events at the tip of a sub-unit nucleated at the grain boundary (grid size = 150^3).

event. Fig. 7 presents the resulting sheaf obtained from repeatedly applying the autocatalysis event of Fig. 5 using MatVisual.
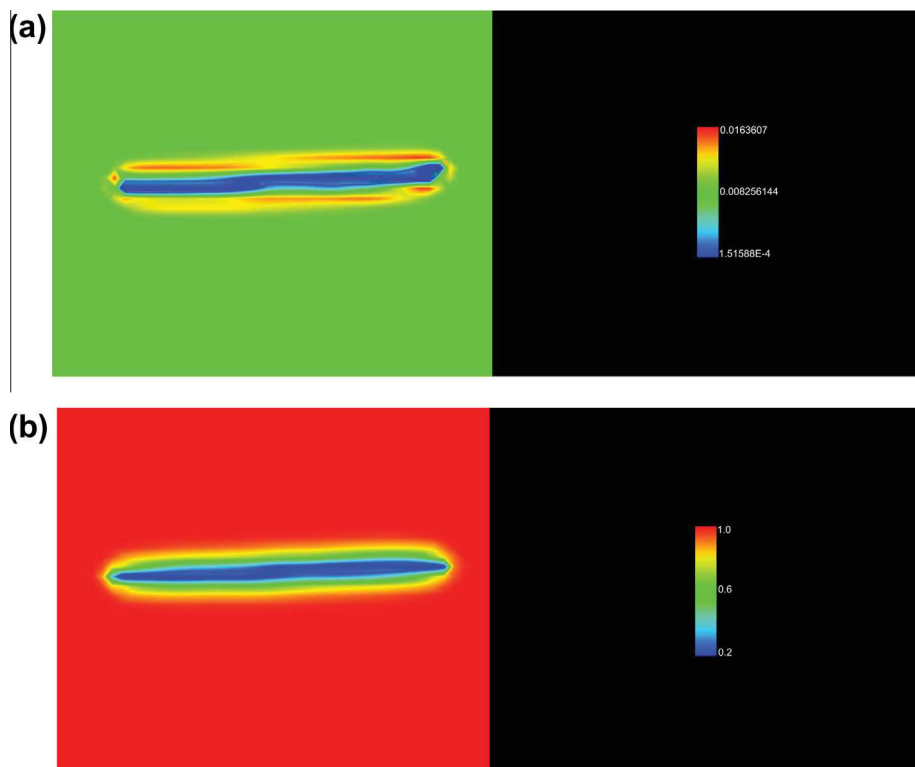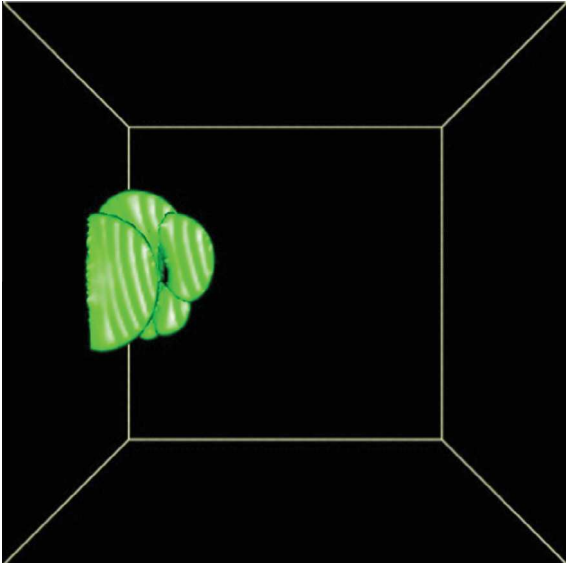
4. Discussion and conclusion

The bainite transformation temperature is chosen as 500 °C so as to concur with all the temperature ranges given by the equations found in [38–41] for 0.241 wt% C. The apparent thickness of bainitic sub-units was shown to depend on temperature [34]. In

this case $c_1(c)$ can be made to depend upon temperature. Carbide precipitation was not considered for the numerical results, however, there are many applications of carbide-free bainitic steel [34].

From the carbon profile in Fig. 4a, we see that enrichment occurs much less in the austenite at the tip of the sub-unit. This is due to the larger surface area available for diffusion of carbon out of the ferrite. The diffusion process continues until chemical equilibrium is reached. The rate at which carbon is ejected from the ferrite into the austenite is much faster than the diffusion rate of carbon in austenite. This causes the austenite adjacent to the sub-unit to become supersaturated for some time while gradually homogenising over the domain. In the case of bainite growth, multiple sub-units are nucleated in close proximity with films of austenite in between. Fig. 6 shows the carbon profile for a single autocatalytic event. Here the carbon is seen to be trapped in the film of austenite between two sub-units. The relatively slow mobility of carbon in austenite along with this trapping effect prolongs the bainite transformation [21,42] enabling a volume fraction of bainite to form that is greater than if the concentration was distributed homogeneously. The concentration levels of the trapped austenite films may then exceed the concentration levels given by the T_0' curve [34].

The driving force distribution about a sub-unit is displayed in Fig. 4b. Due to the increased amount of carbon ejected into the austenite adjacent to the sub-unit, there is a larger reduction in driving force in these areas rather than at the tips of the sub-units where carbon saturation is to a lesser degree.

In models for calculating the kinetics of bainite transformation, an autocatalysis factor is often used to gauge the rate of autocatalysis [21]. In the present phase-field model this is implicitly taken into account by the random number generation along with the driving force so that the location and rate of autocatalysis is governed by the current state of the system. The nature of this method of incorporating autocatalysis enables carbon enrichment to affect
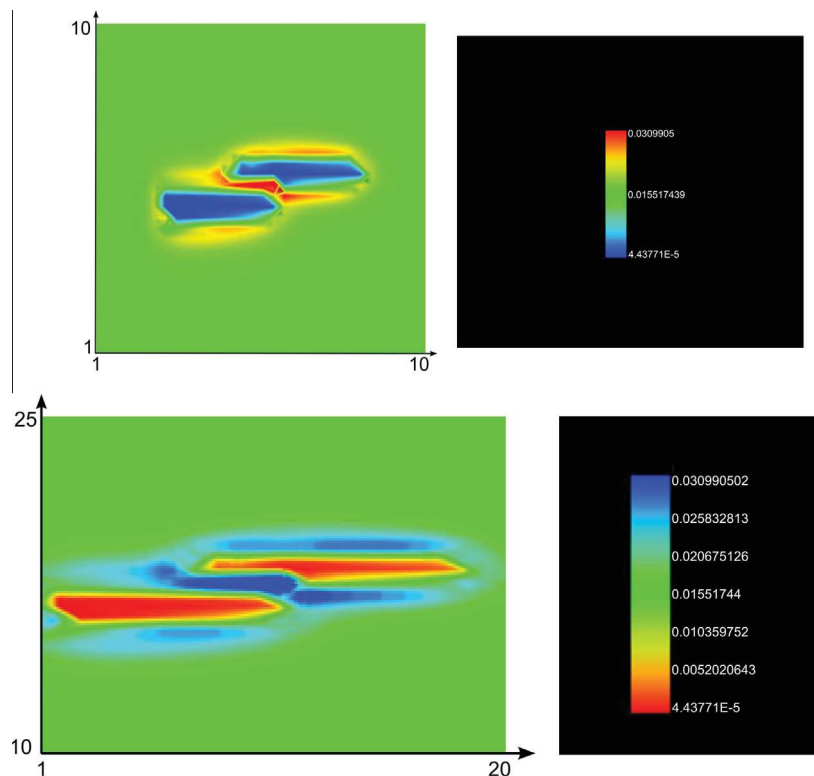

Fig. 6. The carbon concentration profile of a single autocatalysis (grid size = 100^3). The figures are of a small section of the simulation domain and not the entire domain itself.
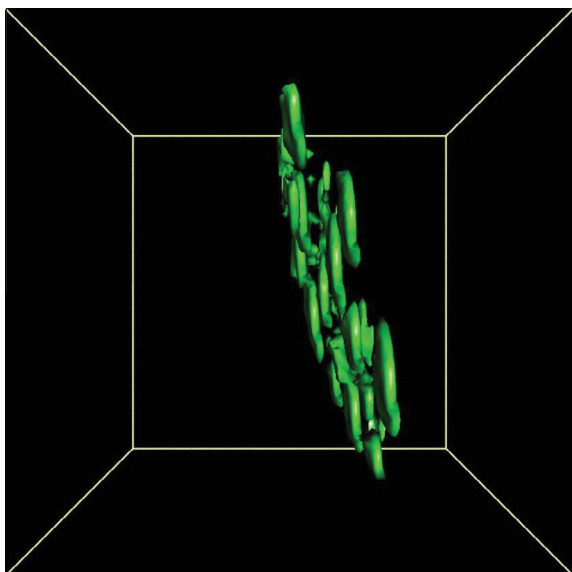
Fig. 7. A sheaf of bainitic sub-units (grid size = 100^3).

a particular sheaf while the less enriched blocky austenite is still allowed to transform [21]. The effect of an increase in carbon concentration is translated into the model through the k term of Eq. (10) reducing the driving force and subsequently the speed of growth until growth is no longer possible. This will enable the reproduction of the incomplete transformation phenomenon frequently seen in bainite formation [21].

The numerical results were obtained for a 100^3 and 150^3 grid. A larger domain will result in a more accurate visual representation since the interface between the two phases while remaining as four grid points will constitute a smaller fraction of the domain. The concentration mobility M_C was chosen as such because the value resulting from Eq. (16) while realistic is too small and subsequently slows the simulation. However, as long as the choice is much smaller than the phase-field mobility so as to not diffuse too far ahead of the interface, the results remain accurate. The current model can be adapted to simulate a whole sheaf by repeatedly applying the autocatalytic process as seen in Fig. 7. The driving force for the nucleation of bainite is expressed imperially as

$$\Delta G_m = G_n - \mu_1(W_s - T)$$

where μ_1 = 7.66 J/(mol K), G_n is the universal nucleation function given by $G_n = \mu_2 W_s - \mu_3$ where μ_2 = 3.6375 J/(mol K) and μ_3 = 2540 J/mol [15,34,35]. Here, W_s is the highest temperature at which ferrite can nucleate via a displacive mechanism. The condition for nucleation at a grain boundary is then $\Delta G_m < G_n$ [21]. In order to produce multiple sheaves of bainite, this condition for nucleation as well as the condition for growth can be used in the present model. The function $\beta(l(c))$ can be determined by simulations such as that in Fig. 1.

The phase-field variable ϕ in this paper is a means of determining the existence of the bainitic ferrite phase. When it comes to bainitic ferrite phases with different orientation, the growth direction (being different for each orientation) is incorporated implicitly into the model through the transformation matrix H_{ij} of Eq. (10). H_{ij} is an input parameter and is specified for each bainite sheaf. When considering multiple austenite grains, the orientation matrix of each austenite grain is then incorporated into H_{ij} by multiplying

it with the bainite sheaf transformation matrix. The presence of this transformation matrix enables the simulation of multiple sheaves of bainite within multiple grains of austenite with only a single phase-field variable.

The developed phase-field model utilises just a single phase-field order parameter reducing the computation time. The order parameter used is related to the volume fraction of bainite formed and can be extracted from the model. The phenomenological description enables a more realistic morphology of bainite formation in steels. Carbide formation has not been considered in the present work and may be considered in the future.

Acknowledgements

References

[1] N. Moelans, B. Blanpain, P. Wollants, Calphad 32 (2008) 268–294.
[2] R.S. Qin, H.K.D.H. Bhadeshia, Mater. Sci. Technol. 26 (2010) 803–811.
[3] A.A. Wheeler, W.J. Boettinger, G.B. McFadden, Phys. Rev. A 45 (1992) 7424–7439.
[4] R.S. Qin, E.R. Wallach, Acta Mater. 51 (2003) 6199–6210.
[5] U. Grafe, B. Böttger, J. Tiaden, S.G. Fries, Scripta Mater. 42 (2000) 1179–1186.
[6] T. Kitashima, Phillos. Mag. 88 (2008) 1615–1637.
[7] S.G. Fries, B. Böttger, J. Eiken, I. Steinbach, Int. J. Mater. Res. 100 (2009) 128–134.
[8] R.S. Qin, E.R. Wallach, R.C. Thomson, J. Cryst. Growth 279 (2005) 163–169.
[9] C.J. Huang, D.J. Browne, S. McFadden, Acta Mater. 54 (2006) 11–21.
[10] I. Loginova, J. Odqvist, G. Amberg, J. Agren, Acta Mater. 51 (2003) 1327–1339.
[11] L.Q. Chen, W. Yang, Phys. Rev. B 50 (1994) 15752–15756.
[12] L.Q. Chen, Annu. Rev. Mater. Res. 32 (2002) 113–140.
[13] J.M. Robertson, J. Iron Steel Inst. 119 (1929) 391–419.
[14] E.S. Davenport, E.C. Bain, Trans. AIME 90 (1930) 117–154.
[15] G. Sidhu, S.D. Bhole, D.L. Chen, E. Essadiqi, Scripta Mater. 64 (2011) 73–76.
[16] H.A. Aglan, Z.Y. Liu, M.F. Hassan, M. Fateh, J. Mater. Proc. Technol. 151 (2004) 268–274.
[17] K. Sawley, J. Kristan, Fatigue Fract. Eng. Mater. Struct. 26 (2003) 1019–1029.
[18] H.K.D.H. Bhadeshia, Steel Technol. Int. (1989) 289–294.
[19] D.V. Edmonds, R.C. Cochrane, Metall. Trans. A 21 (1990) 1527–1540.
[20] H.K.D.H. Bhadeshia, Bainite in Steels, second ed., Institute of Materials, Cambridge University Press, London, 2001.
[21] G.I. Rees, H.K.D.H. Bhadeshia, Mater. Sci. Technol. 8 (1992) 994–996.
[22] R.F. Mehl, Hardenability of alloy steels, American Society for metals, ASM, Cleveland, OH, 1939.
[23] H.K.D.H. Bhadeshia, Mater. Sci. Eng. A 273–275 (1999) 58–66.
[24] J. W. Christian and D.V. Edmonds, In: Phase transformations in ferrous alloys, Warrendale PA TMS-AIME, 1984,pp. 293–327.
[25] W. Song, U, Prahl, W. Bleck, K. Mukherjee, in: TMS 2011 140th Annual Meeting and Exhibition, Materials Fabrication, Properties, Characterization, and Modeling, Wiley, 2011, pp. 417–425 (ISBN 978-1-11802-946-6).
[26] S.G. Kim, W.T. Kim, T. Suzuki, Phys. Rev. E 58 (1998) 3316–3323.
[27] R.S. Qin, H.K.D.H. Bhadeshia, Acta Mater. 57 (2009) 2210–2216.
[28] H.K.D.H. Bhadeshia, Worked examples in the Geometry Of Crystals, second ed., The Institute of Materials, London, 2001.
[29] J. Wang, S. Van der Zwaag, Z. Yang, H.S. Fang, Mater. Lett. 45 (2000) 228–234.
[30] J.W. Cahn, J.E. Hilliard, J. Chem. Phys. 28 (1958) 258–266.
[31] S.L. Wang, R.F. Sekerka, A.A. Wheeler, B.T. Murray, S.R. Coriell, R.J. Braun, G.B. McFadden, Physica D 69 (1993) 189–200.
[32] P. Gustafson, Metall. 14 (1985) 259–267.
[33] B. Sundman, J. Agren, J. Phys. Chem. Solids 42 (1981) 297–301.
[34] G.I. Rees, H.K.D.H. Bhadeshia, Mater. Sci. Technol. 8 (1992) 985–993.
[35] S.M.C. Van Bohemen, M.C. Stefan, J. Sietsma, Int. J. Mater. Res. 99 (2008) 739–747.
[36] Z. Yang, R.A. Johnson, Mater. Sci. Eng. 1 (1993) 707–716.
[37] R.S. Qin, E.R. Wallach, J. Cryst. Growth 253 (2003) 549–556.
[38] J.C. Zhao, Mater. Sci. Technol. 8 (1992) 997–1003.
[39] W. Steven, A.G. Haynes, J. Iron Steel Inst. 183 (1956) 349–359.
[40] J.K. Lee, Prediction of tensile deformation behaviour of formable hot rolled steels. Posco Technical Research Laboratories. Pohang, Korea. (1999).
[41] S.M.C. Van Bohemen, Mater. Sci. Technol. 28 (2012) 487–495.
[42] S.A. Khan, H.K.D.H. Bhadeshia, Metall. Trans. A 21 (1990) 859–875.

Appendix F

A phase-field model for the formation of matensite and bainite

A phase-field model for the formation of martensite and bainite

Tansel T. Arif[1, a] and Rongshan Qin[1,b]

[1] Imperial College London, South Kensington Campus Exhibition Rd, London, UK, SW7 2AZ

[a]t.arif11@imperial.ac.uk, [b]r.qin@imperial.ac.uk

Keywords: Phase-field, displacive, martensite, bainite.

Abstract. The phase-field method is rapidly becoming the method of choice for simulating the evolution of solid state phase transformations in materials science. Within this area there are transformations primarily concerned with diffusion and those that have a displacive nature. There has been extensive work focussed upon applying the phase-field method to diffusive transformations leaving much desired for models that can incorporate displacive transformations. Using the current model, the formation of martensite, which is formed via a displacive transformation, is simulated. The existence of a transformation matrix in the free energy expression along with cubic symmetry operations enables the reproduction of the 24 grain variants of martensite. Furthermore, upon consideration of the chemical free energy term, the model is able to utilise both the displacive and diffusive aspects of bainite formation, reproducing the autocatalytic nucleation process for multiple sheaves using a single phase-field variable. Transformation matrices are available for many steels, one of which is used within the model.

Introduction

The phase-field (PF) modelling of microstructure evolution has evolved considerably with its current forms being established more than 20 years ago by Chen [1], Wang [2] and Langer [3]. However, in comparison to other more established methods, it is considered that the PF method is yet to sufficiently mature. While there have been many works focussed upon diffusion based growth such as solidification [4], grain growth [5,6] and solid-state sintering [7], there are few models established for realistic reproduction of the displacive transformations martensite and bainite.

There are two types of PF models when it comes to the application of the method. The first type (Type A) was derived from microscopic theory ([1,2]) and applied to solid-state phase transformations. The field variables in this type of model are related to physical order parameters such as the local composition and long-range order parameters corresponding to crystal symmetry. In the second type (Type B), the main variable is called the phase-field variable and is phenomenological in nature ([3]). This variable is introduced in order to relieve the computational strain of having to track the interfaces between domains explicitly. This type of model is more popular in solidification models.

We will be applying a PF model of the second type with a single PF variable to martensite formation and with an additional composition field variable to bainite formation. This is due to its phenomenological description and its ability to deal with larger systems with relatively low computational cost. The derivation of the model involves the PF parameters which are determined by comparison with observed macroscopic properties and with the sharp-interface equations at the zero-width limit. The value of the PF variable is considered constant within domains while varying continuously between two domains. The location of the interface between two domains is determined by the value of the PF variable.

Any further mention of the PF method will imply Type B as mentioned previously.

The phase-field model

A PF model begins with the description of the free energy of the system as a functional of the PF variable ϕ, the composition field C, and temperature T [8],

$$G = \int_{\Omega} \left[g(\phi, C, T) + \frac{1}{2} \varepsilon_C^2 (\vec{\nabla} C)^2 + \frac{1}{2} \varepsilon_\phi^2 (\vec{\nabla} \phi)^2 \right] d\vec{r} , \tag{1}$$

where ε_C and ε_ϕ are the gradient energy coefficients corresponding to the composition field and the PF variable respectively. g is the free energy density of the domain Ω. $\phi = 0$ refers to the parent phase and $\phi = 1$ refers to the product phase while $0 < \phi < 1$ is considered the interface between the two.

In steels, MT is accompanied by a transformation from a face-centered-cubic lattice to a body-centered-cubic lattice. The transition from the parent austenite phase to martensite is due to the chemical free energy difference of the two phases. The resulting morphology of the martensite grain is then due to the strain energy difference. While the chemical free energy of the two phases is important, there is no actual change in the composition field during martensite transformation in steel. This means that the free energy density need not involve any gradients of the composition field. The free energy density is then written in terms of the PF variable and the bulk free energy densities $g_{\alpha'}$ and g_γ of the martensite and austenite phases respectively as [8],

$$g = \frac{1}{2} \varepsilon^2 |\nabla \phi|^2 + \frac{1}{4\omega} \phi^2 (1-\phi)^2 + h(\phi) g_{\alpha'} + [1 - h(\phi)] g_\gamma , \tag{2}$$

where $h(\phi) = \phi^3 (6\phi^2 - 15\phi + 10)$ is the volume fraction of martensite. The coefficient ω is related to the kinetic barrier.

The governing equation for the PF variable is obtained by applying the second law of thermodynamics to Eq. 1 [8],

$$\frac{\partial \phi}{\partial t} = M_\phi \left[\varepsilon^2 \nabla^2 \phi - \frac{1}{2\omega} \phi(1-\phi)(1-2\phi) - 30\phi^2 (1-\phi)^2 (g_{\alpha'} - g_\gamma) \right], \tag{3}$$

where M_ϕ is called the PF mobility and is related to the rate of growth of the product phase which in this case is the martensite. $g_{\alpha'} - g_\gamma$ is the driving force for the transformation and we have equilibrium when $g_{\alpha'} = g_\gamma$. Note that this is different from diffusional transformations where the common tangent rule is applied.

The free energy change, $g_{\alpha'} - g_\gamma$, can be seperated into the free energy change due to the chemical free energy difference, $K = g_{\alpha'}{}^{chem} - g_\gamma{}^{chem}$, and that due to the strain energy difference, $g_{\alpha'\gamma}{}^{strain} = g_{\alpha'}{}^{strain} - g_\gamma{}^{strain}$. K is assumed to be constant for MT.

The strain energy difference can be approximated in the following form [9],

$$g_{\alpha'\gamma}{}^{strain} = \frac{c}{a} \mu \cdot \vec{m}^2 , \tag{4}$$

where $\vec{m} = \vec{s} + \vec{\delta}$ is the deformation vector with $\vec{s}$ and $\vec{\delta}$ the shear and dilatation vectors accompanying MT respectively. The dilatation vector is normal to the habit plane whereas the shear vector lies on the habit plane, i.e. $\vec{s} = \vec{s}_x + \vec{s}_y$ where the directions referred to as "x" and "y" are in the habit plane coordinate system. The constants c and a are the dimensions of the oblate ellipsoidal shape of the martensite plates.

The components of the deformation vector are proportional to the rate of change of the PF variable [10],

$$s_x \propto \frac{\partial \phi}{\partial x}, \ s_y \propto \frac{\partial \phi}{\partial y}, \ \delta \propto \frac{\partial \phi}{\partial z}. \tag{5}$$

Using Eq. 4 along with Eq. 5 and assuming an isotropic distribution of the chemical free energy, the free energy difference in Eq. 3 can be written as,

$$g_{\alpha'\gamma} = (k_s^{\ 2} + K)\phi_{,x}^{\ 2} + (k_s^{\ 2} + K)\phi_{,y}^{\ 2} + (k_\delta^{\ 2} + K)\phi_{,z}^{\ 2}, \tag{6}$$

where $\phi_{,x} = \frac{\partial \phi}{\partial x}$ and k_s and k_δ are constants related to the shear and dilatation parameters respectively. Unless $g_{\alpha'\gamma} < 0$, no transformation occurs.

Intuitively, since strain energy works to increase the system free energy, there must be a larger positive contribution from the z direction to the total free energy due to strain. This will deem growth in that direction less favourable and so $k_\delta^{\ 2} > k_s^{\ 2}$.

Eq. 6 is now incorporated into Eq. 3 to give the governing equation in the martensite coordinate system,

$$\frac{\partial \phi}{\partial t} = M_\phi [\varepsilon^2 \nabla^2 \phi - \frac{1}{2\omega} \phi(1-\phi)(1-2\phi)$$
$$- 30\phi^2 (1-\phi)^2 ((k_s^{\ 2} + K)\phi_{,x}^{\ 2} + (k_s^{\ 2} + K)\phi_{,y}^{\ 2} + (k_\delta^{\ 2} + K)\phi_{,z}^{\ 2})]. \tag{7}$$

Given a transformation matrix, H_{ij}, from the martensite coordinate system to the austenite coordinate system, the governing equation can now be written in the austenite coordinate system as,

$$\frac{\partial \phi}{\partial t} = M_\phi [\varepsilon^2 \nabla^2 \phi - \frac{1}{2\omega} \phi(1-\phi)(1-2\phi) - 30\phi^2 (1-\phi)^2$$
$$\times \sum_{i=1}^{3} (k_i^{\ 2} + K)(H_{i1}\phi_{,x} + H_{i2}\phi_{,y} + H_{i3}\phi_{,z})^2 \ ]. \tag{8}$$

This transformation matrix is available for many steels and will be specified later in this work. One can now utilise Eq. 8 to simulate martensite formation in austenite.

Bainite, just like martensite, is displacive in nature but also involves diffusion of the interstitial elements [11]. One big difference is that bainite has a sub-unit structure where a single plate of sheaf is formed of many sub-plates o sub-units. These sub-units are what form via a displacive process as supersaturated ferrite with the diffusion occurring after each sub-unit has grown. So there are brief periods during the growth of a sheaf where diffusion occurs between subsequent growths of sub-units.

To incorporate this into the model, the constant K is no longer assumed constant. Additionally, a concentration field is included to track the local concentration. The evolution of the concentration field is governed by the Cahn-Hilliard diffusion equation [12],

$$\frac{\partial C}{\partial t} = \nabla \cdot [D\nabla C], \tag{9}$$

where $D = M_C \dfrac{\partial^2 g}{\partial C^2}$ is the diffusivity and M_C is the concentration mobility. D can be calculated locally via,

$$\frac{\partial^2 g}{\partial C^2} = h(\phi)\frac{\partial^2 g_{\alpha B}^{chem}}{\partial C^2} + \left[1 - h(\phi)\right]\frac{\partial^2 g_{\gamma}^{chem}}{\partial C^2}, \tag{10}$$

where the subscript $g_{\alpha B}$ refers to the baintie phase. The second derivatives of the bulk free energies with respect to concentration can be calculated using a regular solution model form [10,13].

Simulations

The following parameters are chosen for the simulations: $M_{\phi} = 100$, $M_C = 0.00046$, $\varepsilon^2 = \dfrac{3\lambda\sigma}{1.1}$, $\omega = \dfrac{\lambda}{26.4\sigma}$, $\lambda = 14.3nm$, $\sigma = 0.72$. $k_s - K = 1$ and $k_{\delta} - K = 0.01$ for the martensite plate simulations. The lattice spacing is $\Delta x = 0.5\lambda$. The simulations of bainite are performed at a temperature of $500^{\circ}C$ with a carbon content of $0.241wt\%$ distributed homogeneously. The matrix H_{ij} used here is given for a Fe-8Cr-1C steel as,

$$H = \begin{pmatrix} 0.584634 & 0.519305 & 0.119189 \\ -0.529661 & 0.583719 & 0.059597 \\ -0.046858 & -0.118861 & 0.813418 \end{pmatrix}. \tag{11}$$

By symmetry, another 23 forms of this matrix can be obtained. For the simulation of martensite plates, 2 austenite grains are grown on a 100^3 grid with 80 martensite nuclei placed on the boundaries of the austenite grains. Fig. 1 shows a single plate nucleated at the center of the domain.
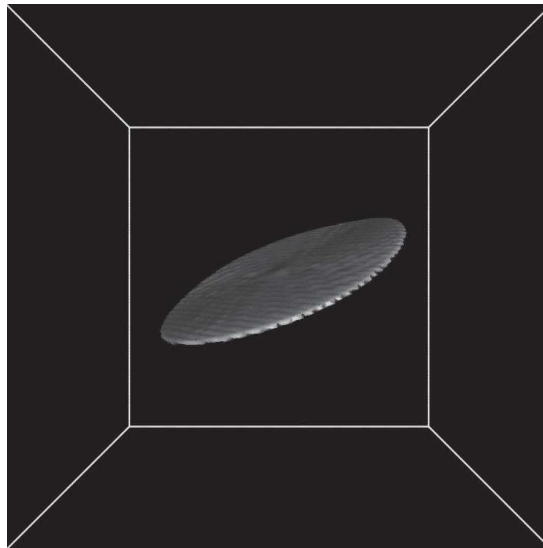
Fig. 1. Simulation of a single plate at the center of the domain using the model. (Domain size 100^3)

A single ferritic sub-unit of a bainite sheaf is simulated to display the diffusion of carbon out of the supersaturated ferrite. This is shown in Fig. 2. A single plate is nucleated at the center of the domain within a homogeneous distribution of carbon. The plate is grown to a given size which is too fast for diffusion. The subsequent diffusion process ejects the carbon from the bainitic ferrite. This process continues until chemical equilibrium is reached within the sub-unit. The large chemical driving force forces the diffusion of carbon from the ferrite into the austenite at a high rate while

reducing in the austenite which causes a build up of carbon concentration in the vicinity of the plate. An entire domain is simulated in Fig. 3 with several autocatalytic reactions forming sheaves. We use a uniform random number generator in the surrounding area of the sub-units which is scaled by the driving force which is dependent on the concentration. The tip of the sub-unit has a lower build-up of carbon and so has a higher driving force and subsequently a higher chance of nucleation.
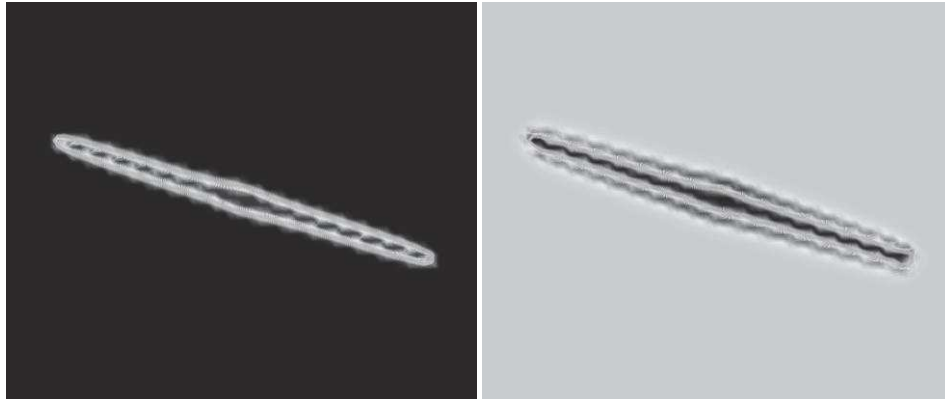

Fig. 2. Figure of a single sub-unit nucleated at the center of the domain. The phase-field profile across a sub-unit (left) and the carbon profile across the same sub-unit during the diffusion process (right).

Fig. 3. Figures of bainite formation at 10,000 time steps (left) and 28,000 time steps (right) in two austenite grains. The part of the domain marked in red indicates the growth of two sheaves via autocatalysis.

Summary

A phase-field model has been presented with the ability to simulate martensite plates and bainite sheaves. The computational cost is only dependent on the size of the domain and not the number of grains of martensite, bainite or austenite. Each grain is assigned a global ID in order to distinguish it from other grains. This is not included in evolution equations and thus does not have any impact on the computational resources. The treatment involving global IDs enables the simulation of two or more grains in close proximity without the model being confused as to the identity of each grain. The treatment of autocatalysis uses a uniform random number generator but the possibility of a new nucleation at a point is gauged by the driving force at that location. This approach enables the simulation of bainite while also taking into account the composition changes during transformation.
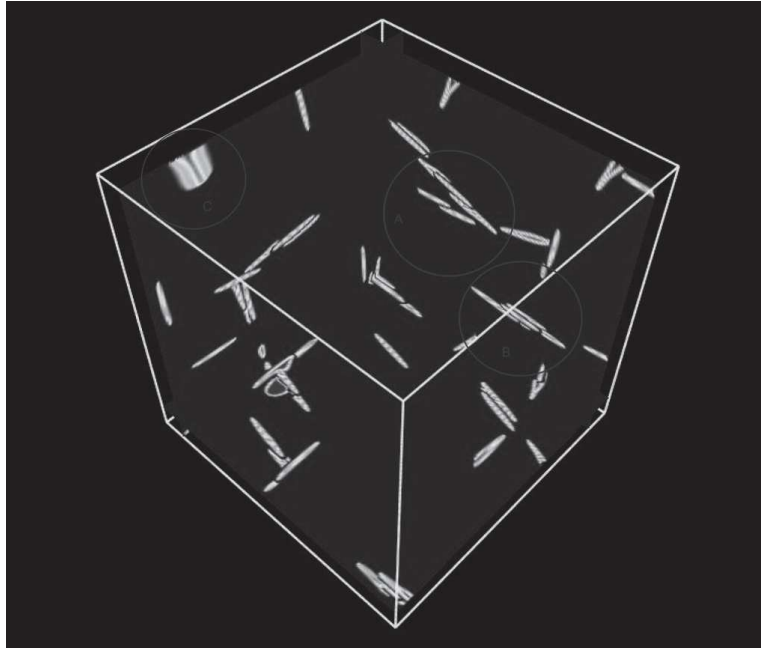
Fig. 4. Cross section views of a simulation for sheaf formation. *A* and *B* are two forming sheaves whereas *C* is an intersection of the cross section with a larger portion of a sub-unit.

References
[1] L. Chen, A. Khachaturyan, Computer simulation of structural transformations during precipitation of an ordered intermetallic phase, Acta metallurgica et materialia 39(1991) 2533–2551.
[2] Y. Wang, L.-Q. Chen, A.G. Khachaturyan, Kinetics of strain-induced morphological transformation in cubic alloys with a miscibility gap, Acta Metallurgica et Materialia 41(1993) 279–296.
[3] J. Langer, Models of pattern formation in first-order phase transitions, in: G. Grinstein and G. Mazenko (Eds.) Directions in Condensed Matter Physics, World scientific, Singapore, 1986, pp. 165–185.
[4] W.J. Boettinger, J.A. Warren, C. Beckermann, A. Karma, Phase-Field Simulation of Solidification 1, Annual Review of Materials Research 32(2002) 163–194.
[5] L. Chen and W. Yang, Computer simulation of the domain dynamics of a quenched system with a large number of nonconserved order parameters: The grain-growth kinetics, Physical Review B 50(1994).
[6] I. Steinbach, F. Pezzolla, B. Nestler, A phase field concept for multiphase systems, Physica D: Nonlinear …, 94(1996) 135–147.
[7] A. Kazaryan, Y. Wang, B. Patton, Generalized phase field approach for computer simulation of sintering: Incorporation of rigi-body motion, Scripta Mater. 41(1999) 487–492.
[8] A. Wheeler, W. Boettinger, G. McFadden, Phase-field model for isothermal phase transitions in binary alloys, Physical Review A 45(1992) 7424–7440.
[9] H. K. D. H. Bhadeshia, Worked examples in the Geometry of Crystals Second edition, London, 1987
[10] T.T. Arif, R.S. Qin, A phase-field model for bainitic transformation, Computational Materials Science 77(2013) 230–235.
[11] H. K. D. H. Bhadeshia, Bainite in steels Second edition, London, 1992.
[12] J. W. Cahn, J. E. Hilliard, Free energy of a nonuniform system. I. Interfacial free energy, J. Chem. Phys. 28(1958) 258–266.
[13] B. Sundman, J. Ågren, A regular solution model for phases with several components and sublattices, suitable for computer applications, Journal of physics and chemistry of solids 42(1981) 297-301.

Appendix G

SPH Kernel and smoothing length influence on the evolution of a van der Waals fluid

Manuscript Submitted for Publication

SPH Kernel and smoothing length influence on the evolution of a van der Waals fluid

T. T. Arif[a,*], R. S. Qin[a,*]

[a]*Department of Materials, Imperial College London, Exhibition Road, London SW7 2AZ, UK*

Abstract

The effects of the smoothed particle hydrodynamics (SPH) smoothing length and kernel on the evolution of a thermodynamic/hydrodynamic system involving van der Waals (vdW) forces is studied. It is natural to assume discrepancy between the evolution of two identical hydrodynamic systems when simulated using different cut-off radii and smoothing function. Different SPH user specified parameters such as the smoothing length and the extent of averaging is shown to have an effect on evolution data of such systems, especially the total entropy change.

Keywords: `Smoothed particle hydrodynamics`, SPH, van der Waals, hydrodynamics, droplet

1. Introduction

Smoothed particle hydrodynamics (SPH) is a popular simulation tool applied to fluid dynamics problems. SPH is a meshfree method in that the interpolation points are the free-moving particles themselves. Each particle represents a volume of the fluid carrying the properties of that region along with them. The typical properties associated with each particle are the mass, velocity, temperature, internal energy, entropy change etc... While often more computationally demanding than grid-based methods developed for specific phenomena, its advantages include improved stability and the ability to deal with high velocities and free surface flow. It exceptionally handles cases with deformable and irregular boundaries/interfaces and provides ease of adding additional effects. These features are naturally extended to three dimensions. SPH codes are often much easier to implement when compared to, say, implicit finite difference schemes. Originally developed for astrophysical problems [1] and applied to moon formation [2, 3], incorporation of special relativity [4, 5], collisions of astronomical objects [6, 7, 8], SPH has been used extensively in the area of fluid mechanics. The value of any field property at a location in space is calculated as a sum over all the weighted contributions from neighbouring particles. The function determining the distance dependent weight of a contribution within this sum is called the kernel function.

Liquid droplet formation due to van der Waals (vdW) forces may involve free surfaces, moving interfaces and in cases of collisions, high impact velocities. Unlike many other methods, SPH can comfortably deal with these issues. The evolution of a vdW droplet towards an equilibrium involves surface tension. This surface tension and its effects on interface properties and forces are important for understanding many phenomena observed in materials science such as, fluid flow in low gravity [9, 10], internal combustion engines [11], cloud behaviour [12] and cavitation [13]. Other applications involve food processing, fuel injection systems, enamelling and metal casting.

Other methods have been used for modelling liquid drop formation and surface tension [14, 15]. Brackbill et al. model surface tension using a grid-based approach by applying a continuous transition region as the interface between two fluids [16] . This transition region is characterised by a continuous function obtained from its discrete counterpart by utilising an interpolation function much like the kernel functions used in SPH formulation.

---

*Corresponding author
Email addresses:* `t.arif11@imperial.ac.uk` (T. T. Arif), `r.qin@imperial.ac.uk` (R. S. Qin)

In Section (2) we present the basic formulation of SPH for application to vdW droplets. Then in Sections (3) and (4), some information and procedures about the simulations are given. In Section (5), we present the simulation results and highlight inconsistencies in results. Once this is done, it is shown that a few simple techniques can reduce inconsistencies.

2. SPH equations for vdW

The governing equations of hydrodynamics are given in particle form as:

$$\left(\frac{d\mathbf{r}}{dt}\right)_i = \mathbf{v}_i \tag{1}$$

$$\left(\frac{d\rho}{dt}\right)_i = -\rho_i(\nabla \cdot \mathbf{v})_i \tag{2}$$

$$\rho_i\left(\frac{d\mathbf{v}}{dt}\right)_i = (\nabla \cdot \sigma)_i + \rho_i g \tag{3}$$

$$T_i\left(\frac{dS}{dt}\right)_i = m_i\frac{\phi_i}{\rho_i} + m_i\frac{\kappa}{\rho_i}(\nabla^2 T)_i \tag{4}$$

$$\rho_i\left(\frac{dU}{dt}\right)_i = \mathbf{P}_i : (\nabla\mathbf{v})_i - (\nabla \cdot \mathbf{q})_i \tag{5}$$

$$(\mathbf{P})_i = -P_i\mathbf{I} + \sigma_i \tag{6}$$

$$(\sigma)_i = \eta\left[(\nabla\mathbf{v})_i + (\nabla\mathbf{v}^T)_i\right] + (\zeta - \frac{2}{d}\eta)(\nabla \cdot \mathbf{v})_i\mathbf{I} \tag{7}$$

$$\phi_i = 2\eta((\overline{\nabla\mathbf{v}})_i : (\overline{\nabla\mathbf{v}})_i) + \zeta(\nabla \cdot \mathbf{v})_i^2 \tag{8}$$

$$(\overline{\nabla\mathbf{v}})_i = \frac{1}{2}((\nabla\mathbf{v})_i + (\nabla\mathbf{v})_i^T) - \frac{1}{d}(\nabla \cdot \mathbf{v})_i\mathbf{I} \tag{9}$$

$$\mathbf{q}_i = -K(\nabla T)_i \tag{10}$$

where $\mathbf{r}$, $\mathbf{v}$, m, P, T, S, U and ρ is the position, velocity, mass, pressure, temperature, entropy, internal energy and mass density respectively. The quantity g is a body force - induced acceleration, $\mathbf{I}$ is the unit tensor, σ is the viscous stress tensor, $\nabla\mathbf{v}^T$ is the transpose of the tensor $\nabla\mathbf{v}$ and : denotes the dyadic product. The constant d denotes the dimension of the problem whereas constants η, ζ and κ are respectively the shear and bulk viscosities and the coefficient of thermal conductivity. U is the internal energy, $\mathbf{P}$ is the stress tensor, $\mathbf{q}$ is the heat flux vector and ϕ is the viscous heating field. The subscript i refers to evaluation at particle i and the operator $\nabla = (\frac{\partial}{\partial x}, \frac{\partial}{\partial y}, \frac{\partial}{\partial z})$ is the spatial derivative operator.

For a van der Waals fluid, the equations of motion are closed by the equations of state for the pressure and the internal energy:

$$P_i \quad = \frac{\bar{k}_B\rho_i T_i}{1 - \bar{b}\rho_i} - \bar{a}\rho_i^2 \tag{11}$$

$$U_i \quad = \frac{\zeta}{2}\bar{k}_B T_i - \bar{a}\rho_i, \tag{12}$$

where $\bar{a} = a/m^2$ and $\bar{b} = b/m$ are the usual vdW fluid parameters with a being responsible for long range attractive forces, and b is related to the finite volume of an atom/molecule.

The typical SPH interpolations for a field variable $f(\mathbf{r})$ and its gradient are:

$$f_i \quad = \sum_{j=0}^{N}\frac{m_j}{\rho_j}f_j W_{ij}$$

$$\nabla f_i \quad = \sum_{j=0}^{N}\frac{m_j}{\rho_j}f_j \nabla_i W_{ij}, \tag{13}$$

2

where $f_i = f(\mathbf{r}_i)$ and $W_{ij} = W(\mathbf{r}_i - \mathbf{r}_j, h)$ is called the kernel function with h the smoothing length. Equations (13) can be used to discretize the variables and their gradients in the equations of motion. For example, the density at each particle may be approximated by replacing f_i with ρ_i in Eq. (13) to give

$$\rho_i = \sum_{j=0}^{N} \frac{m_j}{\rho_j} \rho_j W_{ij} = \sum_{j=0}^{N} m_j W_{ij}. \tag{14}$$

Eq. (13) includes the self term but $\nabla_i W_{ii} = 0$ for the kernels used here. Equation (14) conserves total mass and will be used to evolve density according to particle positions instead of Eq. (2). When it comes to the gradient of a field function, the appearance of paired terms on the right-hand side of the equation is preferred, for example, the appearance of f_i as well as f_j on the right-hand side of Eq. (13) is often desired due to its symmetric contribution. Thus, a variety of different discretization forms are available. This paired form will be apparent in the SPH equations to follow. The effect of the kernel function is to smooth particle properties over a region depending on particle positions and acts as a weighting function. The kernel function also gives SPH the unique ability to form gradients by applying the gradient to the kernel function rather than the property fields (which are discrete). There are many forms for the kernel function and a classic study of SPH involves introduction of different forms that cater for different effects. For instance, the Gaussian kernel often used to simplify SPH analysis from a physical point of view, the quartic and quintic spline kernels introduced to be more stable than the Gaussian kernel [17], the quadratic smoothing function for high velocity impacts [18] and many more. The kernel functions that appear in this paper are the Lucy function [1], cubic spline (CS) [19] and the hyperbolic-shaped kernel (HS) [20]. While there are many other functions used as kernels, we believe the 3 categories represented by these kernels as comprising almost all popular kernel types: piece-wise kernels with a negative second derivative, single-function kernels with a negative second derivative, and kernels with a positive second derivative remedying instability problems. These are given respectively as:

$$W_L(R, h) \quad = \alpha_L \times \begin{cases} (1 + 3R)(1 - R)^3 & 0 \leq R < 1 \\ 0 & R \geq 1 \end{cases} \tag{15}$$

$$W_{cs}(R, h) \quad = \alpha_{cs} \times \begin{cases} (2 - R)^3 - 4(1 - R)^3 & 0 \leq R < 1 \\ (2 - R)^3 & 1 \leq R < 2 \\ 0 & R \geq 2 \end{cases} \tag{16}$$

$$W_{hs}(R, h) \quad = \alpha_{hs} \times \begin{cases} R^3 - 6R + 6 & 0 \leq R < 1 \\ (2 - R)^3 & 1 \leq R < 2 \\ 0 & R \geq 2 \end{cases} \tag{17}$$

where $R = \frac{\mathbf{r}_i - \mathbf{r}_j}{h} = \frac{r_{ij}}{h}$ and for a one dimensional system $\alpha_L = 5/4h$, $\alpha_{cs} = 1/6h$, $\alpha_{hs} = 1/7h$, for a two dimensional system $\alpha_L = 5/\pi h^2$, $\alpha_{cs} = 5/14\pi h^2$, $\alpha_{hs} = 1/3\pi h^2$, and finally for a three dimensional system $\alpha_L = 105/16\pi h^3$, $\alpha_{cs} = 1/4\pi h^3$, $\alpha_{hs} = 15/62\pi h^3$. Kernel functions are subjected to a number of conditions, one of which is the normality condition [21]. This normality condition is how the coefficients α_L, α_{cs} and α_{hs} are determined. The gradient of the kernel function ($\nabla_i W_{ij}$) appearing in Eq. (13) is with respect to position i so that $\nabla_i W_{ij} = -\nabla_j W_{ij}$.

The SPH form for the gradients of the field variables and equations of motion are given as [22, 23, 21]:

$$(\nabla \mathbf{v})_i = \sum_{j=0}^{N} \frac{m_j}{\rho_{ij}} (\mathbf{v}_j - \mathbf{v}_i) \nabla_i W_{ij} \tag{18}$$

$$(\nabla T)_i = \sum_{j=0}^{N} \frac{m_j}{\rho_{ij}} (T_j - T_i) \nabla_i W_{ij} \tag{19}$$

$$(\nabla^2 T)_i = 2\rho_i \sum_{j=0}^{N} m_j \frac{\mathbf{r}_{ij} \nabla W_{ij}}{\rho_i \rho_j} \mathbf{v}_{ij}^2 \tag{20}$$

$$\frac{(\nabla \cdot \mathbf{P})_i}{\rho_i} = \sum_{j=0}^{N} m_j \left(\frac{\mathbf{P}_i}{\rho_i^2} + \frac{\mathbf{P}_j}{\rho_j^2} \right) \cdot \nabla_i W_{ij} \tag{21}$$

$$\frac{(\nabla \cdot \mathbf{q})_i}{\rho_i} = \sum_{j=0}^{N} m_j \left(\frac{\mathbf{q}_i}{\rho_i^2} + \frac{\mathbf{q}_j}{\rho_j^2} \right) \cdot \nabla_i W_{ij} \tag{22}$$

$$(\frac{d\mathbf{v}}{dt})_i = \sum_{j=0}^{N} m_j \left(\frac{\mathbf{P}_i}{\rho_i^2} + \frac{\mathbf{P}_j}{\rho_j^2} \right) \cdot \nabla_i W_{ij} + \mathbf{g}_i \tag{23}$$

$$(\frac{d\mathbf{u}}{dt})_i = \frac{1}{2} \sum_{j=0}^{N} m_j (\frac{\mathbf{P}_i}{\rho_i^2} + \frac{\mathbf{P}_j}{\rho_j^2}) : (\mathbf{v}_j - \mathbf{v}_i) \nabla_i W_{ij}$$
$$- \sum_{j=0}^{N} m_j (\frac{\mathbf{q}_i}{\rho_i^2} + \frac{\mathbf{q}_j}{\rho_j^2}) \cdot \nabla_i W_{ij} \tag{24}$$

$$\phi_i = \frac{m_i}{\rho_i} \left[(\frac{\zeta}{2} - \frac{5\eta}{6}) \sum_j \frac{m_j}{\rho_j} \mathbf{r}_{ij} \frac{\mathbf{v}_{ij}^2}{r^2} \nabla_i W \right.$$
$$\left. - \frac{5}{2}(\zeta + \frac{\eta}{3}) \sum_j \frac{m_j}{\rho_j} \mathbf{r}_{ij} (\hat{\mathbf{r}}_{ij} \cdot \mathbf{v}_{ij})^2 \nabla_i W \right] \tag{25}$$

where $r = |\mathbf{r}_{ij}| = |\mathbf{r}_i - \mathbf{r}_j|$, $\hat{\mathbf{r}}_{ij} = \mathbf{r}_{ij}/r$, $\rho_{ij} = \frac{1}{2}(\rho_i + \rho_j)$ and $\mathbf{v}_{ij} = \mathbf{v}_i - \mathbf{v}_j$. It should be noted that the SPH forms of the equations of motion are not unique. The momentum equation for instance, Eq. (23), is the preferred format of monaghan [21] derived to be symmetric.

Equations (1) - (4), the equations of state (11) and (12) along with suitable boundary conditions are sufficient to completely describe the evolution of a fluid system. However, proceeding with these set of governing equations, one finds unstable results and incorrect dynamics pertaining to vdW droplets. This was attributed to the assumption that the second long range attractive term in Equation (11) acted over the same short range as that of the first short-range repulsive term. It was found that considering the attractive forces to act over a greater smoothing length results in correct dynamics and a better description of surface tension.

Following Nugent and Posch [24], we assume that the cohesive pressure term, second term on the right-hand side of Eq. (11), acts on a larger interaction range and so is considered in SPH with a larger smoothing length $H > h$. Isolating this term in Eqs. (23) and (24) results in the following additional terms to be considered over a larger range:

$$(\frac{d\mathbf{v}}{dt})_i^a = 2\bar{a} \sum_{j=0}^{N} m_j \nabla_i W ij^H \tag{26}$$

$$(\frac{d\mathbf{u}}{dt})_i^a = \bar{a} \sum_{j=0}^{N} m_j (\mathbf{v}_j - \mathbf{v}_i) \cdot \nabla_i W ij^H \tag{27}$$

$$\tag{28}$$

where the superscripts a and H denote the additional cohesive pressure term and the kernel function calculated at a larger

4

smoothing length respectively. This extra term acting on a long range is an attractive, symmetric and central force. This means that its effects are cancelled within the bulk of a homogeneous phase. At the surface or interface however, the asymmetry of the forces resulting from this term contributes to the surface tension [16, 24].

3. Parameter specification and equations

It is common to expect multiple forms of the SPH equations in different circumstances. For instance, recently Yang et al. [20] proposed a new kernel function to resolve instability issues. Even though such suggestions often result in better and more stable results, the effect they have on the evolution process and time is still of great importance. First we consider the effect of using the single step heat conduction equation instead of the form in Eq. (24) [20],

$$(\nabla \cdot q)_i = -\rho_i K \sum_{j=0}^{N} \frac{2m_j \mathbf{r}_{ij} \cdot \nabla_i W_{ij}}{\rho_i \rho_j (r_{ij}^2 + 0.01h^2)} (T_j - T_i) \tag{29}$$

The results are shown in Fig. 1. It can be seen that although the density, temperature and pressure profiles are almost the same, the entropy profile is much more stable and reaches equilibrium much sooner. Based on this and on reports [25, 20] that for higher smoothing lengths the temperature profile obtained is smoother, we will be using the single step heat conduction calculation for the rest of this article.

4. Simulation procedures

The smoothing length, h, is chosen for each kernel function such that the effective smoothing range is equal. For Lucy's function, the support domain of each particle is $\mathfrak{H} = h$ whereas for the HS and CS kernels it's $\mathfrak{H} = 2h$. The effective smoothing range for such simulations are often around $\mathfrak{H} = 5\Delta x$ where Δx is the initial particle spacing. This results in a staggering long range smoothing length of $\mathcal{H} = 10\Delta x$. There are reports of exceedingly long running times for the simulation of vdW forces due to the existence of the long range force. Here we study the effects of the differences in results due to the selection of different smoothing lengths and so the selection of the kernel function should be able to reproduce results at smaller smoothing lengths. A large heat conductivity of $k = 5$ is chosen throughout the simulations in order to reduce density fluctuations due to yet unequilibrated temperature distributions. The initial system domain, unless otherwise stated, is homogeneous as in Fig. (2) with 30x30 particles placed in a square grid initial arrangement with no boundary conditions to simulate vacuum conditions.

4.1. Time step

Due to the large density differences at the liquid droplet/vacuum interface and the high sensitivity of the equation of state to density changes, a smaller time step is required in order for the simulation to retain numerical stability. The numerical instability in question occurs due to the asymptote in the denominator of the equation of state for pressure. Considering only the hydrostatic pressure term in the stress tensor, a plot of the dependence of velocity on density is given in Fig. 3 both for $T = 0.2$ and $T = 0.8$ with the vdW parameters: $\bar{a} = 2$, $\bar{b} = 0.5$ and $\bar{k} = 1$. The gradient of the kernel in Eq. 23 is assumed to be a constant value and so Fig. 3 should only be viewed as a comparison of the density influence between the different temperatures. It is seen from the figure that the velocity gradient is larger for $T = 0.2$ (i.e. more sensitive to changes in density, or equivalently, to particle positions). For this reason we choose a small time step of 0.005 for the liquid drop formation in a vacuum. For the case of agglomeration within a fluid substance, a larger time step of 0.05 can be utilised due to smaller density differences [24].
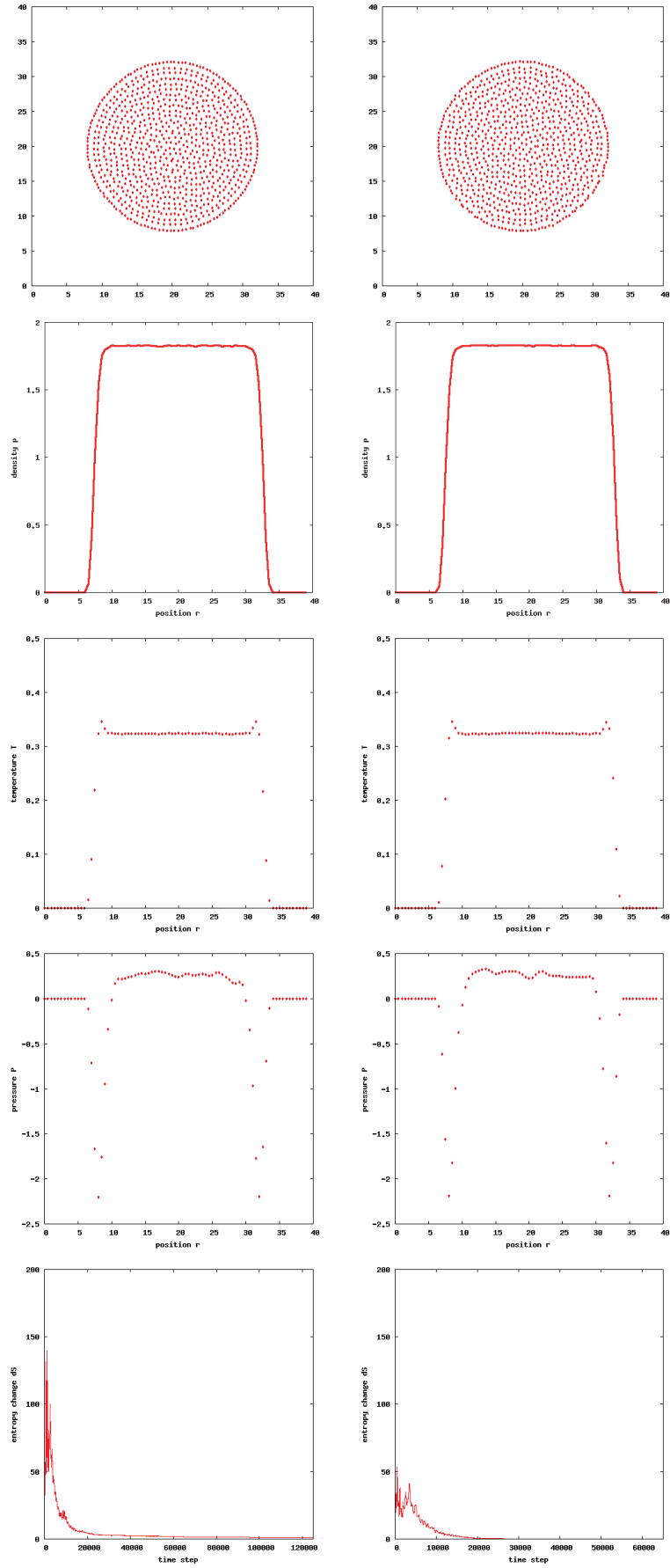
Figure 1: Simulation results with h=2, H=4 using the heat conduction form of Eq. 24 (left) and the single step version (right). Lucy's function is used as the kernel function. The rows from top to bottom, in order, are of the particle positions, density profile, temperature profile, pressure profile and time dependent entropy change.
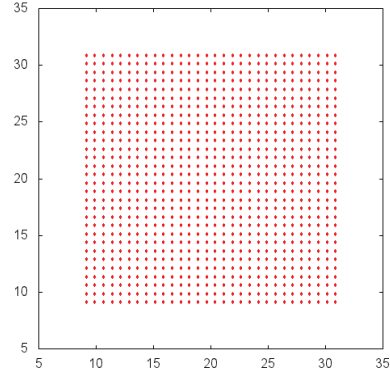
Figure 2: Initial positions of the 30×30 SPH particles.
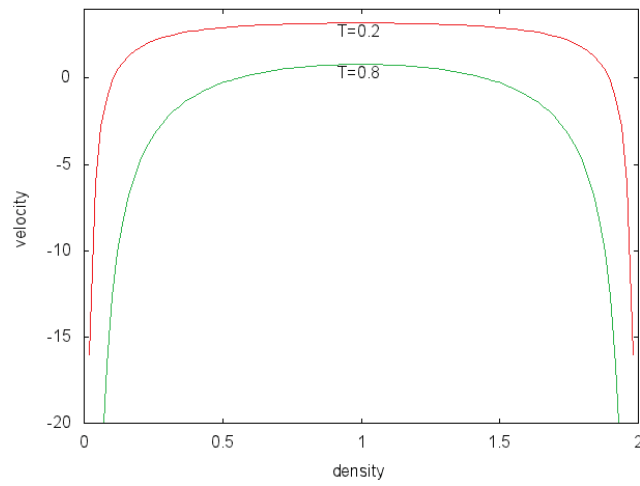

Figure 3: Velocity dependence on the density with $T = 0.2$ (red) and $T = 0.8$ (green). $\bar{k} = 1$ and vdW parameters $\bar{a} = 2$ and $\bar{b} = 0.5$.

4.2. Selection of a suitable kernel function

When it comes to the selection of the kernel function there are many options that have been used in the past years. To begin with, we run simulations using Lucy's function, CS and HS kernels on a vdW homogeneous gas/fluid at initial temperature $T = 0.2$ without periodic boundary conditions (within a vacuum environment) and without random fluctuations. The results are shown in figures 8 - 13. In Fig. 1 the resulting particle positions are nicely spaced out using Lucy's kernel function for $h = 2$ and $H = 4$. However, once the smoothing length is increased to $h = 3$ and $H = 6$, the resulting particle positions involve more clustering as seen in Fig. 4. This clustering above a certain smoothing length can be explained by looking at the second derivatives of Lucy's kernel function (Fig. 5). The initial particle spacing for the simulations is 0.75 and this value changes very little with the parameters used. For $h = 2$, the second derivative of Lucy's kernel is always positive. However, increasing the smoothing length to $h = 3$ but keeping the initial particle spacing as 0.75, results in the second derivative being negative which is associated with tensile instability [26].

4.3. Interpretation of results

As well as using actual particle values to form a profile as a function of radius, the results such as the density and pressure profiles are calculated according to physical positions across the system domain using the SPH smoothing technique by utilising Eq. 13 (i.e. results are displayed for both a smoothing length of h as well as a function of radius). The smoothing length chosen to interpret the results has a larger effect on the interface region rather than the bulk. We consider the entropy change of evolution as an appropriate quantity as an indication of equilibrium. It can be seen from Eq. 4 that the entropy change is a function of relative velocities and temperatures. This can be reinterpreted as the evolution speed of the system. If the entropy change levels of at zero, this means the system is at equilibrium. An entropy change of < 0.0001 is chosen as the equilibrium condition to display results for comparison. Thus, the system may still be evolving toward equilibrium at a very slow speed.

5. Smoothing length study

The following simulations are run for varying smoothing lengths. It is common in literature to see a smoothing length of $\mathfrak{H} = 5\Delta x$ and a long range smoothing length of $\mathcal{H} = 2h$. The latter is almost always the case. Here we study the effect of different smoothing lengths on the results of vdW drops. We begin with a smoothing length of $\mathfrak{H} = 2\Delta x$ and $\mathcal{H} = 2h$ and systematically increase $\mathfrak{H}$ to $4\Delta x$ for the following cases. The particle positions are shown in figures 8 - 13.

From Table 1 it can be seen that there is a large variation in both temperature results and total entropy results for differing smoothing lengths (and this trend continues for larger smoothing lengths). The inconsistency of the resulting entropy change is thought to be due to the clumping up of the SPH particles. Notice the HS has a lower total entropy change when compared to the other two kernels.

Surface pressure is proportional to the interface curvature and surface tension resolves a force normal to the interface toward its center of curvature. The equilibrium shape of a vdW drop in the absence of external forces is a sphere. The results show that the resulting shape differs slightly from being spherical if h is too small.

It is important to note that the temperature profiles as seen in figures 8 - 11 have inconsistencies at the sufaces [24]. However, a plot of the particle temperatures as in Fig. 6 shows that in fact, all particles have equal temperatures and the positive/negative deviations are caused by the free surface and the cut-off distance of the kernel.

It can be seen that such simulations using vdW forces result in oscillations which contribute to the entropy change. In order to keep individual particle oscillations to a minimum, an XSPH variant [27] is introduced in the updating of particle
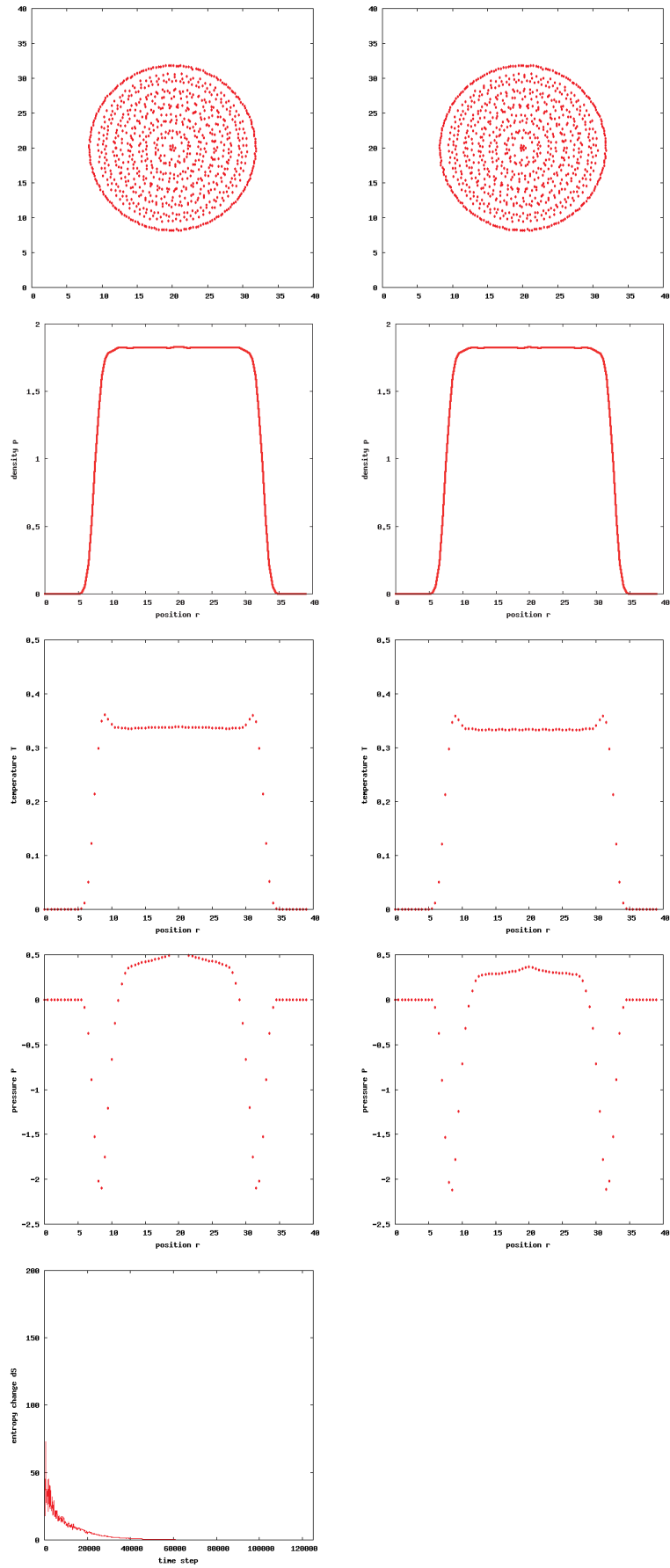
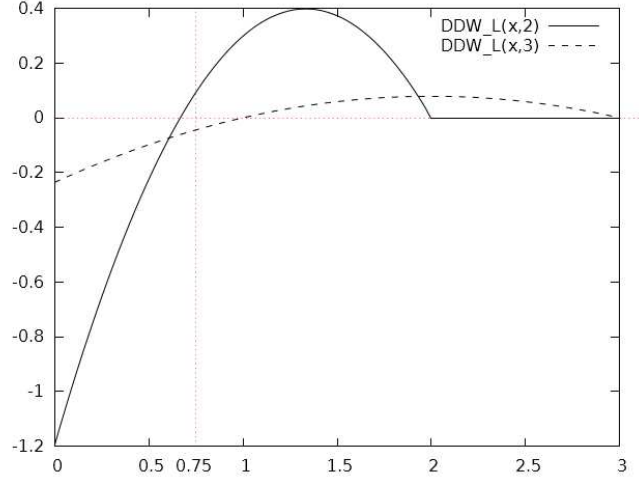Figure 4: h=3, H=6, kernel = Lucy at 60,000 (left column) and 122000 (right column) time steps.

9

Figure 5: The second derivative of Lucy's function DDW_L(x,h) with h = 2 (solid line) and h = 3 (dashed line). An initial particle spacing of 0.75 is marked with small dashes.

Table 1: The total entropy change and average temperature for the respective kernels and effective smoothing lengths.

	Lucy's function		Hyperbolic-shaped kernel		Cubic spline	
$\mathfrak{H}$	Total S	Average T	Total S	Average T	Total S	Average T
1.5	2215	0.2875	N/A	N/A	231	0.3145
1.75	1428	0.3141	1256	0.1857	421	0.3130
2.25	2277	0.3217	389	0.2606	3499	0.3189
2.5	1790.7	0.3277	896	0.2807	2296	0.3251
2.75	1580.7	0.3317	908.9	0.2942	5349	0.3274

Table 2: The total entropy change and average temperature for the respective kernels and effective smoothing lengths using Equation (30). The last row specifies that the domain consists of 35×35 particles instead of 30×30.

	Lucy's function		Hyperbolic-shaped kernel	
$\mathfrak{H}$	Total S	Average T	Total S	Average T
3.0	29.12	0.311	11.20	0.284
3.45	25.5	0.314	13.52	0.295
3.0 (35×35)	29.14	0.311	48.04	0.311

positions in the hopes that unnecessary oscillations of individual particles is sufficiently dampened. The application of XSPH involves an adjustment to the method of updating particle positions. We replace Eq. (1) with

$$\left(\frac{d\mathbf{r}}{dt}\right)_i = \mathbf{v}_i + \epsilon \sum_j \frac{m_j}{\rho_{ij}}(\mathbf{v}_j - \mathbf{v}_i)W_{ij} = \tilde{\mathbf{v}}_i \tag{30}$$

where $\rho_{ij} = 0.5(\rho_i + \rho_j)$. The results are given in Table (2). The effect of applying an average velocity through Eq. (30) is to reduce the capability of any single SPH particle to act alone. This way velocities and the effects of forces are smoothed resulting in a number of particles acting in response to that force. Artificial viscosity has also been introduced in some works [28] in the past to prevent post-shock oscillations. The positive parameter ϵ is a constant value less than 1. We choose $\epsilon = 0.1$. Simulations with this adjustment to the velocity, while reducing the disagreement between different smoothing lengths, the differences are still unacceptable. Increasing the number of particles within the domain and reducing the mass associated with each particle makes it possible to keep the mass within the kernel domain constant while increasing the number of interpolation points.
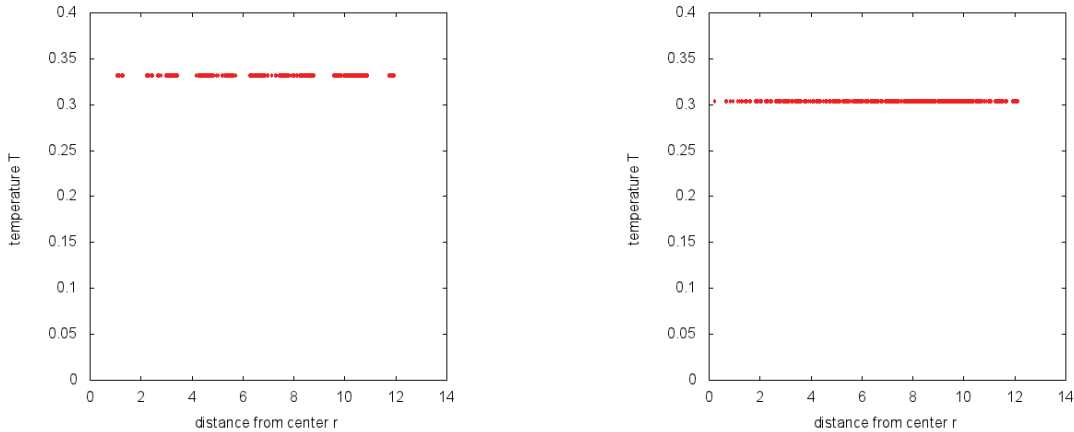

Figure 6: The temperature dependence on the radial distance from the centre of the vdW drop for the Lucy function with h = 2.75 (left) and the HS kernel with h = 1.5. Unsmoothed.

It can be seen from the results that different kernel functions perform better at different smoothing lengths. The density profiles given by the raw unsmoothed particle densities in Fig. 7 are smooth for all kernels. When the density profiles are calculated at arbitrary points in the domain it seems the density profiles for the HS kernel is not as smooth. This is due to the fixed, more rigid particle locations. At larger smoothing lengths/more particles, this effect is of lesser importance. However, Lucy's function does not suffer from this even though the particle spacing is more erratic. The generated density profile is always smooth even for relatively small smoothing lengths. This has also been reported previously on drops using an

11

equation of state different from vdW [29]. It is logical to assume that no matter the particle distributions, the forces through the equation of state will push toward an equilibrium where the particle densities are smooth (the raw particle densities of Fig. 7). However, the pressure profile generated for the HS kernel seems to always be smooth unlike that generated for Lucy's function and the CS kernel. The differences are seen when this data is translated through the smoothing function for arbitrary locations. Given enough time, the pressure profiles for CS and Lucy's function will eventually become smoother, however, HS evolves toward equilibrium with a smoother pressure profile. Application of Equation (30) to CS and Lucy's function results in their pressure profiles also being smoother throughout evolution. This reduces the total time steps required to achieve equilibrium considerably.
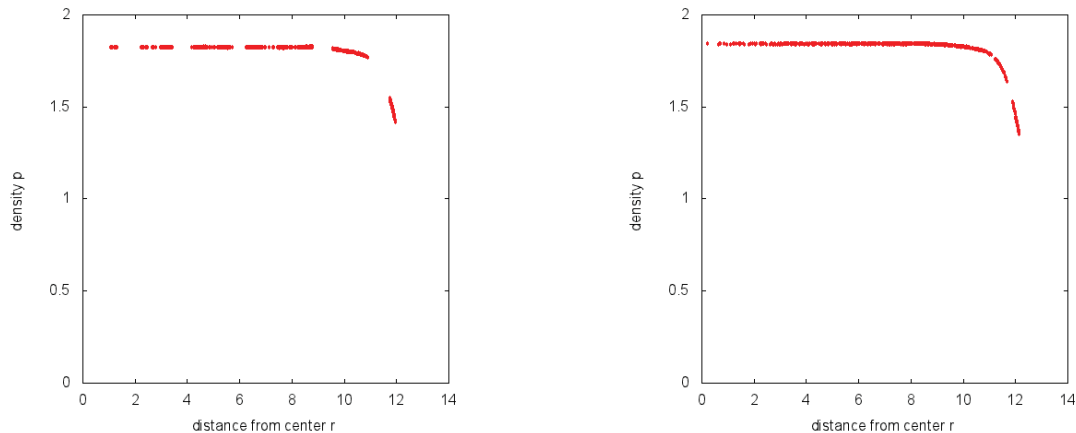

Figure 7: The mass density dependence on the radial distance from the centre of the vdW drop for the Lucy function with h = 2.75 (left) and the HS kernel with h = 1.5. Unsmoothed.

When the initial state of the system is placed out of equilibrium, as is the case here, the evolution toward equilibrium involves oscillations while forces tend toward a point in which they cancel each other. It is clear from Table (1) that a smaller h decreases oscillations and subsequently the total temperature change of the system during its evolution to the final equilibrium state. On a positive side note the SPH method reproduces this dampening effect such that the entropy change reaches zero in all cases. These effects can also be seen in the final temperature achieved since the viscous heating term generates heat through relative motion. A logical solution to this is to reduce the time step as equilibrium is approached to ensure the oscillations are the result of the evolution dynamics and not due to numerical effects. However, this leads to excessive simulation times. For the HS kernel, the particles move more as a group and so the local velocity gradients between neighboring particles are small. (notice for the Lucy and CS kernels with a smaller h have much lower average temperatures due to ordered particles.) Understandably, there isn't a relationship between the total entropy change and the smoothing length due to different clumping effects at different h.

6. Conclusion and remarks

It is seen from the results that Lucy's function, the CS and the HS kernels perform best at $\mathfrak{H} = 3.7\Delta x$, $\mathfrak{H} = 3\Delta x$ and $\mathfrak{H} = 4\Delta x$ respectively. If one requires a better approximation, we have seen that in the case of Lucy's function, an increase of interpolation points rather than an increase of the smoothing length is necessary since an increase of smoothing length does not give consistent results especially when the total entropy change is concerned. This is shown in Table (2). For the CS kernel the resulting value for the temperature for the 30×30 system at $\mathfrak{H} = 3$ is 0.310 with the total entropy change 14.09. The corresponding values for the 35×35 system is 0.310 and 17.25. However, increasing the smoothing length results

in a larger value discrepancy. Increasing the number of particles, unlike increasing the smoothing length, does not change the obtained temperature values for CS and Lucy's function. In addition to this, the radius of curvature to smoothing ratio remains constant. The HS kernel does not seem follow this trend. This is possibly due to its second derivative not being as steep as that for Lucy's function and CS.

When tensile instability is observed, comparison of the total entropy change becomes meaningless. This is due to the clumping of the SPH interpolation points. It is seen that application of an XSPH variant to the velocity calculation with a coefficient as small as $\epsilon = 0.1$ is sufficient in reducing some clumping. More importantly, the total entropy change becomes more consistent.

It is important for the evolution of a thermodynamic system to be associated with a stable and consistent entropy change rather than an entropy change that is large and erratic. Without the incorporation of Equation (30), the total entropy is very unpredictable since SPH particles vibrate excessively relative to one another. When it comes to the magnitude of the total entropy change, since the total volume change observed here is very small given the initial conditions and that we are dealing with a single phase fluid, we should not expect much rearrangement of mesoscopic fluid volumes hence the total entropy change should be small and certainly shouldn't be subjected to a smoothing length dependence which results in differences as seen from Table (1).

References

[1] L. Lucy, A numerical approach to the testing of the fission hypothesis, The astronomical journal 82 (12) (1977) 1013–1024.
   URL http://medcontent.metapress.com/index/A65RM03P4874243N.pdfhttp://adsabs.harvard.edu/full/1977AJ.....82.1013L7

[2] W. Benz, W. L. Slattery, A. G. W. Cameron, The origin of the moon and the single-impact hypothesis I., Icarus 66 (1986) 515–535.
   URL http://www.ncbi.nlm.nih.gov/pubmed/11542164

[3] W. Benz, W. L. Slattery, A. G. W. Cameron, The origin of the moon and the single-impact hypothesis II., Icarus 71 (1987) 30–45.
   URL http://www.ncbi.nlm.nih.gov/pubmed/11542164

[4] J. Monaghan, Particle methods for hydrodynamics, Computer Physics Reports 3 (2) (1985) 71–124. doi:10.1016/0167-7977(85)90010-3.
   URL http://linkinghub.elsevier.com/retrieve/pii/0167797785900103

[5] A. Kheyfets, W. Miller, W. Zurek, Covariant smoothed particle hydrodynamics on a curved background, Physical Review D 41 (2) (1990) 451–454.
   URL http://journals.aps.org/prd/abstract/10.1103/PhysRevD.41.451

[6] W. Benz, F. Thielemann, Convective instabilities in SN 1987A, The Astrophysical Journal 348 (1990) L17–L20.
    URL http://adsabs.harvard.edu/full/1990ApJ...348L..17B

[7] W. Benz, a. G. Cameron, H. J. Melosh, The origin of the moon and the single-impact hypothesis III., Icarus 81 (1989) 113–31.
    URL http://www.ncbi.nlm.nih.gov/pubmed/11542164

[8] W. Benz, R. Bowers, A. Cameron, W. Press, Dynamic mass exchange in doubly degenerate binaries. I-0.9 and 1.2 solar mass stars, The Astrophysical . . . 348 (1990) 647–667.
    URL http://adsabs.harvard.edu/full/1990ApJ...348..647B

[9] S. Ostrach, Low-Gravity Fluid Flows, Annual Review of Fluid Mechanics 14 (1) (1982) 313–345. doi:10.1146/annurev.fl.14.010182.001525.
    URL http://www.annualreviews.org/doi/abs/10.1146/annurev.fl.14.010182.001525

[10] A. Myshkis, V. Babskii, N. Kopachevskii, L. Slobozhanin, A. Tyuuptsov, Low-Gravity fluid mechanics.pdf, Springer-Verlag, New York, 1987.

[11] E. Oran, J. Boris, Numerical simulation of reactive flow, Elsevier, 2005.
    URL http://books.google.com/books?hl=en&lr=&id=6KzA7QBvoNwC&oi=fnd&pg=PP1&dq=Numerical+Simulation+of+reactive+flow&ots=jWSW3PCC3i&sig=AM5iqUTq2hWdyUn9OOOWobvbJZE

[12] H. Pruppacher, J. Klett, Microphysics of Clouds and Precipitation, Vol. 18 of Atmospheric and Oceanographic Sciences Library, Springer Netherlands, Dordrecht, 2010. doi:10.1007/978-0-306-48100-0.
    URL http://link.springer.com/10.1007/978-0-306-48100-0

[13] G. Batchelor, An introduction to fluid dynamics, Cambridge University Press, Cambridge, 2000.

[14] R. Qin, Mesoscopic interparticle potentials in the lattice Boltzmann equation for multiphase fluids, Physical Review E 73 (6) (2006) 066703. doi:10.1103/PhysRevE.73.066703.
    URL http://link.aps.org/doi/10.1103/PhysRevE.73.066703

[15] R. S. Qin, Bubble formation in lattice Boltzmann immiscible shear flow., The Journal of chemical physics 126 (11) (2007) 114506. doi:10.1063/1.2711433.
    URL http://www.ncbi.nlm.nih.gov/pubmed/17381219

[16] J. Brackbill, D. Kothe, C. Zemach, A continuum method for modeling surface tension, Journal of computational physics 100 (1992) 335–354.
    URL http://www.sciencedirect.com/science/article/pii/002199919290240Y

[17] J. P. Morris, A Study of the Stability Properties of Smooth Particle Hydrodynamics, Pub. Astron. Soc. of Australia 13 (1) (1996) 97–102.

[18] G. R. Johnson, R. a. Stryk, S. R. Beissel, SPH for high velocity impact computations, Computer Methods in Applied Mechanics and Engineering 139 (1-4) (1996) 347–373. doi:10.1016/S0045-7825(96)01089-4.
    URL http://linkinghub.elsevier.com/retrieve/pii/S0045782596010894

[19] J. Monaghan, J. Lattanzio, A refined particle method for astrophysical problems, Astronomy and astrophysics 149 (1985) 135–143.
URL `http://adsabs.harvard.edu/full/1985A%26A...149..135M`

[20] X. Yang, M. Liu, S. Peng, Smoothed particle hydrodynamics modeling of viscous liquid drop without tensile instability, Computers & Fluids (January). `doi:10.1016/j.compfluid.2014.01.002`.
URL `http://linkinghub.elsevier.com/retrieve/pii/S0045793014000036`

[21] J. Monaghan, Smoothed Particle Hydrodynamics, Annual Review of Astronomy and Astrophysics 30 (1) (1992) 543–574. `doi:10.1146/annurev.astro.30.1.543`.
URL `http://astro.annualreviews.org/cgi/doi/10.1146/annurev.astro.30.1.543`

[22] H. Posch, W. Hoover, Simulation of two-dimensional Kolmogorov flow with smooth particle applied mechanics, Physica A: Statistical Mechanics and its . . . 240 (1997) 286–296.
URL `http://www.sciencedirect.com/science/article/pii/S0378437197001520`

[23] P. Español, M. Revenga, Smoothed dissipative particle dynamics, Physical Review E 67 (2) (2003) 026705. `doi:10.1103/PhysRevE.67.026705`.
URL `http://link.aps.org/doi/10.1103/PhysRevE.67.026705`

[24] S. Nugent, H. Posch, Liquid drops and surface tension with smoothed particle applied mechanics, Physical review. E, Statistical physics, plasmas, fluids, and related interdisciplinary topics 62 (4 Pt A) (2000) 4968–75.
URL `http://www.ncbi.nlm.nih.gov/pubmed/11089045`

[25] J. J. Monaghan, Smoothed particle hydrodynamics, Reports on Progress in Physics 68 (8) (2005) 1703–1759. `doi:10.1088/0034-4885/68/8/R01`.
URL `http://stacks.iop.org/0034-4885/68/i=8/a=R01?key=crossref.c562820df517a049ca7f11d0aefe49b4`

[26] J. Swegle, D. Hicks, S. Attaway, Smoothed particle hydrodynamics stability analysis, Journal of computational physics 134 (1995) 123–134.
URL `http://www.sciencedirect.com/science/article/pii/S0021999185710108`

[27] J. Monaghan, On the problem of penetration in particle methods, Journal of Computational Physics 82 (1) (1989) 1–15. `doi:10.1016/0021-9991(89)90032-6`.
URL `http://linkinghub.elsevier.com/retrieve/pii/0021999189900326`

[28] T. Olson, W. Hiscock, Stability, causality, and hyperbolicity in Carter's" regular" theory of relativistic heat-conducting fluids, Physical Review D 41 (12).
URL `http://journals.aps.org/prd/abstract/10.1103/PhysRevD.41.3687`

[29] W. Hoover, T. Pierce, C. Hoover, Molecular dynamics, smoothed-particle applied mechanics, and irreversibility, . . . & Mathematics with . . . 28 (19) (1994) 155–174.
URL `http://www.sciencedirect.com/science/article/pii/089812219400191X`

15
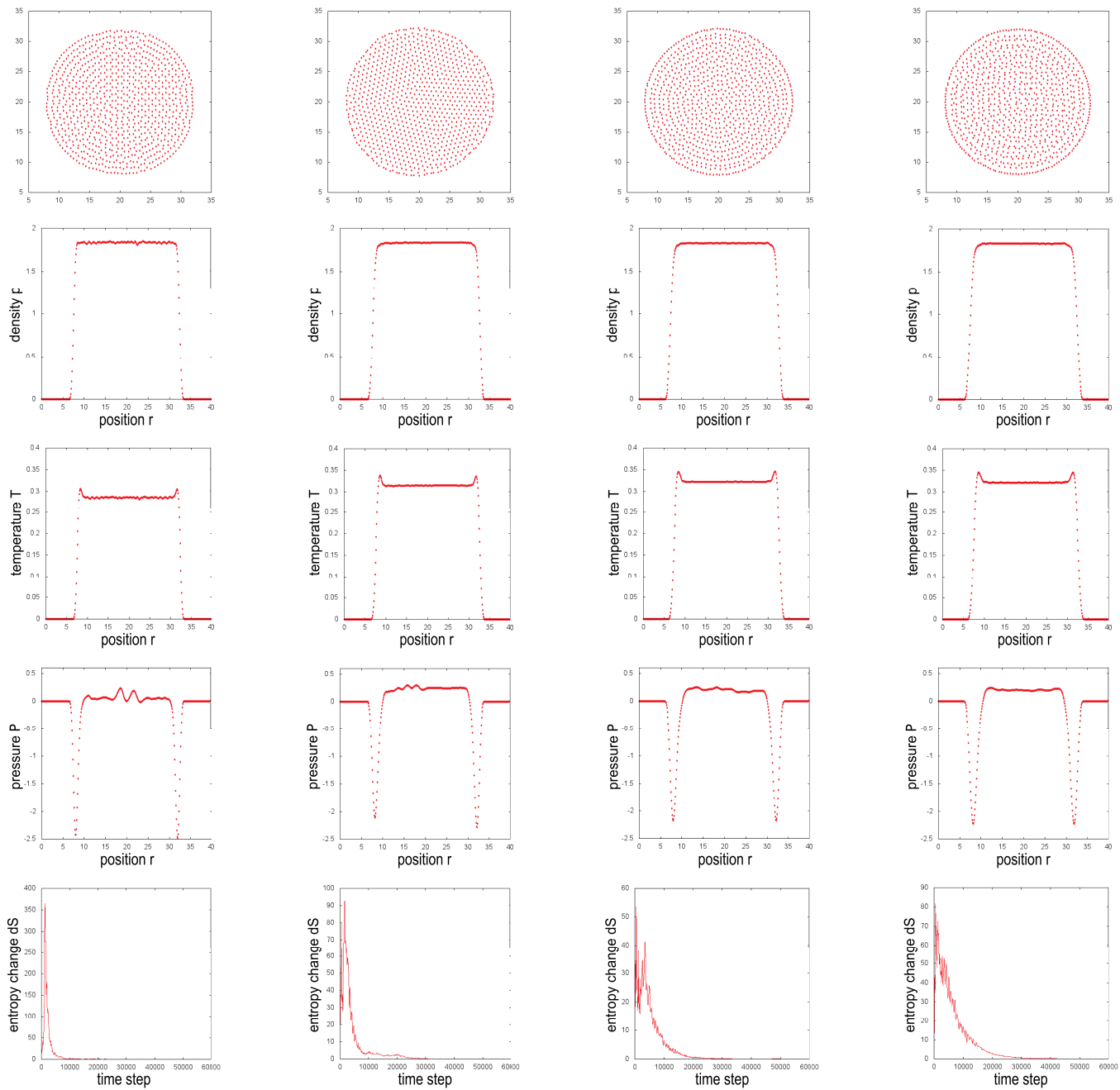
Figure 8: Lucy's function results for h=1.5 at 85,500 time steps (left column), h = 1.75 at 106,500 time steps (second column), h = 2 at 145,000 time steps (third column) and h = 2.25 at 133,500 time steps (fourth column)

Figure 9: Lucy's function results for h = 2.5 at 172,500 time steps (first column), h = 2.75 at 148,500 time steps (second column) and h = 3 at 206,000 time steps (last column)

17

Figure 10: The HS results for h=0.75 at 150 time steps (left column), h=0.875 at 500,000+ time steps (second column), h=1 at 140,000 time steps (third column) and h=1.125 at 165,000 time steps (last column). The system becomes unstable for h=0.75. (500,000+ indicates more time steps are required to achieve $dS < 0.0001$.)
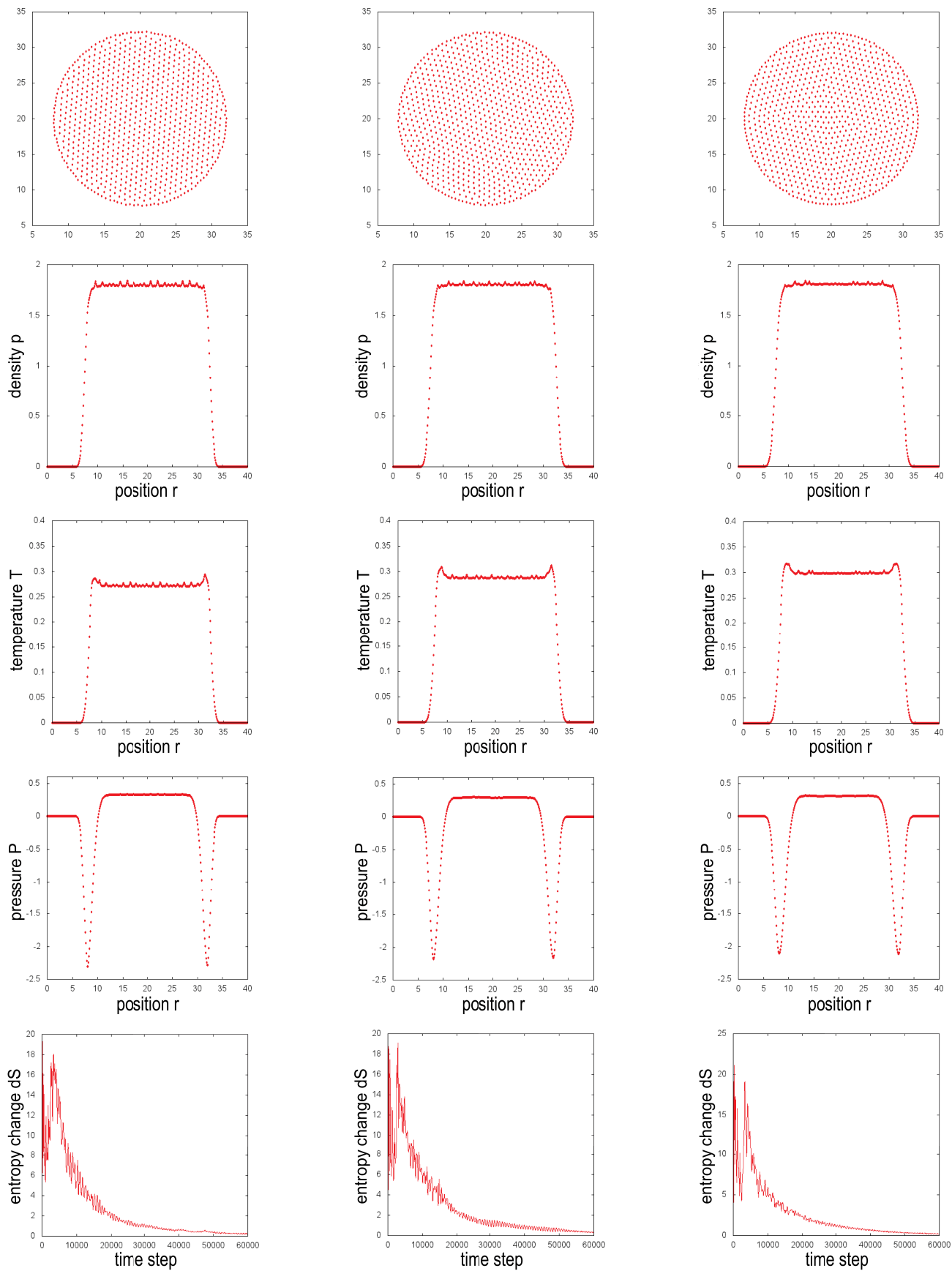
Figure 11: The HS results for h=1.25 at 281,500 time steps (second column), h=1.375 at 322,500 time steps (third column), h=1.5 at 273,500 time steps (last column)

19

Figure 12: The CS results for h=0.75 at 90,500 time steps (left column), h=0.875 at 500,000+ time steps (second column), h=1 at 140,000 time steps (t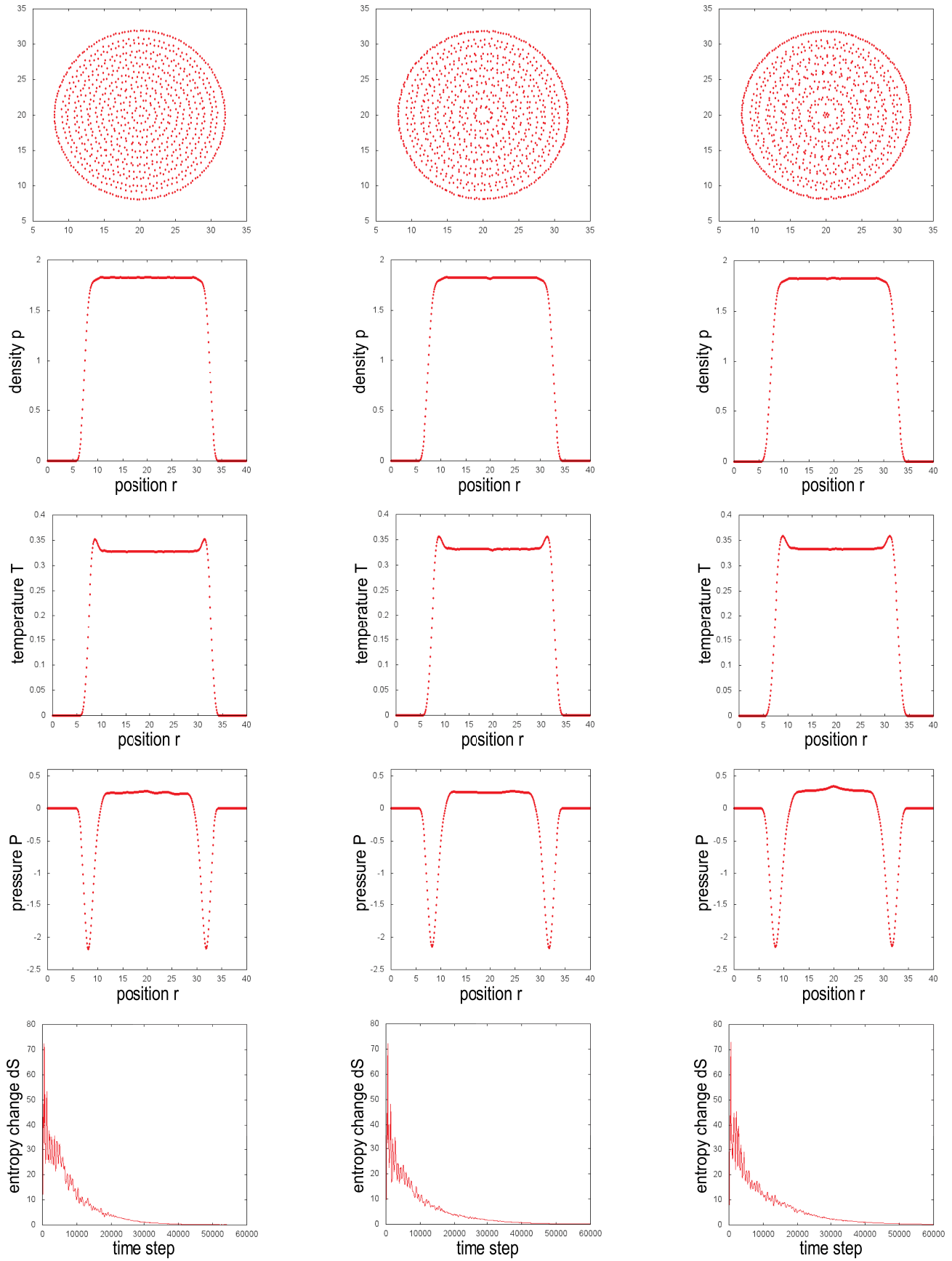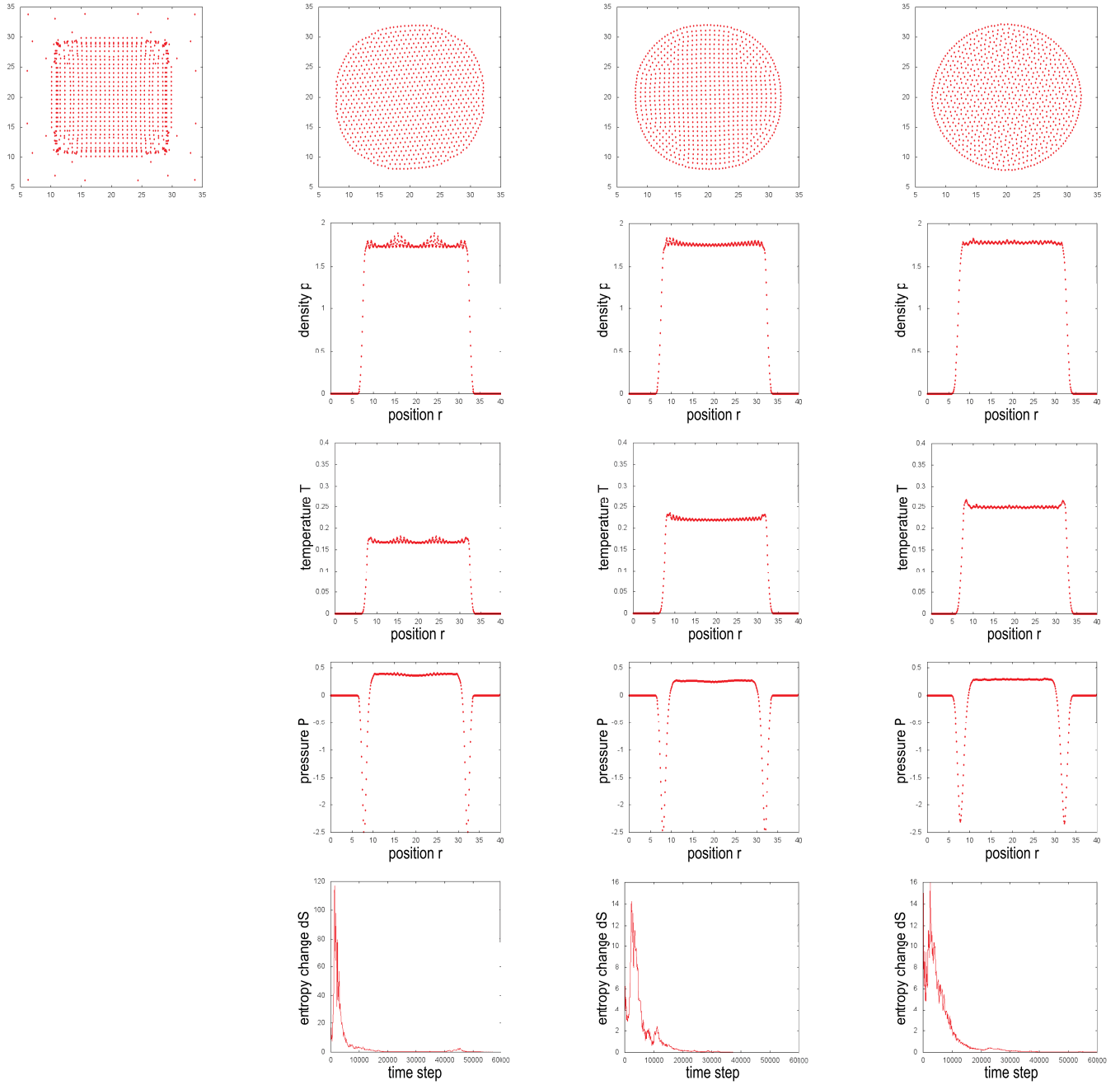hird column) and h=1.125 at 165,000 time steps (last column). (500,000+ indicates more time steps are required to achieve $dS < 0.0001$.)

20

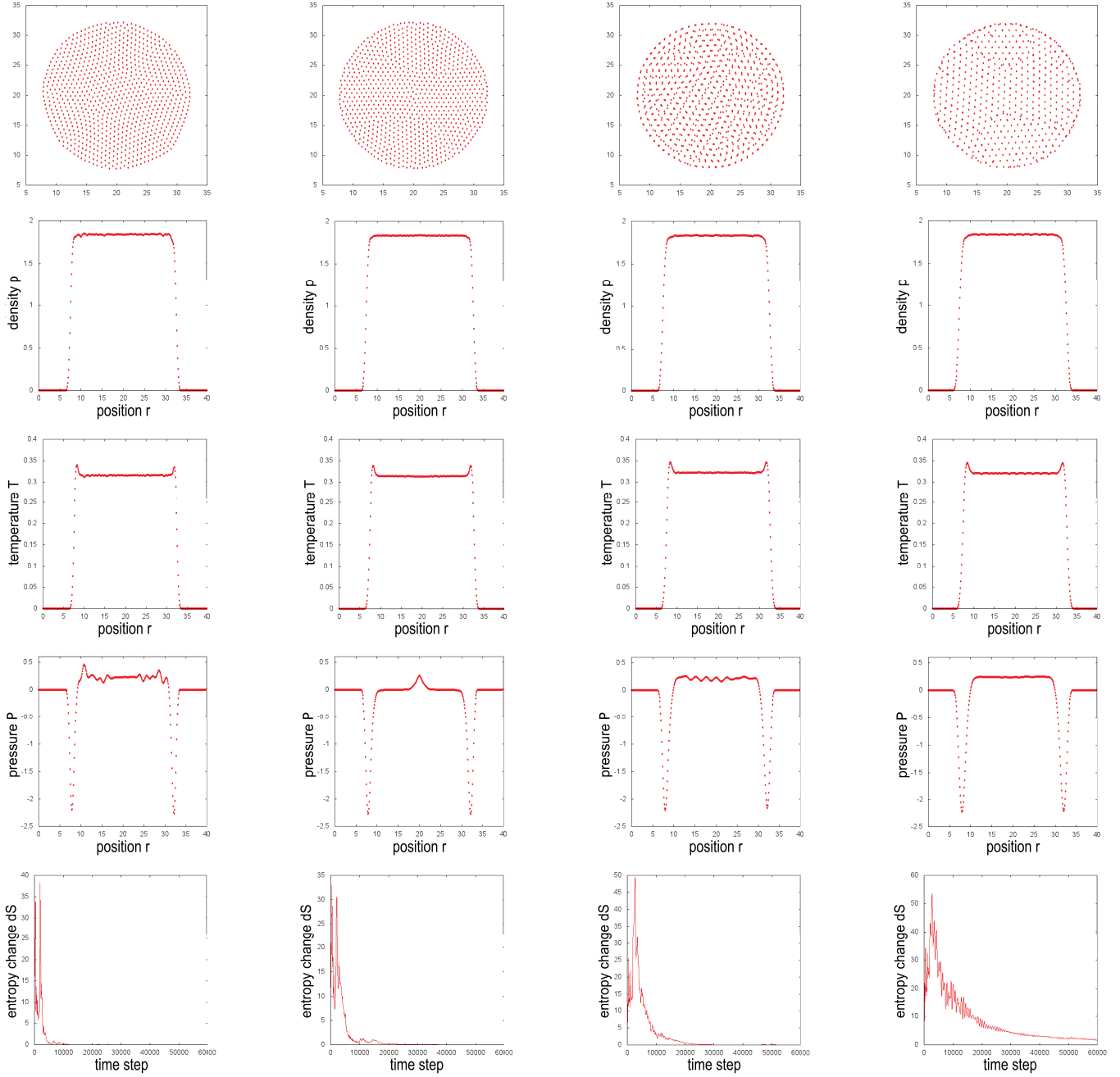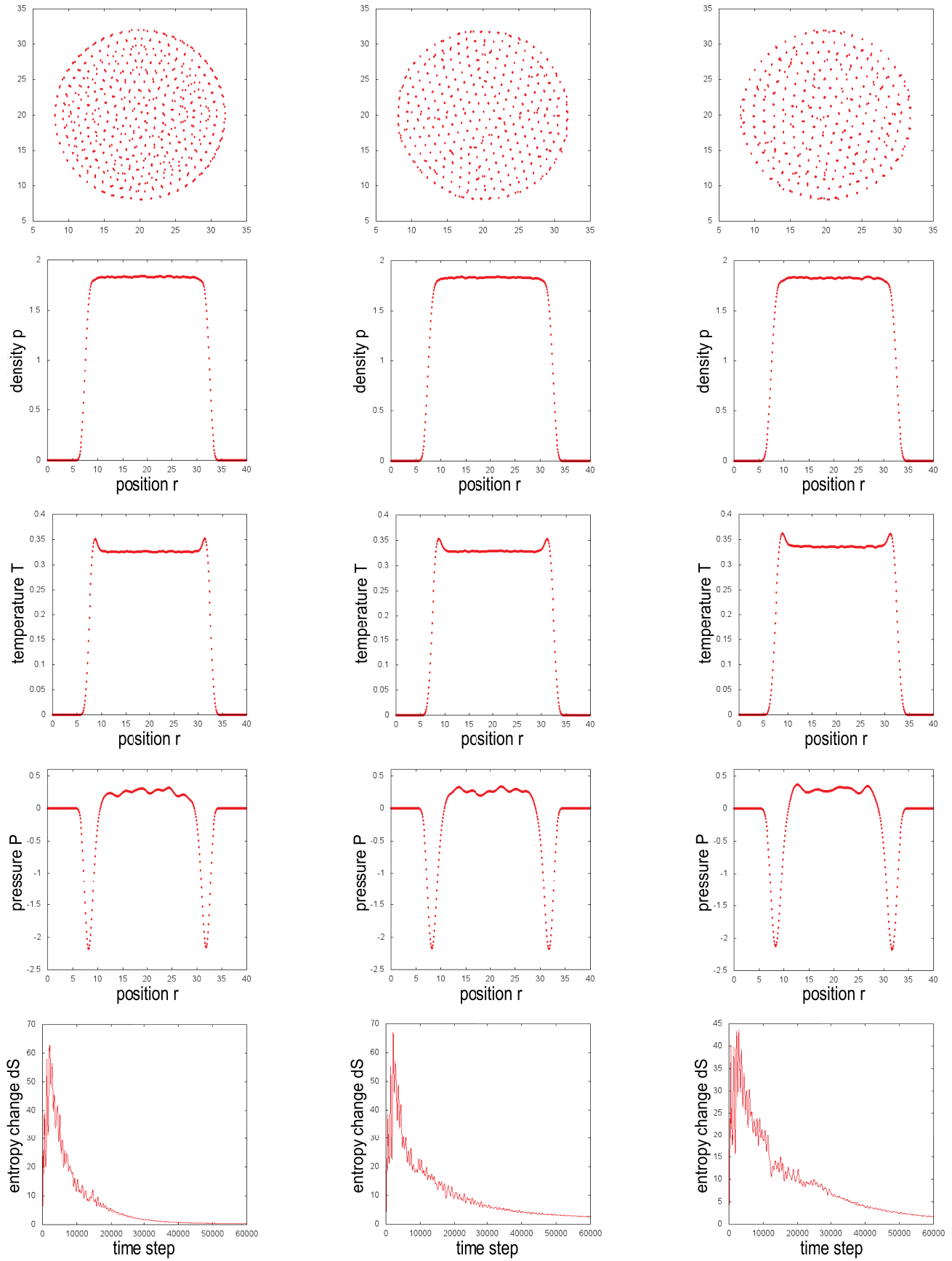Figure 13: The CS results for h=1.25 at 500,000+ time steps (left column), h=1.375 at 500,000+ time steps (second column), h=1.5 at 500,000+ time steps (third column). (500,000+ indicates more time steps are required to achieve $dS < 0.0001$.)

21

Appendix H

Permissions

ELSEVIER LICENSE
TERMS AND CONDITIONS

Feb 12, 2015

This is a License Agreement between Tansel T Arif ("You") and Elsevier ("Elsevier") provided by Copyright Clearance Center ("CCC"). The license consists of your order details, the terms and conditions provided by Elsevier, and the payment terms and conditions.

All payments must be made in full to CCC. For payment instructions, please see information listed at the bottom of this form.

Supplier	Elsevier Limited The Boulevard,Langford Lane Kidlington,Oxford,OX5 1GB,UK
Registered Company Number	1982084
Customer name	Tansel T Arif
Customer address	46 Bousfield Road
	London, SE14 5TR
License number	3566561432031
License date	Feb 12, 2015
Licensed content publisher	Elsevier
Licensed content publication	Computational Materials Science
Licensed content title	A phase-field model for bainitic transformation
Licensed content author	None
Licensed content date	September 2013
Licensed content volume number	77
Licensed content issue number	n/a
Number of pages	6
Start Page	230
End Page	235
Type of Use	reuse in a thesis/dissertation
Intended publisher of new work	other
Portion	full article
Format	both print and electronic
Are you the author of this Elsevier article?	Yes
Will you be translating?	No
Title of your thesis/dissertation	Mesoscale modelling of steel processing
Expected completion date	Apr 2015
Estimated size (number of	227

pages)

Elsevier VAT number	GB 494 6272 12
Permissions price	0.00 GBP
VAT/Local Sales Tax	0.00 GBP / 0.00 GBP
Total	0.00 GBP

Terms and Conditions

INTRODUCTION

1. The publisher for this copyrighted material is Elsevier. By clicking "accept" in connection with completing this licensing transaction, you agree that the following terms and conditions apply to this transaction (along with the Billing and Payment terms and conditions established by Copyright Clearance Center, Inc. ("CCC"), at the time that you opened your Rightslink account and that are available at any time at http://myaccount.copyright.com).

GENERAL TERMS

2. Elsevier hereby grants you permission to reproduce the aforementioned material subject to the terms and conditions indicated.

3. Acknowledgement: If any part of the material to be used (for example, figures) has appeared in our publication with credit or acknowledgement to another source, permission must also be sought from that source. If such permission is not obtained then that material may not be included in your publication/copies. Suitable acknowledgement to the source must be made, either as a footnote or in a reference list at the end of your publication, as follows:

"Reprinted from Publication title, Vol /edition number, Author(s), Title of article / title of chapter, Pages No., Copyright (Year), with permission from Elsevier [OR APPLICABLE SOCIETY COPYRIGHT OWNER]." Also Lancet special credit - "Reprinted from The Lancet, Vol. number, Author(s), Title of article, Pages No., Copyright (Year), with permission from Elsevier."

4. Reproduction of this material is confined to the purpose and/or media for which permission is hereby given.

5. Altering/Modifying Material: Not Permitted. However figures and illustrations may be altered/adapted minimally to serve your work. Any other abbreviations, additions, deletions and/or any other alterations shall be made only with prior written authorization of Elsevier Ltd. (Please contact Elsevier at permissions@elsevier.com)

6. If the permission fee for the requested use of our material is waived in this instance, please be advised that your future requests for Elsevier materials may attract a fee.

7. Reservation of Rights: Publisher reserves all rights not specifically granted in the combination of (i) the license details provided by you and accepted in the course of this licensing transaction, (ii) these terms and conditions and (iii) CCC's Billing and Payment terms and conditions.

8. License Contingent Upon Payment: While you may exercise the rights licensed immediately upon issuance of the license at the end of the licensing process for the transaction, provided that you have disclosed complete and accurate details of your proposed use, no license is finally effective unless and until full payment is received from you (either by publisher or by CCC) as provided in CCC's Billing and Payment terms and conditions. If full payment is not received on a timely basis, then any

license preliminarily granted shall be deemed automatically revoked and shall be void as if never granted. Further, in the event that you breach any of these terms and conditions or any of CCC's Billing and Payment terms and conditions, the license is automatically revoked and shall be void as if never granted. Use of materials as described in a revoked license, as well as any use of the materials beyond the scope of an unrevoked license, may constitute copyright infringement and publisher reserves the right to take any and all action to protect its copyright in the materials.

9. Warranties: Publisher makes no representations or warranties with respect to the licensed material.

10. Indemnity: You hereby indemnify and agree to hold harmless publisher and CCC, and their respective officers, directors, employees and agents, from and against any and all claims arising out of your use of the licensed material other than as specifically authorized pursuant to this license.

11. No Transfer of License: This license is personal to you and may not be sublicensed, assigned, or transferred by you to any other person without publisher's written permission.

12. No Amendment Except in Writing: This license may not be amended except in a writing signed by both parties (or, in the case of publisher, by CCC on publisher's behalf).

13. Objection to Contrary Terms: Publisher hereby objects to any terms contained in any purchase order, acknowledgment, check endorsement or other writing prepared by you, which terms are inconsistent with these terms and conditions or CCC's Billing and Payment terms and conditions. These terms and conditions, together with CCC's Billing and Payment terms and conditions (which are incorporated herein), comprise the entire agreement between you and publisher (and CCC) concerning this licensing transaction. In the event of any conflict between your obligations established by these terms and conditions and those established by CCC's Billing and Payment terms and conditions, these terms and conditions shall control.

14. Revocation: Elsevier or Copyright Clearance Center may deny the permissions described in this License at their sole discretion, for any reason or no reason, with a full refund payable to you. Notice of such denial will be made using the contact information provided by you. Failure to receive such notice will not alter or invalidate the denial. In no event will Elsevier or Copyright Clearance Center be responsible or liable for any costs, expenses or damage incurred by you as a result of a denial of your permission request, other than a refund of the amount(s) paid by you to Elsevier and/or Copyright Clearance Center for denied permissions.

LIMITED LICENSE

The following terms and conditions apply only to specific license types:

15. **Translation**: This permission is granted for non-exclusive world **English** rights only unless your license was granted for translation rights. If you licensed translation rights you may only translate this content into the languages you requested. A professional translator must perform all translations and reproduce the content word for word preserving the integrity of the article. If this license is to re-use 1 or 2 figures then permission is granted for non-exclusive world rights in all languages.

16. **Posting licensed content on any Website**: The following terms and conditions apply as follows: Licensing material from an Elsevier journal: All content posted to the web site must maintain the copyright information line on the bottom of each image; A hyper-text must be included

to the Homepage of the journal from which you are licensing at
http://www.sciencedirect.com/science/journal/xxxxx or the Elsevier homepage for books at
http://www.elsevier.com; Central Storage: This license does not include permission for a scanned
version of the material to be stored in a central repository such as that provided by Heron/XanEdu.

Licensing material from an Elsevier book: A hyper-text link must be included to the Elsevier
homepage at http://www.elsevier.com . All content posted to the web site must maintain the
copyright information line on the bottom of each image.

Posting licensed content on Electronic reserve: In addition to the above the following clauses
are applicable: The web site must be password-protected and made available only to bona fide
students registered on a relevant course. This permission is granted for 1 year only. You may obtain
a new license for future website posting.

17.**For journal authors:** the following clauses are applicable in addition to the above: Permission
granted is limited to the author accepted manuscript version* of your paper.

*Accepted Author Manuscript (AAM) Definition: An accepted author manuscript (AAM) is
the author's version of the manuscript of an article that has been accepted for publication and which
may include any author-incorporated changes suggested through the processes of submission
processing, peer review, and editor-author communications. AAMs do not include other publisher
value-added contributions such as copy-editing, formatting, technical enhancements and (if
relevant) pagination.

You are not allowed to download and post the published journal article (whether PDF or HTML,
proof or final version), nor may you scan the printed edition to create an electronic version. A
hyper-text must be included to the Homepage of the journal from which you are licensing at
http://www.sciencedirect.com/science/journal/xxxxx. As part of our normal production process,
you will receive an e-mail notice when your article appears on Elsevier's online service
ScienceDirect (www.sciencedirect.com). That e-mail will include the article's Digital Object
Identifier (DOI). This number provides the electronic link to the published article and should be
included in the posting of your personal version. We ask that you wait until you receive this e-mail
and have the DOI to do any posting.

18.**Posting to a repository:** Authors may post their AAM immediately to their employer's
institutional repository for internal use only and may make their manuscript publically available after
the journal-specific embargo period has ended.

Please also refer to Elsevier's Article Posting Policy for further information.

19. **For book authors** the following clauses are applicable in addition to the above: Authors are
permitted to place a brief summary of their work online only.. You are not allowed to download
and post the published electronic version of your chapter, nor may you scan the printed edition to
create an electronic version. **Posting to a repository:** Authors are permitted to post a summary of
their chapter only in their institution's repository.

20. **Thesis/Dissertation**: If your license is for use in a thesis/dissertation your thesis may be
submitted to your institution in either print or electronic form. Should your thesis be published
commercially, please reapply for permission. These requirements include permission for the Library
and Archives of Canada to supply single copies, on demand, of the complete thesis and include
permission for Proquest/UMI to supply single copies, on demand, of the complete thesis. Should

your thesis be published commercially, please reapply for permission.

Elsevier Open Access Terms and Conditions

Elsevier publishes Open Access articles in both its Open Access journals and via its Open Access articles option in subscription journals.

Authors publishing in an Open Access journal or who choose to make their article Open Access in an Elsevier subscription journal select one of the following Creative Commons user licenses, which define how a reader may reuse their work: Creative Commons Attribution License (CC BY), Creative Commons Attribution – Non Commercial - ShareAlike (CC BY NC SA) and Creative Commons Attribution – Non Commercial – No Derivatives (CC BY NC ND)

Terms & Conditions applicable to all Elsevier Open Access articles:

Any reuse of the article must not represent the author as endorsing the adaptation of the article nor should the article be modified in such a way as to damage the author's honour or reputation.

The author(s) must be appropriately credited.

If any part of the material to be used (for example, figures) has appeared in our publication with credit or acknowledgement to another source it is the responsibility of the user to ensure their reuse complies with the terms and conditions determined by the rights holder.

Additional Terms & Conditions applicable to each Creative Commons user license:

CC BY: You may distribute and copy the article, create extracts, abstracts, and other revised versions, adaptations or derivative works of or from an article (such as a translation), to include in a collective work (such as an anthology), to text or data mine the article, including for commercial purposes without permission from Elsevier

CC BY NC SA: For non-commercial purposes you may distribute and copy the article, create extracts, abstracts and other revised versions, adaptations or derivative works of or from an article (such as a translation), to include in a collective work (such as an anthology), to text and data mine the article and license new adaptations or creations under identical terms without permission from Elsevier

CC BY NC ND: For non-commercial purposes you may distribute and copy the article and include it in a collective work (such as an anthology), provided you do not alter or modify the article, without permission from Elsevier

Any commercial reuse of Open Access articles published with a CC BY NC SA or CC BY NC ND license requires permission from Elsevier and will be subject to a fee.

Commercial reuse includes:

- Promotional purposes (advertising or marketing)

- Commercial exploitation (e.g. a product for sale or loan)

- Systematic distribution (for a fee or free of charge)

Please refer to Elsevier's Open Access Policy for further information.

21. **Other Conditions**:

v1.7

Questions? customercare@copyright.com or +1-855-239-3415 (toll free in the US) or +1-978-646-2777.

Gratis licenses (referencing $0 in the Total field) are free. Please retain this printable license for your reference. No payment is required.